INÊS MOREIRA TENENTE

The role of Myogenic Regulatory Factors in Rhabdomyosarcoma: insights from zebrafish and beyond

Tese de Candidatura ao grau de Doutor em Biologia Básica e Aplicada submetida ao Instituto de Ciências Biomédicas Abel Salazar da Universidade do Porto.

Orientador: Doutor David M. Langenau
Categoria: Associate Professor
Afiliação: Harvard Medical School /Massachusetts General Hospital

Co-orientador: Doutor João Carlos Bettencourt de Medeiros Relvas
Categoria: Investigador Principal
Afiliação: Instituto de Biologia Molecular e Celular/Instituto de Inovação e Investigação em Saúde

Acknowledgments

> "The Society of Knowledge demands several things from us: truth; tolerance from and to others; humility because time and new technologies might prove us wrong in the future; and pride for being the first to have seen the truth or fought for the truth."
>
> *Maria de Sousa*
> *at the event 'Women in Science', Ciência Viva*
> *(Lisbon, March 8th, 2015)*

My path to Here and Now is filled with challenges and accomplishments, failures and successes, dullness and excitement. This road to Growth wouldn't have been complete without the important people in my life, from whom I learn so much.

First, my parents, brothers and family, who support me at every step and are a constant reminder to what should really matter in life and are always close, even at distance. One misses out on family events, on the growth of children, and only with the strength of unconditional love our paths remain tied in a close knot. I thank you all for that.

Samuel, thank you for being the Alberto Caeiro in my life, for being the Quiet of my Disquiet, for just Being a constant in the inconstant life. As Caeiro wrote: "Para alèm da curva da estrada/ Talvez haja um poço, e talvez um castelo,/ E talvez apenas a continuação da estrada. /Não sei nem pergunto.". We'll go together.

Moving to another country teaches us more about ourselves than anything else. That is what I said when interviewing for the GABBA Program - "I want to grow as a scientist and as a person". Growing at distance is a challenge to friendships. I am amazingly fortunate to have real friends in my life, which teach me every day more about myself and are always there, in a succession of virtual and face-to-face moments that I remember and cherish like photographs in a

beautiful album. As a Citizen of the World, I will now leave behind new friends, who made me feel like Home. I hope to meet you all again soon on the "other side of the pond".

Obviously, this would not have been possible without GABBA. More than a PhD Program, GABBA gave me the opportunity to learn, to question critically, to be among the best citizens of the Society of Knowledge, and to be part of the family. Yes, the GABBA family (particularly my GABBA 14th edition) exceeds any expectation of a sense of belonging in the pursuit of the Truths. The words of the All Time GABBAs and the program Founders and Scientific Committee members are always the best inspiration. A particular thank you to the program directors over the years, Prof. Dr. Alexandre do Carmo and Prof. Dr. António Amorim, to my always present co-advisor Prof. Dr. João Relvas and to Catarina Carona, without whom none of it would be possible.

I would like to finish by thanking my advisor David M. Langenau for the opportunity to join his lab and lead this challenging project. To all current and former members of the Langenau Lab, thank you for everything you taught me. Also, to the MGH and the Boston area scientific community, including Dr. A. Thomas Look, Dr. Leonard Zon, Dr. Amy Wagers, Dr. Louis Kunkel and Dr. Mathew Alexander, Molecular Pathology Unit and Center for Cancer Research faculty and fellows. As Prof. Maria de Sousa nicely puts it: "*Your peers, regardless of whether they work at a near bench or in a near continent, are your most important support. They are the ones who will try to corroborate your results*". Thank you all for raising questions along the way and helping me learn the necessary tools to answer them to the best of my abilities.

Aos meus pais,
Teresa e Luís

Resumo

O Rabdomiosarcoma (RMS) ẽ o sarcoma mais comum em crianças e caracteriza-se pela expressão de proteínas de músculo esquelético, como os fatores de transcrição miogénicos (MYF5, MYOD1, MYOG e MRF4/MYF6) e as proteínas estruturais Desmina e Miosina. O tratamento agressivo é eficaz em eliminar células com capacidade de auto-renovação, mas conduz frequentemente a elevada toxicidade. As células com capacidade de auto-renovação que evadem o tratamento conduzem a recidivas. É portanto importante investigar os mecanismos que regulam estas células em Rabdomiosarcomas, para que se possam desenvolver tratamentos direcionados e menos tóxicos que efetivamente eliminem estas células, prevenindo recidivas.

Foi desenvolvido previamente um modelo de peixe-zebra que recapitula morfologicamente e em termos moleculares o subtipo histológico Rabdomiosarcoma embrionário (ERMS). Através da análise molecular das células destes tumores identificou-se uma sub-população de células com capacidade de auto-renovação que expressa o fator de transcrição miogénico MYF5 e um conjunto de genes característicos de células satélite do músculo ativadas. Dado que MYF5 e MYOD1 são necessários para o desenvolvimento embrionário de músculo, e aos papéis que desempenham na auto-renovação de células satélite no processo regenerativo, nós postulámos que estes genes e os seus genes-alvo podem ser responsáveis por induzir programas de auto-renovação numa sub-população de células destes tumores. Através da utilização de uma série de peixes-zebra transgénicos multi-coloridos, em que diferentes sub-populações de células do tumor são distinguidas com base na expressão de genes de diferentes estádios de diferenciação, visuaizámos populações distintas de células em proliferação e com capacidade de auto-renovação que expressam MYF5 e células migratórias que expressam MYOG, *in vivo*. Adicionalmente, mostrámos funcionalmente que MYF5 é um marcador destas células propagadoras de tumores ou TPCs em RMS.

Para além de ser um marcador, mostramos ainda que MYF5 é capaz de induzir esta capacidade de auto-renovação a células diferenciadas contidas nos RMSs no modelo de peixe-zebra. Estes tumores surgem mais cedo, com maior

penetrância e são tendencialmente maiores do que os tumores-controlo. Consistentemente com os papéis redundantes de MYF5 e MYOD1 nos processos de desenvolvimento, regeneração e auto-renovação de células estaminais de músculo, indentificámos a existência de duas classes de ERMS em células humanas, expressando níveis mais elevados de um ou outro destes fatores. Ambos os fatores são necessários para progressão no ciclo celular, viabilidade e crescimento *in vitro* e/ou *in vivo*. Através da técnica ChIP-seq, observámos ainda que MYF5 e MYOD1 se ligam a elementos regulatórios comuns no ADN relacionados com estados de diferenciação muscular e progressão no ciclo celular.

Propomos assim um modelo em que MYF5 e MYOD1 regulam programas moleculares comuns de auto-renovação e crescimento em Rabdomiosarcoma, à semelhança da redundância dos seus papéis no desenvolvimento e regeneração de músculo. Em suma, os nosso dados são consistentes com a ideia de que vias de auto-renovação em tumores são semelhantes às de células estaminais do tecido não-maligno e de que estes processos são ativados aberrantemente durante a transformação maligna, um conceito emergente na biologia do cancro.

Palavras Chave

Rabdomiosarcoma; MYF5; MYOD; Músculo; Cancro; Células Estaminais; Peixe-zebra

Abstract

Rhabdomyosarcoma (RMS) is the most common pediatric sarcoma with skeletal muscle differentiation features, such as the expression of Myogenic Regulatory Factors (MRFs) (MYF5, MYOD1, MYOG, MRF4/MYF6) and skeletal muscle structural proteins (Desmin and Myosin). The aggressive treatment regimen eliminates self-renewing cells, but often leads to toxicity. Remaining self-renewing cells can evade treatment and lead to relapse. Understanding the molecular mechanisms of self-renewing cells in these cancers is thus paramount for the development of less toxic, targeted treatments that effectively eliminate these cells to prevent relapse.

A transgenic zebrafish model that is morphologically and molecularly similar to the human ERMS subtype was developed previously. Molecular analysis of mononuclear ERMS cells identified a sub-population of self-renewing tumor cells that is most similar to a MYF5-expressing, activated satellite cell. Given that MYF5 and MYOD1 are required for normal muscle development, are involved in muscle regeneration, and have roles in satellite cell self-renewal, we hypothesized that these genes and their transcriptional targets are responsible for eliciting stem cell self-renewal programs in a subset of ERMS cells. Through a series of transgenic multi-colour zebrafish, where sub-populations of RMS cells are labelled based on the expression of muscle differentiation markers, we were able to image discrete populations of proliferating MYF5-positive self-renewing cells and migratory MYOG-positive cells within RMS in live animals. Furthermore, we show that MYF5 is a marker of functionally-defined ERMS Tumor Propagating Cells.

Additionally to being a marker of these cells, we show that MYF5 is sufficient to confer self-renewal to differentiated zebrafish ERMS cells. These tumors initiate earlier, have higher penetrance and a tendency to be larger than control tumors. Consistent with redundant roles for MYF5 and MYOD1 in muscle development, regeneration and stem cell self-renewal, we identified two classes of human ERMS that express either high levels of MYF5 or MYOD1, with either MRF being required for sustained tumor growth *in vitro* and/or *in vivo*. ChIP-seq experiments went on to reveal that MYF5 and MYOD1 bind common DNA regulatory

elements likely to arrest human ERMS in early stages of muscle development while simultaneously promoting cell cycle progression.

We suggest a model where MYF5 and MYOD1 converge on common molecular pathways to regulate human RMS growth and self-renewal, similar to their overlapping roles in muscle development and regeneration. Taken together, we show that cancer self-renewal pathways are likely shared with their non-malignant counterparts and that these processes are aberrantly activated during malignant transformation, an emerging concept in cancer biology.

Keywords

Rhabdomyosarcoma; MYF5; MYOD; Muscle; Cancer; Stem Cells; Zebrafish

Contents

List of Acronyms

ALK Anaplastic Lymphoma Receptor Tyrosine Kinase

APL Acute Promyelocytic Leukemia

ARMS Alveolar RMS

ASCL1 Achaete-Scute Family bHLH Transcription Factor 1

ATM ATM serine/threonine kinase

bHLH basic Helix-loop-Helix

CDH15 Cadherin 15

CDKN1C Cyclin-Dependent Kinase Inhibitor 1C

CDKN2A Cyclin-Dependent Kinase Inhibitor 2A

ChIP-seq Chromatin Immunoprecipitation Sequencing

CNV Copy Number Variation

CTNNB1 beta-Catenin

DNA Deoxyribonucleic Acid

dpf days post fertilization

ECL External Cell Layer

EdU 5-ethynyl-2'-deoxyuridine

EMA European Medicines Agency

ERMS Embryonal RMS

FACS Fluorescence Activated Cell Sorting

FDA Food and Drug Administration

FGFR Fibroblast Growth Factor Receptor

FN-RMS Fusion Negative RMS

FOXO1 Forkhead box O1

FP-RMS Fusion Positive RMS

GLI Glioma-Associated Oncogene Family Zinc Finger

GSK3b Glycogen Synthase Kinase 3 beta

HDAC Histone Deacethylase

HGF Hepatocyte growth Factor

HMT Histone Methyl-Transferase

HRAS Harvey Rat Sarcoma Viral Oncogene Family (RAS) Homolog

IF Immunofluorescence

IGF1R Insulin like Growth Factor 1 Receptor

IGF2 Insulin-Like Growth Factor 2

IHC Immunohistochemistry

KRAS Kirsten RAS Homolog

LOH Loss of Heterozygozity

MAPK Mitogen-associated Protein Kinase

MDM2 MDM2 proto-oncogene

MEF2 Myocyte Enhancer Factor-2

MET MET proto-oncogene, receptor tyrosine kinase

MRF Myogenic Regulatory Factor

MRF4/MYF6 Myogenic Regulatory Factor 4

MSC Musculin

MSCell Mesenchymal Stem Cell

MYC v-Myc avian Myelocytomatosis Viral Oncogene Homolog

MYCN v-Myc Avian Myelocytomatosis Viral Oncogene Neuroblastoma Derived Homolog

MYF5 Myogenic Factor 5

MyHC Myosin Heavy Chain

MYLPF Myosin Light Chain, Phosphorylatable, Fast Skeletal Muscle

MYOD1 Myogenic Differentiation 1

MYOG Myogenin

NEUROD1 Neuronal Differentiation 1

NF1 Neurofibromin 1

NRAS Neuroblastoma RAS Homolog

OLIG1/2 Oligodendrocyte Transcription Factor 1

PAX3 Paired box 3

PAX7 Paired box 7

PI3K Phosphatidylinositol-4,5-bisphosphate 3-kinase

PPTC Pediatric Preclinical Testing Consortium

PTCH1 Patched 1

RAS Rat Sarcoma Viral Oncogene Family

RB1 Retinoblastoma 1

RMS Rhabdomyosarcoma

RMS NOS RMS Not Otherwise Specified

RNA Ribonucleic Acid

RNA-seq Ribonucleic Acid (RNA) sequencing

RTK Receptor Tyrosine Kinase

SHH Sonic Hedgehog

SUV39H1 Suppressor of Variegation 3-9 Homolog 1

TAL1 T-cell acute lymphocytic leukemia 1

T-ALL T-cell Acute Lymphoblastic Leukemia

TCF3 Transcription Factor 3/ E2A

TCF4 Transcription Factor 4/ E2-2

TCF12 Transcription Factor 12/ HEB

TCR T-cell Receptor

TERT Telomerase Reverse Transcriptase Catalytic Unit

TP53 Tumor Protein p53

TPC Tumor Propagating Cell

T/t-Ag SV40 large-T and small-t antigen oncoproteins

UPS Undifferentiated Pleomorphic Sarcoma

USA United States of America

WGS Whole Genome Sequencing

WNT Wingless-type Protein Family

YAP1 Yes Associated Protein 1

1

General Introduction

"We are drowning in information while starving for wisdom. The world henceforth will be run by synthesizers, people able to put together the right information, think critically about it, and make important choices wisely."

Edward O. Wilson
Consilience: the Unity of Knowledge (1998)

1.1 Rhabdomyosarcoma

Rhabdomyosarcoma (RMS) is the most common pediatric soft-tissue sarcoma, with an incidence of 4 to 7 cases per million children in the United States of America (USA) (Ognjanovic et al., 2009; Perez et al., 2011). This corresponds to a conservative estimate of an average of 300 children per year in North America, with similar numbers reported in Europe (Weihkopf et al., 2008). As all pediatric malignancies it is thus a rare disease, a fact that has contributed to the relatively slow progress in our understanding of its basic molecular mechanisms and toward better and targeted treatments on the clinical front (Sokolowski et al., 2014).

RMSs comprise heterogeneous tumors with common features of skeletal muscle differentiation, including muscle striations by electron microscopy and protein expression of key factors involved in skeletal muscle differentiation (such as

MYOD1, MYOG and Desmin) (Sebire and Malone, 2003). The anatomical location of primary tumors is fairly diverse, with a predominance for the regions of the head and neck, extremities and genitourinary tract (reviewed in Kikuchi et al., 2011).

Treatment includes intensive, multi-agent chemotherapy, radiation therapy and surgical resection (reviewed in Hawkins et al., 2014). Risk stratification and the employment of aggressive therapy regimens has provided relatively high survival rates (ranging from 70% to 95% in low-risk, 35% in intermediate-risk and 15% in high-risk groups), which have remained relatively constant over the last 25 years (Ognjanovic et al., 2009; Perez et al., 2011; Weihkopf et al., 2008). Moreover, the current treatment modality often leads to high levels of short-term or long-term toxicity (reviewed in Hawkins et al., 2014). Importantly, survival upon relapse remains one of the major clinical challenges in treating this disease (Hettmer et al., 2014). Several initiatives have been developed toward promoting drug development for rare pediatric cancers. These include patent protection policies, alleviated numbers in clinical trial design and a shorter review process from regulatory agencies (FDA and EMA) (Sokolowski et al., 2014). However, despite such efforts, treatment options for RMS have largely remained unchanged (Malempati and Hawkins, 2012).

RMSs can be subdivided into two most common RMS subtypes - Embryonal RMS (ERMS) and Alveolar RMS (ARMS) - which differ in histology, genetics, clinical presentation and outcome (Kikuchi et al., 2011; Saab et al., 2011) (see Figure 1.1).

ARMS comprises approximately 25 to 30% of the RMS cases in the USA and affects older children and adolescents. It generally arises in the trunk and extremities and is associated with poorer outcome (Ognjanovic et al., 2009; Perez et al., 2011).

The majority of ARMS is accompanied by recurrent reciprocal chromosomal translocations that fuse PAX3 or PAX7 with FOXO1 to generate hyper-stable chimeric PAX3 or PAX7-FOXO1 oncogenes (therefore designated Fusion Positive RMS (FP-RMS)) (Barr et al., 1993; Shapiro et al., 1993). Several affected downstream pathways include IGF1R, FGFR4 and MET. Fusion Negative RMS (FN-RMS) ARMS cases are often accompanied by ALK overexpression, which is also common to the ERMS subtype (Hawkins et al., 2014).

ERMS is the most common RMS subtype (60 to 70% of the cases), has an earlier onset and includes most of the head and neck cases (Ognjanovic et al., 2009; Perez et al., 2011). It is associated with better prognosis under current

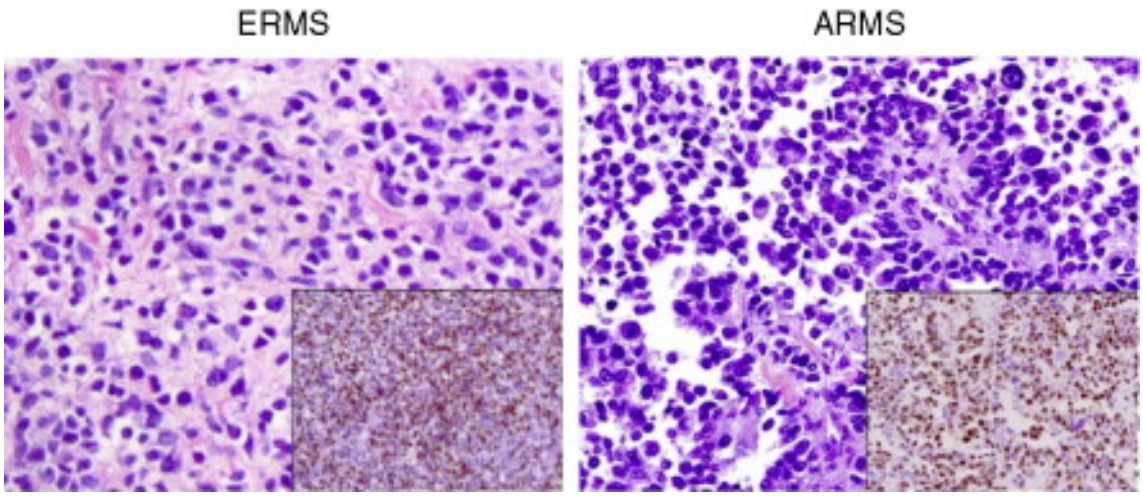

Figure 1.1: *Representative hematoxylin- and eosin-stained sections of ERMS and ARMS rhabdomyosarcoma.* The insets show typical immuno-histochemical staining for MYOG in each subtype (reproduced with permission from Saab et al., 2011).

treatment but in recurring and/or metastatic cases the survival rates decrease drastically to less than 25% (Breneman et al., 2003).

The genomic landscape of ERMS is more complex with no fusion events (solely comprising FN-RMS) but a recurrent chromosomal alteration (Loss of Heterozygozity (LOH) of 11p15.5) and specific mutations including members of the TP53 pathway (TP53 or CDKN2A loss, MDM2 overexpression), RAS pathway (comprising $HRAS^{G12V}$, $KRAS^{G12D}$, or NRAS mutations) and deletions of NF1, FGFR4 pathway, IGF2 and CDKN1C. Other cases include dysfunctional SHH signaling (PTCH1 and GLI loss), RB1 loss or PI3K and CTNNB1 activation (Sokolowski et al., 2014).

Recent genomic studies have provided a more complete description of the molecular alterations in RMS. Through a series of whole-genome, whole-exome, and transcriptome sequencing of primary and recurrent rhabdomyosarcoma samples, Chen et al., 2013 have confirmed the existence of a common set of Copy Number Variations (CNVs) (more significant in FN-RMS) and fusion events (such as PAX3- or PAX7- FOXO1) in RMSs. The most common consensus gene mutations in ERMS were on the Rat Sarcoma Viral Oncogene Family (RAS) pathway and were particularly prevalent in high and intermediate risk clinical groups. Additional common mutations were found in TP53 and FGFR pathways. Additionally, by analyzing pre- ad post- treatment matched samples, the authors were also able to describe the disappearance and emergence of specific mutations during the process of tumor evolution (for example, in ALK). This is explained

at least partially by the existence of intra-tumor heterogeneous clones that harbor specific LOH and CNV mutations. Also, arising from Ribonucleic Acid (RNA) sequencing (RNA-seq) and methylation analyses, this study confirmed several reports pointing to an enrichment of WNT and SHH signalling pathway genes and/or mutations in FN-RMS tumors (Annavarapu et al., 2013; Chen et al., 2014; Zibat et al., 2010) . Finally, this study points to the MAPK pathway and functional sensitivity to oxidative stress-inducing drugs as a potential actionable hallmark of FN-RMS tumors.

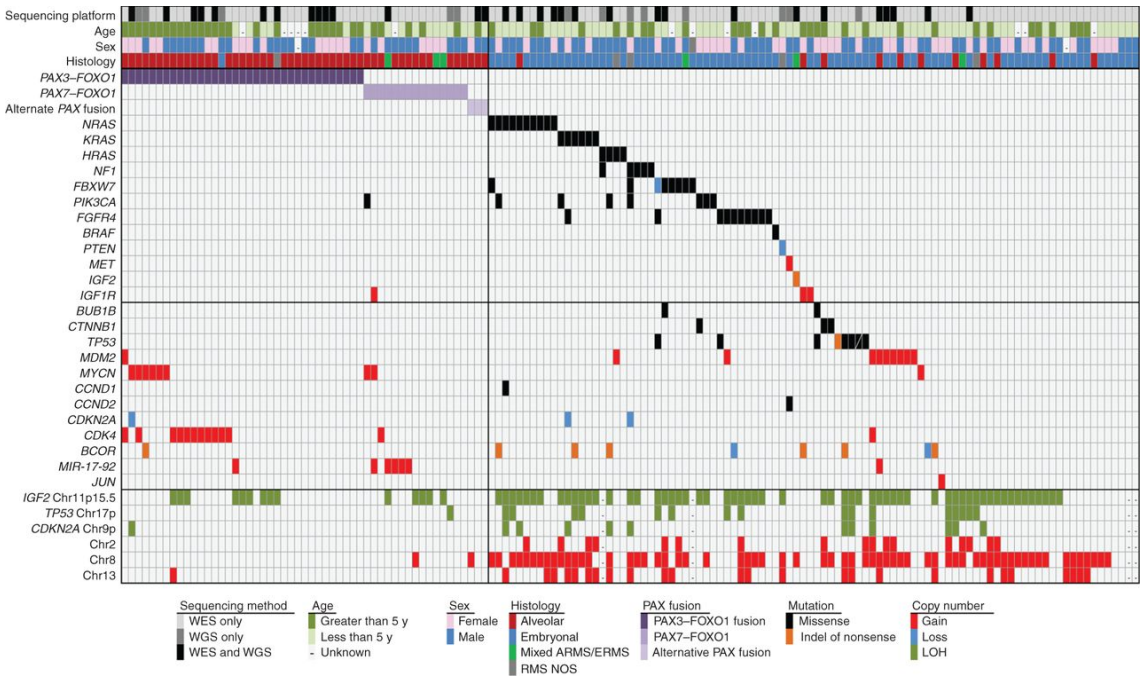

Figure 1.2: *The genomic landscape of pediatric RMS highlighting candidate alterations.* Demographic characteristics, histologic subtypes, and selected genes with copy-number alterations or somatic mutations across 147 rhabdomyosarcoma cases. Unique sample identifier and sequencing platform. Sex: males in blue, females in pink. Age: years at diagnosis divided into fewer than 5 years and greater than 5 years. Histologic diagnosis: red, ARMS; blue, ERMS including spindle and botryoid subtypes; gray, RMS NOS. Mixed alveolar and embryonal histology in green. Copy-number gains and losses for selected genes. Blue, losses; red, gains; green, LOH. Selected genes with somatic mutations. Purple, fusion protein; black, missense; orange, nonsense/splice site/indel mutations (reproduced with permission from Shern et al., 2014).

The largest-scale study to date was reported by Shern et al., 2014 (see Figure 1.2). Similar to what was reported by Chen et al., 2013, PAX3- and PAX7-FOXO1 fusions were found in a majority of ARMS FP-RMSs. Mutations in the RAS pathway, TP53 cell cycle regulators plus other Receptor Tyrosine Kinases

(RTKs) such as FGFR4 were found in FN-RMS. Additionally, mutations were found in genes involved in DNA damage (ex: ATM), muscle cell differentiation (MET, MYOD1), MAPK, chromatin modification, induction of apoptosis and insulin receptor signaling (IGF1R and IGF2) predominantly in FN-RMS and MYCN in FP-RMS. Importantly, several altered genes in FN-RMS (such as MET and MYOD1) were known downstream PAX3 and PAX3-FOXO1 targets, suggesting common mechanisms underlying cancer processes in both groups.

Taken together, these reports highlight common mutations of the RTK, RAS, and PI3K axis in 93% of the FN-RMS cases, providing a framework for genomics-directed therapies that might improve outcomes for patients with RMS.

Given the heterogeneous molecular presentation of the classical histological subtypes, including ARMS, ERMS and also the less common Undifferentiated Pleomorphic Sarcoma (UPS), stratification based on presence or absence of FOXO1 fusions was shown to be preferable, by dividing RMS simply into FP-RMS and FN-RMS (Williamson et al., 2010). Additionally, within each clinical subgroup, several molecular marker signatures have emerged that provide a better predictive and prognostic alternative (Davicioni et al., 2010; Hingorani et al., 2015).

Moving forward, a better mechanistic understanding of the involvement of these pathways in tumor growth, metastasis and especially relapse may help to establish more prognostic markers and educate the development of new, efficient and less toxic therapies. The recent emergence of novel genomic and transcriptomic analysis studies (mentioned above) as well as the establishment and exploitation of diverse animal models that recapitulate this heterogeneous disease (discussed below, and the purpose of this work) should contribute to a better understanding of the biology of these tumors in the near future.

1.2 RMS as an aberrant skeletal muscle differentiation tissue

In spite of all differences between RMS cases, they share the inability to achieve terminal myogenic differentiation.

During embryonic skeletal muscle development, lineage-specific basic Helix-loop-Helix (bHLH) Myogenic Regulatory Factors (MRFs) act as competing binding partners of the Transcription Factor 3/ E2A (TCF3), Transcription Factor 4/ E2-2 (TCF4) and Transcription Factor 12/ HEB (TCF12) and orchestrate a faithful succession of cellular states that ultimately leads to the formation of skeletal muscle fibers (Figure 1.3) (Buckingham and Rigby, 2014; Tapscott, 2005). These events are similarly recapitulated in response to injury in the adult tissue (Tajbakhsh, 2009).

In RMS, albeit the characteristic expression of these markers (PAX3, PAX7, MYF5, MYOD1, MRF4/MYF6 and MYOG) (Barr, 2001; Sebire and Malone, 2003), the tissue acts as dysfunctional developing muscle that is locked in incomplete stages of the myogenic differentiation cascade by several mechanisms. In recent years, great effort has been placed toward understanding these mechanisms, so that a differentiation strategy by means of overcoming those constrains could act as a promising therapeutic avenue for the treatment of RMS.

A non-exhaustive but comprehensive overview of current knowledge on the role of MRFs in muscle development and regeneration and on mechanisms that are aberrantly operating in RMS tumors is provided below.

1.2.1 Myogenic Regulatory Factors and their role in muscle development and regeneration

The role of MRFs in muscle specification has been long appreciated, since the first reports of the capacity of MYOD1 (Tapscott et al., 1988) and MYF5 (Braun et al., 1989) to specify skeletal muscle cells *in vitro* in fibroblast to myoblast conversion assays.

From the very beginning, the complex redundancy and interactions between these MRFs was evident. While single MYOD1 (Rudnicki et al., 1992) and MYF5 (Braun et al., 1992, 1994) *knock-out* mice develop with minor defects, double MYF5/MYOD1 *knock-out* animals are born immobile and die soon after birth (Rudnicki et al., 1993). However, different muscle populations were later shown to be more reliant on the action of one of these factors. For example, limb muscles,

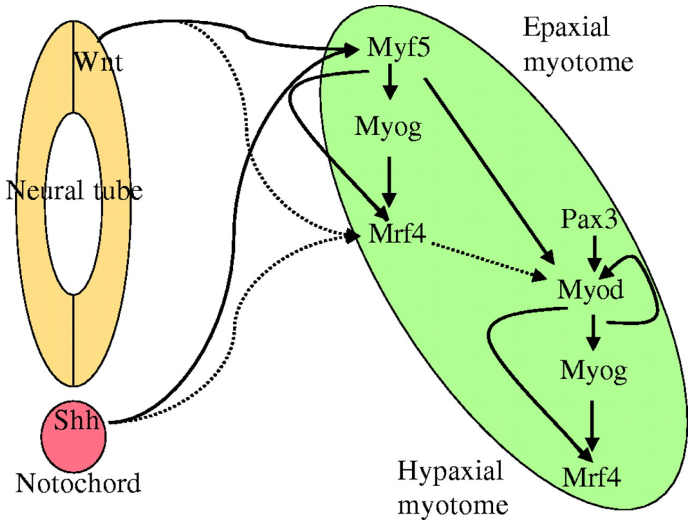

Figure 1.3: *Epistatic relations among myogenic bHLH factors.* Figure shows acting MRF networks and main signaling operating during trunk skeletal muscle specification in mammalian organisms (reprinted with permission from Tapscott, 2005)

originated from the hypaxial somite, were shown to be mostly MYOD1-dependent and MYF5-independent (Tajbakhsh and Buckingham, 1994) and the esophagus muscle seems to be more reliant on MYF5 in both mouse (Kablar et al., 2000) and zebrafish (Minchin et al., 2013). This differential requirement is at least partially due to the signaling pathways established in the developing embryo and emanating from the neural tube, influencing the epaxial myotome, and the dorsal ectoderm, influencing the hypaxial myotome (see Figure 1.3) (Cossu et al., 1996; Kablar et al., 1997; Tajbakhsh et al., 1998; Tapscott, 2005).

In addition to this spatial heterogeneity in MRF requirement, there is also differential temporal regulation throughout the cell cycle, with MYF5 protein being degraded at Mitosis while MYOD1 is still present (Doucet et al., 2005; Lindon et al., 1998; Lindon et al., 2000; Singh and Dilworth, 2013), and in order of emergence, with MYF5 being firstly expressed *in vivo* (Buckingham, 1992).

A more recent report shined new light on the specific roles of these factors in the induction of myogenic programs. Through Chromatin Immunoprecipitation Sequencing (ChIP-seq) studies in mouse embryonic fibroblasts expressing physiologically-relevant levels of MYF5 and/or MYOD1, Conerly et al., 2016 show that they have overlapping binding sites but distinct roles. On one hand, MYF5 is proficient in inducing histone acetylation but fails to recruit RNA polymerase II to elicit robust gene activation, whereas MYOD1 induces histone acetylation, recruits Pol II, and robustly activates transcription at these physiological expression levels, in a protein domain-dependent manner. Furthermore, when MYF5 levels

are expressed to higher levels, it is capable of activating transcription of downstream targets with similar efficiency. This observation provides an explanation for the higher efficiency of MYOD1 in pushing precursor cells toward myogenic differentiation in conversion assays (Ishibashi et al., 2005).

Besides the role of MYF5 and MYOD1 in embryonic development, these factors are also needed for the process of muscle regeneration from satellite cells, the resident stem cells of adult skeletal muscle. Initial findings that MYOD1 *knock-out* mice have delayed regeneration were later explained by the observation that the compensating MYF5-positive, MYOD1-negative cells isolated from mature muscle are less proficient in inducing MYOG expression and myotube formation (Yablonka-Reuveni et al., 1999). MYF5 null mice also show aberrant muscle regeneration with a progressive muscle fibre hypertrophy, delayed differentiation, adipocyte accumulation, and fibrosis after freeze-injury (Gayraud-Morel et al., 2007). The functional redundancy and divergence of specific roles of these factors is thus also evident in post-natal myogenesis. Additionally, the existence of defined heterogeneous populations of muscle satellite cells, that express MYF5 or not, is still a matter of active research. Reports of this heterogeneity, initially reported by Gensch et al., 2008, Haldar et al., 2008 and Gayraud-Morel et al., 2012 are currently under active debate (Comai et al., 2014; Haldar et al., 2014). MRFs are therefore crucial determinants of skeletal muscle tissue during embryonic development and post-natal myogenesis.

Other bHLH proteins are also crucial in the specification and differentiation of other tissues with related embryo origins. The most classical examples are the neurogenic/glial factors Neuronal Differentiation 1 (NEUROD1), Oligodendrocyte Transcription Factor 1 (OLIG1/2) and Achaete-Scute Family bHLH Transcription Factor 1 (ASCL1) that are specified within the neural tube (Imayoshi and Kageyama, 2014). Interestingly, MYF5-expressing cells have been detected in the developing neural tube, most likely due to failure in responding to positional cues in the developing embryo (Tajbakhsh and Buckingham, 1995; Tajbakhsh et al., 1996; Tajbakhsh et al., 1994). This myogenic to neuronal plasticity was recently further explored by Fong et al., 2015, which demonstrated that MYOD1 can be converted to NEUROD1 simply by replacing its DNA binding domain to induce neuronal differentiation from fibroblasts. Additionally, MYF5 was also recently shown to be expressed in myo-adipogenic precursors (Sanchez-Gurmaches and Guertin, 2014; Sanchez-Gurmaches et al., 2012).

1.2.2 Mechanisms of impaired skeletal muscle differentiation in RMS

Given that MRFs expression is a common feature of all RMSs, a major effort has been put toward understanding the epigenetic and transcriptionally elicited mechanisms that prevent complete muscle differentiation. This knowledge could in turn translate into the exploitation of those mechanisms to improve tumor differentiation ultimately exhausting self-renewing cells - a therapeutic approach referred to as differentiation therapy.

Differentiation therapy has been successful in treating other malignancies. The most striking example is in Acute Promyelocytic Leukemia (APL) treatments, which benefited immensely from introduction of Retinoic Acid-induced differentiation therapy to cure rates of approximating 80% (Stone et al., 1988) . Also in other sarcomas, some compounds have been shown to effectively induce differentiation in the clinical setting (in liposarcomas) (Demetri et al., 1999).

Below is an overview of the current knowledge on mechanisms of impaired differentiation in RMS.

In the case of FP-RMS, the PAX3- and PAX7-FOXO1 fusions were shown to directly increase the stability of MRFs, desensitize them to cytoplasmic accumulation and foster the over-activation, or *de novo* activation of genes involved in cell cycle regulation, growth and apoptosis resistance, while suppressing downstream pro-differentiation genes (Jothi et al., 2012). Surprisingly, PAX3-FOXO1 does not impair the Myogenic Differentiation 1 (MYOD1) pro-differentiation activity by directly inhibiting its transcription, localization, phosphorilation or subsequent interaction with its binding partners. It appears instead to directly affect the chromatin state around MYOD1 target genes (such as the MYOG locus), as assessed by *in vitro* studies using well-established PAX3-FOXO1 positive ARMS cell lines (reviewed in Keller and Guttridge, 2013).

Interestingly, in FN-RMS, MYOD1 function is impaired by similar mechanisms, despite the absence of the fusions. In the ERMS cell line RD, MYOD1 activity is inhibited partially due to an increased expression of Musculin (MSC) and of a spliced form of TCF3, competing for binding to E-box motifs at the target genes (Yang et al., 2009). Additionally, MYOD1-target microRNAs miR-133, miR-1 and miR-206 are also deregulated (MacQuarrie et al., 2012; Rota et al., 2011; Sweetman et al., 2008) and expression levels positively correlate with clinical outcome (Missiaglia et al., 2010). Chromatin-associated factors like the Histone Deacethylase3 (HDAC3) and the Histone Methyl-Transferase (HMT) SUV39H1 add a layer

of complexity to the differentiation cascade pathway and are deregulated in RMS (Albacker et al., 2013; Demmerle et al., 2013; Mal, 2006; Storer et al., 2013). Importantly, several reports have identified mutations in MYOD1 in primary RMS samples (Agaram et al., 2014; Kohsaka et al., 2014; Szuhai et al., 2014).

The role of MYOD1 has been the central focus of mechanistic studies on RMS differentiation. However, other parallel and cooperating pathways important for skeletal muscle differentiation have also been implicated in recent years. MET proto-oncogene, receptor tyrosine kinase (MET) is the receptor of the Hepatocyte growth Factor (HGF). This pathway is over-activated in a variety of human cancers (Graveel et al., 2013) and drives tumor growth and metastasis. It is also relevant to the muscle tissue as it is expressed in muscle precursors, inducing cell proliferation and migration to their proper sites during development (Buckingham and Montarras, 2008) and muscle regeneration (reviewed in Wagers and Conboy, 2005). MET over-activation occurs in some RMS cases (see Section 1.1) and there is functional evidence for its implication in RMS tumor growth in xenograft mouse models (Yan et al., 2009). Other muscle differentiation pathways that are deregulated and implicated in RMS tumorigenesis include IL4R (Hosoyama et al., 2011), TP53/MDM2 (Fiddler et al., 1996; Yang et al., 2009), WNT (Annavarapu et al., 2013; Chen et al., 2014) and genes from the NOTCH family (Belyea et al., 2011; Raimondi et al., 2012; Roma et al., 2011).

The increasing accessibility of ChIP-seq, RNA-seq and Whole Genome Sequencing (WGS) technologies has opened doors in recent years for a more complete picture of the differentiation blockade in RMS. These include the above-mentioned (Section 1.1) WGS studies of multiple, sometimes paired, patient-derived samples (Chen et al., 2013; Shern et al., 2014) and the description of the chromatin environment of muscle specific promoters in greater detail through ChIP-seq (Cao et al., 2010a; Cao et al., 2010b; Conerly et al., 2016; Dilworth and Blais, 2011; MacQuarrie et al., 2013a,b; Roy et al., 2002).

Toward the goal of finding novel therapeutic options to differentiate RMSs, Chen et al., 2014 have screened for several drugs that would both differentiate RMS cell lines *in vitro*, as assessed high throughput Immunofluorescence (IF) for Myosin Heavy Chain (MyHC), and tumors *in vivo* in a zebrafish RAS-driven ERMS model (see Subsection 1.4.1 below). The most relevant compounds emerging are Glycogen Synthase Kinase 3 beta (GSK3b) inhibitors, a negative regulator of the beta-catenin-dependent WNT pathway, thus conforming with concomitant genomics reports of WNT pathway de-regulation in RMS (Chen et al., 2013; Shern et al., 2014). Also, Tremblay et al., 2014 showed that Yes Associated

Protein 1 (YAP1) plays a role in the differentiation blockade by upregulating pro-proliferative genes and interfering with MYOD1 and the pro-differentiation factor Myocyte Enhancer Factor-2 (MEF2).

However, it is important to continue to explore these differentiation blockade mechanisms before effective therapies can be translated into the clinic. It is possible that, due to the known plasticity of these cells toward different fates (See Section 1.3) (Abraham et al., 2014; Rubin et al., 2011), incomplete differentiation could push cells toward perhaps more aggressive cell states (Svalina and Keller, 2014). Understanding intra- and inter-tumor heterogeneity and selection and evolution processes in these tumors is thus paramount.

1.3 Tumor heterogeneity in Rhabdomyosarcoma

1.3.1 Inter-tumor heterogeneity and the RMS cell-of-origin

The precise cell-of-origin of RMS is currently controversial. It is possible that the existence of several diverging reports and proposed cells-of-origin for RMS simply reflects the biological heterogeneity of different tumors in different patients and between animal models (reviewed in Kashi et al., 2015).

The question of the cell-of-origin and inter-tumor heterogeneity seems to be biologically and clinically relevant, as shown by Abraham et al., 2014, whom reported a trend for different sensitivities and response to pharmacological compounds depending on the cell-of-origin of the ERMS tumor model deployed.

Rhabdomyosarcomas seem therefore to still encompass a heterogeneous group of tumors. Recent discoveries of novel biomarkers and molecular stratification (see Section 1.1), allied to a recent explosion in the cellular (Hinson et al., 2013) and animal models available (Kashi et al., 2015) are furthering our understanding of this heterogeneity and pave the way for better and tailored preclinical studies (Langenau et al., 2015) and personalized care for RMS patients.

Mouse models of FP-RMS were first generated by Keller C. and colleagues (Keller et al., 2004a,b). Importantly, PAX3-FOXO1 ARMS can arise from Myogenic Regulatory Factor 4 (MRF4/MYF6)-expressing myoblast cells but not dermamyotome or satellite cells that express Paired box 7 (PAX7) (Keller and Capecchi, 2005). In contrast, tumors with ERMS histology are formed from either satellite cells or myoblasts that eventually reinitiate molecular programs found in satellite cells (Rubin et al., 2011). This and a similar study by Blum et al., 2013, where

different oncogenic drivers are directed toward different cells of origin, point to a model where RMS and UPS lie in a "continuum", with distinct but overlapping cells-of-origin. Another model of ARMS histology PAX3-FOXO1 FP-RMS is obtained by expressing the fusion protein in human skeletal muscle progenitor cells *in vitro* and transplanting into immune-deficient mice (Linardic et al., 2007). When the same cells are transformed with T/t-Ag, Telomerase Reverse Transcriptase Catalytic Unit (TERT) and oncogenic Harvey RAS Homolog (HRAS)^{G12V}, the tumors generated have a ERMS or UPS histology, depending on the progenitor cell subtype utilized (Linardic et al., 2007). Similarly, targeting Cyclin-Dependent Kinase Inhibitor 2A (CDKN2A) and Kirsten RAS Homolog (KRAS)^{G12V} mutations to isolated mouse muscle progenitor cells leads to RMS of pleomorphic histology, that are molecularly similar to both ERMS and ARMS (Hettmer et al., 2011). Genetic alterations also seem to influence the site of RMS emergence. The Tumor Protein p53 (TP53)/c-FOS double mutant mouse develops ERMS with high penetrance in the face and orbit (Fleischmann et al., 2003), while TP53/ERBB2 mutant animals have a later onset of RMS in the genitourinary tract (Nanni et al., 2003). More recently, Hettmer et al., 2015 also reported different metastatic behaviors and histology for FN-RMS arising from different oncogenic lesions with KRAS and p16/19 null tumors being more metastatic than Hedgehog-activated associated tumors in mice.

These reports suggest that pathology and histological presentation can be determined by the combination of cell-of-origin and oncogenic mutations that are drivers of disease.

Another important theme underlying the question of the cell-of-origin and RMS heterogeneity is the link between skeletal muscle regeneration and RMS. By combining TP53 *knock-out* mice with the Duchenne Muscle Dystrophy mouse model (*mdx*), Camboni et al., 2012 show that the presence of a regenerative microenvironment collaborates with TP53 deficiency to induce ERMS in young mice. Similarly, Tremblay et al., 2014 report that targeting YAP1 to activated, but not quiescent satellite cells of muscle (through injury or through targeting to MYF5-expressing cells in post-natal muscle), also leads to robust development of ERMS. These reports provide a mechanistic explanation for reports of RMS in patients (Rossbach et al., 1999) and mouse models (Chamberlain et al., 2007) of muscle dystrophies.

Rhabdomyosarcomas were also shown to arise from non-myogenic precursor cells. Intriguing reports of myosin-expressing RMS tumors in non-myogenic locations, such as in the bone marrow with no other primary location, have long led

to speculation that these tumors could originate from Mesenchymal Stem Cells (MSCells) (Charytonowicz et al., 2009; Lisboa et al., 2008; Shinkoda et al., 2009). Additionally, Nitzki et al., 2011, 2015 have shown that RMS tumors can arise from uncommited mesodermal progenitor cells in the context of Sonic Hedgehog (SHH)-driven FN-RMS. Consistent with the existence of MYF5-positive myo-adipogenic precursors (see Section 1.2) (Sanchez-Gurmaches and Guertin, 2014; Sanchez-Gurmaches et al., 2012), Hatley et al., 2012 have also derived RMS from the adipogenic lineage. Given the plasticity of MSCells toward differentiation of several mesenchymal lineages *in vitro* and the fact that MSCells have been identified as the cell-of-origin of other sarcomas (Riggi et al., 2005, 2008) it is possible that the origin of sarcomas is more closely linked than what was previously appreciated.

1.3.2 Intra-tumor heterogeneity, tumor-propagating cells and self-renewal in RMS

In 1976, Peter Nowell proposed a novel view of cancer as a dynamic process of evolution of cell populations through selection of clones with diverse molecular and functional properties (Nowell, 1976). This intra-tumor heterogeneity can be accompanied by an increased capacity of some clones to self-renew as assessed by transplantation assays into immune-compromised mice and, more recently, through *in vivo* lineage tracing strategies (Beck and Blanpain, 2013; Driessens et al., 2012). Whether tumor cell heterogeneity follows a *hierarchical* stem cell model or a more *stochastic* model, or a combination of both (Magee et al., 2012; Meacham and Morrison, 2013), it has been suggested that these self-renewing clones, or Tumor Propagating Cells (TPCs), can be the ones escaping common therapies and that are responsible for relapsed disease (Bedard et al., 2013). Moreover, this clonal heterogeneity and tumor evolution processes pose a problem for clinical biopsy-based molecular diagnosis and stratification of treatment, since sampling of a particular region of a tumor may not represent the full range of cellular hierarchies and molecular alterations or be predictive of the emergence of dominant or de novo dominant clones(Bedard et al., 2013).

Important steps toward resolving the issue of intra-tumor heterogeneity involve the development of single-cell genomic technologies (Patel et al., 2014), the characterization of isolated liquid biopsies from the blood (Alix-Panabieres and Pantel, 2016), active research in animal models to visualize and test self-renewal during tumor initiation and progression *in vivo* (Beck and Blanpain, 2013) and the characterization of self-renewing cell types*in vitro* (Suva et al., 2014). Self-renewing

TPCs have been already characterized in many malignancies. A molecularly-defined cell population that can be enriched by cell surface markers has been defined in breast cancer, acute myeloid leukemia and glioblastoma (Beck and Blanpain, 2013; Dalerba et al., 2007; Eyler et al., 2011; Rheinbay et al., 2013).

However, a RMS-propagating cell that is required for continued tumor growth has not yet been described *in vivo* in mice or humans. Komuro et al., 2007 identified a stem-like cell population in RMS cell lines, based on the exclusion of the DNA binding dye, Hoechst 33342 and Flow Cytometry analysis. More recently, Walter et al., 2011 found that ERMS form spheres (rhabdospheres) in a stem cell medium containing defined growth factors over several passages. These spheres have increased growth ability and express stem cell markers, including CD133, that can select for subcultures with increased tumor-formation ability. The SHH pathway, upregulated in these cells, has then been shown to play a role on self-renewal in ERMS (Satheesha et al., 2015). Important findings toward RMS intra-tumor heterogeneity have emerged from a zebrafish model of ERMS and will be discussed in detail in Subsection 1.4.1, below.

1.4 Zebrafish models of cancer

Existing zebrafish cancer models were shown to mimic human disease and were developed for diverse cancer types including T- and B-cell leukemia/lymphoma (Langenau et al., 2003; Sabaawy et al., 2006), acute myeloid leukemia (Zhuravleva et al., 2008), melanoma (Patton et al., 2005), pancreatic neuroendocrine carcinoma (Yang et al., 2004), pancreatic adenocarcinoma (Park et al., 2008), intestinal hyperplasia and fibrosarcoma (Le et al., 2007) and embryonal rhabdomyosarcoma (Langenau et al., 2007) (see Subsection 1.4.1, below).

Zebrafish have many attributes that provide an advantage over other vertebrate model systems to act as complementary models in studying cancer processes. These include:

1. *Fecundity*: each female can produce 100-200 eggs per week and can mate weekly;

2. *Small size*, which facilitates husbandry: many animals can be utilized to increase statistic power of experiments;

3. *External development*: animals can be experimentally manipulated from the one-cell stage through adulthood;

4. *Transgenesis*: simple and mosaic transgenic approaches can create robust cancer models and easily deliver fluorescent proteins to tissues of interest, enabling *in vivo* cell tracking and imaging of tumor development;

5. *Conserved molecular pathways in development and disease*: zebrafish and human malignancies share similar oncogenes and molecular pathway activation;

6. *Cell transplantation*: muscle, hematopoietic, and cancer cells can be engrafted into irradiated or syngeneic recipients allowing direct assessment of self-renewal *in vivo*.

These advantages, recently reviewed in detail by White et al., 2013, make zebrafish increasingly useful for studying cancer.

1.4.1 The RAS-driven zebrafish RMS model

Zebrafish rhabdomyosarcomas can be generated by injecting one cell-stage embryos with linearized DNA containing a minimal *rag2* promoter driving the expression of the human $KRAS^{G12D}$ oncogene in the mononuclear component of muscle (Langenau et al., 2007, 2008). RMS tumors develop with approximately 40% incidence at 40 days post fertilization (dpf) and are histologically and molecularly similar to human ERMS as assessed by Immunohistochemistry (IHC) and gene-expression analysis through Microarray.

Bioinformatics analyses of these tumors show two major molecular signatures: one RAS-pathway-related, and one ERMS-specific, that includes the overexpression of the MRF MYF5 (Langenau et al., 2007). A dual-fluorescence transgenic approach was used to label less differentiated mononuclear cells, including satellite cells and myoblasts (using the *rag2* promoter), and differentiated cells (using the *alpha-actin* promoter). Subsequent cell transplantation and limiting dilution analysis demonstrated the existence of a prospectively definable TPC that is *rag2*-DsRed positive and *alpha-actin*-GFP negative and molecular analysis showed that it resembles a muscle activated satellite cell signature with expression of *myf5*, *m-cadherin* and *met*, but not *pax3* or *pax7* or mature muscle markers (Langenau et al., 2007).

Importantly, co-injection of up to three linear DNA fragments was shown to co-integrate in genomic Deoxyribonucleic Acid (DNA) and to be inherited equally and co-expressed by daughter cells throughout the zebrafish embryonic development (Langenau et al., 2008). This co-injection strategy allows for rapid and efficient assessment of a modifying or oncogenic effect of an over expressed gene or the multi-colour labelling of cell populations within tumors (see Figure 1.4).

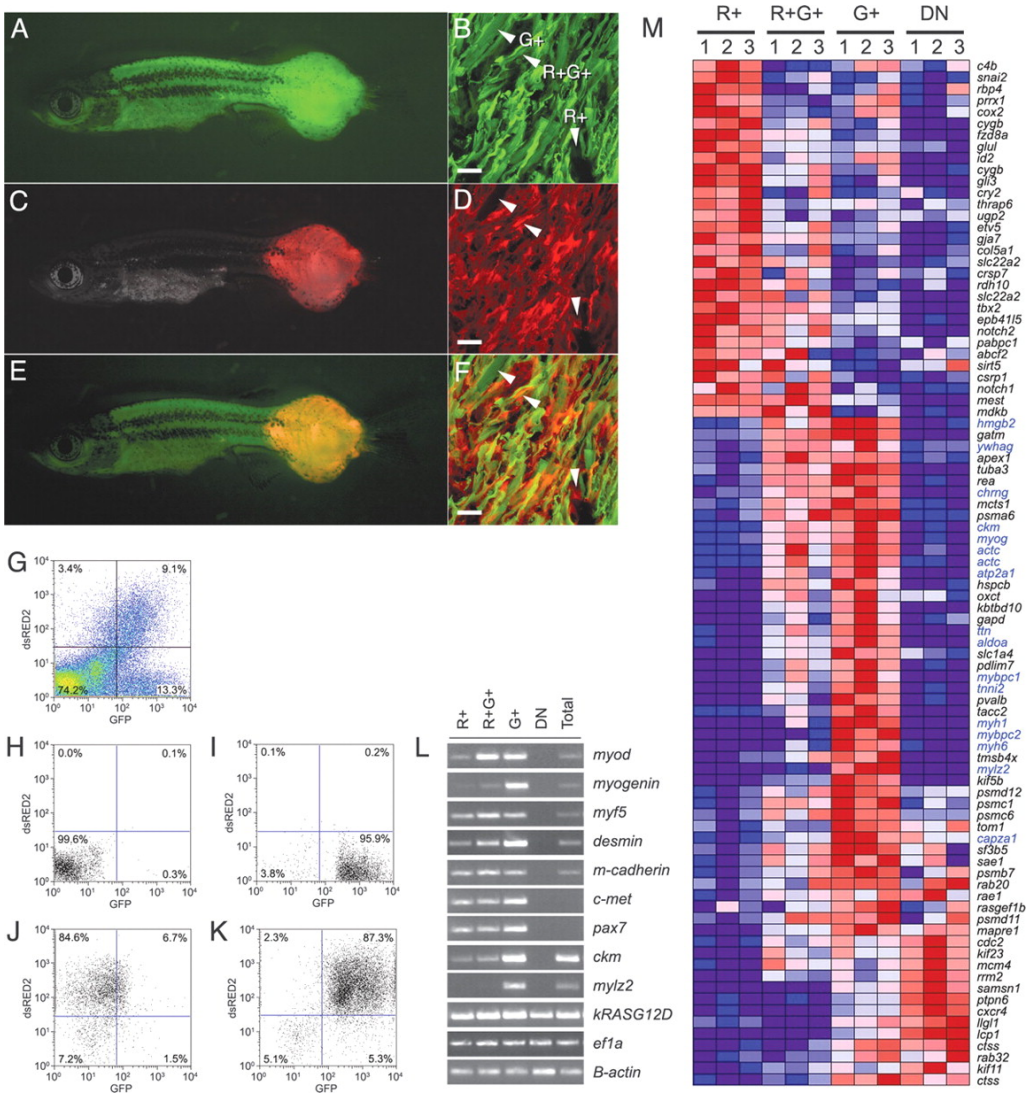

Figure 1.4: *Coinjection strategies can be used to label distinct cell populations within zebrafish RMS*. **(A)** GFP fluorescent image of RMS developing in a *rag2-DsRED2+/alpha-actin-GFP+*-injected animal. **(B)** GFP fluorescence in cryostat section. **(C)** DsRED2 fluorescence image of injected fish shown in A. **(D)** DsRED2 fluorescence in cryostat section. **(E,F)** Merged images. Bars: B,D,F, 20um. **(G)** FACS profile of a-actin-GFP transgenic animal injected at the one-cell stage with *rag2-DsRED2* and *rag2-kRAS*^{G12D}. **(H-K)** The four cell populations can be isolated to relative purity by FACS. **(L)** Semiquantitative RT-PCR analysis confirms that expression of DsRED2+ and GFP+ can be used to identify discrete populations of tumor cells based on their stage of muscle differentiation. **(M)** Microarray analysis of sorted cell populations from three tumors (numbered 1-3 at top of heat map) (reproduced with permission from Langenau et al., 2007)

2

Novel Zebrafish Transplantation Tools

"The art of research [is] the art of making difficult problems soluble by devising means of getting at them."

Sir Peter B. Medawar
Pluto's Republic (1982)

2.1 Chapter 2 - Preamble

Allograft transplantation, from a tissue of a donor animal to another of the same species, is the hallmark functional assay to assess tumor-propagating ability and self-renewal properties of stem cells and cancers. In zebrafish, this can be achieved through the utilization of a unique syngeneic, genetically identical, zebrafish line (Blackburn et al., 2011; Mizgirev and Revskoy, 2006; Smith et al., 2010), by suppression of the immune system through dexamethasone treatments (Stoletov et al., 2007) or sublethal irradiation (Smith et al., 2010), or by transplantation into developing zebrafish larvae, prior to the emergence of a competent immune system (reviewed in Stoletov and Klemke, 2008).

However, despite the widely recognized advantage of the utilization of immune-compromised animals in mouse model studies (reviewed in Zhou et al., 2014), similar immune-compromised zebrafish models were not available to date.

In order to be able to perform experiments described in Chapter 4, and others, I was involved in a team effort to develop a suite of these lines, particularly of the *rag*^{E450fs} mutant zebrafish.

2.2 Chapter 2 - Contribution

My contribution to this work:

- Maintenance of several transgenic zebrafish lines, including *AB/a-actin-RFP, TuAB/myf5-GFP, AB/myogenin-H2B-mRFP, AB/mylpfa-lyn-cyan, AB/mylpfa-mCherry, AB/mylpfa-GFP, casper/myf5-GFP* and generation by multiple genetic crosses and maintenance of triple-colour *myf5-GFP; myogenin-H2B-mRFP; mylpfa-lyn-cyan* zebrafish from previously-generated single transgenic lines;
- Generation of zebrafish Embryonal RMS (ERMS) primary and secondary tumors from a variety of transgenic lines and genetic backgrounds;
- Optimization of protocols for efficient transplantation of normal and malignant skeletal muscle cells into these immune-compromized zebrafish recipients;
- Confocal microscopy imaging support;
- Performance of all experiments and writing of the publication Tenente et al., 2014 to serve as a detailed methodology resource for the field.

2.3 Chapter 2 - Publications

These collaborations resulted in:

- A first-authored publication, reprinted in full in this Chapter

Tenente, I. M. et al. (2014). “Normal and Malignant Muscle Cell Transplantation into Immune Compromised Adult Zebrafish”. In: *J. Vis. Exp.* 94. ISSN: 1940-087X. DOI: 10.3791/52597

- Two co-authored publications, reprinted in full in Apendix A

Tang, Q. et al. (2014). “Optimized cell transplantation using adult rag2 mutant zebrafish.” In: *Nat. Methods* 11, pp. 821–824. ISSN: 1548-7105. DOI: 10.1038/nmeth.3031

Tang, Q. et al. (2016). “Imaging tumour cell heterogeneity following cell transplantation into optically clear immune-deficient zebrafish”. In: *Nat. Commun.* 7, p. 10358. ISSN: 2041-1723. DOI: 10.1038/ncomms10358. URL: http://www.nature.com/doifinder/10.1038/ncomms10358

Video Article

Normal and Malignant Muscle Cell Transplantation into Immune Compromised Adult Zebrafish

Inês M. Tenente*[1,2,3], Qin Tang*[1,2], John C. Moore[1,2], David M. Langenau[1,2]

[1]Molecular Pathology, Cancer Center and Center for Regenerative Medicine, Massachusetts General Hospital

[2]Harvard Stem Cell Institute

[3]GABBA - Instituto de Ciências Biomédicas Abel Salazar, Universidade do Porto

*These authors contributed equally

Correspondence to: John C. Moore at moore.john@mgh.harvard.edu, David M. Langenau at DLANGENAU@mgh.harvard.edu

URL: http://www.jove.com/video/52597
DOI: doi:10.3791/52597

Keywords: Immunology, Issue 94, zebrafish, immune compromised, transplantation, muscle, rhabdomyosarcoma, *rag2*^{E450fs}, *rag2*^{fb101}, fluorescent, transgenic

Date Published: 12/26/2014

Citation: Tenente, I.M., Tang, Q., Moore, J.C., Langenau, D.M. Normal and Malignant Muscle Cell Transplantation into Immune Compromised Adult Zebrafish. *J. Vis. Exp.* (94), e52597, doi:10.3791/52597 (2014).

Abstract

Zebrafish have become a powerful tool for assessing development, regeneration, and cancer. More recently, allograft cell transplantation protocols have been developed that permit engraftment of normal and malignant cells into irradiated, syngeneic, and immune compromised adult zebrafish. These models when coupled with optimized cell transplantation protocols allow for the rapid assessment of stem cell function, regeneration following injury, and cancer. Here, we present a method for cell transplantation of zebrafish adult skeletal muscle and embryonal rhabdomyosarcoma (ERMS), a pediatric sarcoma that shares features with embryonic muscle, into immune compromised adult *rag2*^{E450fs} homozygous mutant zebrafish. Importantly, these animals lack T cells and have reduced B cell function, facilitating engraftment of a wide range of tissues from unrelated donor animals. Our optimized protocols show that fluorescently labeled muscle cell preparations from *α-actin-RFP* transgenic zebrafish engraft robustly when implanted into the dorsal musculature of *rag2* homozygous mutant fish. We also demonstrate engraftment of fluorescent-transgenic ERMS where fluorescence is confined to cells based on differentiation status. Specifically, ERMS were created in AB-strain *myf5-GFP; mylpfa-mCherry* double transgenic animals and tumors injected into the peritoneum of adult immune compromised fish. The utility of these protocols extends to engraftment of a wide range of normal and malignant donor cells that can be implanted into dorsal musculature or peritoneum of adult zebrafish.

Video Link

The video component of this article can be found at http://www.jove.com/video/52597/

Introduction

Zebrafish are an excellent model for regenerative studies because they can regenerate amputated fins, as well as a damaged brain, retina, spinal cord, heart, skeletal muscle and other tissues[1]. Stem cell and regenerative studies in adult zebrafish have largely focused on the characterization of regeneration in response to injury, while identification of stem and progenitor cells from various tissues by cell transplantation has only recently been explored[2]. Zebrafish have also become increasingly used for the study of cancer through the generation of transgenic cancer models that mimic human disease[3–10].

In the setting of cancer, cell transplantation approaches have become widely adopted and permit the dynamic assessment of important cancer processes including self-renewal[11], functional heterogeneity[12,13], neovascularization[14], proliferation, therapy responses[15], and invasion[16,17]. However, engrafted cells are often rejected from recipient fish due to host immune defenses that attack and kill the graft[18]. Several methods have been used to overcome rejection of engrafted cells. For example, the recipient animals immune system can be transiently ablated by low dose gamma-irradiation prior to transplantation[18,19]. However, the recipient immune system will recover by 20 days post-irradiation and kill donor cells[18]. Alternatively, dexamethasone treatment has been used to suppress T and B cell function, providing longer immune suppressive conditioning and facilitating engraftment of a wide range of human tumors for up to 30 days[14]. These experiments require constant drug dosing and are limited to study of solid tumors. Long-term engraftment assays have used genetically-identical syngeneic lines[20–22], where the donor and recipient cells are immune matched. However, these models require transgenic lines of interest to be crossed into the syngeneic background for more than four generations to produce fully syngeneic lines. To obviate issues of immune rejection in recipient fish, our group has recently developed an immune compromised *rag2*^{E450fs} homozygous mutant (ZFIN allele designation *rag2*^{fb101}) line that have reduced T and B cell function and which permit engraftment of a wide range of tissues[23]. Similar immune compromised mouse models have been used extensively for cell transplantation of mouse and human tissues[24].

Here, we present methods for transplantation of skeletal muscle and embryonal rhabdomyosarcoma (ERMS), a pediatric sarcoma that shares features with skeletal muscle, into the newly described *rag2* homozygous mutant zebrafish. The availability of an immune compromised adult

Copyright © 2014 Creative Commons Attribution-NonCommercial License

zebrafish expands our ability to perform large-scale cell transplantation studies to directly visualize and assess stem cell self-renewal within normal and malignant tissues. With this method, fluorescently labeled muscle cell preparations from adult *α-actin-RFP*[25] transgenic zebrafish robustly engraft in *rag2* homozygous mutant zebrafish following injection into the dorsal musculature. Moreover, we demonstrate engraftment and expansion of primary *myf5*-GFP; *mylpfa*-mCherry transgenic ERMS following intraperitoneal injection into *rag2*^{E450fs} homozygous mutant zebrafish. The utility of these protocols goes beyond the examples shown and can be easily applied to additional zebrafish regenerative tissues and cancers.

Protocol

All animal procedures were approved by Massachusetts General Hospital Subcommittee on Research Animal Care, under protocol #2011N000127.

Section 1. Skeletal Muscle Cell Transplantation into Adult *rag2*^{E450fs} Homozygous Mutant Zebrafish

1. Preparation of Adult Zebrafish Donor Skeletal Muscle Cells

1. Obtain transgenic adult zebrafish that have fluorescently labeled muscle. In this experiment, 30 α-*actin-RFP* donor fish[25] were utilized to transplant 1 x 10^6 cells per recipient fish.
2. Sacrifice donor zebrafish in 1.6 mg/ml tricaine methanesulfonate (MS222) for 10 min or until no operculum movement is evident.
3. Place donor fish on an absorbent paper towel and excise the dorsal muscle using a clean razor blade. The cut should be made near the anus at a 45° angle to maximize tissue collection (as noted in **Figure 1A**). Place dissected tissue into a clean 10 cm Petri dish.
4. Add 500 µl suspension buffer (pre-chilled 0.9x Phosphate Buffer Saline (PBS) supplemented with 5% Fetal Bovine Serum (FBS)) to the dissected tissue. Up to 10 donor zebrafish can be placed together in this volume.
5. Mince the tissue with a razor blade >20 times until cells are in a uniform suspension. The entire dorsal musculature is homogenized including skin, bones and fins. Add 2 ml of suspension buffer. Using a 5 ml pipette, triturate the cell suspension ≥20 times to dissociate cells.
6. Filter the cell suspension through a 40 µm mesh strainer into a 50 ml conical tube placed on ice.
7. Wash the Petri dish with an additional 2.5 ml of suspension buffer to collect remaining tissue and filter through the same strainer and conical tube, to a final volume of 5 ml (10 donor fish can be used per isolate).
   NOTE: Skin, bones and fins will be excluded following filtration.
8. If applicable, combine similar suspensions into the same conical tube.
9. Count the total number of viable cells using trypan blue dye and a hemocytometer.
10. Reserve 500 µl for flow cytometry, if desired (optional, step 2).
11. Centrifuge cell suspension at 1,000 x g, for 10 min, at 4 °C.
12. Discard supernatant and resuspend cells at 3.33 x 10^5 cells/µl (0.9x PBS + 5% FBS). In total, 3 µl will be injected per recipient fish for a total of 1 x 10^6 cells per recipient (step 3).
    NOTE: Less than 3 µl of cell suspension should be transplanted into the recipient fish. If cell number is limiting, as low as 5 x 10^4 cells per recipient can lead to successful engraftment (**Table 1**).

2. Flow Cytometry Analysis of Donor Skeletal Muscle Cell Preparation (Optional)

1. Isolate muscle from a *wild type*, non-transgenic fish as outlined in step 1.1. This sample serves as the negative control and is useful for setting Flow Cytometry gates.
2. Add an appropriate viability dye. For example, add 5 µl of stock DAPI solution (500 ng/µl) to 500 µl of muscle preparation. Vortex slightly prior to analysis. Acquire 5 x 10^3 to 1 x 10^4 events. Analyze *wild type* control samples first to place gates followed by analysis of muscle cells isolated from transgenic fish.
   NOTE: Flow cytometry analysis is usually performed within 1 hr after muscle tissue dissection, during which time the dissected cells retain more than 60% viability (**Figure 2**). Cells should be kept on ice at all times. Total cell viability can be re-assessed prior to transplantation using trypan blue dye and a hemocytometer.

3. Intramuscular Transplantation of Skeletal Muscle Cells into Adult *rag2* Homozygous Mutant Zebrafish

1. Clean a 10 µl 26S G micro-syringe by drawing in and expelling 10% bleach solution (5 times), followed by 70% ethanol (5 times), and then followed by suspension buffer (0.9x PBS + 5% FBS, 10 times).
2. Anesthetize 2-4 month old homozygous *rag2* mutant fish or *wild type* recipient fish (as controls) by adding single drops of tricaine methanesulfonate (MS222, 4 mg/ml stock solution) into a Petri dish containing the fish in system water until operculum movements slow and fish are still.
   NOTE: Dose of tricaine anesthesia will depend on age and size of recipient zebrafish.
3. Place anesthetized recipient zebrafish on a damp paper towel or sponge, with the left side facing up.
4. Insert the syringe needle into the latero-dorsal musculature (refer to **Figure 1A**). Ensure that injections are performed at a 45° angle. Inject 3 µl of the cell suspension (prepared in step 1.12) per fish for a total of 1 x 10^6 cells per recipient.
5. Carefully transfer injected zebrafish into a clean tank using a plastic spoon to recover.

Copyright © 2014 Creative Commons Attribution-NonCommercial License

6. Assess recipient zebrafish for engraftment rates at 10, 20, 30 days post-transplantation by imaging anesthetized fish under bright field and epifluorescence microscopy.

Section 2. Embryonal Rhabdomyosarcoma (ERMS) Transplantation into Adult Homozygous *rag2* Mutant Zebrafish

4. DNA Microinjection of Zebrafish Embryos

1. Linearize the *rag2-kRASG12D* plasmid[7] by digesting 10 µg of DNA with *XhoI*, at 37 °C for 6 hr or O/N.
2. Purify DNA by standard phenol:chloroform extraction and precipitate with ethanol. Resuspend in 20 µl of deionized water (alternatively, commercial DNA fragment purification columns can be used).
3. Run the undigested and digested DNA on a 1% agarose gel and determine the concentration of DNA by spectrometer reading. Alternatively, run samples at 1:1, 1:5, and 1:10 dilutions on a 1% agarose gel and quantify compared to a DNA ladder.
4. Prepare an injection mix at a final concentration of 15 ng/µl of digested *rag2-kRASG12D* DNA in 0.1 M KCl and 0.5x Tris-EDTA. The final DNA amount injected in 2 nl of injection volume will be 30 pg.
   NOTE: Up to three different DNA constructs can be efficiently co-injected in a maximum of 60 pg of DNA per embryo. These transgenes become integrated into the genome and co-expressed within the developing tumor[26].
5. Inject linearized *rag2-kRASG12D* into one-cell stage embryos essentially as described[27] into a zebrafish strain of interest (**Figure 1B**). Injections should be performed in the cell and not in the yolk for higher efficiency. In this experiment, a double transgenic AB-strain; *myf5-GFP, mylpfa-mCherry* was used. Raise zebrafish using standard rearing protocols[28].
   NOTE: Injection survival is often dependent upon the zebrafish strain used. On average, 30% of injected embryos will develop ERMS. 300-600 embryos should be injected per experiment in order to ensure that enough GFP-positive and mCherry-positive primary tumors are generated for transplantation and analysis.

5. Screening for Primary ERMS in Zebrafish Larvae

1. Observe injected zebrafish from 10 to 30 days post injection for the emergence of externally visible primary ERMS.
2. At 30 days post injection, anesthetize recipient zebrafish by adding single drops of tricaine methanesulfonate (MS222 4 mg/ml stock solution) into a Petri dish containing fish system water until operculum movements slow and fish are still.
   NOTE: Dose of tricaine anesthesia will depend on the age and size of recipient zebrafish. Primary tumor-bearing zebrafish require lower doses of tricaine.
3. Select primary ERMS-bearing fish that are *myf5-GFP*-positive and *mylpfa-mCherry*-positive, using an epifluorescence microscope.

6. ERMS Tumor Preparation

1. Sacrifice selected primary ERMS-bearing zebrafish in 1.6 mg/ml tricaine methanesulfonate (MS222) for 10 min or until no operculum movement is evident.
2. Process each tumor-bearing zebrafish separately. Place fish in a clean Petri dish and dissect around the tumor using a razor blade and fine forceps (as shown in **Figure 1B**). Transfer the dissected tumor tissue to a clean Petri dish.
3. Add 100 µl of pre-chilled 0.9x Phosphate Buffer Saline (PBS) supplemented with 5% Fetal Bovine Serum (FBS). Mince tissue with a clean razor blade >20 times until cells are in a uniform suspension.
4. Add 900 µl of the same buffer (0.9x PBS + 5% FBS), pipette up and down several times to dissociate cells using a 1000 µl filtered pipette tip. Filter through a 40 µm mesh strainer into the corresponding 50 ml conical tube. Store on ice.
5. Wash the Petri dish with an additional 2-4 ml of buffer, and pass through the same mesh strainer and into the corresponding conical tube.
6. Centrifuge at 1,000 x g, for 10 min, at 4 °C.
7. Discard supernatant and resuspend in 100 µl of buffer.
8. Count the total number of viable cells using trypan blue dye and a hemocytometer.
9. Dilute cells to desired concentration in the same buffer (0.9x PBS + 5% FBS). Cells should be diluted to 5 x 10^3 cells/µl for transplanting 5 µl per recipient zebrafish in a total of 2.5 x 10^4 cells per recipient.
10. Flow Cytometry analysis can also be performed with a small amount of the suspension from step 6.5 to quantize the relative ratios of fluorescent cells within the sample.
    NOTE: Set aside 100 µl of cell suspension (following filtering in step 3.5) and dilute with 400 µl of 0.9x PBS + 5% FBS suspension buffer for Flow Cytometry analysis. To ensure proper gating, perform additional analysis using single transgenic tumor tissue or muscle isolated from adult *wild type*, *myf5-GFP* and *mylpfa-mCherry* fish. Perform Flow Cytometry essentially as described in step 2 of Section 1.

7. Transplantation of ERMS into Adult *rag2* Homozygous Mutant Zebrafish

1. Clean a 10 µl 26S G micro-syringe by drawing in and expelling 10% bleach solution (5 times), followed by 70% ethanol (5 times), and then followed by suspension buffer (0.9x PBS + 5% FBS, 10 times).
2. Anesthetize recipient homozygous *rag2* mutant fish by adding single drops of tricaine methanesulfonate (MS222 4 mg/ml stock solution) into a Petri dish containing the fish in system water until operculum movements are slow and fish are still.
3. Place anesthetized recipient zebrafish on a wet paper towel or sponge, with the ventral side facing up.
4. Inject 5 µl of the cell suspension into the peritoneal cavity (2.5 x 10^4 cells per recipient).

Copyright © 2014 Creative Commons Attribution-NonCommercial License

NOTE: The injection needle should be cleaned between injections of different tumors as described in step 4.1. 5 to 10 µl can be efficiently transplanted intraperitoneally, depending on recipient fish size. Tumor engraftment can be accomplished by injecting 1 x 10^4 to 5 x 10^5 unsorted cells per recipient fish (**Table 1**).

5. Carefully place recipient zebrafish into a clean tank with a plastic spoon.
6. Assess recipient zebrafish for engraftment rates at 10, 20, 30 days post-transplantation by imaging anesthetized fish under bright field and epifluorescence microscopy.
7. Utilize engrafted fish for downstream applications including Fluorescence Activated Cell Sorting (FACS) to assess differentiation status (**Figure 3H**), standard histological analysis (**Figure 3F**), imaging therapy responses[15], and/or serial transplantation approaches including limiting dilution analysis[11].

Representative Results

A procedure for preparing and transplanting skeletal muscle cells from *α-actin-RFP* transgenic donors into immune compromised homozygous rag2 mutant zebrafish has been demonstrated (Protocol Section 1, **Figure 1A** and **Figure 2**). Skeletal muscle tissue was prepared from *α-actin-RFP* transgenic donors and the resulting single cell suspension contained 84.3% viable cells as assessed by DAPI exclusion following Flow Cytometry analysis (**Figure 2B**). RFP-positive cells comprised 35.3% of this single cell suspension (**Figure 2C**). Transplantation of cells into the dorsal skeletal muscle of *rag2* homozygous mutant recipient fish led to consistent and strong engraftment as assessed by differentiation of single cells into multinucleated fibers (1 x 10^6 cells injected per fish, **Table 1**, **Figure 2D-I**). *Wild type* recipient fish failed to engraft muscle fibers over the 30-day experiment (n = 13). By 10 days post transplantation, 9 out of 14 *rag2* homozygous mutant zebrafish contained RFP-positive muscle fibers near the site of injection (64.3%, **Figure 2E,F**). Importantly, engrafted RFP-positive muscle persisted to 30 days post-transplantation (**Figure 2G-I**), with a subset of animals being followed for 115 days post-engraftment and exhibiting robust and persistent muscle engraftment (data not shown). These results are similar to those reported previously by our group[23] using the same protocol (**Table 1**).

We have also presented a method for the generation, preparation and transplantation of ERMS tumor cells into the peritoneal cavity of *rag2* homozygous mutant recipient fish (Protocol Section 2, **Figure 1B** and **Figure 3**). ERMS were generated in double transgenic *myf5-GFP*; *mylpfa-mCherry* fish that have been shown to allow the visualization of intra-tumoral heterogeneity and functional analysis of tumor cell subpopulations following transplantation[11]. However, further molecular characterization of each subpopulation is difficult because fish are small when they develop ERMS between 10 to 30 days of life and the number of tumor cells are limiting for downstream applications. One solution is to expand tumor cell numbers by engrafting ERMS into adult recipient zebrafish. To date, similar experiments have been completed using CG1-strain syngeneic fish and required in excess of 4 generations of backcrossing to develop syngeneic lines that were transgenic for *myf5-GFP; mylpfa-mCherry*. To circumvent these issues, we demonstrated the utility of immune compromised *rag2* homozygous mutant recipient zebrafish to engraft primary ERMS from a AB-strain zebrafish. All primary ERMS engrafted into *rag2* homozygous mutant animals, facilitating expansion of the tumor (**Table 1**). Similar results were recently reported where 24 of 27 *rag2* homozygous mutant zebrafish engrafted ERMS, while 0 of 7 *wild type* siblings engrafted disease[23]. A representative example of an engrafted ERMS is shown at 30 days post-transplantation in **Figure 3E**. Engrafted ERMS share histological features of embryonal rhabdomyosarcoma, similar to that found in the primary tumor (**Figure 3B** and **3F**). FACS analysis confirmed that ERMS contained functionally distinct tumor propagating cells and differentiated cells that express *myf5-GFP* and/or *mylpfa-mCherry*. Survival rates following the intraperitoneal injection procedure were in excess of 95%. Recipient zebrafish commonly succumb from tumor burden after the 30 days post-transplantation time point.

Copyright © 2014 Creative Commons Attribution-NonCommercial License

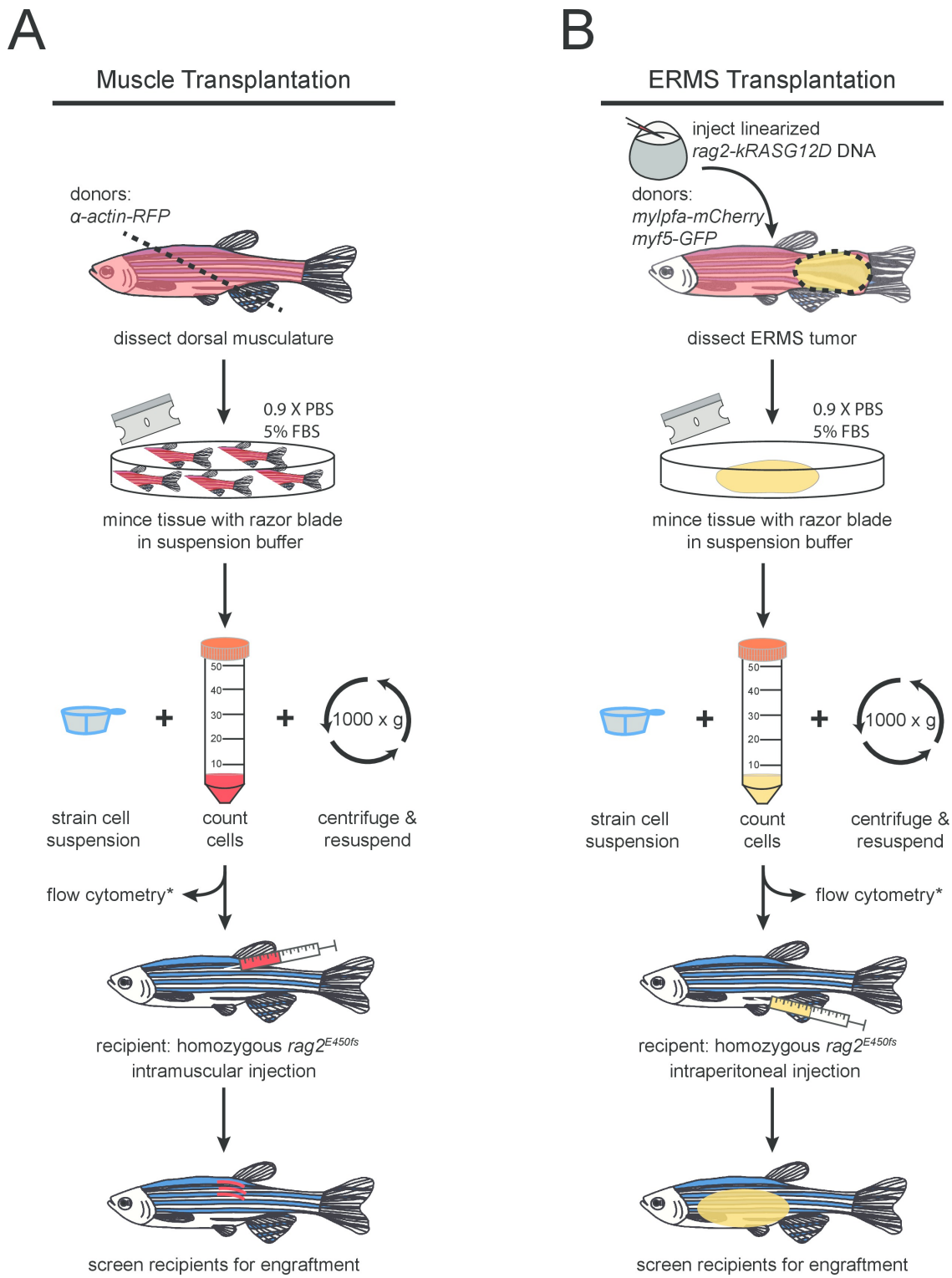

Figure 1. Protocol schematic for (A) normal and (B) malignant skeletal muscle cell transplantation into *rag2* homozygous mutant zebrafish. Optional steps are marked with (*).

Copyright © 2014 Creative Commons Attribution-NonCommercial License

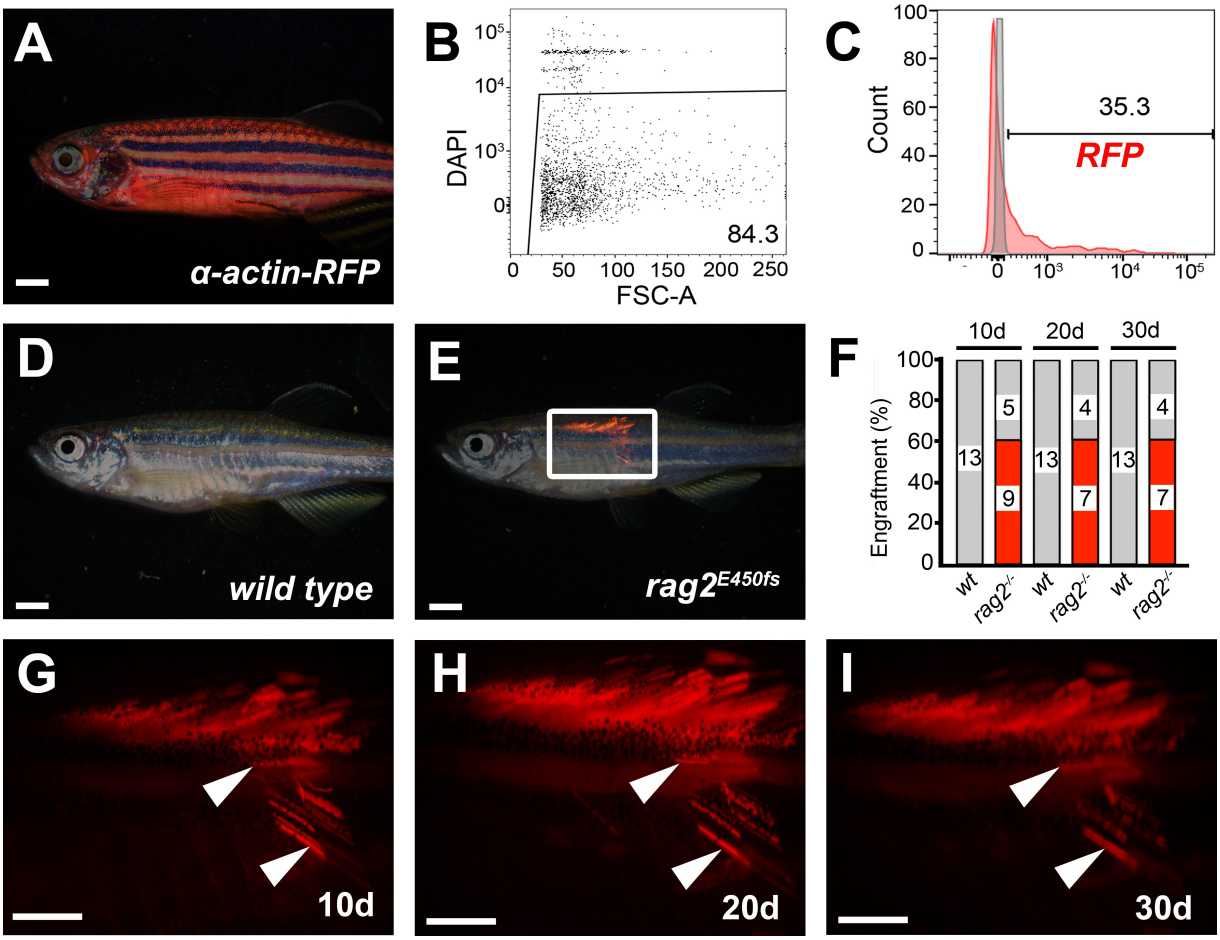

Figure 2. Skeletal muscle engraftment into *rag2* homozygous mutant zebrafish. (**A**) *α-actin-RFP* transgenic donor zebrafish. (**B**) Cell viability of isolated muscle cell suspension as assessed by DAPI dye exclusion and flow cytometry. (**C**) Proportion of RFP-positive cells found within the muscle cell suspension from *α-actin-RFP* donor (red), compared to a *wild type* control (grey). (**D-E**) Merged bright field and fluorescent images of *wild type* animals (**D**) or *rag2* homozygous mutant fish (**E**) at 30 days post-transplantation. (**F**) Engraftment rates over time. Red denotes number of engrafted animals while grey shows non-engrafted fish. Number of animals analyzed at each time point are indicated. (**G-I**) High magnification images of boxed region in panel E shown at 10 (**G**), 20 (**H**) and 30 (**I**) days post-transplantation, showing retention of differentiated muscle fibers over time (arrowheads). Scale bars equal 2 mm. Please click here to view a larger version of this figure.

Copyright © 2014 Creative Commons Attribution-NonCommercial License

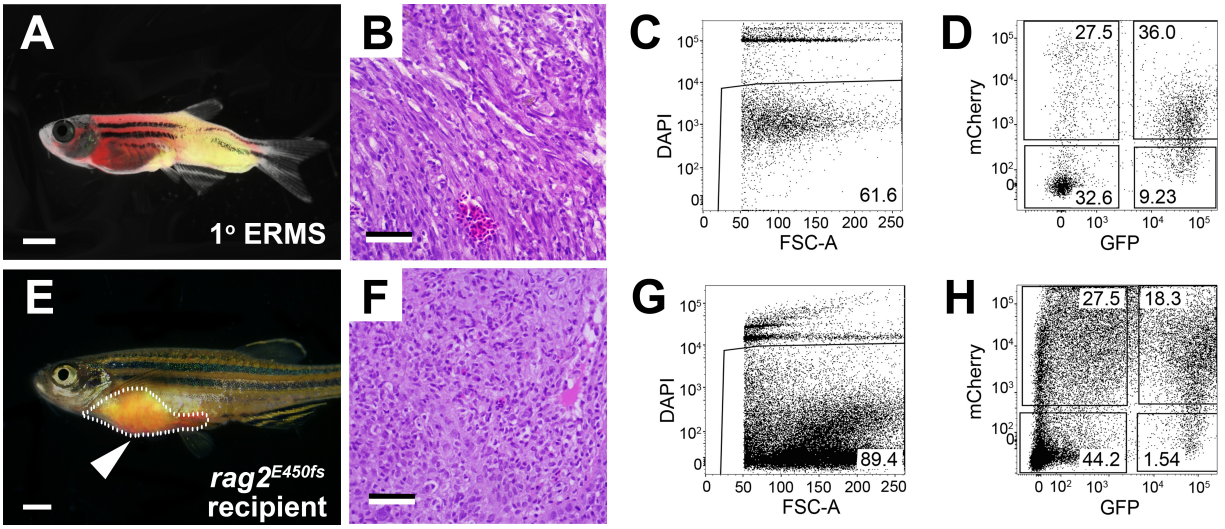

Figure 3. Transplantation of *myf5-GFP*; *mylpfa-mCherry* ERMS into *rag2* homozygous mutant zebrafish. (**A-D**) *rag2-kRASG12D* induced primary ERMS arising in AB-strain *myf5-GFP; mylpfa-mCherry* zebrafish at 30 days of life. (**E-H**) *rag2* homozygous mutant zebrafish engrafted with ERMS and analyzed at 30 days post-transplantation. (**A**, **E**) Merged bright field and fluorescent images of primary and transplanted ERMS. Tumor area is outlined and arrowhead indicates injection site in **E**. (**B**, **F**) Hematoxylin- and eosin-stained paraffin sections of primary (**B**) and engrafted ERMS (**F**) showing areas of increased cellularity associated with cancer. (**C**, **G**) Cell viability as assessed by DAPI dye exclusion and flow cytometry. (**D**, **H**) Fluorescent tumor cell sub-populations, as assessed by flow cytometry. Scale bars equal 2 mm (**A**, **E**) and 50 µm (**B**, **F**). Please click here to view a larger version of this figure.

Tissue		Donor			Recipient				Engraftment (30 dpt)	
cell type	transgenic line	donor age (months)	cell number obtained per pooled donor preparation	number of donors used	age at transplantation (months)	site of injection	injection volume	cell number transplanted per fish	wild type (control)	*rag2* homozygous mutant
muscle	*α-actin-RFP*	3	$7.2x10^7$	30	3	Left side, dorsal musculature	3 µl	$1x10^6$	0+/13	7+/11
muscle	*mylpfa-GFP*	3	$1.8x10^7$	30	3	Left side, dorsal musculature	3 µl	$3x10^5$	0+/9	10+/14
muscle	*mylpfa-GFP*	>12	$8.4x10^7$	31	4	Left side, dorsal musculature	5 µl	$1x10^6$	0+/10	5+/11
muscle	*α-actin-RFP**	6	$5x10^6$	10	3	Left side, dorsal musculature	2 µl	$2.5x10^5$	0+/5	5+/5
muscle	*ubi-EGFP**	>12	$6x10^6$	12	3	Left side, dorsal musculature	2 µl	$5x10^4$	0+/4	3+/3
ERMS 1°	*myf5-GFP; mylpfa-mCherry*	1	$1.2x10^6$	1	3	intraperitoneal	5 µl	$2.5x10^4$	NA	3+/5
ERMS 1°	*myf5-GFP; mylpfa-mCherry*	1	$2.5x10^6$	1	3	intraperitoneal	5 µl	$2.5x10^4$	NA	2+/4
ERMS 1°	*myf5-GFP; mylpfa-mCherry*	1	$1.16x10^6$	1	3	intraperitoneal	5 µl	$2.5x10^4$	NA	2+/2
ERMS 1°	*myf5-GFP; mylpfa-mCherry*	1	ND	1	3	intraperitoneal	8 µl	$1x10^4$	NA	4+/5
ERMS 1°	*myf5-GFP; mylpfa-mCherry**	0.75	ND	1	2	intraperitoneal	8 µl	$1x10^4$	NA	5+/5
ERMS 1°	*myf5-GFP; mylpfa-mCherry**	0.5	ND	1	2	intraperitoneal	8 µl	$1x10^4$	NA	3+/5
ERMS 2°	*myf5-GFP; mylpfa-mCherry**	4	$3.6x10^7$	1	2.25	intraperitoneal	5 µl	$1x10^6$	0+/4	13+/13
ERMS 2°	*myf5-GFP; mylpfa-mCherry**	5	$8x10^6$	1	3.5	intraperitoneal	5 µl	$5x10^5$	0+/3	3+/4

Table 1. Engraftment results for muscle and ERMS cell transplantation. (*) denotes previously reported data using the same techniques[23]. Data is reprinted with permission from *Nature Methods*. Please click here to view a larger version of this table.

Discussion

Efficient and robust engraftment of adult dorsal skeletal muscle was attained with a very simple cell preparation method followed by injection of cells into the dorsal musculature of *rag2 homozygous* mutant fish. In general, intramuscular injection procedures were very robust, with some

Copyright © 2014 Creative Commons Attribution-NonCommercial License

associated death immediately following the implantation procedure, ranging from 10% to 35% depending on experiment. Additional optimization will likely center on utilization of smaller gauge needles for injection and development of stationary injection apparatus using a microscope and micromanipulator, which will facilitate ease of implanting cells. Our approach also used unsorted muscle cells from donor animals and only contained approximately 30% muscle progenitor cells. Use of transgenic reporter lines that label stem cells and FACS isolation will likely provide enriched cell suspensions that lead to increased engraftment into recipient fish. Skeletal muscle cells could also be enriched and cultured prior to transplantation, as previously described[29]. Remarkably, our results also indicate that the steps of niche establishment and differentiation of donor muscle tissue occur before 10 days post transplantation, establishing this model as a robust and fast experimental platform to assess muscle engraftment and regeneration. Moreover, these experiments starkly contrast with those completed in mice, where pre-injury of muscle with cardiotoxin or barium chloride is required two days prior to engraftment[30,31]. It is likely that needle injury produced during the transplantation procedure potentiates engraftment by stimulating the production of a regenerative environment within the recipient animal[32,33]. We also envision that our method will be easily adapted to the transplantation of skeletal muscle tissue from younger zebrafish, allowing assessment of genetic mutations that affect early skeletal muscle development but lead to lethality at the larval stages.

We have also provided a detailed protocol for engraftment of zebrafish ERMS by intraperitoneal injection into non-conditioned, *rag2* homozygous mutant fish. This approach was useful for expansion of double transgenic primary tumors without the need for generating tumors within a syngeneic transgenic line. Our recent work has shown that cell transplantation approaches provide novel experimental models to assess ERMS drug sensitivity *in vivo,* where a single tumor can be expanded into thousands of animals and assessed for effects on growth, self-renewal, and neovascularization[15]. Moreover, we have successfully engrafted a wide range of tumors into *rag2* homozygous mutant fish including T cell acute lymphoblastic leukemia, melanoma, and ERMS[23]. Looking toward the future, we envision these lines will be useful for assessing important functional properties of cancer *in vivo* including assessing intra-tumoral heterogeneity, invasion, metastasis, angiogenesis, and therapy resistance. Moreover, the generation of *rag2* homozygous mutant fish in the optically clear Casper strain zebrafish[34] will likely facilitate direct imaging of many of these hallmarks of cancer.

In total, we provide detailed protocols for the successful engraftment of fluorescently-labeled normal and malignant skeletal muscle in to adult *rag2* homozygous mutant immune compromised zebrafish.

Disclosures

The authors have no competing financial interests.

Acknowledgements

This work is supported by Alex's Lemonade Stand Foundation (D.M.L.), American Cancer Society (D.M.L.), the MGH Howard Goodman Fellowship (D.M.L.), and US National Institutes of Health grants R24OD016761 and 1R01CA154923 (D.M.L.). CNY Flow Cytometry Core and Flow Image Analysis, shared instrumentation grant number 1S10RR023440-01A1. I.M.T. is funded by a fellowship from the Portuguese Foundation for Science and Technology (Fundação para a Ciência e Tecnologia – FCT). Q.T. is funded by the China Scholarship Council. We thank Angela Volorio for her helpful comments and advice.

References

1. Gemberling, M., Bailey, T. J., Hyde, D. R., & Poss, K. D. The zebrafish as a model for complex tissue regeneration. *Trends in genetics : TIG.* **29** (11), 611–20, doi:10.1016/j.tig.2013.07.003 (2013).
2. Boatman, S., Barrett, F., Satishchandran, S., Jing, L., Shestopalov, I., & Zon, L. I. Assaying hematopoiesis using zebrafish. *Blood cells, molecule., & diseases.* **51** (4), 271–6, doi:10.1016/j.bcmd.2013.07.009 (2013).
3. Langenau, D. M., Traver, D., *et al.* Myc-induced T cell leukemia in transgenic zebrafish. *Science.* **299** (5608), 887–90, doi:10.1126/science.1080280 (2003).
4. Yang, H. W., Kutok, J. L., *et al.* Targeted Expression of Human MYCN Selectively Causes Pancreatic Neuroendocrine Tumors in Transgenic Zebrafish Targeted Expression of Human MYCN Selectively Causes Pancreatic Neuroendocrine Tumors in Transgenic Zebrafish. *Cancer Research*. 7256–7262 (2004).
5. Patton, E. E., Widlund, H. R., *et al.* BRAF mutations are sufficient to promote nevi formation and cooperate with p53 in the genesis of melanoma. *Current Biology.* **15** (3), 249–54, doi:10.1016/j.cub.2005.01.031 (2005).
6. Sabaawy, H. E., Azuma, M., Embree, L. J., Tsai, H.-J., Starost, M. F., & Hickstein, D. D. TEL-AML1 transgenic zebrafish model of precursor B cell acute lymphoblastic leukemia. *Proceedings of the National Academy of Sciences of the United States of America.* **103** (41), 15166–71, doi:10.1073/pnas.0603349103 (2006).
7. Langenau, D. M., Keefe, M. D. M. D. M. D. M. D., *et al.* Effects of RAS on the genesis of embryonal rhabdomyosarcoma. *Gene., & development.* **21** (11), 1382–95, doi:10.1101/gad.1545007 (2007).
8. Le, X., Langenau, D. M., Keefe, M. D., Kutok, J. L., Neuberg, D. S., & Zon, L. I. Heat shock-inducible Cre/Lox approaches to induce diverse types of tumors and hyperplasia in transgenic zebrafish. *Proceedings of the National Academy of Sciences of the United States of America.* **104** (22), 9410–5, doi:10.1073/pnas.0611302104 (2007).
9. Park, S. W., Davison, J. M., Rhee, J., Hruban, R. H., Maitra, A., & Leach, S. D. Oncogenic KRAS induces progenitor cell expansion and malignant transformation in zebrafish exocrine pancreas. *Gastroenterology.* **134** (7), 2080–90, doi:10.1053/j.gastro.2008.02.084 (2008).
10. Zhuravleva, J., Paggetti, J., *et al.* MOZ/TIF2-induced acute myeloid leukaemia in transgenic fish. *British journal of haematology.* **143** (3), 378–82, doi:10.1111/j.1365-2141.2008.07362.x (2008).
11. Ignatius, M. S., Chen, E. Y., *et al. In vivo* imaging of tumor-propagating cells, regional tumor heterogeneity, and dynamic cell movements in embryonal rhabdomyosarcoma. Suppl Data. *Cancer cell.* **21** (5), 680–93, doi:10.1016/j.ccr.2012.03.043 (2012).
12. Blackburn, J. S., Liu, S., *et al.* Clonal Evolution Enhances Leukemia-Propagating Cell Frequency in T Cell Acute Lymphoblastic Leukemia through Akt/mTORC1 Pathway Activation. *Cancer cell.* **25** (3), 366–78, doi:10.1016/j.ccr.2014.01.032 (2014).

Copyright © 2014 Creative Commons Attribution-NonCommercial License

13. Blackburn, J. S., & Langenau, D. M. Zebrafish as a model to assess cancer heterogeneity, progression and relapse. *Disease model., & mechanisms.* **7** (7), 755–762, doi:10.1242/dmm.015842 (2014).
14. Zhao, C., Wang, X., *et al.* A novel xenograft model in zebrafish for high-resolution investigating dynamics of neovascularization in tumors. *PloS one.* **6** (7), e21768, doi:10.1371/journal.pone.0021768 (2011).
15. Chen, E. Y., DeRan, M. T., *et al.* Glycogen synthase kinase 3 inhibitors induce the canonical WNT/β-catenin pathway to suppress growth and self-renewal in embryonal rhabdomyosarcoma. *Proceedings of the National Academy of Sciences of the United States of America.* **111** (14), 5349–54, doi:10.1073/pnas.1317731111 (2014).
16. Yang, X.-J., Cui, W., *et al.* A novel zebrafish xenotransplantation model for study of glioma stem cell invasion. *PloS one* **8** (4), e61801, doi:10.1371/journal.pone.0061801 (2013).
17. Chapman, A., Fernandez del Ama, L., Ferguson, J., Kamarashev, J., Wellbrock, C., & Hurlstone, A. Heterogeneous Tumor Subpopulations Cooperate to Drive Invasion. *Cell Reports.* (8), 1–8, doi:10.1016/j.celrep.2014.06.045 (2014).
18. Smith, A. C. H., Raimondi, A. R., *et al.* High-throughput cell transplantation establishes that tumor-initiating cells are abundant in zebrafish T-cell acute lymphoblastic leukemia. *Blood.* **115** (16), 3296–303, doi:10.1182/blood-2009-10-246488 (2010).
19. Iyengar, S., Houvras, Y., & Ceol, C. J. Screening for melanoma modifiers using a zebrafish autochthonous tumor model. *Journal of visualized experiments : JoVE.* (69), e50086, doi:10.3791/50086 (2012).
20. Mizgireuv, I. ., & Revskoy, S. Y. Transplantable tumor lines generated in clonal zebrafish. *Cancer research.* **66** (6), 3120–3125, doi:10.1158/0008-5472.CAN-05-3800 (2006).
21. Streisinger, G., Walker, C., Dower, N., Knauber, D., & Singer, F. Production of clones of homozygous diploid zebra fish (Brachydanio rerio). *Nature.* **291**, 293–296 (1981).
22. Blackburn, J. S., Liu, S., & Langenau, D. M. Quantifying the frequency of tumor-propagating cells using limiting dilution cell transplantation in syngeneic zebrafish. *Journal of visualized experiments : JoVE.* (53), e2790, doi:10.3791/2790 (2011).
23. Tang, Q., Abdelfattah, N. S., *et al.* Optimized cell transplantation using adult rag2 mutant zebrafish. *Nature methods.* **11**, 821–824, doi:10.1038/nmeth.3031 (2014).
24. Zhou, Q., Facciponte, J., Jin, M., Shen, Q., & Lin, Q. Humanized NOD-SCID IL2rg–/– mice as a preclinical model for cancer research and its potential use for individualized cancer therapies. *Cancer letters.* **344** (1), 13–9, doi:10.1016/j.canlet.2013.10.015 (2014).
25. Higashijima, S., Okamoto, H., Ueno, N., Hotta, Y., & Eguchi, G. High-frequency generation of transgenic zebrafish which reliably express GFP in whole muscles or the whole body by using promoters of zebrafish origin. *Developmental biology.* **192** (2), 289–99 (1997).
26. Langenau, D. M., Keefe, M. D. D. D., *et al.* Co-injection strategies to modify radiation sensitivity and tumor initiation in transgenic Zebrafish. *Oncogene.* **27** (30), 4242–8, doi:10.1038/onc.2008.56 (2008).
27. Rosen, J. N., Sweeney, M. F., & Mably, J. D. Microinjection of zebrafish embryos to analyze gene function. *Journal of visualized experiments : JoVE.* (25), 1–5, doi:10.3791/1115 (2009).
28. Westerfield, M. *The zebrafish book. A guide for the laboratory use of zebrafish (Danio rerio).* University of Oregon Press: Eugene, (2000).
29. Alexander, M. S., Kawahara, G., *et al.* Isolation and transcriptome analysis of adult zebrafish cells enriched for skeletal muscle progenitors. *Muscl., & nerve.* **43** (5), 741–50, doi:10.1002/mus.21972 (2011).
30. Motohashi, N., Asakura, Y., & Asakura, A. Isolation, culture, and transplantation of muscle satellite cells. *Journal of visualized experiments : JoVE.* (86), 1–7, doi:10.3791/50846 (2014).
31. Gerli, M. F. M., Maffioletti, S. M., Millet, Q., & Tedesco, F. S. Transplantation of induced pluripotent stem cell-derived mesoangioblast-like myogenic progenitors in mouse models of muscle regeneration. *Journal of visualized experiments : JoVE.* (83), e50532, doi:10.3791/50532 (2014).
32. Siegel, A. L., Gurevich, D. B., & Currie, P. D. A myogenic precursor cell that could contribute to regeneration in zebrafish and its similarity to the satellite cell. *The FEBS journal.* **280** (17), 4074–88, doi:10.1111/febs.12300 (2013).
33. Rowlerson, a, Radaelli, G., Mascarello, F., & Veggetti, a Regeneration of skeletal muscle in two teleost fish: Sparus aurata and Brachydanio rerio. *Cell and tissue research.* **289** (2), 311–22 (1997).
34. White, R. M., Sessa, A., *et al.* Transparent adult zebrafish as a tool for *in vivo* transplantation analysis. *Cell stem cell.* **2** (2), 183–9, doi:10.1016/j.stem.2007.11.002 (2008).

Copyright © 2014 Creative Commons Attribution-NonCommercial License

3

MYF5 is a Marker of TPCs in a Zebrafish Model of ERMS

"[...] by the help of Microscopes, there is nothing so small, as to escape our inquiry; hence there is a new visable World discovered to the understanding"

Robert Hooke
Micrographia (1665)

3.1 Chapter 3 - Preamble

A population that enriches for Tumor Propagating Potential was identified previously in the most undifferentiated, mononuclear compartment of the zebrafish skeletal muscle. These cells were isolated by Fluorescence Activated Cell Sorting (FACS) of *rag2-DsRed*-positive; *alpha-actin-GFP*-negative tumors and subsequently transplanted by limiting dilution transplantation to assess efficient engraftment (Langenau et al., 2007).

By devising several multi-colour labelling approaches, this population was now further narrowed into a *myf5-GFP*-positive, *mylpfa-mCherry*-negative population.

Furthermore, through live *in vivo* imaging, we were able to image for the first time tumor initiation and intra-tumor heterogeneity in a model of ERMS at single-cell resolution, based on the expression of muscle differentiation state-specific

promoters. While proliferating, more undifferentiated *myf5-GFP* cells are the first to expand from resident satellite cell-like cells, mid-differentiating, myoblast-like *myogenin-H2B-mRFP* cells emerge later, seed new areas of growth and cross collagenous matrix between myotomes as well as enter the vasculature. We also describe that a subset of RMS cells undergoes fusion and differentiates into aberrant long, multinucleated, *mylpfa-lyn-cyan*-positive muscle fibers.

My involvement in the last stages of this work led to the main focus of my research work on the role of MYF5 and MYOD1 in RMS self-renewal and growth, which is featured in Chapter 4.

3.2 Chapter 3 - Contribution

My contribution to this work:

- Maintenance of several transgenic zebrafish lines, including *AB/a-actin-RFP, TuAB/myf5-GFP, AB/myogenin-H2B-mRFP, AB/mylpfa-lyn-cyan, AB/mylpfa-mCherry and myf5-GFP*;
- Preparation, sectioning and IF against Myosin Heavy Chain in frozen sections followed by confocal microscopy imaging of double colour *myf5-GFP*; *mylpfa-mCherry* zebrafish ERMS tumors;
- Zebrafish ERMS tumor preparation, FACS and transplantation into syngeneic recipients

3.3 Chapter 3 - Publications

This collaboration resulted in:

- Co-authorship for the following publication (reprinted in full below):

Ignatius, M. S. et al. (2012). “In vivo imaging of tumor-propagating cells, regional tumor heterogeneity, and dynamic cell movements in embryonal rhabdomyosarcoma.” In: *Cancer Cell* 21.5, pp. 680–93. ISSN: 1878-3686. DOI: 10.1016/j.ccr.2012.03.043

Cancer Cell
Article

In Vivo Imaging of Tumor-Propagating Cells, Regional Tumor Heterogeneity, and Dynamic Cell Movements in Embryonal Rhabdomyosarcoma

Myron S. Ignatius,[1,3] Eleanor Chen,[1,3,4] Natalie M. Elpek,[2] Adam Z. Fuller,[1,3] Inês M. Tenente,[1,3,5] Ryan Clagg,[1,3] Sali Liu,[1,3] Jessica S. Blackburn,[1,3] Corinne M. Linardic,[6] Andrew E. Rosenberg,[1] Petur G. Nielsen,[1] Thorsten R. Mempel,[2] and David M. Langenau[1,3,*]
[1]Department of Pathology and Center for Cancer Research
[2]Center for Immunology and Inflammatory Diseases
Massachusetts General Hospital, Charlestown, MA 02129, USA
[3]Harvard Stem Cell Institute, Boston, MA 02114, USA
[4]Department of Pathology, Brigham and Women's Hospital, Boston, MA 02115, USA
[5]Instituto de Ciências Biomédicas Abel Salazar, 4099-003 Porto, Portugal
[6]Departments of Pediatrics, Pharmacology, and Cancer Biology, Duke University Medical Center, Durham, NC 27710, USA
*Correspondence: dlangenau@partners.org
DOI 10.1016/j.ccr.2012.03.043

SUMMARY

Embryonal rhabdomyosarcoma (ERMS) is an aggressive pediatric sarcoma of muscle. Here, we show that ERMS-propagating potential is confined to *myf5*+ cells and can be visualized in live, fluorescent transgenic zebrafish. During early tumor growth, *myf5*+ ERMS cells reside adjacent normal muscle fibers. By late-stage ERMS, *myf5*+ cells are reorganized into distinct regions separated from differentiated tumor cells. Time-lapse imaging of late-stage ERMS revealed that *myf5*+ cells populate newly formed tumor only after seeding by highly migratory *myogenin*+ ERMS cells. Moreover, *myogenin*+ ERMS cells can enter the vasculature, whereas *myf5*+ ERMS-propagating cells do not. Our data suggest that non-tumor-propagating cells likely have important supportive roles in cancer progression and facilitate metastasis.

INTRODUCTION

Rhabdomyosarcoma (RMS) is a pediatric malignancy that shares common features with skeletal muscle arrested in embryonic development (Xia et al., 2002). The two main subtypes of pediatric rhabdomyosarcoma, embryonal RMS (ERMS) and alveolar RMS (ARMS), differ in their clinical, biological, and molecular characteristics. For example, ERMS and ARMS can be distinguished based on histology and have different long-term prognoses, with ERMS patients having better overall outcome than ARMS patients. These divergent clinical features likely reflect the use of different molecular programs that lead to transformation. For example, we have identified that the RAS pathway is active in a majority of human ERMS (Hettmer et al., 2011; Langenau et al., 2007). By contrast, 85% of ARMS cells have recurrent chromosomal translocations that juxtapose PAX3 or PAX7 with the forkhead transcription factor (FKHR) (Xia et al., 2002). Finally, it is likely that ERMS and translocation-positive ARMS arise in different cell types that eventually undergo transformation. Keller et al. (2004) found that PAX3-FKHR+ ARMS can arise from Myf6-expressing myoblast cells but not dermamyotome or satellite cells that express Pax7. By contrast, ERMS can arise from either satellite cells or myoblasts that eventually reinitiate molecular programs found in satellite cells (Rubin et al., 2011). Despite elegant studies defining possible cells of origin in RMS, identification of an ERMS-propagating cell that is required for continued tumor growth in vivo has not been described in mice or humans.

Significance

Tumor-propagating potential is not found in all malignant cells, and, in most cancers, cells with more differentiated features are largely incapable of remaking tumor and yet constitute a majority of the tumor mass. A role for differentiated malignant cells in tumor growth, including dissemination and metastasis, has not been fully explored. We find that mid-differentiated *myogenin*-positive ERMS cells lack tumor-propagating potential yet are responsible for local invasion and can enter the vasculature. Slow-moving *myf5*+ ERMS-propagating cells are recruited to new sites of tumor growth after seeding by differentiated ERMS cells. This finding may explain the clinical observation that Myogenin positivity correlates with poor clinical outcome in human ERMS and suggests that differentiated tumor cells play critical roles in metastasis.

Tumor-propagating cells have been characterized in many malignances, and in some tumors, this potential is confined to a molecularly definable cell population that can be enriched by cell surface markers. For example, in acute myeloid leukemia, a rare $CD34^{+}CD38^{-}$ cell enriches for leukemia-propagating potential while in breast cancer $CD44^{+}CD24^{low/-}$expression is associated with tumor-propagating potential (reviewed in Dalerba et al., 2007). Molecularly defined, rare $CD133^{+}$ tumor-propagating cells have also been identified in a subset of gliomas and exhibit striking differences in response to nitric oxide and hypoxia inducible factor signaling when compared to more differentiated tumor cells (Eyler et al., 2011; Li et al., 2009). Thus, it is likely that many tumors contain hierarchically organized cell subpopulations that retain the capacity to remake tumor and yet give rise to differentiated tumor cell progeny. One might expect that selection would favor the evolution of tumors with high numbers of tumor-propagating cells at a cost of differentiated cell types. Paradoxically, however, in most malignancies, tumor-propagating cells are far less abundant than differentiated tumor cells that are incapable of remaking tumor. These data suggest that differentiated tumor cells may provide important supportive roles in overall growth and maintenance. To date, a role for differentiated, non-tumor-propagating ERMS cells has yet to be fully explored.

Stem cells often reside in distinct niches in normal tissue, and their functions are exquisitely controlled by local factors secreted by supporting cells. For example, hematopoietic stem cells (HSCs) have been shown to home to niches within the calvarium that are tightly associated with osteoblasts (Lo Celso et al., 2009). These and other niche-associated cells presumably provide paracrine-signaling factors to recruit and maintain these cells in a specific niche. Unlike other tissues, the muscle stem cell niche is defined by juxtaposition of satellite cells next to differentiated muscle fibers, and their numbers and differentiation capacity are controlled by complex signaling pathways regulated by mature muscle cells (reviewed in Bentzinger et al., 2012). Despite a large body of data defining stem cell niches in normal tissue, few studies have identified tumor-specific niches and/or regions of compartmentalized tumor cell function and fewer still have used microscopic imaging to directly visualize tumor-propagating cells within live animals. In one example, Sipkins et al. (2005) used a combination of multiphoton and confocal microscopy to image the HSC niche in the calvarium of mice and demonstrated that these sites can attract multiple tumor cell types; however, it is unknown if these malignant cells are capable of reinitiating tumors. In ERMS, as with most solid tumors, it is unknown whether tumor-propagating cells reside in distinct regions within the tumor mass and whether the more differentiated cells play a role in promoting tumor progression.

Here, we utilize a transgenic zebrafish model of ERMS to identify the tumor-propagating cell in this disease and to define the functional consequences of tumor cell heterogeneity within live animals. Because ERMS cell subpopulations can be fluorescent labeled based on myogenic factor expression, ERMS cell subtypes can be visualized in live animals and the processes of cell growth, division, and local dissemination can be visualized as dynamic processes in live animals. Our data provide an explanation for the large number of non-tumor-propagating cells in established cancers and reveal an important supportive role for differentiated tumor cell types in local dissemination and metastasis.

RESULTS

Imaging Distinct Stages of ERMS Growth

Externally visible ERMS can develop as early as 10 days of life in zebrafish injected with *rag2-KRASG12D* (Langenau et al., 2007), and >80% of ERMS develop in the tail musculature (n > 50). To assess how tumors initiate and evolve in zebrafish ERMS, we injected *α-actin-GFP* transgenic zebrafish at the one-cell stage of development with *rag2-dsREDexpress* and *rag2-KRASG12D* (Figures 1A–1F), facilitating imaging of ERMS cells in relation to normal muscle. Microinjection of multiple transgenes into one-cell-stage animals leads to cointegration and coexpression in animals that develop ERMS (Langenau et al., 2008). This approach provides a robust method to create mosaic transgenic animals with fluorescently labeled ERMS cell subpopulations (Langenau et al., 2007).

Sequential confocal imaging over several days showed that ERMS forms in a choreographed and stereotypical manner (Figures 1A–1F and 1J–1M). Specifically, dsRed+ ERMS mononuclear cells arise at the extreme outer borders of the myotome segments and move toward the midline where they are initially unable to bypass the horizontal myosepta—a single cell layer that separates myotome segments (Figure 1A; stage 1, n = 7). After several days, a subset of cells cross the horizontal myosepta and take up residence between normal muscle fibers within the newly colonized myotome segment (stage 2; Figures 1B and 1C; n = 5). Differentiated ERMS cells that express both *rag2-dsREDexpress* and *α-actin-GFP* can move laterally into neighboring muscle segments by transiting through the collagen matrix of the myoseptum (n = 6; Figures 1D–1F; Movie S1 available online) or stream into new myotome segments by growing past the edge of myoseptum (n = 3, early stage 3). The collagen matrix of the muscle myoseptum is a cell-impermeable barrier that is the site of muscle attachment in teleost fish and is similar in function to tendons in mouse and humans. Late-stage ERMS cells undergo rapid loss of fibers, breakdown of normal muscle architecture including collagen remodeling, and development of mononuclear tumor cells, reminiscent of the spindle variant of human ERMS.

Neovascularization is a hallmark of cancer and an ideal surrogate for assessing tumorigenicity. To assess when KRASG12D-expressing cells are transformed, we monitored neovascularization in *fli1-GFP* transgenic animals that were injected at the one-cell stage of life with *rag2-KRASG12D* and *rag2-dsREDexpress.* Animals were monitored for tumor growth by confocal microscopy beginning at 10 days of life (n = 22; Figures 1G–1I). ERMS at stage 1 failed to recruit new vasculature (n = 0 of 3), but stage 2 and early stage 3 ERMS had begun to recruit new vasculature (n = 8 of 8; Figure 1H) with new branches arising from both the intersegmental vessels and vertebral artery. By late stage 3, ERMS developed intricate networks of new vessels (n = 11 of 11; Figure 1I). Our imaging studies define distinct stages of ERMS growth and suggest that RAS-expressing cells become fully transformed by stage 2 of tumor development (Figures 1J–1M).

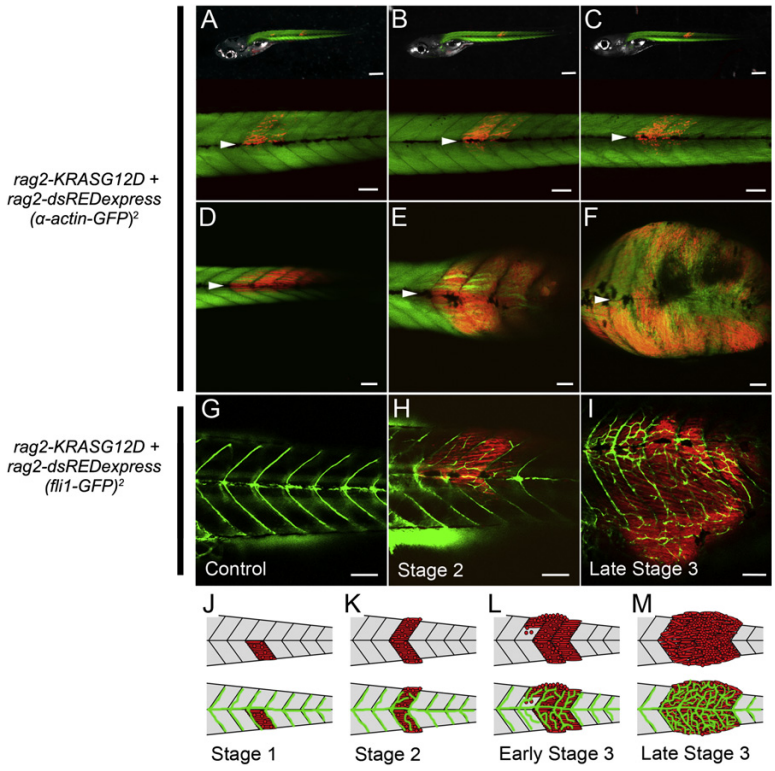

Figure 1. Visualizing Distinct Stages of Embryonal RMS Growth

(A–F) *rag2-dsRED*-labeled ERMS arising in *α-actin-GFP* transgenic zebrafish. The same animal imaged at 6, 9, and 12 days postfertilization (dpf) is shown in (A), (B), and (C), respectively. A representative zebrafish where dsRED+ ERMS cells have already bypassed the horizontal myoseptum and migrated into new segments that were previously free of tumor (F, stage 3) at 13, 18, and 24 dpf is shown in (D), (E), and (F), respectively. The horizontal myoseptum is denoted by white arrows.

(G–I) *fli1-GFP* transgenic control animal (G) compared with a *rag2-dsRED*-labeled ERMS arising in *fli1-GFP* transgenic zebrafish at early stage 2 (H) or a late stage 3 (I).

(J–M) Schematic of stages of ERMS growth.

Scale bars in the upper panels of (A) through (C), 500 μm. Scale bars in the lower panels of (A) through (C) and in (D) through (I), 100 μm.

See also Movie S1.

Identification of Molecularly Distinct Fluorescent-Labeled ERMS Cell Subpopulations

Previous experiments in zebrafish have identified an ERMS cell subpopulation that had superior tumor-propagating potential when compared to other tumor-derived cells. This ERMS-propagating cell was *rag2-dsREDexpress+/α-actin-negative* and expressed high levels of *myf5*, *c-met*, and *m-cadherin*—markers of satellite and early muscle progenitor cells (Langenau et al., 2007). *MYF5* is highly upregulated in human ERMS compared to both translocation positive ARMS and normal muscle (Zibat et al., 2010) and in comparing zebrafish ERMS to normal muscle (Langenau et al., 2007). To directly assess whether *myf5* labels distinct ERMS cell subpopulations, *myf5-GFP/myosin light chain 2-mCherry* (*mylz2*) syngeneic animals were created by four rounds of outcrossing to CG1 syngeneic animals (Smith et al., 2010) and injected at the one-cell stage with *rag2-KRASG12D*. *myf5*-GFP transgenic animals exhibit green fluorescent protein (GFP) expression in early somitogenesis and later in satellite cells and early muscle progenitor cells (Chen et al., 2007; Seger et al., 2011) while the *mylz2* promoter drives expression in differentiated muscle cells (Ju et al., 2003; Smith et al., 2010). Fluorescent-labeled ERMS cell subpopulations were isolated from double transgenic animals by fluorescence-activated cell sorting (FACS). Reanalysis of sorted cells by FACS confirmed that ERMS contained four distinct populations of cells (purity > 87% and viability > 97%).

To verify that discrete fluorescent-labeled ERMS cell subpopulations were molecularly distinct, sorted cell populations were assessed for gene expression differences based on microarray (Figure 2A; Table S1) and real-time PCR (Figures 2B and S1). Gene expression analysis was completed on FACS-sorted ERMS cells derived from serially passaged tumors, ensuring that fluorescent-labeled cells were tumor derived. Microarray analysis confirmed that each cell subpopulation exhibited wide differences in gene expression. Subsequent real-time PCR analysis established that the *myf5-GFP+/mylz2-mCherry-negative* cells expressed high levels of *myf5*, *c-met*, and *m-cadherin* but not *pax7a*, *pax7b*, or differentiated markers (Figures 2B and S1). By contrast, *mylz2-mCherry+* ERMS cells expressed high levels of mature muscle markers including *myod*, *myogenin*, *troponin I fast-twitch isoform 2* (*tnni2a*), *α-actin 1b* (*acta1b*), *ventricular myosin heavy chain-like* (*vmhcl*), *actin-related protein 2/3 complex subunit 5B* (*arpc5b*), *carboxypeptidase vitellogenic-like (cpvl)*, and *chemokine (C-X-C motif) receptor 4b* (*cxcr4b*). Finally, the double-negative cell population comprised predominantly blood cells that express *myeloid-specific peroxidase* (*mpx*) and *lymphocyte-specific protein tyrosine kinase* (*lck*). Our data confirm that fluorescent-labeled ERMS cell subpopulations can be prospectively isolated to relative purity following FACS and are molecularly distinct.

Given that FACS could identify unique ERMS cell subpopulations that exhibited wide differences in gene expression, we questioned whether these cells also differ in rates of proliferation and cellular turnover. Proliferation was assessed at 6 hr following intraperitoneal injection of EDU into ERMS-affected animals (Figures 2C–2E and S1). *myf5-GFP+/mylz2-mCherry-negative* cells (24.1% ± 4.8%) incorporated EDU over a 6 hr pulse, whereas differentiated ERMS cells that express *mylz2-mCherry* were far less proliferative (8.9% ± 5.0%; $p < 0.00001$). By contrast, following 3-day administration of EDU, all fluorescent-labeled ERMS cell subfractions exhibited equal proliferative capacity, suggesting that *myf5-GFP+/mylz2-mCherry-negative*

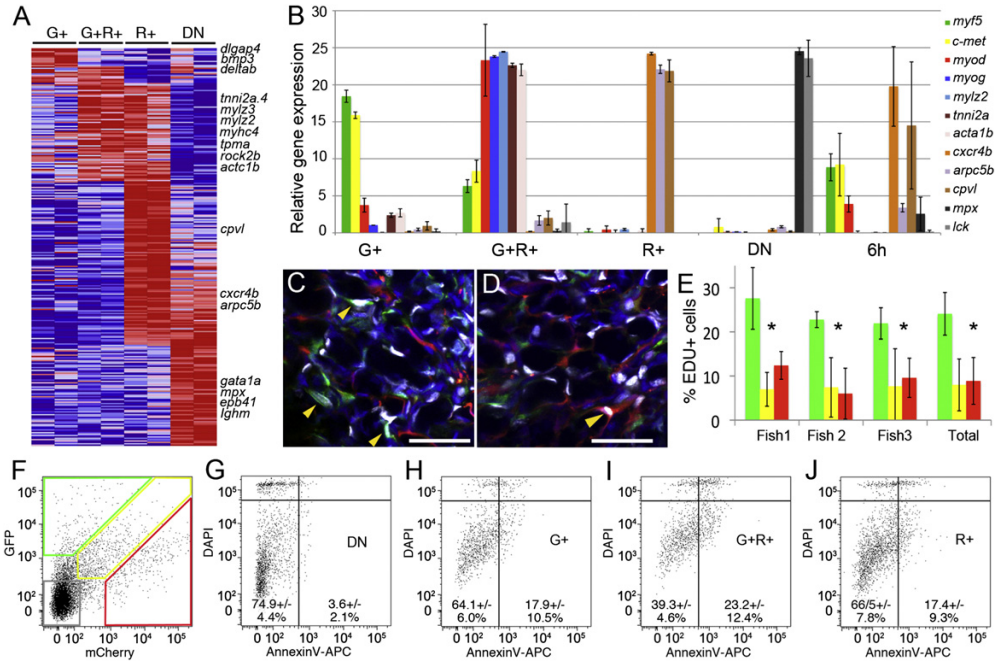

Figure 2. Fluorescent Transgenic Approaches Identify Discrete and Molecularly Definable ERMS Cell Subpopulations in *myf5-GFP/mylz2-mCherry* Transgenic Fish

(A) Heat map showing differential gene expression between FACS-sorted ERMS cell subpopulations isolated from serially passaged *myf5-GFP/ mylz2-mCherry* ERMS (microarray log fold-change > 1.5). *myf5-GFP+/mylz2-mCherry-negative* (G+), *myf5-GFP+/mylz2-mCherry+* (G+R+), *myf5-GFP-negative/mylz2-mCherry+* (R+), and double negative (DN).

(B) Quantitative real-time PCR of sorted ERMS cell subpopulations. Expression values, ±1 SD.

(C and D) Confocal images of EDU-stained sections from serially passaged *myf5-GFP+/mylz2-mCherry+* ERMS. Tumor regions with large numbers of either *myf5-GFP+* (C) or *mylz2-mCherry+* ERMS cells (D). Blue denotes DAPI+ nuclei, and white denotes EDU+ nuclei. Yellow arrows indicate EDU-labeled cells. Scale bar, 25 μm.

(E) Quantification of EDU incorporation over a 6 hr EDU pulse. Data for *myf5-GFP+/mylz2-mCherry-negative* ERMS cells are denoted by green bars, data for *myf5-GFP+/mylz2-mCherry+* cells are indicated by yellow bars, and data for *myf5-GFP-negative/mylz2-mCherry+* cells are indicated by red bars. Three individual tumors shown as well as cumulative data across all tumors (Total). *$p < 0.00001$. Error bars, ±1 SD.

(F) FACS plot of serially passaged *myf5-GFP/mylz2-mCherry* ERMS.

(G–J) Gated ERMS cells assessed for DAPI and AnnexinV-APC staining (double negative, DN) (G); *myf5-GFP+/mylz2-mCherry-negative* (G+) (H); *myf5-GFP+/mylz2-mCherry+* (G+R+) (I); and *myf5-GFP-negative/mylz2-mCherry+* (R+) (J). Live cells are shown within the DAPI-negative/AnnexinV-negative gates.

See also Figure S1 and Table S1.

cells divided and differentiated over this time (data not shown). In addition to striking differences in cell proliferation between ERMS cell subpopulations, *myf5-GFP+/mylz2-mCherry+* cells had higher levels of apoptotic cellular turnover when compared with *myf5-GFP+/mylz2-mCherry-negative* and *myf5-GFP-negative/mylz2-mCherry+* cells ($p < 0.01$, Fisher's exact test; Figures 2F–2J). Taken together, our fluorescent transgenic approach identifies unique ERMS cell subpopulations that have different fluorescent reporter expression, divergent gene expression profiles, and varied capacities for proliferation and apoptosis.

myf5-GFP+ Cells Are the ERMS-Propagating Cell Population

To assess if *myf5-GFP* transgene expression enriches for ERMS-propagating potential, cells were isolated from transplant animals that developed *myf5-GFP+/mylz2-mCherry+* ERMS (Figures 3A–3G) and subjected to two rounds of FACS in the presence of propidium iodide or DAPI to isolate highly purified and viable cells (Figures 3H–3K; 87.7%–99.7% purity and >98% viability). ERMS cell subpopulations were introduced into CG1 syngeneic recipient animals at limiting dilution (Figure 3L–3R), and animals were assessed for engraftment from 10 to 120 days posttransplantation (Table 1). All animals developed ERMS before 45 days posttransplantation, confirming that slower cycling ERMS-propagating cell types would not be missed in our analysis. In three ERMS tumors tested, the tumor-propagating activity was confined to the *myf5-GFP+/mylz2-mCherry-negative* cell subpopulation (Table 1), with an average frequency of 1 in 146 cells capable of reinitiating tumors in recipient animals (range 1 in 87–245, 95% confidence interval). By contrast, only 1 in 4,206 *myf5-GFP+/mylz2-mcherry+* cells were capable of inducing tumors (range 1 in 1,550 to 11,409, 95% confidence interval, $p = 3.38e\text{-}15$ when compared to ERMS-propagating activity in *myf5-GFP+/mylz2-mcherry-negative* cells). Of 61 animals, none

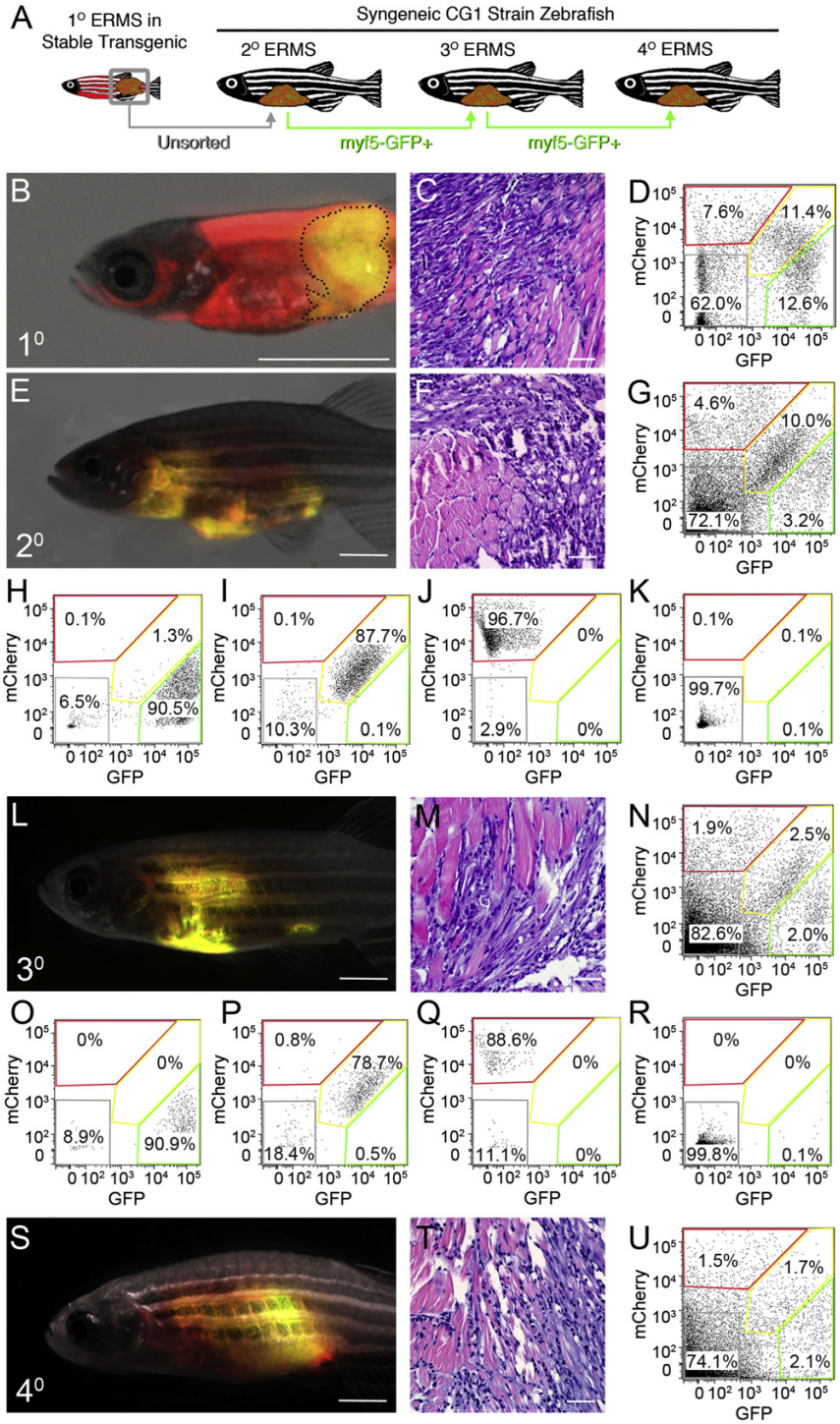

Figure 3. ERMS-Propagating Cells Express *myf5-GFP* but Not the *mylz2-mCherry* Differentiated Muscle Marker

(A) Schematic of experimental design.

(B–D) A primary ERMS arising in syngeneic *myf5-GFP/mylz2-mCherry* transgenic zebrafish (35 dpf). Broken black line denotes tumor area.

Table 1. Limiting Dilution Cell Transplantation Identifies that *myf5-GFP+/mylz2-mCherry-negative* Cells Are the ERMS-Propagating Cells

ERMS #1 2° Transplants					3° Transplants
Cell #	G+	G+R+	R+	Neg	G+
1,000	6 of 6	2 of 7	0 of 6	0 of 7	6 of 6
10	5 of 9	0 of 9	0 of 8	0 of 10	7 of 8
10	0 of 8	0 of 8	0 of 9	0 of 7	0 of 10
TPC #	1 in 140**	1 in 3,461	NA	NA	1 in 67
95% CI	59–329	872–13,740	NA	NA	31–143
ERMS #2 2° Transplants					
Cell #	G+	G+R+	R+	Neg	
1,000	6 of 6	0 of 6	0 of 6	0 of 6	
10	4 of 7	2 of 10	0 of 10	0 of 10	
10	1 of 8	0 of 9	0 of 10	0 of 8	
TPC #	1 in 109**	1 in 3,495	NA	NA	
95% CI	44–270	808–15,120	NA	NA	
ERMS #3 2° Transplants					
Cell #	G+	G+R+	R+	Neg	
1,000	2 of 3	0 of 2	0 of 3	0 of 4	
10	8 of 9	0 of 8	0 of 8	1 of 8	
10	1 of 8	0 of 9	0 of 9	0 of 9	
TPC #	1 in 159**	NA	NA	1 in 4,840	
95% CI	63–401	NA	NA	632–37,094	

Asterisks denote significant differences in tumor-propagating cell number (TPC #) between *myf5-GFP+/mylz2-mCherry-negative* and double-positive ERMS cells (**$p < 0.00001$). Neg, negative; NA, not applicable; 95% CI, 95% confidence interval.

engrafted disease from terminally differentiated *myf5-GFP-negative/mylz2-Cherry+* cells (lower bound for ERMS-propagating potential was 1 in >5,969 cells). In total, we observed a remarkable 28- to >40-fold enrichment of tumor-propagating potential within our *myf5-GFP+/mylz2-mCherry-negative* cell type when compared with other sorted ERMS cell subpopulations. Similar results were also observed in primary ERMS. Specifically, three primary ERMS tumors were isolated from 20- to 30-day-old larval zebrafish, pooled, and fluorescent-labeled ERMS cell subpopulations were isolated by FACS. Of eight animals, three engrafted disease from 10^2 *myf5-GFP+/mylz2-mCherry-negative* cells, whereas the remaining ERMS cell subpopulations could not transfer disease at this cell dose (0 of 23, purity 83%–98% and viability > 98.6%, $p = 0.012$, Fisher's exact test). These results further support our finding that the *myf5-GFP+/mylz2-mCherry-negative* population is highly enriched for ERMS-propagating activity.

To assess the long-term tumor-propagating potential of the *myf5-GFP+/mylz2-mCherry-negative* ERMS cells, cells were re-isolated from transplant recipient animals (Figure 3N) and introduced into CG1, syngeneic recipient animals (>78.9% purity and 96% viable; Figures 3O–3R). Again, the *myf5-GFP+/mylz2-mCherry-negative* cell subpopulation was capable of remaking ERMS (Figure 3S–3U; Table 1). Histological analysis showed that primary and serially transplanted ERMS arising from *myf5-GFP+/mylz2-mCherry-negative* cell populations have similar morphology and overall proportions of fluorescent-labeled ERMS cell subpopulations (Figures 3C, 3D, 3F, 3G, 3M, 3N, 3T, and 3U).

Visualizing *myf5-GFP+* ERMS-Propagating Cells In Vivo

To assess whether *myf5-GFP+* ERMS cells could be directly visualized in live animals, *rag2-dsREDexpress* and *rag2-KRASG12D* were coinjected into one-cell-stage *myf5-GFP* transgenic animals and assessed by confocal microscopy. Discrete *myf5-GFP+* tumor cells could be readily identified by confocal imaging with a majority of *myf5-GFP+* ERMS cells coexpressing both GFP and dsREDexpress (97.5 ± 2.9%; n = 568 cells counted in three animals). Moreover, *myf5-GFP+* early muscle progenitor cells from control animals were relatively rare (n = 3 [animals]; 2.3 ± 2.3 cells per imaging field), whereas *myf5-GFP+* cells were abundant in ERMS (n = 3; 194.2 ± 23.7 cells per field, t test, $p = 0.0002$). Taken together, our data suggest that a vast majority of *myf5-GFP+* cells contained within the boundaries of the ERMS mass are tumor derived.

To further refine the ERMS cell subpopulations for imaging studies, triple fluorescent transgenic ERMS animals were created by microinjecting *myogenin-H2B-RFP*, *mylz2-lyn-cyan*, and *rag2-KRASG12D* into one-cell-stage *myf5-GFP* transgenic animals (Figures 4A–4C). Histone fusion proteins are long lived and confined to the nucleus, whereas *lyn-cyan* encodes for membrane localized blue fluorescent protein. Because transgenes cointegrate as concatamers (Langenau et al., 2008), ERMS cells coexpress all three transgenes and label distinct tumor cell compartments associated with stages of muscle development (Figure S2). In normal development, *myf5* is expressed in satellite cells and early muscle progenitor cells, *myogenin* is expressed in committed, mid-differentiated muscle myoblasts, and *mylz2* is expressed in differentiated myoblasts. Transgenic reporters have been described for all three of these promoters, and each drives expression within the correct cellular compartments during normal muscle development (Chen et al., 2007; Du et al., 2003; Ju et al., 2003). Moreover, gene expression studies confirm that these promoters drive correct tissue-specific gene expression in ERMS (Figure S2), and additional cell transplantation experiments establish that *myf5-GFP+/myogenin-negative* cell types exclusively retain ERMS-propagating potential (Figure S2). For example, 4 of 18 animals engrafted ERMS from 10^2 *myf5-GFP+/myogenin-H2B-RFP-negative* sorted ERMS cells

(E–G) Fluorescent-labeled ERMS engraft into syngeneic secondary recipient animals when transplanted with unsorted primary ERMS cells.
(H–K) FACS plots of fluorescent-labeled ERMS cells isolated from secondary recipient fish following two rounds of FACS.
(L–R) Transplantation of *myf5-GFP+/mylz2-mCherry-negative* FACs sorted cells induced ERMS in tertiary transplant animals (L–R) and quaternary recipients (S–U).
Hematoxylin- and eosin-stained sections (C, F, M, and T) and FACS (D, G, N, and U) of primary and serially passaged ERMS. Scale bars, 2 mm (for B, E, L, and S) and 100 μm (for C, F, M, and T).

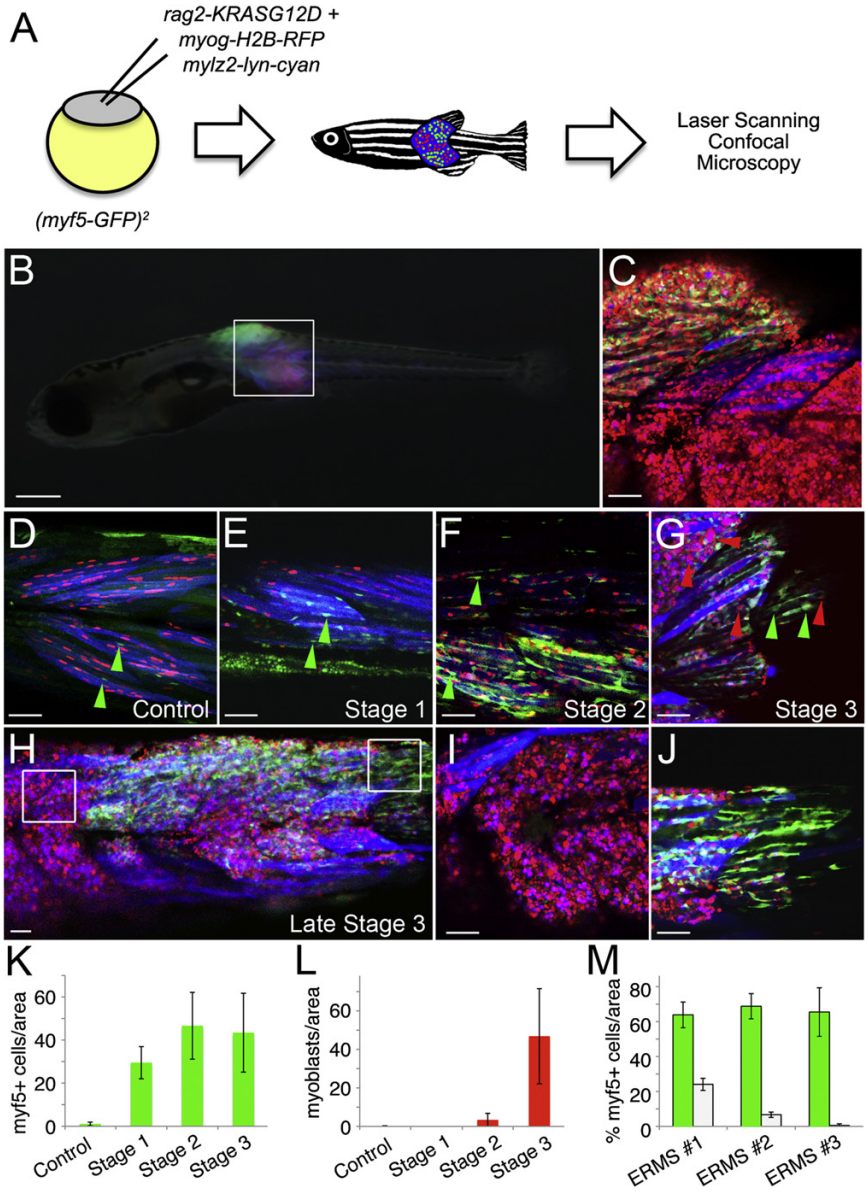

Figure 4. *myf5-GFP*+ ERMS-Propagating Cells Are Dynamically Reorganized during Tumor Growth

(A) Schematic of the experimental design.

(B) A *myf5-GFP* transgenic animal injected at the one-cell stage of life with *rag2-KRASG12D*, *myogenin-H2B-RFP*, and *mylz2-lyn-cyan* with triple fluorescent-labeled ERMS at 16 days of life.

(C) A merged confocal image of the boxed region shown in (B).

(D) Control *myf5-GFP* transgenic animal injected with *myogenin-H2B-RFP* and *mylz2-lyn-cyan*. *myf5-GFP*+ muscle precursor cells are denoted by green arrowheads.

(E–G) Representative image of an ERMS-affected zebrafish labeled with *myf5-GFP*, *myogenin-H2B-RFP*, and *mylz2-lyn-cyan* at stages 1, 2, and 3, respectively. Green arrowheads denote *myf5-GFP*+ cells, whereas red arrowheads denote mononuclear *myogenin-H2B-RFP*+ ERMS cells.

(H) Late stage 3 ERMS from a triple fluorescent-labeled animal.

(I and J) Boxed regions in (H) imaged at higher magnification show regional partitioning of differentiated cells (I) compared with *myf5-GFP*+ ERMS-propagating cells (J).

(K) Quantification of *myf5-GFP*+ cells during stages of ERMS growth when compared to control animals.

(L) Quantification of mononuclear *myogenin-H2B-RFP*+ cells during stages of ERMS growth when compared to control animals.

(68.5% purity, 99.8% viable), whereas *myogenin-H2B-RFP*+ cell types could not induce tumors, regardless of whether they expressed *myf5-GFP* (n = 0 of 32, p = 0.013, Fisher's exact test).

Confocal imaging of fluorescent-transgenic ERMS fish that express *myf5-GFP/myogenin-H2B-RFP/mylz2-lyn-cyan* easily identified *myf5-GFP*+ cells, of which a small subset coexpress *myogenin-H2B-RFP* (Figure 4C). Some *myogenin-H2B-RFP*+ cells with nuclear fluorescent protein expression fail to express either *myf5-GFP* or *mylz2-lyn-cyan*, indicating that these cells are most similar to midmyoblast stages. Gene expression studies confirm that *myogenin*-promoter expression drives H2B-fluorescent protein expression in a subset of myosin-heavy-chain-expressing muscle cell populations, implying that these represent differentiated cell types (Figure S2). Nearly all *mylz2-lyn-cyan*+ cells coexpress *myogenin-H2B-RFP* (99.5% ± 1%; n = 8 ERMS, n > 1,700 cells counted), reflecting that H2B-fluorescent protein expression persists in more differentiated ERMS cells.

myf5-GFP+ cells Are Reorganized into Discrete Compartments during Late-Stage Tumor Growth

We next wanted to define the location of ERMS cell subpopulations during various stages of tumor growth. *myf5-GFP* transgenic animals were injected with *rag2-KRASG12D, myogenin-H2B-RFP*, and *mylz2-lyn-cyan* and imaged by confocal microscopy starting at 10 days of life. Stage 1 ERMS exhibited greatly expanded numbers of *myf5-GFP*+ cells when compared to control animals and were confined to regions immediately adjacent to muscle fibers (Figures 4D–4G and 4K). Mononuclear *myogenin-H2B-RFP*+ and double-positive *myogenin-H2B-RFP*+/ *mylz2-lyn-cyan*+ ERMS cells were not observed in stage 1 ERMS; however, they were detected by stage 2 and increased in number as tumors progressed to stage 3 (Figures 4F–4I and 4L). By late stage 3 ERMS, *myf5-GFP*+ cells lost fiber contacts and began to populate discrete portions of the tumor that were physically separated from more differentiated *myogenin-H2B-RFP*- and *mylz2-lyn-cyan*-expressing ERMS cells (Figures 4H–4J and 4M). The *myf5-GFP*+ cells were often located within different myotome segments compared to differentiated ERMS cell subpopulations; however, regional partitioning of cells based on differentiation status was also observed within a single myotome segment and in transplanted animals (Figure S2), confirming that compartmentalization did not result from physiological constraints imposed during development but rather was an intrinsic property of ERMS growth.

Human ERMS Cells Are Also Compartmentalized Based on Myogenic Factor Expression

To assess whether human RMS cells also contain distinct regions of tumor cells based on myogenic factor expression, primary human ERMS and xenografted human ERMS derived from RD and SMS-CTR cell lines (Linardic et al., 2005) were assessed for myogenic marker expression, including Myogenin, PAX7, and MYOD. Distinct regions of high and low Myogenin-expressing cells were seen in a vast majority of primary tumor samples (n = 12 of 14, p < 0.03, Student's t test) and were present in all xenograft tumors (n = 7, six regions per tumor, p < 0.02, Students's t test; Figure 5 and Figure S3; Table S2). By contrast, most ARMS cells expressed Myogenin, and its expression was not confined to specific areas within the tumor mass (n = 10; range = 79%–99%), suggesting that regional partitioning of tumor cells based on Myogenin expression is specific to ERMS. We also stained four primary human ERMS tumors for PAX7 and identified regions of high and low expression in two of the four tumors. In one ERMS sample, expression was diffuse while the other tumor was PAX7 negative, indicating that not all primary ERMS cells express PAX7. Unfortunately, MYF5 antibodies have not been developed to detect human protein within paraffin-embedded sections, precluding analysis of less differentiated regions contained within the tumors.

myogenin+ ERMS Cells Are Highly Migratory and Precede the Recruitment of *myf5*+ ERMS-Propagating Cells into Newly Colonized Areas of Growth

Having established that the *myf5-GFP*-expressing ERMS cell population contains tumor-propagating activity, we wanted to assess if these cells also promote invasive tumor growth. Multiphoton intravital microscopy recordings from *myf5-GFP/myogenin-H2B-RFP* or *myf5-GFP/myogenin-H2B-Amcyan* transgenic tumor zebrafish revealed that *myf5-GFP*+ single-positive ERMS cells were largely stationary and displayed only confined crawling movements (Figures 6A–6F and S4; Movies S2, S3, S4, and S5). In contrast, *myogenin*+ ERMS cells were robustly migratory and had the ability to invade across myotome segments through a normally impenetrable collagen matrix. Cells that expressed lower amounts of the H2B-fluorescent fusion protein were orderly arranged along the direction of muscle fibers, had uniform nuclear shape, and did not show any motility (Movies S2 and S3), suggesting that these were differentiated tumor cells of which a subset had undergone fusion (Figure 6F, right).

ERMS cell subpopulations also differ in their proliferative capacity. Primary ERMS cells from *myf5-GFP*+/*myogenin-H2B-RFP*+ animals were pulsed with EDU for 6 hr and then sectioned and assessed for EDU incorporation (Figures 6G–6I). *myf5-GFP*+ ERMS cells were highly proliferative (39.4% ± 9.4%; n = 3), whereas *myf5-GFP-negative/myogenin-H2B-RFP*+ cells rarely proliferated (2.6% ± 3.8%; n = 3, p = 0.0001). In vivo multiphoton imaging of transplant and primary ERMS confirmed that *myf5-GFP*+/*mylz2-negative* ERMS-propagating cells are highly proliferative, with 27 of 90 GFP+ cells dividing into two daughter cells (n = 3 tumors). Multiphoton imaging revealed that resting *myf5-GFP*+ ERMS cells are elongated (Figure 6J) and then round up in shape just prior to cell division (Figure 6K). Following this dynamic shape change, *myf5-GFP*+ ERMS cells quickly divide

(M) Quantification of regional compartmentalization of ERMS cells based on differentiation status in late stage 3 tumors (n = 3). Green bars denote regions that contain higher percentages of *myf5-GFP*+ ERMS-propagating cells compared to white bars where *myf5-GFP*+ cells are less abundant and conversely more differentiated.

Error bars in (K–M), ±1 SD. Scale bar, 500 μm for (B) and 50 μm for (C–J).

See also Figure S2.

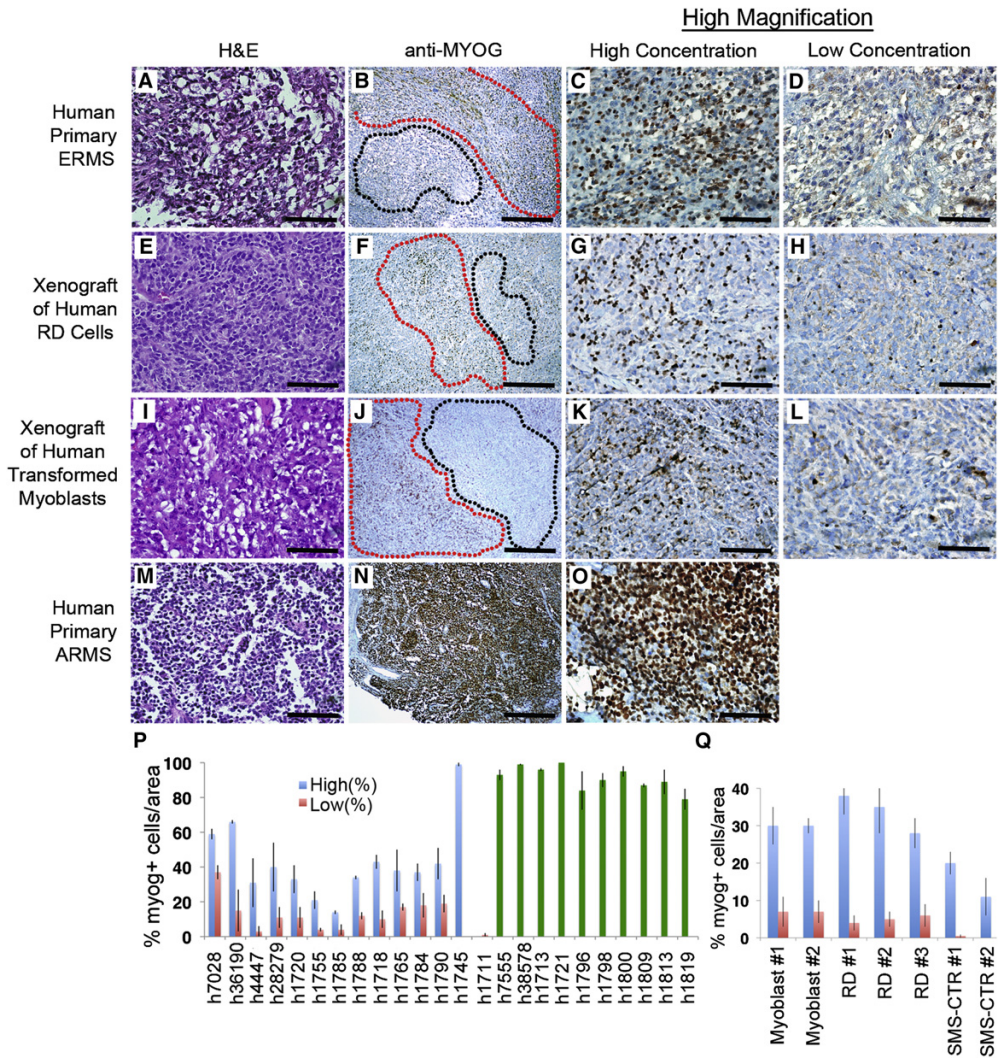

Figure 5. Human Embryonal RMS Exhibit Regional Portioning of Cells Based on Myogenic Factor Expression

(A–D) Primary human ERMS.

(E–L) RD human cell lines (E–H) or human RAS-transformed myoblasts (I–L) introduced into SCID/*beige* mice.

(M–O) Primary human ARMS. Hematoxylin/Eosin-stained sections (A, E, I, and M) and anti-Myogenin immunohistochemistry performed on adjacent sections (B, F, J, and N). Regions containing high numbers of Myogenin+ cells are denoted by red outline, while regions with low numbers of Myogenin+ cells are denoted by black outline (B, F, and J). ARMS did not show regional portioning based on Myogenin staining (N). Magnified views of areas with high concentrations of Myogenin+ cells (C, G, K, and O) or areas with low or absent expression (D, H, and L).

(P–Q) Quantification of regional compartments in primary and metastatic human RMS (P) and in mice xenografted with human RD and SMS-CTR ERMS cells and human RAS-transformed myoblasts (myoblasts, in Q). Numbers in (Q) denote tumors arising in separate animals. Blue bars denote areas with high percentages of Myogenin+ cells compared to areas with low numbers of cells (red bars). Green bars denote diffuse and ubiquitous expression of Myogenin within ARMS. Error bars, ±1 SD. Scale bars, 50 μm (for A, C–E, G–I, K–M, and O) and 200 μm (for B, F, J, and N).

See also Figure S3 and Table S2.

into two GFP-labeled daughter cells (Figures 6L–6M). Subsequently, these daughter cells begin to reacquire parental morphology (Movie S6), reminiscent of normal *myf5-GFP*+ muscle precursors. By contrast, 0 of 90 *mylz2*+ cells proliferated over this time, regardless of whether they expressed *myf5-GFP*.

To further visualize the dynamic movements of ERMS cells in vivo, late stage 3 triple transgenic ERMS affected animals were serially imaged over 16 hr to capture cell movements (Figures 7A–7H; Movie S7). As was seen in our multiphoton imaging, *myf5-GFP*+ cells that lack differentiated marker

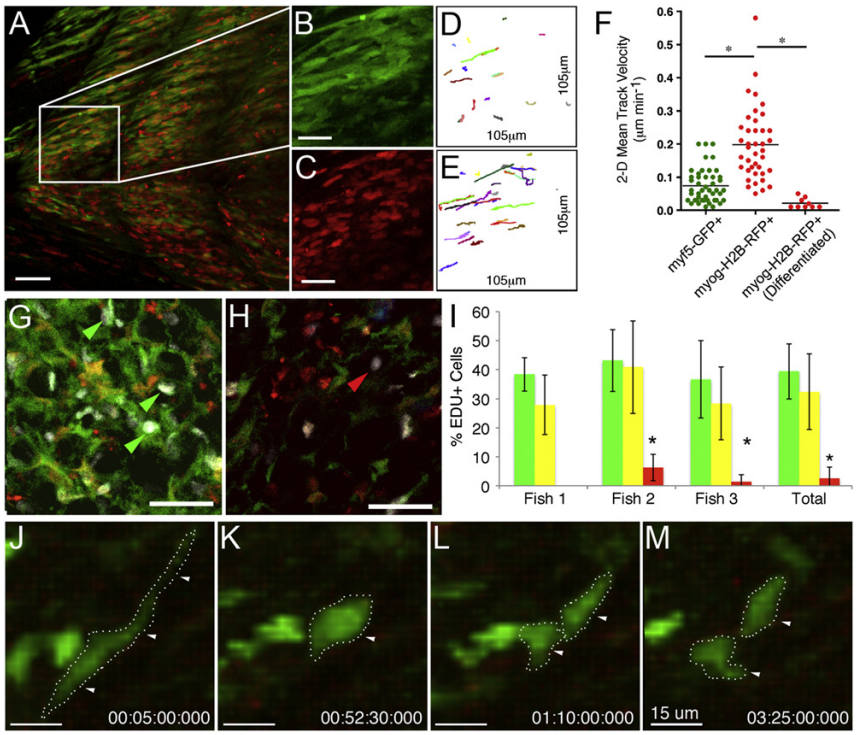

Figure 6. *myf5-GFP*+ ERMS-Propagating Cells Are Slow Moving but Highly Proliferative while *myogenin-H2B-RFP*+ Cells Do Not Divide but Are Highly Migratory

(A–E) Multiphoton recording of a stage 3 ERMS arising in *myf5-GFP/myogenin-H2B-RFP* transgenic zebrafish (B and C) Magnified view of the boxed region in (A) showing *myf5-GFP*+ (B) or *myogenin-H2B-RFP*+ ERMS cells (C).

(D and E) Tracks of cell movement over the 6.7-hr observation period. The same areas are shown as in (B) and (C), respectively.

(F) Mean track velocities of representative cell types contained within the tumor mass. *p < 0.001.

(G and H) EDU staining of double transgenic *myf5-GFP+/myogenin-H2B-RFP*+ primary zebrafish ERMS (35 dpf). Confocal image of a tumor section with high numbers of *myf5-GFP*+ ERMS cells (G) compared to a section with high numbers of *myogenin-H2B-RFP*+ cells (H). White denotes nuclei that have incorporated EDU. EDU incorporation into *myf5-GFP*+ or *myogenin-H2B-RFP*+ ERMS cells denoted by green or red arrows, respectively.

(I) Quantification of proliferation over the 6 hr EDU pulse. *myf5-GFP+/myogenin-H2B-RFP-negative* (green bars), double positive (yellow bars), and *myf5-GFP-negative/ myogenin-H2B-RFP*+ (red bars). Error bars, ±1 SD. Asterisk denotes significant differences, *p = 0.0001.

(J–M) Static images of a *myf5-GFP*+ ERMS cells dividing. Scale bars, 50 μm (for A, G, and H), 25 μm (for B–E), and 15 μm (for J–M).

See also Figure S4 and Movies S2, S3, S4, S5, and S6.

expression move only locally within the tumor and exhibit regional crawling movements, whereas *myogenin-H2B-RFP+/mylz2-lyn-cyan-negative* cells are highly motile and could be easily visualized migrating into adjacent nonaffected normal tissue (Figures 7A–7D; Movie S7). By contrast, differentiated ERMS cells that express *myogenin-H2B-RFP* and *mylz2-lyn-cyan* are largely stationary.

To investigate which ERMS cells were the first to migrate into unaffected tissue, we conducted serial imaging experiments over longer observation intervals, focusing on regions that were adjacent to expanding tumor. Serial confocal imaging of fluorescent ERMS fish over several days revealed that *myogenin-H2B*+ ERMS cells precede the recruitment of *myf5-GFP*+ cells into newly colonized areas of tumor growth (n = 7; Figures 7I, 7J, and S4). Not only do fluorescent-labeled *myogenin-H2B*+ ERMS cells move locally within the tumor, but they also enter the vasculature (Movie S8). A small portion of *myogenin-H2B-RFP+/myf5-GFP-negative* cells were associated with vasculature and could invade neovascular beds in *fli1-GFP* transgenic animals (Figures 7K and 7L). To verify the fidelity of H2B-fluorescent labeling of ERMS cell subfractions and to directly visualize if *myf5-GFP*+ ERMS cells can enter the vasculature, we induced ERMS in stable transgenic animals that express *myf5-GFP/flk1-mCherry* by coinjecting both *rag2-KRASG12D* and *myogenin-H2B-Amcyan*. As was seen using the H2B-RFP transgenic reporter, we found that *myogenin-H2B-Amcyan*+ cells are highly migratory (Movies S4 and S5), were the first cell type to colonize new areas of tumor growth, and could be observed transiting the vasculature (Figures 7M and 7N; Movies S5 and S9). By contrast, *myf5-GFP*+ ERMS cells exhibited reduced motility when compared with *myogenin*+ ERMS cells and were never observed entering the vasculature

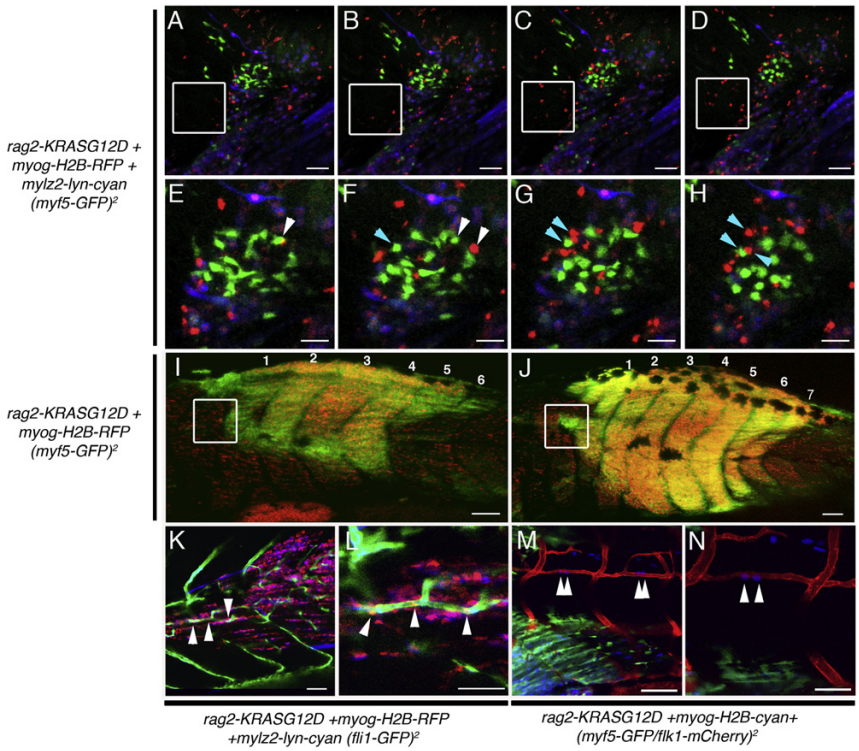

Figure 7. *myf5-GFP*+ ERMS-Propagating Cells Are Recruited to New Areas of Tumor Growth Only after Seeding by *myogenin*+ ERMS Cells

(A–H) Time-lapse images of *myf5-GFP* transgenic animal injected with *rag2-KRASG12D, myogenin-H2B-RFP* and *mylz2-lyn-cyan*. Panels are merged image planes taken every hour. *myogenin-H2B-RFP*+ cells migrate into normal tissues over time (white boxed region). Magnified views of time-lapse images documenting that *myf5-GFP*+ cells are largely stationary while *myogenin-H2B-RFP*+ cells are highly migratory and migrate away from GFP+ cells (denoted by arrows in E–H).

(I and J) Serial imaging of a *myf5-GFP* transgenic animal injected with *rag2-KRASG12D* and *myogenin-H2B-RFP* shown at 14 and 17 dpf, respectively. White boxes denote a region that initially contained only *myogenin-H2B-RFP*+ cells (I) but was later colonized by *myf5-GFP*+ cells (J).

(K and L) ERMS developing in a *fli1-GFP* transgenic animal injected with *rag2-KRASG12D*, *myogenin-H2B-RFP*, and *mylz2-lyn-cyan.* (K) Merged z-stacks showing three *myogenin-H2B-RFP*+ cells associated with and inside *fli1-GFP*+ vessels, which was confirmed by imaging a single image plane at higher magnification (L, white arrowhead).

(M and N) ERMS developing in a *flk1-mCherry* transgenic animal injected with *rag2-KRASG12D* and *myogenin-H2B-cyan* showing four cells entering the vasculature (white arrowheads in M) and a single plane image showing two cells transiting into the vasculature at higher magnification (white arrowheads in N).

Scale bar, 50 μm (for A–H, K, L, and N) and 100 μm (for I, J, M).

See also Figure S4 and Movies S7, S8, and S9.

(n = 10 animals). Again, slow-moving *myf5-GFP*+ cells were found in newly colonized regions only after initial invasion by *myogenin*+ ERMS cells.

DISCUSSION

Myf5 as a Marker of ERMS-Propagating Cells

The limiting dilution cell transplantation studies outlined here confirm the existence of a highly purified and molecularly definable ERMS-propagating cell that expresses *myf5*, *m-cadherin*, and *c-met* but not differentiated muscle markers. The *myf5-GFP*+ ERMS-propagating cell gives rise to all the other differentiated ERMS cells contained within the tumor mass and exhibits enhanced proliferative capacity as assessed by EDU incorporation and direct in vivo cell imaging. These results are in keeping with our previous work showing that ERMS-propagating activity was largely confined to the *rag2-dsRED+/α-actin-negative* ERMS cell population that preferentially expressed *myf5* and other activated satellite cell markers (Langenau et al., 2007). However, *rag2-dsRED+/α-actin-negative* ERMS cells exhibited only a modest 3-fold enrichment for tumor-propagating potential when compared to *rag2-dsRED+/alpha-actin+* ERMS cells (Langenau et al., 2007). By contrast, experiments outlined here using new fluorescent transgenic reporter lines and syngeneic zebrafish show that the *myf5-GFP+/mylz2-negative* ERMS cells exhibit a remarkable 28- to >40-fold enrichment of tumor-propagating potential when compared to other ERMS-derived cell populations.

Myf5 is a myogenic regulatory factor related to MyoD and has important roles in muscle development. For example,

MyoD/Myf5-deficient mice lack muscle, while deficiencies in only one of these genes does not affect muscle specification (Rudnicki et al., 1993), suggesting important and yet redundant functions of these genes in development. It has also been shown that *Myf5* is highly expressed in activated satellite cells and has important roles in postnatal muscle regeneration in response to injury (Cooper et al., 1999; Gayraud-Morel et al., 2009; Ustanina et al., 2007), suggesting that Myf5 may regulate self-renewal in normal muscle satellite cells. Microarray analysis and cross-species comparisons have shown that *MYF5* is upregulated in both zebrafish and human ERMS but not translocation-positive ARMS (Langenau et al., 2007; Zibat et al., 2010), and recent work from Rubin et al. (2011) has shown that *Myf5* is differentially expressed in murine ERMS regardless of which muscle cell subpopulation is initially targeted for transformation. These results suggest that *Myf5* gene programs are likely reinitiated in transformed cells and may have important roles in driving ERMS growth. By contrast, translocation-positive ARMS fail to express *MYF5*, precluding *MYF5* marker expression as an identifying characteristic of ARMS-propagating cells and raising the interesting possibility that the molecular mechanisms regulating tumor-propagating potential differ between molecular subtypes of RMS. Given the critical roles of the Myf5 transcription factor in muscle development and regeneration in mice, it will be important to assess if *myf5* is a marker of ERMS-propagating cells or if it plays a regulatory role in ERMS self-renewal and growth.

Regional Partitioning of ERMS Cells Based on Differentiation Status

Evidence in solid tumors to support a discrete, specialized microenvironment that augments tumor growth and proliferation is now just beginning to emerge. For example, tumor-propagating cells, including those of glioblastomas, have been shown to reside in a vascular niche that promotes both their maintenance and their ability to divide and produce daughter cells capable of inducing tumors (reviewed by Gilbertson and Rich, 2007). In other solid tumors arising in skin, prostate, and breast, tumor stromal fibroblasts also serve an essential role in maintaining a favorable microenvironment for tumor growth and expansion. For example, work by Orimo et al. (2005) has shown that stromal fibroblasts associated with invasive breast carcinoma cells can promote tumor growth and angiogenesis through secretion of SDF-1. In normal muscle, stem cell numbers are exquisitely regulated by paracrine factors like Wnt5a (Polesskaya et al., 2003), Myostatin (McCroskery et al., 2003), and Notch ligands (Conboy et al., 2003). Many of these factors are secreted by normal fibers that can sense injury and elicit recruitment and expansion of muscle progenitors that are required for regeneration. Thus, mature muscle provides a supportive microenvironment that facilitates homeostatic regulation of muscle stem cells. In our zebrafish ERMS model, we document that *myf5-GFP*+ ERMS-propagating cells are initially juxtaposed to muscle fibers in an expanded muscle satellite/progenitor cell niche, suggesting that early stage ERMS cells cannot escape the constraints of muscle architecture or are held in check by local secreted factors emanating from normal muscle. By the late stages of ERMS growth, ERMS-propagating cells are reorganized and take up residence in defined regions within the tumor mass. Following this regional partitioning of ERMS cells, mid-differentiated *myogenin*+ ERMS cells show enhanced migratory capability and move away from the ERMS-propagating cells from which they had arisen. These mid-differentiated myogenin+ ERMS cells are highly migratory, seed new areas of tumor growth, and cease to move once they turn on differentiated muscle markers including muscle myosin light chain. Such biologically constrained characteristics of ERMS cells would ensure that tumor-propagating cells remain confined to regionally defined areas and do not compete with differentiated ERMS cells for local resources including growth factors and oxygen. The extent to which regional partitioning of tumor cells occurs in other solid tumors is unknown; however, assuming this phenomenon is found in diverse cancer types, it will be important to determine if regional partitioning of tumor cells provides protective advantages to tumor-propagating cells, facilitating the retention of a small number of cancer cells that evade treatment and eventually give rise to disease relapse.

A Role for Differentiated, Non-Tumor-Propagating Cells in Facilitating Tumor Growth and Metastasis

Myogenin immunohistochemical reactivity found in >80% of RMS cells distinguishes patients with poor clinical outcome (Heerema-McKenney et al., 2008), suggesting that *Myogenin*+ cells have a unique role in RMS progression and metastasis. In our model, *myogenin-H2B*+ cells arise from *myf5-GFP*+ ERMS-propagating cells, lack tumor-propagating potential, and are the first cell type to migrate into new areas of tumor growth. A subset of *myogenin*+ ERMS cells infiltrate blood vessels—a first step toward metastasis—and are also the first to colonize new areas of tumor growth, only to be infiltrated later by slow-migrating *myf5*+ ERMS-propagating cells. Our work raises the interesting possibility that differentiated, non-ERMS-propagating cells may create a supportive environment that augments growth and is responsible for local tumor invasion. For example, it is possible that once mid-differentiated *myogenin*+ cells infiltrate new areas of growth, that they secrete factors that recruit slow-moving *myf5*+ ERMS-propagating cells, facilitating tumor spread. Alternatively, it is possible that *myogenin*+ cells break down collagen and cell-cell contacts, acting as trailblazers to establish migratory tracks that allow slow-moving *myf5*+ ERMS-propagating cells to transit into newly forming tumor. Our work also highlights that metastatic capacity and tumor-propagating potential need not be confined to the same tumor cell subpopulations, but rather that local infiltration and metastasis may be facilitated by differentiated, non-tumor-propagating cells. We expect that these same principles may be more broadly applicable to a diversity of cancers, accounting for why tumors retain large numbers of differentiated cell types that themselves are incapable of reconstituting tumor.

Our findings of a *myf5*+ ERMS-propagating cell population and a *myogenin*+ migratory population both contributing to tumorigenesis may have profound therapeutic implications. Instead of targeting only tumor-propagating cells for destruction, drug design should also take into account the mechanisms regulating the homeostasis of more differentiated tumor cells and their nonproliferative roles in regulating growth. Moreover, therapies that focus on modulating the differentiation status of ERMS cells should attempt to force the conversion of tumor-propagating cells into cells with terminally differentiated

myoblast characteristics that are incapable of recreating tumor, cannot migrate, and fail to enter into the vasculature.

EXPERIMENTAL PROCEDURES

Study Approval

These studies were approved by the Massachusetts General Hospital Subcommittee on Research Animal Care under protocol #2011N000127 (zebrafish), the Duke University Institutional Animal Care & Use Committee under protocol A 036-03-02 (mouse), and the Partners Human Research Committee under protocol #2009-P-002756 (human). Samples were obtained from the Pathology Department of Massachusetts General Hospital. Use of decoded, paraffin-embedded human tissue samples does not require informed consent.

Animals

CG1-strain (Smith et al., 2010), *α-actin-GFP* (Higashijima et al., 1997), *myf5-GFP* (Chen et al., 2007), *fli1-GFP* (Lawson and Weinstein, 2002), *flk1-mCherry* (Wang et al., 2010), and *mylz2-mCherry* transgenic zebrafish (Smith et al., 2010) have been reported previously.

The *rag2-KRASG12D*, *rag2-dsREDexpress*, *myogenin-H2B-RFP*, *myogenin-H2B-Amcyan*, and *mylz2-lyn-cyan* constructs were microinjected into one-cell-stage zebrafish singly (*rag2-KRASG12D* injected into *myf5-GFP/mylz2-mCherry* syngenic zebrafish, 60 ng/μl) or as combinations with linearized DNA at a final combined concentration of 120 ng/μl essentially as described (Langenau et al., 2008).

FACS and ERMS Cell Transplantation

FACS analysis and ERMS cell transplantation were completed essentially as described elsewhere (Smith et al., 2010; Langenau et al., 2007). Sort gates were placed based on wild-type control fish and *myf5-GFP+*, *mylz2-mCherry+*, or *mylz2-lyn-cyan+* ERMS. DAPI, propidium iodide, or TOPRO3 was used to isolate viable cells. ERMS tumors were double sorted to obtain pure, viable cell populations. Sort purity was assessed after two rounds of sorting when possible. Following limiting dilution cell transplantation into nonirradiated syngeneic CG1-recipient animals, fish were analyzed for fluorescent tumor engraftment from 10 to 120 days posttransplantation. Tumor-propagating potential was quantified using the Extreme Limiting Dilution Analysis software (http://bioinf.wehi.edu.au/software/elda/). A subset of transplanted fish was sectioned and stained with hematoxylin and eosin to confirm the presence or absence of ERMS.

Immunohistochemistry, EDU Staining, and Annexin V Staining

Paraffin embedding and sectioning, cryostat sectioning, and immunohistochemical analysis were performed essentially as described elsewhere (Langenau et al., 2007; see also Supplemental Experimental Procedures). EDU staining was performed using the Click-iT Alexa Fluor 647 imaging kit (Invitrogen). Annexin analysis for apoptotic cells was performed via FACS using annexin V conjugated to Alexa Fluor 647 (Invitrogen).

Gene Expression Analysis

Total RNA was isolated from AB-strain embryos 6 and 24 hr postfertilization and FAC-sorted ERMS cell subpopulations (TRIzol, GIBCO/BRL) in the presence of glycol blue. Quantitative real-time PCR utilized gene-specific PCR primers (Supplemental Experimental Procedures), and expression was normalized to 18 s and β-actin controls to obtain relative transcript levels using the $2^{-\Delta\Delta CT}$ method. Relative gene expression was normalized within individual samples, and cumulative transcript expression across the four ERMS cell subpopulations was set to 25. Samples were assessed in relation to embryos 6 and 24 hr postfertilization to ensure that results for $2^{-\Delta\Delta CT}$ results for any given gene were not lower than 10-fold expression found in normal development. Microarray experiments were completed essentially as described (fold change cutoff > 1.5-fold log scale; Langenau et al., 2007). Microarray data have been deposited into the GEO database (GSE32425).

Laser Scanning Confocal Microscopy and Dual Photon Imaging

Larval zebrafish were anesthetized in Tricaine and embedded in a single drop of low melt 1% agarose on a glass bottom petri dish (No 1.5, Mat Tek Corporation). Each petri dish was supplemented with fish water and imaged using an inverted Pascal or LSM510 Zeiss laser scanning confocal microscope or an upright Ultima IV multiphoton microscope (Prairie Technologies). Quantification was completed by counting the total numbers of fluorescent-labeled ERMS cell subpopulations contained in two 250 × 150 μm areas per animal (Figures 4K and 4L; control, n = 7; stage 1, n = 3; stage 2, n = 4; stage 3, n = 7). Because regional niches can be compartmentalized within a single myotome segment, a smaller area was assessed for total numbers of *myf5-GFP+* and *myogenin-H2B-RFP+ ERMS* cells (50 × 50 μm^2 area, six areas per tumor; Figure 4M).

For cell tracking, sequences of image stacks were transformed into maximum intensity-projected movies using Imaris 7.1 software (Bitplane) and exported as Quicktime movies. Manual two- or three-dimensional tracking was performed using the manual tracking plugin in ImageJ or using Imaris 7.1. Annotation and further processing of movies was completed using ImageJ and Quicktime 7.

SUPPLEMENTAL INFORMATION

Supplemental Information includes nine movies, two tables, four figures, and Supplemental Experimental Procedures and can be found with this article online at doi:10.1016/j.ccr.2012.03.043.

ACKNOWLEDGMENTS

E.C. and J.S.B. are supported by the National Institutes of Health (NIH) Training Grants T32 HL007627 and 5T32CA09216-26, respectively. C.M.L. is supported by R01 CA122706 and K12 HD043494. D.M.L. is supported by NIH Grants K01 AR055619, 1RO1CA154923, and 1R21CA156056; the Alex's Lemonade Stand Foundation; the Sarcoma Foundation of America; the American Cancer Society; and the Harvard Stem Cell Institute. I.M.T. is supported by Fundação para a Ciência e Tecnologia (the Portuguese Foundation for Science and Technology) through Fellowship SFRH/BD/51288/2010. We thank Huai-Jen Tsai for *myf5-GFP* transgenic animals and Clarrisa Henry for critical review of our manuscript.

Received: September 20, 2011
Revised: February 6, 2012
Accepted: March 12, 2012
Published: May 14, 2012

REFERENCES

Bentzinger, C.F., Wang, Y.X., and Rudnicki, M.A. (2012). Building muscle: molecular regulation of myogenesis. Cold Spring Harb. Perspect. Biol. *4*, 4.

Chen, Y.H., Wang, Y.H., Chang, M.Y., Lin, C.Y., Weng, C.W., Westerfield, M., and Tsai, H.J. (2007). Multiple upstream modules regulate zebrafish myf5 expression. BMC Dev. Biol. *7*, 1.

Conboy, I.M., Conboy, M.J., Smythe, G.M., and Rando, T.A. (2003). Notch-mediated restoration of regenerative potential to aged muscle. Science *302*, 1575–1577.

Cooper, R.N., Tajbakhsh, S., Mouly, V., Cossu, G., Buckingham, M., and Butler-Browne, G.S. (1999). In vivo satellite cell activation via Myf5 and MyoD in regenerating mouse skeletal muscle. J. Cell Sci. *112*, 2895–2901.

Dalerba, P., Cho, R.W., and Clarke, M.F. (2007). Cancer stem cells: models and concepts. Annu. Rev. Med. *58*, 267–284.

Du, S.J., Gao, J., and Anyangwe, V. (2003). Muscle-specific expression of myogenin in zebrafish embryos is controlled by multiple regulatory elements in the promoter. Comp. Biochem. Physiol. B Biochem. Mol. Biol. *134*, 123–134.

Eyler, C.E., Wu, Q., Yan, K., MacSwords, J.M., Chandler-Militello, D., Misuraca, K.L., Lathia, J.D., Forrester, M.T., Lee, J., Stamler, J.S., et al. (2011). Glioma stem cell proliferation and tumor growth are promoted by nitric oxide synthase-2. Cell *146*, 53–66.

Gayraud-Morel, B., Chrétien, F., and Tajbakhsh, S. (2009). Skeletal muscle as a paradigm for regenerative biology and medicine. Regen. Med. *4*, 293–319.

Gilbertson, R.J., and Rich, J.N. (2007). Making a tumour's bed: glioblastoma stem cells and the vascular niche. Nat. Rev. Cancer *7*, 733–736.

Heerema-McKenney, A., Wijnaendts, L.C., Pulliam, J.F., Lopez-Terrada, D., McKenney, J.K., Zhu, S., Montgomery, K., Mitchell, J., Marinelli, R.J., Hart, A.A., et al. (2008). Diffuse myogenin expression by immunohistochemistry is an independent marker of poor survival in pediatric rhabdomyosarcoma: a tissue microarray study of 71 primary tumors including correlation with molecular phenotype. Am. J. Surg. Pathol. *32*, 1513–1522.

Hettmer, S., Liu, J., Miller, C.M., Lindsay, M.C., Sparks, C.A., Guertin, D.A., Bronson, R.T., Langenau, D.M., and Wagers, A.J. (2011). Sarcomas induced in discrete subsets of prospectively isolated skeletal muscle cells. Proc. Natl. Acad. Sci. USA *108*, 20002–20007.

Higashijima, S., Okamoto, H., Ueno, N., Hotta, Y., and Eguchi, G. (1997). High-frequency generation of transgenic zebrafish which reliably express GFP in whole muscles or the whole body by using promoters of zebrafish origin. Dev. Biol. *192*, 289–299.

Ju, B., Chong, S.W., He, J., Wang, X., Xu, Y., Wan, H., Tong, Y., Yan, T., Korzh, V., and Gong, Z. (2003). Recapitulation of fast skeletal muscle development in zebrafish by transgenic expression of GFP under the mylz2 promoter. Dev. Dyn. *227*, 14–26.

Keller, C., Arenkiel, B.R., Coffin, C.M., El-Bardeesy, N., DePinho, R.A., and Capecchi, M.R. (2004). Alveolar rhabdomyosarcomas in conditional Pax3:Fkhr mice: cooperativity of Ink4a/ARF and Trp53 loss of function. Genes Dev. *18*, 2614–2626.

Langenau, D.M., Keefe, M.D., Storer, N.Y., Guyon, J.R., Kutok, J.L., Le, X., Goessling, W., Neuberg, D.S., Kunkel, L.M., and Zon, L.I. (2007). Effects of RAS on the genesis of embryonal rhabdomyosarcoma. Genes Dev. *21*, 1382–1395.

Langenau, D.M., Keefe, M.D., Storer, N.Y., Jette, C.A., Smith, A.C., Ceol, C.J., Bourque, C., Look, A.T., and Zon, L.I. (2008). Co-injection strategies to modify radiation sensitivity and tumor initiation in transgenic Zebrafish. Oncogene *27*, 4242–4248.

Lawson, N.D., and Weinstein, B.M. (2002). In vivo imaging of embryonic vascular development using transgenic zebrafish. Dev. Biol. *248*, 307–318.

Li, Z., Bao, S., Wu, Q., Wang, H., Eyler, C., Sathornsumetee, S., Shi, Q., Cao, Y., Lathia, J., McLendon, R.E., et al. (2009). Hypoxia-inducible factors regulate tumorigenic capacity of glioma stem cells. Cancer Cell *15*, 501–513.

Linardic, C.M., Downie, D.L., Qualman, S., Bentley, R.C., and Counter, C.M. (2005). Genetic modeling of human rhabdomyosarcoma. Cancer Res. *65*, 4490–4495.

Lo Celso, C., Fleming, H.E., Wu, J.W., Zhao, C.X., Miake-Lye, S., Fujisaki, J., Côté, D., Rowe, D.W., Lin, C.P., and Scadden, D.T. (2009). Live-animal tracking of individual haematopoietic stem/progenitor cells in their niche. Nature *457*, 92–96.

McCroskery, S., Thomas, M., Maxwell, L., Sharma, M., and Kambadur, R. (2003). Myostatin negatively regulates satellite cell activation and self-renewal. J. Cell Biol. *162*, 1135–1147.

Orimo, A., Gupta, P.B., Sgroi, D.C., Arenzana-Seisdedos, F., Delaunay, T., Naeem, R., Carey, V.J., Richardson, A.L., and Weinberg, R.A. (2005). Stromal fibroblasts present in invasive human breast carcinomas promote tumor growth and angiogenesis through elevated SDF-1/CXCL12 secretion. Cell *121*, 335–348.

Polesskaya, A., Seale, P., and Rudnicki, M.A. (2003). Wnt signaling induces the myogenic specification of resident CD45+ adult stem cells during muscle regeneration. Cell *113*, 841–852.

Rubin, B.P., Nishijo, K., Chen, H.I., Yi, X., Schuetze, D.P., Pal, R., Prajapati, S.I., Abraham, J., Arenkiel, B.R., Chen, Q.R., et al. (2011). Evidence for an unanticipated relationship between undifferentiated pleomorphic sarcoma and embryonal rhabdomyosarcoma. Cancer Cell *19*, 177–191.

Rudnicki, M.A., Schnegelsberg, P.N., Stead, R.H., Braun, T., Arnold, H.H., and Jaenisch, R. (1993). MyoD or Myf-5 is required for the formation of skeletal muscle. Cell *75*, 1351–1359.

Seger, C., Hargrave, M., Wang, X., Chai, R.J., Elworthy, S., and Ingham, P.W. (2011). Analysis of Pax7 expressing myogenic cells in zebrafish muscle development, injury, and models of disease. Dev. Dyn. *240*, 2440–2451.

Sipkins, D.A., Wei, X., Wu, J.W., Runnels, J.M., Côté, D., Means, T.K., Luster, A.D., Scadden, D.T., and Lin, C.P. (2005). In vivo imaging of specialized bone marrow endothelial microdomains for tumour engraftment. Nature *435*, 969–973.

Smith, A.C., Raimondi, A.R., Salthouse, C.D., Ignatius, M.S., Blackburn, J.S., Mizgirev, I.V., Storer, N.Y., de Jong, J.L., Chen, A.T., Zhou, Y., et al. (2010). High-throughput cell transplantation establishes that tumor-initiating cells are abundant in zebrafish T-cell acute lymphoblastic leukemia. Blood *115*, 3296–3303.

Ustanina, S., Carvajal, J., Rigby, P., and Braun, T. (2007). The myogenic factor Myf5 supports efficient skeletal muscle regeneration by enabling transient myoblast amplification. Stem Cells *25*, 2006–2016.

Wang, Y., Kaiser, M.S., Larson, J.D., Nasevicius, A., Clark, K.J., Wadman, S.A., Roberg-Perez, S.E., Ekker, S.C., Hackett, P.B., McGrail, M., and Essner, J.J. (2010). Moesin1 and Ve-cadherin are required in endothelial cells during in vivo tubulogenesis. Development *137*, 3119–3128.

Xia, S.J., Pressey, J.G., and Barr, F.G. (2002). Molecular pathogenesis of rhabdomyosarcoma. Cancer Biol. Ther. *1*, 97–104.

Zibat, A., Missiaglia, E., Rosenberger, A., Pritchard-Jones, K., Shipley, J., Hahn, H., and Fulda, S. (2010). Activation of the hedgehog pathway confers a poor prognosis in embryonal and fusion gene-negative alveolar rhabdomyosarcoma. Oncogene *29*, 6323–6330.

Cancer Cell, Volume, *21*

Supplemental Information

In Vivo Imaging of Tumor-Propagating Cells, Regional Tumor Heterogeneity, and Dynamic Cell Movements in Embryonal Rhabdomyosarcoma

Myron S. Ignatius, Eleanor Chen, Natalie M. Elpek, Adam Z. Fuller, Inês M. Tenente, Ryan Clagg, Sali Liu, Jessica S. Blackburn, Corinne M. Linardic, Andrew E. Rosenberg, Petur G. Nielsen, Thorsten R. Mempel, and David M. Langenau

Inventory of Supplemental Information

Supplemental Data

Movie S1, related to Figure 1. Provided as a Quicktime movie file. Z-stack images of an *alpha-actin-GFP* transgenic fish injected at the one-cell stage of life with *rag2-KRASG12D* and *rag2-dsREDexpress* that developed ERMS by 17 days of life. Movie shows a differentiated *rag2-dsRED+/alpha-actin-GFP+* cell that transits through the collagen-rich, cell-impermeable myoseptum that separate myotome segments (see cells denoted by arrow heads).

Table S1, related to Figure 2. Provided as an Excel file. Affymetrix probes and gene list for microarray analysis shown in Figure 2A. The microarray data can be accessed with Geo accession number GSE32425.

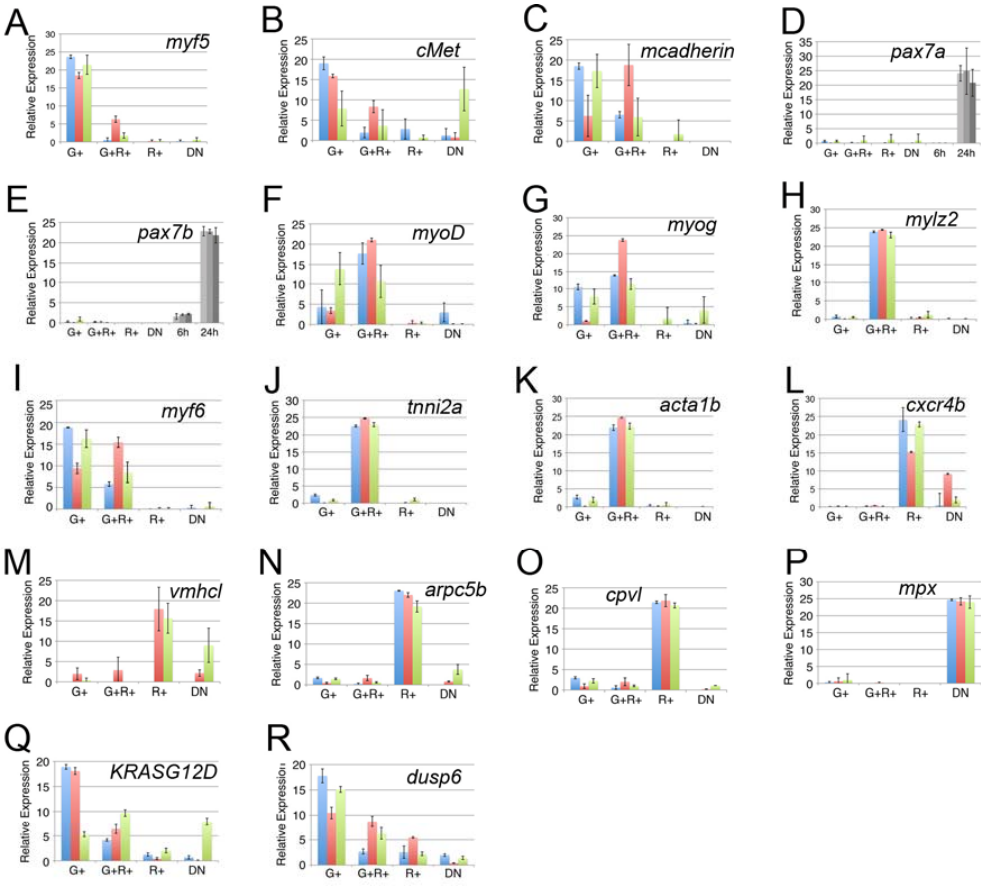
A
myf5
B
cMet
C
mcadherin
D
pax7a
E
pax7b
F
myoD
G
myog
H
mylz2
I
myf6
J
tnni2a
K
acta1b
L
cxcr4b
M
vmhcl
N
arpc5b
O
cpvl
P
mpx
Q
KRASG12D
R
dusp6
Relative Expression
G+
G+R+
R+
DN
6h
24h

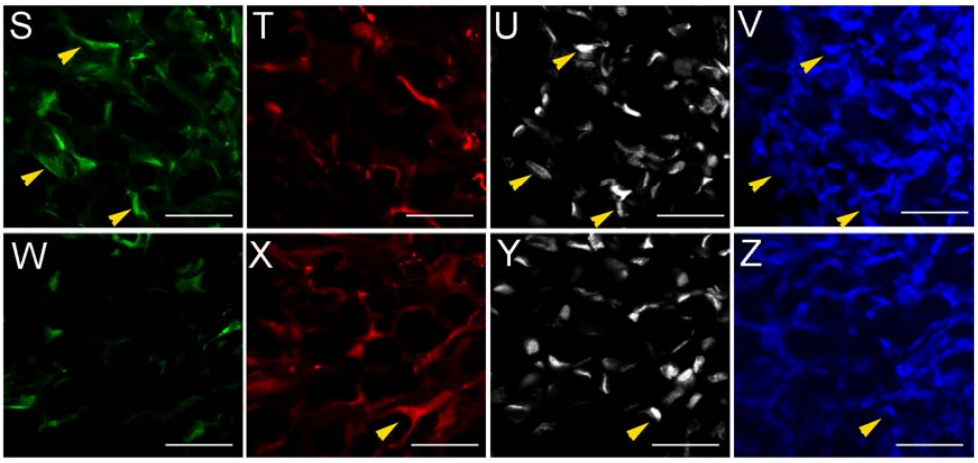
S
T
U
V
W
X
Y
Z

Figure S1, related to Figure 2. ERMS cell subpopulations from *myf5-GFP/mylz2-mCherry* transgenic zebrafish exhibit differences in gene expression and cell proliferation.

(A-R) Quantitative real-time PCR analysis of myogenic factors (A-O), a myeloid cell marker (*mpx,* P), the KRASG12D transgene (Q), or a MAP-kinase regulated gene (*dusp6,* R). *myf5-GFP+/mylz2-mCherry-negative* (G+), *myf5-GFP+/mylz2-mCherry+* (G+R+), *myf5-GFP-negative/mylz2-mCherry+* (R+), and double negative (DN). *Myogenin (myog), myosin light-chain 2 (mylz2), myogenic factor 6 (myf6), troponin I fast-twitch isoform 2* (*tnni2a)*, *alpha-actin 1b (acta1b), chemokine (C-X-C motif) receptor 4b (cxcr4b), ventricular myosin heavy chain-like (vmhcl), actin related protein 2/3 complex subunit 5B (arpc5b), carboxypeptidase vitellogenic-like (cpvl), myeloid-specific peroxidase (mpx)*, and *dual specificity phosphatase 6* (*dusp6*). Expression is depicted as relative fold change where the total expression value of all transcripts was normalized to 25 within a given sample. RT-PCR of 6- and 24-hour embryos ensured that relative expression was in the correct range. The blue, green and red bars represent analysis of three independent tumors. Expression values +/- one standard deviation.

(S-Z) Transplanted *myf5-GFP+/mylz2-mCherry+* ERMS pulsed with EDU for 6 hours and stained to analyze EDU incorporation. Single fluorescent planes for images shown in Figure 2C-D. Sections show areas with higher numbers of *myf5-GFP+* (S-V) or *mylz2-mCherry+ cells* (W-Z). (S, W) GFP alone, (T, X) mCherry alone, (U, Y) EDU alone, (V, Z) DAPI alone. Yellow arrows indicate EDU-labeled cells. Scale bar equals 25 μm.

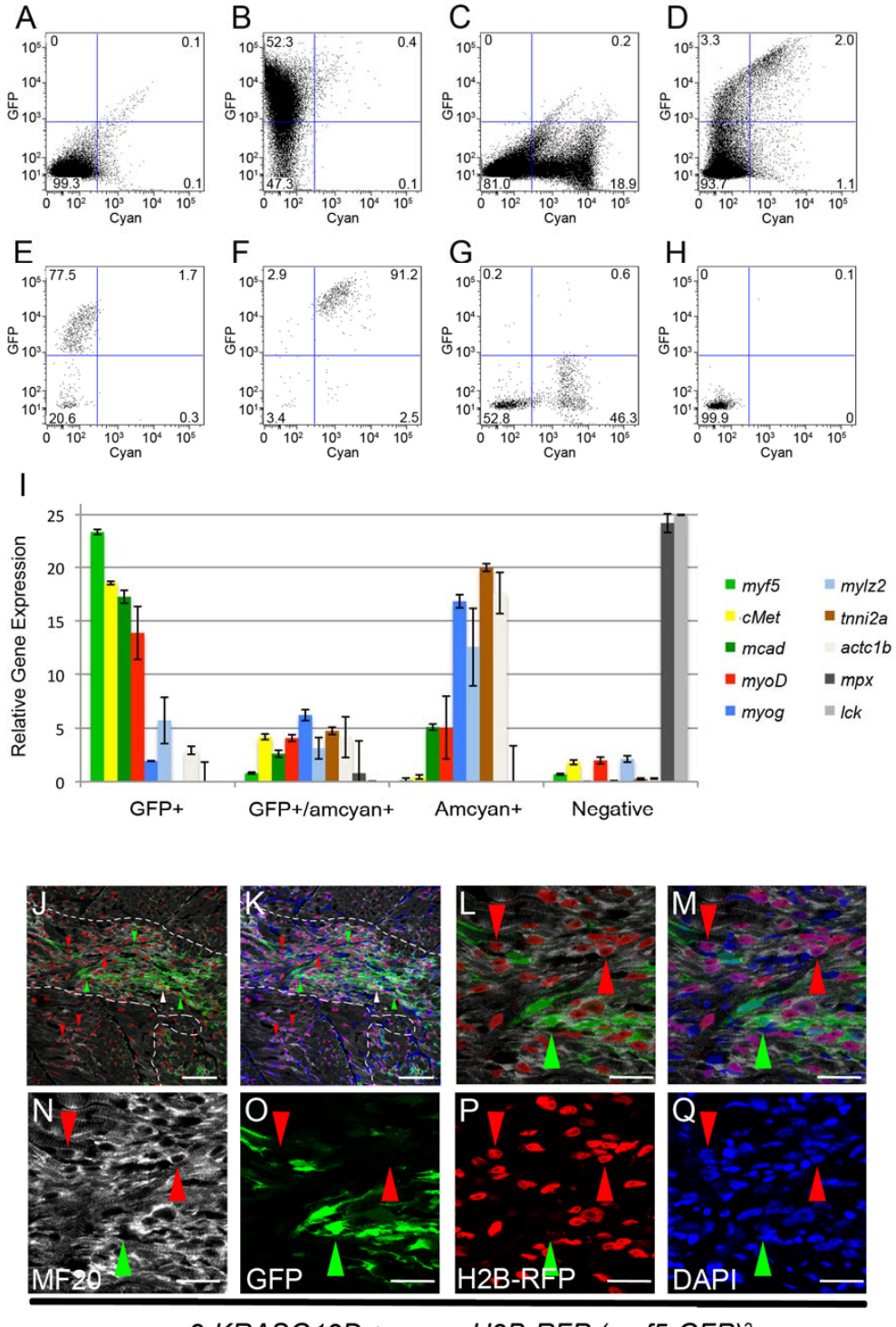

rag2-KRASG12D + myog-H2B-RFP (myf5-GFP)²

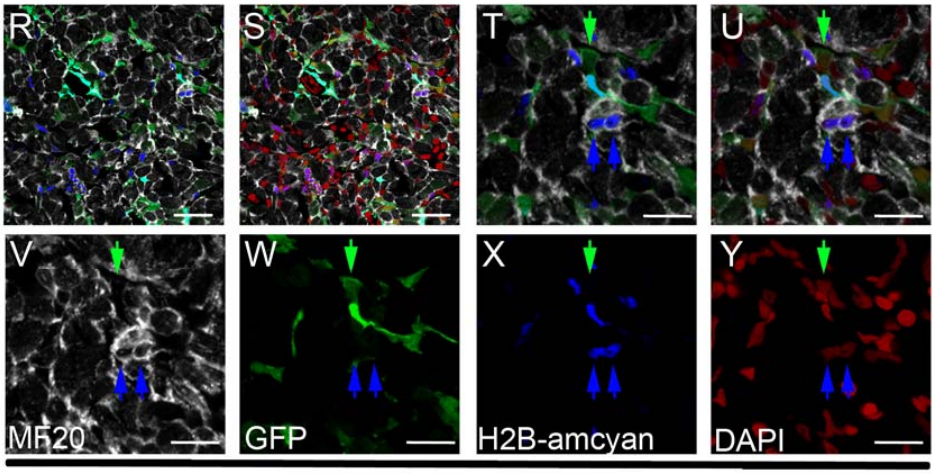

rag2-KRASG12D + myog-H2B-Amcyan (myf5-GFP)²

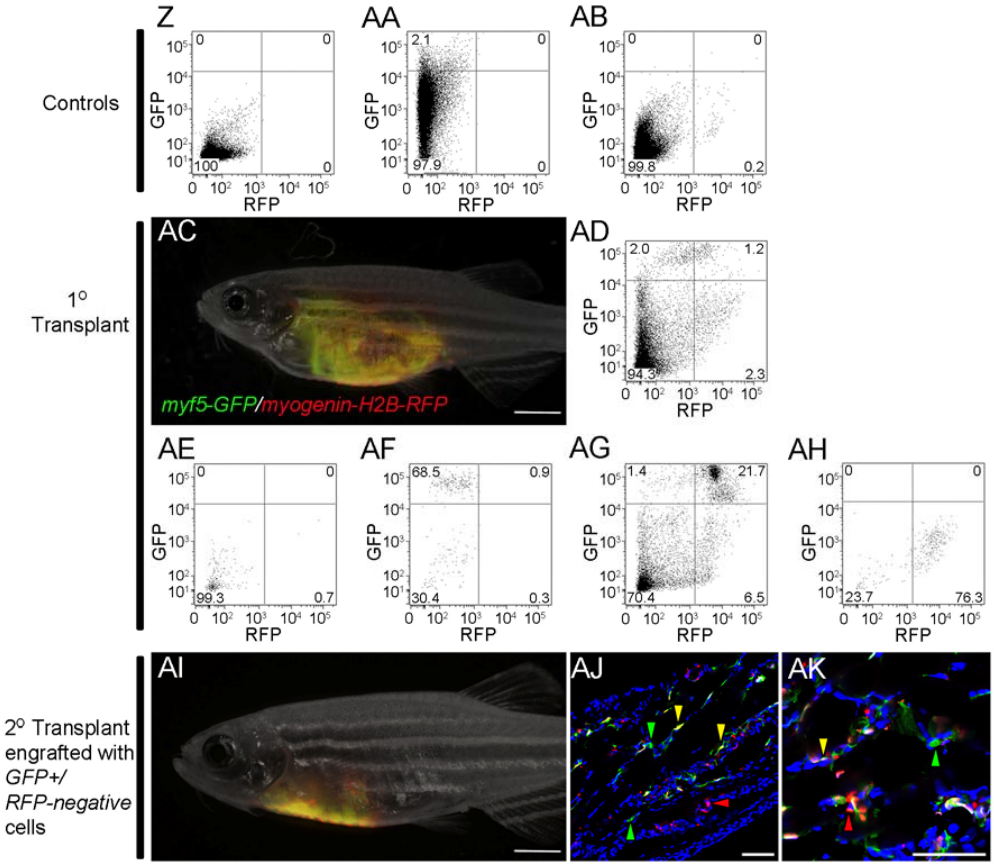

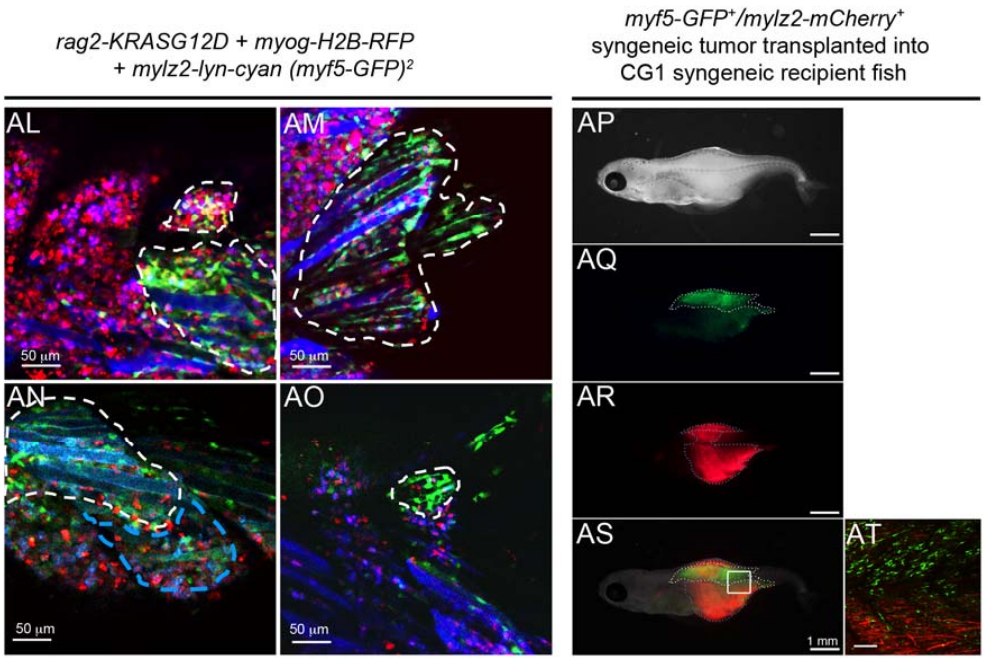

Figure S2, related to Figure 4. The myogenin promoter labels differentiated ERMS cells subfractions. (A-C) FACS plots of muscle cells from non-transgenic (A), *myf5-GFP+* ERMS (B), and *myogenin-H2B-Amcyan+* ERMS (C) that were used to place the sort gates. (D) FACS analysis of ERMS arising in *myf5-GFP* transgenic fish coinjected with *rag2-KRASG12D + myogenin-H2B-Amcyan*. Four primary *myf5-GFP/ myogenin-H2B-Amcyan+* ERMS tumors were pooled in this analysis and subsequently, cell subfractions isolated by FACS.

(E-H) Purity of the isolated cell subfractions following two-rounds of FACS, *myf5-GFP+/myogenin-H2B-Amcyan-negative* (E), *myf5-GFP+/myogenin-H2B-Amcyan+* (F), and *double negative* cells (H). Assessment of post-sort purity of the *myf5-GFP-negative/myogenin-H2B-Amcyan+* cell type was not possible due to limiting numbers of

cells obtained from the first sort. We show the high enrichment of cells following the first round sort (G).

(I) Quantitative real-time PCR of fluorescent-labeled ERMS cell subpopulations. *myf5-GFP+/myogenin-negative* (GFP+), *myf5-GFP+/myogenin-H2B-Amcyan+* (GFP+/Amcyan+), *myf5-GFP-negative/myogenin-H2B-Amcyan+* (Amcyan+), double negative cells (Negative). *m-cadherin (mcad)*, *myogenin (myog), myosin light chain 2 (mylz2), troponin I fast-twitch isoform 2, (tnni2a), alpha-actin 1b (acta1b), myeloid-specific peroxidase (mpx),* and *lymphocyte-specific protein tyrosine kinase (lck).* Expression values are +/- one standard deviation.

(J-Y) The myogenin promoter drives fluorescent protein expression in a subset of differentiated ERMS cells that stain with a myosin heavy chain antibody, MF20. ERMS arising from *myf5-GFP* transgenic animals that were injected with *rag2-KRASG12D* and *myogenin-H2B-RFP* (J-Q). Sections were stained with the MF20 antibody and imaged at low (J, K) and high magnification (L-Q). Single image planes are shown for MF20 (N), GFP (O), H2B-RFP (P), or DAPI (Q). Merged images of MF20, GFP, and H2B-RFP (J, L) or MF20, GFP, H2B-RFP, and DAPI (K, M). *Myogenin-H2B-RFP+* cells that co-localized with MF20 (Red arrows) or *myf5-GFP* are denoted (White arrow). Not all *myf5-GFP+* cells expressed *myogenin-H2B-RFP* (Green arrows). In total, 94.8%+/-2.4% of *myogenin-H2B-RFP+* cells expressed either GFP or MF20 within the tumor mass (n=653 cell counted across 3 tumors, tumor mass denoted by broken white lines). Moreover, a large subset of infiltrating *myogenin-H2B-RFP/myf5-GFP-negative* cells found in newly colonized areas also coexpress MF20 (see red arrows to in panels J, K). Scale bars are 50 μm (J, K) and 20 μm (L-Q).

(R-Y) ERMS from *myf5-GFP* animals co-injected with *rag2-KRASG12D* and *myogenin-H2B-Amcyan*. Sections were stained with MF20 and imaged at low (R, S) and high magnification (T-Y). Single image planes are shown for MF20 (V), GFP (W), H2B-Amcyan (X), or DAPI (Y). Dapi was pseudocolored red to enhance contrast in images and easily identify co-expressing cells. Merged images of MF20, GFP, and H2B-Amcyan (R, T) or MF20, GFP, H2B-Amcyan, and DAPI (S, U). 90.5% *myogenin-H2B-Amcyan+* cells expressed either *myf5-GFP* or MF20, confirming that these cells share muscle characteristics and are not labeling large numbers of off-target cell types. *myf5-GFP+/myogenin-H2B-Amcyan-negative/*MF20-negative cell (green arrow) and *myf5-GFP-negative/myogenin-H2B-Amcyan+/MF20+ cells* (blue arrows) are denoted in S-X. Scale bars equal 50 μm (R, S) and 20 μm (T-Y).

(Z-AK) Tumor-propagating potential is confined to the *myf5-GFP+/myogenin-H2B-RFP-negative* ERMS cell population. FACS analysis of muscle from non-transgenic control animals (Z), a single-positive *myf5-GFP+* ERMS (AA) and a single-positive *myogenin-H2B-RFP+* ERMS (AB) used to place the sort gates.

(AC) Unsorted primary cells from a *myf5-GFP/myogenin-H2B-RFP* ERMS engraft robustly into syngeneic recipient animals when transplanted with $2.5x10^4$ cells. Animal shown at 30 days post-transplantation. Scale bar is 2 mm (AC).

(AD-AH) Fluorescent-labeled ERMS cell sub-populations were isolated from primary transplant animals and sort purity assessed following two rounds of FACS (AE, AF, AG, AH). Post-sort purity for *myf5-GFP-negative/myogenin-H2B-RFP-negative* (AE), *myf5-GFP+/myogenin-H2B-RFP-negative* (AF), and *myf5-GFP-negative/myogenin-H2B-RFP+* (AH) cells. Cell numbers were limiting for the *myf5-GFP+/myogenin-H2B-RFP+*

ERMS cells sub-fraction, precluding post-sort analysis following two rounds of FACS. Data is presented here for the first round sorting, which shows high enrichment for this cell sub-fraction (AG).

(AI) Only the *myf5-GFP+/ myogenin-H2B-RFP-negative* cells induce ERMS in recipient animals ($1x10^2$ sorted cells, n=4 of 18). Scale bar is 2 mm (AI).

(AJ, AK) Sections of ERMS arising in animals engrafted with *myf5-GFP+/ myogenin-H2B-RFP-negative* cells. Engrafted ERMS contained single positive *myf5-GFP+* (green arrow heads), *myf5-GFP+/ myogenin-H2B-RFP+* double positive (yellow arrow heads), and *myogenin-H2B-RFP+* ERMS cells (red arrow head) validating that *myf5-GFP+/myogenin-H2B-RFP-negative* tumor-propagating cell gives rise to all other fluorescent-labeled ERMS cell sub-fractions. Scale bars are 50 μm (AJ, AK).

(AL-AT) Zebrafish primary and transplanted ERMS have distinct tumor compartments comprised of myf5+ ERMS cells and differentiated cells that can be found within adjacent or the same myotome segment.

(AL-AO) Regional partitioning of cells based on differentiation status in primary ERMS arising in a *myf5-GFP* transgenic animal that had been injected at the one-cell stage of life with *rag2-KRASG12D, myogenin-H2B-RFP,* and *mylz2-lyn-cyan. myf5-GFP+* cells and *myogenin-H2B-RFP+/mylz2-lyn-cyan+* ERMS cells confined to different myotome segments (AL, AM) or within the same myotome segment (AN, AO). Regions enriched for *myf5-GFP+* cells are denoted by white dashed lines. Scale bar equals 50 μm (AL-AO).

(AP-AT) ERMS arising in transplanted fish also exhibit regional compartmentalization of tumor cells based on differentiation status. Serially passaged *myf5-GFP+/mylz2-*

mCherry+ ERMS cells from CG1-strain fish were injected into the musculature of non-transgenic, 5-day-old syngeneic recipient embryos ($1x10^3$ unsorted ERMS cells/transplant recipient). A representative animal with prominent ERMS was photographed at 15 days of life using standard epiflourescence stereomicroscopy (AP-AS) or multiphoton microscopy (AT). Bright field (AP), GFP (AQ), mCherry (AR), or merged fluorescent images (AS). Broken white and blue lines demarcate regions with higher numbers of *myf5-GFP+ or mylz2-mCherry+* ERMS cells, respectively. (AT) Merged Z-static image showing clear demarcation of ERMS cell subfractions based on differentiation status. Scale bar equals 1mm (AP-AS), 100 μm (AT).

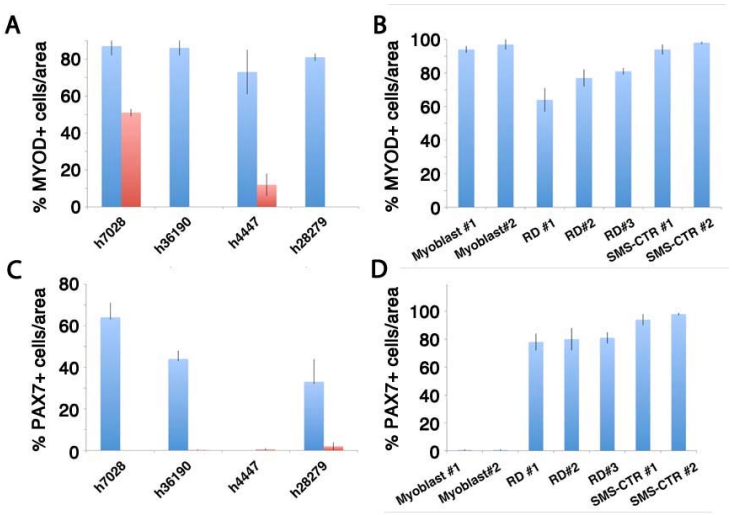

Figure S3, related to Figure 5. Immunohistochemistry for MYOD and PAX7 in human RMS. Quantification carried out over 6 areas. Percentages are shown as the total number of IHC+ cells divided by tumor cells in each area. (A-B) MYOD expression in human primary ERMS (A) and xenograft tumors derived from human ERMS cell lines and transformed myoblasts (B). (C-D) PAX7 expression in human primary ERMS (C) and xenograft tumors derived from human ERMS cell lines and transformed myoblasts (D). Human ERMS cell lines are denoted by RD and SMS-CTR. Transformed myoblasts are denoted Myoblast. Numbers following each designation (i.e. RD #1) describe individual tumors that arose in independent xenograft animals. Blue columns indicate regions of high-staining and red columns indicate regions of low staining. Samples with only blue columns indicate diffuse ubiquitous staining. Error bars +/- one standard deviation.

Table S2, related to Figure 5. Quantification of regional expression of myogenic factors in human RMS.

MYOGENIN

SAMPLE ID	LOW (%)	SD	HIGH (%)	SD	T-TEST	TOTAL CELLS COUNTED
Human Primary ERMS						
h7028	37	4	59	3	0.0018	1282
h36190	15	12	66	1	0.0021	1939
h4447	3	3	31	14	0.029	3331
h13837	0	0	92	1	N/A	361
h28279	11	6	40	14	0.03	365
Human TMA						
1720	11	6	33	8	0.015	318
1755	4	1	21	5	0.0041	310
1785	4	3	14	1	0.001	443
1788	12	2	34	1	0.00011	211
1718	10	5	43	4	0.00097	765
1765	17	2	38	12	0.04	304
1784	18	7	37	5	0.017	393
1790	19	5	42	9	0.018	512
1745	N/A		99	1		150
1711	1	1	N/A			250
Human Xenografts						
HTR-IRF	7	4	30	5	0.0031	2075
THR-2LF	7	3	30	2	0.00046	1929
RD2	4	2	38	5	0.00033	3569
RDV1	5	2	35	7	0.0023	1667
RDV2	6	3	28	4	0.0015	2782
Mouse						
SMP0311	2	0.2	12	1	0.00027	1577
SMP3011	3	2	24	12	0.034	987
SMP0318	1	0.3	55	30	0.038	756
SMP04-Tu3	1	0.8	20	3	0.00056	769
SMP0303	2	0.9	10	3	0.014	937
SMP04-Tu1	2.6	0.7	26	9	0.0094	1065
SMP04-Tu2	0.9	0.2	13	3	0.0028	711

Pax7

SAMPLE ID	LOW (%)	SD	HIGH (%)	SD	T-TEST	TOTAL CELLS COUNTED
Human Primary ERMS						
h7028	N/A		64	7		1916
h36190	0.2	0.2	44	4	0.00003	753
h4447	0	0	N/A			453

h13837	28	13	51	12	0.08	1587
h28279	2	2	33	11	0.01	505
Human Xenografts						
HTR-IRF	N/A		94	4		358
THR-2LF	N/A		98	1		324
RD2	N/A		78	6		432
RDV1	N/A		80	8		384
RDV2	N/A		81	4		357

MyoD

Human Primary ERMS

SAMPLE ID	LOW (%)	SD	HIGH (%)	SD	T-TEST	TOTAL CELLS COUNTED
7028	51	2	87	5	0.0002	1866
36190	N/A		86	4		248
4447	12	6	73	12	0.0012	546
13837	N/A		95	2		314
60654	0					250
28270	N/A		81	2		252

Human Xenografts	LOW	SD	HIGH (%)	SD		TOTAL CELLS COUNTED
HTR-IRF	N/A		94	2		268
THR-2LF	N/A		97	3		252
RD2	N/A		64	7		348
RDV1	N/A		77	5		390
RDV2	N/A		81	2		386

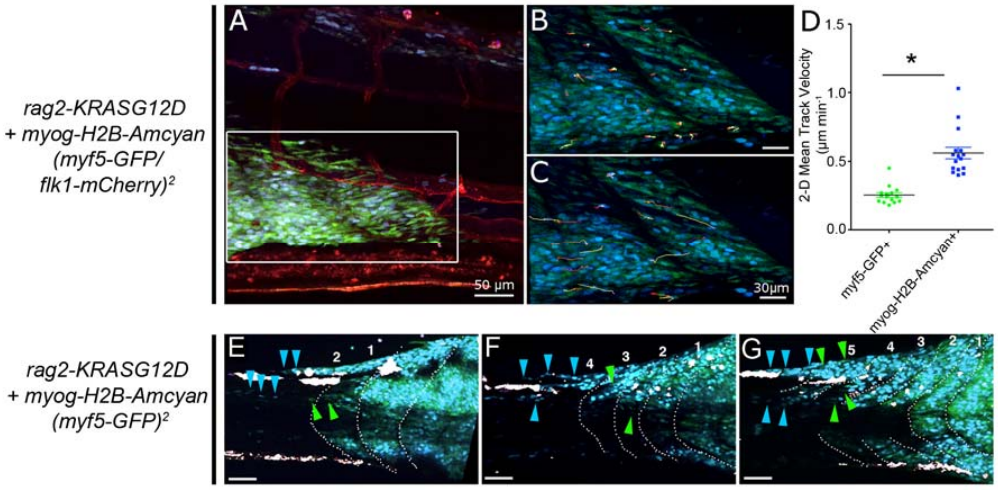

Figure S4, related to Figure 6. *myf5-GFP*+ ERMS-propagating cells are highly migratory and are recruited to new areas of tumor growth only after seeding by *myogenin-H2B-Amcyan*+ ERMS cells.

(A-D) Migratory characteristics of *myf5-GFP*+ and *myogenin-H2B-Amcyan*+ ERMS cells. ERMS arising in an 18-day-old *myf5-GFP/flk1-mCherry* stable transgenic animal injected at the one-cell-stage with *rag2-KRASG12D* + *myogenin-H2B-Amcyan*. Animal was imaged using a multiphoton microscope every 2.5 minutes for >6 hours. Amcyan is not retained in phagocytic cells and 100% of cells show correct nuclear morphology (n=5 tumors, >2,500 cells analyzed, see Supplemental Movies S5 and S6). (B-C) Magnified view of boxed regions shown in panel A. Representative cell tracking of *myf5-GFP*+ (B) or *myogenin-H2B-Amcyan*+ ERMS cells (C). (D) Mean track velocities for representative cell types contained within the tumor mass. Asterisk denotes $p < 0.0001$. Mean track velocities error bars are expressed as +/- one standard deviation.

(E-G) Serial imaging of an ERMS arising in a *myf5-GFP* transgenic animal injected with *rag2-KRASG12D* and *myogenin-H2B-Amcyan* imaged using a multiphoton microscope at 14, 17 and 20 dpf. Blue arrows indicate *myogenin-H2B-Amcyan*+ cells and green arrows point to single positive *myf5-GFP*+ cells. The anterior is oriented to the left with the tumor developing the in extreme posterior portion of the tail. The ERMS is growing from right to left. Dotted white outline highlights myotome boundaries. The large white areas are pigment cells that auto-fluoresce during multiphoton imaging. Scale bar is 50 μm (A), 30 μm (B-C), 100 μm (E-G).

Movie S2, related to Figure 6. Provided as a Quicktime movie file. A 16-day-old *myf5-GFP* transgenic fish injected with *rag2-KRASG12D* and *myogenin-H2B-RFP* that developed prominent ERMS was imaged for 6.7 hours by multi-photon intravital microscopy. A 409 x 409 x 30 μm volume was recorded every 2.5 minutes. Note that in addition to the stationary, RFP^{dim} cells that likely represent differentiated ERMS cells, two highly motile intratumoral populations of RFP^{high} cells can be identified: One with nuclear RFP pattern, and one with a punctate pattern, which likely represents the lysosomes of a rare phagocytic cells that have infiltrated the tumor and engulfed RFP labeled tumor cells. This latter cell type is rare and largely confined to a specific region to the right in this movie. While nuclear RFP+ tumor cells migrate larger distances, *myf5-GFP*+ cells show mostly confined motility. Movie is accelerated 9000 over real time. Scale bar is 50 μm.

Movie S3, related to Figure 6. Provided as a Quicktime movie file. Left panel shows a frame from movie S2 with magnified views of intatumoral regions. 1: Peripheral tumor mass with *myf5-GFP+* and *myogenin-H2B-RFP* single+ as well as some double-positive tumor cells. 2: *myogenin-H2B-RFP* low expressing cells likely representing differentiated ERMS cells, some of which have fused into fibers. 3: Central tumor mass with the highest concentration of cells with punctate RFP pattern, likely representing rare, phagocytic immunocytes that have engulfed tumor cells. Phagocytic cell types are easily discerned in our movies based on morphology (they do not have nuclear labeling of the RFP protein) and are relatively rare. In this image, 577 of 599 RFP+ cells express nuclear RFP and do not have phagocytic cell morphology (cells within boxed region #3 were excluded in this analysis). Movie is accelerated 9000 over real time. Scale bar on left is 50 μm. Scale bar on right is 25 μm.

Movie S4, related to Figure 6. Provided as a Quicktime movie file. An 18-day-old *myf5-GFP/flk1-mCherry* transgenic fish injected with *rag2-KRASG12D* and *myogenin-H2B-Amcyan* that developed prominent ERMS was imaged for 6.7 hours by multi-photon intravital microscopy. A 409 x 409 x 39 μm volume was recorded every 2.5 minutes. *myogenin-H2B-Amcyan+* ERMS cells have prominent nuclear labeling and are highly migratory, whereas *myf5-GFP+* ERMS cell subpopulations are largely stationary. Note that phagocytic cells are not present in these movies, allowing easy tracking of ERMS cells sub-fractions. Movie is accelerated 9000x over real time. Scale bar is 50 μm full frame, and 30 μm cropped fields.

Movie S5, related to Figure 6. Provided as a Quicktime movie file. A 14-day-old *flk1-mCherry* transgenic fish injected with *rag2-KRASG12D* and *myogenin-H2B-Amcyan* that developed prominent ERMS was imaged for approximately 6 hours by multi-photon intravital microscopy. A 409 x 409 x 20 μm volume was recorded every 2.5 minutes. Highly motile intratumoral populations of Amcyan+ cells can be identified and tracks for 5 highly motile cells are represented. Also highlighted is a single *myogenin-H2B-Amyan+* ERMS cell that is entering the *flk1-mCherry*-labeled vasculature. Movie is accelerated 9000x over real time. Scale bar is 50 μm full frame, and 30 μm cropped fields.

Movie S6, related to Figure 6. Provided as a Quicktime movie file. Cell division within *myf5-GFP+/mylz2-mCherry-negative* ERMS cell subpopulation in a 15-day-old fish. Serially passaged ERMS cells from *myf5-GFP/mylz2-mCherry* CG1-strain fish were injected into the musculature of non-transgenic, 5-day-old syngeneic recipient embryos ($1x10^3$ unsorted ERMS cells/transplant recipient). A 222 minute movie captured every 2.5 minutes of a dividing *myf5-GFP+/mylz2-mCherry-negative* cell. The movie is accelerated 2000x real time. Scale bar is 15 μm.

Movie S7, related to Figure 7. Provided as a Quicktime movie file. 16 hour time-lapse movie of a late stage 3 *myf5-GFP/myogenin-H2B-RFP/mylz2-lyn-cyan* expressing ERMS arising in a 22-day-old animal. Images were captured using a standard point-scanning laser confocal in four Z-planes and merged to create a 20 μm slice viewed every hour.

Movie S8, related to Figure 7. Provided as a Quicktime movie file. A 180 minute time-lapse movie of a stage 3 *myf5-GFP/myogenin-H2B-RFP* expressing ERMS at 14 dpf. Image capture rate was 24 frames/hour and each frame represents a merged Z-stack image. Note a single RED+ cell that slowly migrates into the image plane and then rapidly transits away from the tumor, indicative of entering the circulatory system and being shuttled away from the tumor.

Movie S9, related to figure 7. Provided as a Quicktime movie file. A 3-D rendering of a z-stack made in Quicktime showing two *myogenin-H2B-Amcyan+/myf5-GFP-negative* cells entering the *flk1-mCherry*-labeled vasculature (same fish and region as shown in Figure 7M, N within the main text). Z-stacks were captured every1.5 μm apart.

Supplemental Experimental Procedures

Vectors

The *rag2-KRASG12D* and *rag2-dsREDexpress* constructs have been described previously (Langenau et al., 2007). *myogenin* and *mylz2*-transgenic promoter expression has been reported (Du et al., 2003; Ju et al., 2003; Smith et al., 2010); however, our promoter constructs were modified to be three-way gateway compatible. Specifically, the *myogenin* and *mylz2* promoters were cloned into a pENTR5'TOPO cloning (Invitrogen) gateway vector to create 5' entry clones. Middle gateway clones were created by PCR amplification of H2B-RFP, H2B-Amcyan and lyn-cyan and cloning into the pENTR-D-TOPO vectors (Invitrogen). The 3' entry clone and pDestTol2pA2 destination vectors were obtained form the Tol2kit (Kwan et al., 2007). All reactions were completed as described (Kwan et al., 2007), ultimately producing the *myogenin-H2B-RFP, myogenin-H2B-Amcyan* and *mylz2-lyn-cyan* constructs. Each was linearized using restriction enzyme digest, purified, and injected as combinations with other transgenes into one-cell stage animals as previously described (Langenau et al., 2008).

Fluorescence-activated cell sorting (FACS) and ERMS cell transplantation

Single cell suspensions were made from primary ERMS arising in 20 to 52-day-old *myf5-GFP/mylz2-mCherry* syngeneic zebrafish and $5X10^3$ unsorted cells were injected into the peritoneum of CG1-strain syngeneic zebrafish as described (Smith et al., 2010). ERMS cells were isolated from engrafted animals between 18-45 days post-transplantation and FACS was completed in the presence of DAPI or propidium iodide to identify live cells. During the second round of FACS sorting, $2.5x10^4$ cells were sorted

directly into 800 microliters of Trizol, while $1x10^1$, $1x10^2$, $1x10^3$ fluorescent-labeled ERMS cells were sorted into wells of a 96-well plate which also contained $2x10^4$ whole-blood carrier cells from CG1 animals ($2x10^4$). Samples were resuspended in 5 microliters of 0.9X PBS+5% FBS and injected into the peritoneal cavity of CG1-strain adult fish. Sort-purity was assessed following two rounds of FACS.

Microarray

Serially passaged *myf5-GFP+/mylz2-mCherry+* ERMS were harvested from two individual tumors and cell subpopulations isolated following two rounds of FACS. Cells were resuspended in RNAlater solution. RNA was isolated and purified using a Qiagen RNA purification kit. Samples were amplified, labeled, and hybridized to Affymetrix zebrafish microarrays as described previously (Langenau et al, 2007). CEL files were imported into D-Chip and normalized in batch to an invariant set using log2 fold-change. Samples were compared in D-Chip to identify probe sets with >20% presence calls and fold-change of >1.5. A GCT file was created in D-Chip and then used for visualization of the data in Genepattern. The microarray data can be accessed with Geo accession number GSE32425.

Primers used for quantitative real time PCR (qRT-PCR)

Gene	Primer 5'-3' sequence
hKRAS-QRT-F-137	TTGATGGAGAAACCTGTCTCTTGG
hKRAS-QRT-R-247	CAAATACACAAAGAAAGCCCTCCC
myf5-QRT-F-707	CCAGACAGTCCAAACAACAGACC
myf5-QRT-R-795	TGAGCAAGCAGTGTGAGTAAGCG

myoD-QRT-F-638	CAGTGGAGACTCTGATGCTTCCAG
myoD-QRT-R-744	AGCTGTCATAGCTGTTCCGTCTTC
pax7a-331F	ACACCCGACGTTGAAAAGAG
pax7a-431R	TCACACACTCCGTCCTTCAG
pax7a-1281F	GCACCACTCTCTCACAAGACGGC
pax7a-1375R	GCTGTCAGCCGAGAGTCCGC
pax7b-16F	GGAACAGTACCGCGAATGAT
pax7b135R	GAATACACCGCCAAGCTGAT
myog-QRT-F-775	GTGGACAGCATAACGGGAACAG
myog-QRT-R-868	TCTGAAGGTAACGGTGAGTCGG
myf6-QRT-F-580	TCCCAGATGGCAGGTCATAGAG
myf6-QRT-R-683	GGCTCTTCAGTGGAAATGCTGTC
cdh15-QRT-F-1875	TGACATCCGAGACAACGTCTTTC
cdh15-QRT-R-1969	CACTGGGGCTCCTCAGAAAATC
mylz2-452F	ACCGCAGAGGAGATGAAGAA
mylz2-547R	TCCGTGTGTGATGACGTAGC
desmin-QRT-F-771	CGAGATTGACTCTCTCAAGGGCAC
desm-QRT-R-877	GGGCGATAGTGTCCTGATAACCAC
myh1/vmhcl-276F	GCTGACCTTTCTCCATGAGC
myh1/vmhcl-370R	TGACACAAAACAGCCCTGAG
c-MET-1369F	GTCATCCAGGTGGTGGTTTC
c-MET-1483R	CGTTGTGATGCTGTGGAGAC
mpo-1096F	GCCACTCGTCAGAAAATCCT
mpo-1180R	GATTCTCATCGACACGAGCA
dusp6-339F	ATTGCGGGAAAATCAGTTTG
dusp6-437R	CTGGAGCCAGAACCTCTCAC
tnni2a-445F	TCAGGCTCTGCTGGGCTCCA
tnni2a-559R	TACGCCAGTCGCCGACCTGT
acta1b-645F	CTGAGCGCGGTTATTCTTTC
acta1b-729R	TCCAGAGCCACATAGCACAG
cpvl-184F	TTGGAGCTGACCCGGGCAAA
cpvl-266R	CACCAGGAAGGGGACCCACC
cxcr4b-2044F	GAGGGGTCCGAGCCAACTCC
cxcr4b-2130R	AGAGCATGATGGCTGATAGCAGGT
arpc5b-286F	TCATGGGTGCTCTACAGGCAGTATT
arpc5b-392R	AGCACCTTCAGCACCAGACCTTC
b-actin-QRT-F	GCTGTTTTCCCCTCCATTGTT
b-actin-QRT-R	TCCCATGCCAACCATCACT
ef1a-QRT-F-188	CATCGAGAAGTTCGAGAAGGAAGC
ef1a-QRT-R-296	GTCAATGGTGATACCACGCTCAC
18s-QRT-1-F	TCGCTAGTTGGCATCGTTTATG
18s-QRT-1-R	CGGAGGTTCGAAGACGATCA

Xenograft cell transplantation into mice

Human ERMS cell lines and human skeletal muscle myoblasts transformed to mimic ERMS were evaluated as xenografts by subcutaneous injection into immunodeficient SCID/*beige* mice as described (Linardic et al., 2005). Resulting tumors were harvested at necropsy, with portions fixed in formalin for paraffin embedding. Mouse experiments were approved by the Duke University Institutional Animal Care & Use Committee under protocol A 036-03-02.

Immunohistochemistry, EDU and Annexin V staining

Paraffin embedding and sectioning, cryostat sectioning, and immunohistochemical analysis were performed essentially as described (Guyon et al., 2003; Langenau et al., 2005). Human samples were stained with PAX7 (Developmental Studies Hybridoma Bank Hybridoma bank), MyoD1 (Richard Allen Scientific), and Myogenin (DAKO Corporation), secondary antibodies used were biotinylated horse anti-mouse/Vector, BA-2000 and UltraView HRP-conjugated multimer antibody reagents (Vectorlabs, Ventana Medical Systems) and subsequently slides were stained with DAB. Three areas of high- and low- staining were photographed per tumor sample at 100X and 400X magnification. Cell counts represent the number of antibody stained cells divided by the total number of tumor cells within a given area. Human RMS samples were obtained from the MGH pathology tissue bank or from the Stanford collection where myogenin-staining was previously completed on a larger cohort of patient samples (Heerema-McKenney et al., 2008).

EDU was injected into the peritoneum of ERMS fish (10mM EDU, 5 microliters,

Click-iT Alexa Fluor 647 imaging kit, Invitrogen). After 6 h or 72h post-injection, animals were anesthetized, fixed in 4% paraformaldehyde at 4 ˚C over night, and subsequently imbedded in OCT. Frozen blocks were sectioned at 10 micron-thickness and stained for EDU. Sections were mounted using Vectashield with or without Dapi, coverslipped, and imaged by confocal microscopy.

For analysis of apoptosis, ERMS tumor cells were first transplanted intraperitoneally into 6-7 week-old zebrafish. Approximately 10 days post-engraftment, the tumor was dissected from each fish. Tumor cells were dissociated using a razor blade and filtered through a 40-micron cell strainer. Cells resuspended in 5%FBS/0.9X PBS were stained with annexin V conjugated to Alexa Fluor 647 (Invitrogen) following the manufacturer's protocol. Stained cells were analyzed by flow cytometry. For gating, DAPI was used to identify dead cells. Cells isolated from *mylz2-mCherry* transgenic fish, *mylz2-GFP* transgenic fish and TuAB wild-type fish were used as controls to place the fluorescent gates, respectively.

Multiphoton Intravital Microscopy

Fluorescent transgenic animals that developed ERMS were imaged at 14 - 21 dpf. Animals were embedded in 1% low melting temperature agarose and immersed in fish water containing tricaine in 6 cm tissue culture dishes, which were placed on a custom-built heating plate to maintain the buffer temperature at 25 ˚C. The heating plate was transferred to the stage of an Ultima IV upright multiphoton microscope (Prairie Technologies) equipped with an infrared-optimized Olympus 20x/0.95 NA water immersion objective and controlled by Prairieview software. For multiphoton excitation a

Ti:sapphire laser with a 10-W MilleniaXs pump laser (Mai Tai DeepSee, Spectra-Physics) was tuned to 990 nm for optimal excitation of both EGFP and mRFP. For imaging Amcyan, EGFP and mCherry a combination of Deepsee at 930 nm to detect Amcyan and EGFP and Mai Tai pulsed at 1030 nm to detect mCherry was used. To detect a combination of Amcyan and EGFP we used Deep See at 830 nm and Mai Tai at 930 nm. For four-dimensional recordings of cell movement, stacks of 13 - 36 optical sections spaced 1.5-2.5 µm apart were acquired every 150 seconds for up to 7 hours in order provide image volumes of 30 - 40 µm in depth and 409 µm in width. Emitted light was detected through 525/50 and 595/50 nm bandpass filters with non-descanned detectors to generate two-color images. Sequences of image stacks were transformed into maximum intensity-projected movies using Imaris 7.1 software (Bitplane) and exported as Quicktime movies. Motion-artifacts in recordings were corrected using the auto-alignment plugin (stackreg) of ImageJ (http://rsb.info.nih.gov/ij/). Manual 2-D tracking was performed using the manual tracking plugin in ImageJ and Spots tool in Imaris 7.1 software (Bitplane). Annotation and further processing of movies were done in ImageJ and Quicktime 7.

Supplemental References

Guyon, J. R., Mosley, A. N., Zhou, Y., O'Brien, K. F., Sheng, X., Chiang, K., Davidson, A. J., Volinski, J. M., Zon, L. I., and Kunkel, L. M. (2003). The dystrophin associated protein complex in zebrafish. Hum Mol Genet *12*, 601-615.

Kwan, K. M., Fujimoto, E., Grabher, C., Mangum, B. D., Hardy, M. E., Campbell, D. S., Parant, J. M., Yost, H. J., Kanki, J. P., and Chien, C. B. (2007). The Tol2kit: a multisite gateway-based construction kit for Tol2 transposon transgenesis constructs. Dev Dyn 236, 3088-3099.

Langenau, D.M., Feng, H., Berghmans, S., Kanki, J.P., Kutok, J.L., and Look, A.T. (2005). Cre/lox-regulated transgenic zebrafish model with conditional myc-induced T cell acute lymphoblastic leukemia. Proc Natl Acad Sci U S A *102*, 6068-6073.

Livak, K. J., and Schmittgen, T. D. (2001). Analysis of relative gene expression data using real-time quantitative PCR and the 2(-Delta Delta C(T)) Method. Methods 25, 402-408.

4

Myogenic Regulatory Factors Induce Self-renewal and Growth in ERMS

"In the attempt to make scientific discoveries, every problem is an opportunity, and the more difficult the problem, the greater will be the importance of its solution."

Edward O. Wilson
at TEDtalks, Advice to Young Scientists
(2012)

4.1 Chapter 4 - Preamble

As discussed in the General Introduction (Chapter 1), consensus in the Rhabdomyosarcoma field has been that expression of MRFs likely reflects the target cell of transformation rather than myogenic transcriptional programs being required for continued tumor growth.

Despite the well-known roles for MYOD1 and MYF5 in muscle development, their importance in regulating self-renewal during regeneration, and their ability to reprogram fibroblasts into a muscle cell fate, a functional role for these factors in regulating RMS tumor growth has yet to be reported.

We have previously reported that MYF5 is a marker of Tumor Propagating Cells in a fluorescent transgenic zebrafish RMS model (see Chapter 3 and Ignatius et al., 2012).

Here, we have used this model to show that MYF5 is sufficient to confer self-renewal to ERMS cells. Transgenic tumors that aberrantly express MYF5 in differentiated RMS cells initiate earlier, have higher penetrance and tend to be larger than control tumors. These tumors also have increased numbers of self-renewing TPCs. Consistent with redundant roles for MYF5 and MYOD1 in normal muscle regeneration and stem cell self-renewal, we identified two classes of human ERMS that largely express only one of these factors. Loss-of-function studies revealed that MYF5 and MYOD1 are required for sustained human RMS growth both *in vitro* and in mouse xenograft experiments. ChIP-seq experiments went on to reveal that MYF5 and MYOD1 bind common DNA regulatory elements likely to arrest human ERMS in early stages of muscle development while simultaneously promoting cell cycle progression.

We propose a model where MYF5 and MYOD1 converge on common molecular pathways to regulate human RMS growth and self-renewal, similar to their overlapping roles in muscle development and regeneration. Taken together, we show that cancer self-renewal pathways are likely shared with their non-malignant counterparts and that these processes are aberrantly activated during malignant transformation, an emerging concept in cancer biology with few better examples than that reported here.

4.2 Chapter 4 - Contribution

I contributed to the main body of work here presented. I was responsible for driving this project from its very beginning, including experimental design, experimental work, analysis, writing and the establishment of collaborations.

4.3 Chapter 4 - Publications

This work, of which I am the first author, was submitted to a scientific journal at this date. The unpublished manuscript is reproduced below in this Chapter.

Myogenic regulatory transcription factors induce self-renewal and growth in embryonal rhabdomyosarcoma

Inês M. Tenente[1,2,3], Myron S. Ignatius[1,2], Karin McCarthy[1,2], Marielle Yohe[4], Sivasish Sindiri[4], Madeline Hayes[1,2], Berkley Gryder[4], Ashwin Ramakrishnan[1,2], Qin Tang[1,2], Eleanor Chen[5], G. Petur Nielsen[6], Javed Khan[4], David M. Langenau[1,2]

[1] Molecular Pathology, Cancer Center, and Regenerative Medicine, Massachusetts General Hospital, Boston, MA 02129, USA

[2] Harvard Stem Cell Institute, Cambridge, MA 02139, USA

[3] GABBA, Abel Salazar Biomedical Sciences Institute, University of Porto, Porto, 4099-003, Portugal

[4] Oncogenomics Section, Pediatric Oncology Branch, Advanced Technology Center, National Cancer Institute, Gaithersburg, MD 20877, USA

[5] Department of Pathology, University of Washington, Seattle, WA 98195, USA

[6] Department of Pathology, Massachusetts General Hospital, Boston, MA 02129, USA

*Corresponding Author: dlangenau@mgh.harvard.edu

Short Title: MRFs regulate RMS self-renewal and growth

Keywords: Rhabdomyosarcoma, MYF5, MYOD, cancer, self-renewal, zebrafish

Abstract

Rhabdomyosarcoma (RMS) is a common pediatric sarcoma of muscle. Myogenic regulatory transcription factors, including Myogenic factor 5 (MYF5) and Myoblast determination protein D (MYOD), are highly expressed in RMS. These factors are required for normal muscle development and self-renewal of stem cells during regeneration. Moreover, *myf5* is a marker of self-renewing, tumor-propagating cells in zebrafish *kRAS*^{G12D}-induced embryonal rhabdomyosarcoma (ERMS) and is highly expressed in 60% of human ERMS. Yet, roles for MYF5 or MYOD in regulating ERMS growth, self-renewal, and tumor maintenance have not been defined. Here, we show that Myf5 is sufficient to confer self-renewal to differentiated zebrafish ERMS cells. These tumors initiate earlier, have higher penetrance and are larger than control tumors. Consistent with redundant roles for Myf5 and MyoD in normal muscle regeneration and stem cell self-renewal, we identified two classes of human ERMS that express either high levels of MYF5 or MYOD. Human ERMS largely express only one of these genes, with either MYF5 or MYOD being required for sustained tumor growth *in vitro* and *in vivo*. We propose a model where MYF5 and MYOD bind common promoter/enhancer elements and act redundantly to regulate ERMS proliferation and self-renewal, similar to their overlapping roles in muscle development and regeneration.

Introduction

Rhabdomyosarcoma (RMS) is the most common pediatric sarcoma and is characterized by impaired myogenic differentiation. RMS commonly express myogenic regulatory transcription factors (MRFs) including Myogenic factor 5 (Myf5) and Myoblast determination protein D (MyoD) (Clark et al. 1991; Parham 2001; Kumar et al. 2000; Sebire and Malone 2003). RMS is comprised of two molecular subtypes. Alveolar RMS (ARMS) harbor *Pax7-FOXO* and *Pax3-FOXO* genomic fusions (Sorensen et al. 2002) and have few recurrent genomic changes (Chen et al. 2013b; Shern et al. 2014). By contrast, 90% of human embryonal rhabdomyosarcoma (ERMS) have RAS pathway activation and a higher mutation burden when compared with ARMS (Langenau et al. 2007; Chen et al. 2013b; Shern et al. 2014). Common mutations found in ERMS include inactivation of *Tp53* and activating mutations of *FGFR4, PDGFA,* and *NOTCH1* (Chen et al. 2013b; Shern et al. 2014). Despite a favorable prognosis for a majority of RMS patients, the outcome for relapsed disease remains poor irrespective of subtype, with 50% of patients succumbing to disease (Hettmer et al. 2014). Importantly, continued tumor growth and relapse are driven by molecularly defined tumor propagating cells (TPCs). These self-renewing TPCs are often retained following treatment and ultimately drive refractory, metastatic, and relapse disease (Reya et al. 2001). TPCs have been identified in animal models and human RMS (Ignatius et al. 2012; Chen et al. 2014; Walter et al. 2011). However, to date, the molecular mechanisms driving TPC frequency and self-renewal in ERMS have not been fully defined.

Despite the similarity of RMS cells with embryonic and regenerating muscle, the cell-of-origin for these tumors is still controversial. For example, RMS can arise from muscle stem cells and myogenic precursor cells (Blum et al. 2013; Hettmer et al. 2011, 2015; Abraham et al. 2014; Rubin et al. 2011; Tremblay et al. 2014; Langenau et al. 2007; Storer et al. 2013), mesenchymal stem cells (Shinkoda et al. 2009; Lisboa et al. 2008), or adipocyte precursors (Hatley et al. 2012). Given the heterogeneity of cell types found in RMS and the suggested multiple cells-of-origin, several groups have posited that sarcomas comprise a continuum of myogenic differentiation, reflecting the target cell of transformation rather than myogenic programs being required for continued tumor growth (Keller and Guttridge 2013; Rubin et al. 2011; MacQuarrie et al. 2013; Kikuchi et al. 2011). MYF5 and MYOD have important roles in muscle development and regeneration (reviewed in Buckingham and Rigby 2014), are highly expressed in human and animal models of RMS (Langenau et al. 2007; Rubin et al. 2011), and can reprogram fibroblasts into proliferating myoblasts (Tapscott et al. 1988; Braun et al. 1989); yet, a functional requirement for these MRFs in regulating RMS growth and self-renewal has not yet been described.

Cellular and animal models of RMS have facilitated a detailed understanding of the molecular pathogenesis of this disease and have provided new insights into the self-renewal mechanisms required for RMS growth (Hinson et al. 2013; reviewed in Kashi et al. 2015). For example, a zebrafish transgenic model of *kRAS*^{G12D}-induced ERMS has been developed that accurately recapitulates the molecular underpinnings of human disease (Langenau et al. 2007; Le et al. 2007, 2013; Chen et al. 2013a; Storer et al. 2013; Chen et al. 2014). Using this model, we have previously identified a molecularly-defined

population of tumor cells that drives continued tumor growth (Langenau et al. 2007; Ignatius et al. 2012). These tumor-propagating cells (TPCs) have self-renewal properties akin to normal stem cells and express high transcript levels for muscle stem cell markers, including *c-met*, *cdh15* (*m-cadherin)*, and *myf5* (Langenau et al. 2007; Ignatius et al. 2012). Remarkably, *MYF5* is also reactivated in a large subset of human ERMS and is commonly re-expressed in animal models of ERMS, irrespective of the cell of origin (Abraham et al. 2014; Rubin et al. 2011; Storer et al. 2013; Tremblay et al. 2014). Based on these findings, we reasoned that MYF5 might have a major role in regulating growth and self-renewal in a subset of ERMS.

Here, we show that *Myf5* is not only a marker of zebrafish TPCs, but is sufficient to impart self-renewal to differentiated ERMS cells *in vivo*. *Myf5* re-expression also lead to tumors that initiate earlier, had higher penetrance of disease, and were larger than when compared with $kRAS^{G12D}$-alone expressing ERMS. Experiments in human ERMS uncovered significant inter-tumor heterogeneity of MRF expression with MYF5 or MYOD defining largely mutually exclusive groups of tumors. Functional studies uncovered that both MYF5 and MYOD are required for continued ERMS proliferation, likely acting redundantly with one another to regulate the same self-renewal programs found in normal muscle development and regeneration. Consistent with this interpretation, ChIP-seq analysis identified common binding sites of MYF5 and MYOD in promoter and enhancer regions of genes that regulate cell cycle and muscle differentiation. Finally, we show that MYF5 is also required for continued human ERMS tumor growth *in vivo*. Our data supports a previously unappreciated role for MYF5 and MYOD in regulating growth, proliferation, and self-renewal in rhabdomyosarcoma.

Results

Re-expression of myf5 in zebrafish ERMS cells leads to highly differentiated tumors, increased penetrance, and early tumor onset

myf5 is highly expressed in undifferentiated, self-renewing ERMS cells in the zebrafish *kRAS^{G12D}*-induced ERMS model (Langenau et al. 2007; Ignatius et al. 2012). For example, cell transplantation and direct live cell imaging has revealed that *myf5-GFP*+ cells drive tumor growth and label TPCs in the zebrafish model (Chen et al. 2014; Ignatius et al. 2012). To assess roles for *myf5* in regulating ERMS growth, we forced its expression in differentiated ERMS cells that lack self-renewal and tumor-propagating potential. Specifically, *rag2-kRAS^{G12D}* was coinjected with a transgene that overexpressed *myf5* within the differentiated, myosin expressing cells (*mylpfa-myf5*) (Xu et al. 1999). Importantly, *myf5*-GFP+; *mylpfa*-mCherry+ ERMS cells do not normally express high levels of *myf5*, have low proliferative capacity, and do not sustain ERMS growth *in vivo* (Ignatius et al. 2012). Histological analysis revealed that ERMS arising in *rag2-kRAS^{G12D};mylpfa-myf5* AB-strain transgenic fish were histologically more differentiated than when compared to those that express only *kRAS^{G12D}* (Fig. 1A-F), consistent with imparting self-renewal to more differentiated ERMS cells. Tumors were histologically staged based on differentiation as described previously (Storer et al. 2013). Briefly, undifferentiated RMS were scored as stage 1 and were comprised mostly of small round blue cells, while the most differentiated tumors were classified as stage 3 and were comprised of large numbers of rhabdomyoblasts and cells with fiberous and spindle cell morphology (Fig. S1A). Primary *kRAS^{G12D}*-induced ERMS were comprised of 50%

undifferentiated stage 1 ERMS (n=5 of 10, Fig. 1B,C and Fig. S1). By contrast, *mylpfa-myf5* expressing primary ERMS contained only 7.7% stage 1 ERMS (n=2 of 26, p=0.015, Chi-square, Fig. 1E-F). These latter ERMS samples had highly differentiated tumor cells and were scored histologically as stage 2 and 3 ERMS (Fig. 1F and Fig. S1A). Transcriptional profiling of bulk tumor cells by qRT-PCR confirmed that *mylpfa-myf5* expressing ERMS cells had high *myf5* transgene expression, were more differentiated, and had elevated expression of TPC-associated markers including *c-met* and *cdh15* (Fig. 1G). These data show that re-expression of *myf5* in more differentiated myosin-expressing ERMS cells leads to tumors with differentiated morphology and was consistent with the re-activation of muscle stem cell self-renewal programs in differentiated cell types.

Tumors arising in double transgenic *rag2-kRAS^{G12D}*; *mylpfa-myf5* expressing ERMS were also larger by 30 days of life than those that express only *kRAS^{G12D}* (Fig. 1H, p=0.0108, Student's t-test). However, apoptosis and proliferation rates were not altered following re-expression of *myf5* (Fig. S2), supporting our findings that *mylpfa-myf5* expressing ERMS initiate earlier and with higher penetrance than those that express only *rag2-kRAS^{G12D}* (Fig. 1I, p<0.001, log-rank Mantel-Cox test). Together, these data show that re-expression of *myf5* in more differentiated myosin+ ERMS cells not only leads to more differentiated tumors, but also accelerated tumorigenesis by enhancing initiation and penetrance of *kRAS^{G12D}*-induced ERMS.

To confirm that differentiation changes seen on histological review were confined to fully transformed ERMS cells, we next assessed the histology of ERMS following transplantation into immune-deficient *rag2^{E450fs}* recipient fish (Fig. 2A-F) (Tang et al.

2014). As expected, *kRAS*^{G12D}-expressing ERMS were comprised exclusively of undifferentiated stage 1 tumors (Fig. 2B,C and Fig. S1, n=10 transplanted fish arising from 4 independent tumors). By contrast, ERMS that re-expressed *myf5* had differentiated histology and were comprised of only stage 2 and 3 tumors (Fig. 2E,F and Fig. S1, n=15 transplanted fish from 4 independent tumors, p<,0.001, Chi-square test). Consistent with our histological evaluation, flow cytometric analysis revealed that differentiated, *mylpfa-mCherry-positive* (R+) tumor cells were greatly expanded in ERMS that aberrantly express *myf5* (Fig. 2G-I, p=0.006, Student's t-test). These same tumors had reduced numbers of *myf5-GFP* (G+) and double-positive (G+R+) cells. As was seen in primary ERMS, *mylpfa-myf5* expressing ERMS also initiated earlier with higher penetrance when engrafted into *rag2*^{e450fs} recipient animals (Fig. 2J, 2.5x10^5 cells/fish, p=0.046, Mantel-Cox log-rank statistic) and had a trend toward being larger when assessed at 30 days post-transplantation (Fig. 2K). Effects on ERMS differentiation were confirmed in CG1 strain syngeneic animals, showing that *mylpfa-myf5* expressing ERMS were more differentiated based on morphology (Fig. S3, p<0.01, Chi-square test) and contained larger numbers of differentiated, *mylpfa-mCherry-positive* (R+) ERMS cells following engraftment into syngeneic recipient fish (Fig. 2L, p<0.001, Student's t-test). These transplanted tumors also had significant reductions in *myf5-GFP* (G+) and double-positive (G+R+) ERMS cells. Together, these data confirm that *mylpfa-myf5* expressing ERMS were fully transformed and yet more differentiated than ERMS that express only *kRASG12D*.

myf5 confers self-renewal and tumor-propagating ability to differentiated ERMS cells

Because endogenous *myf5* expression labels self-renewing TPCs in zebrafish *kRAS*^{G12D}-induced ERMS (Ignatius et al. 2012; Chen et al. 2014), we next questioned if self-renewal and TPC frequency might be altered in *mylpfa-myf5* expressing ERMS. Specifically, *rag2-kRAS*^{G12D} was coinjected with or without *mylpfa-myf5* into one-cell stage, CG1 syngeneic *myf5-GFP/mylpfa-mCherry* transgenic animals. Following tumor growth, cell subpopulations were isolated by FACS and transplanted into syngeneic recipient fish at limiting dilution (1x10^3-10 cells/fish, purity >85%, and >95% viability). As previously reported (Ignatius et al. 2012), only the *myf5-GFP*+ single-positive ERMS cells from *kRAS*^{G12D}-alone expressing ERMS could efficiently engraft tumors into CG1-strain syngeneic recipient animals (Fig. S3, Table 1; n=3 ERMS). By contrast, both the *myf5-GFP*+ single-positive (G+) and differentiated *myf5-GFP+; mylpfa-mCherry*+ double positive (G+R+) ERMS cells could engraft disease when isolated from *mylpfa-myf5* expressing ERMS (n=3 tumors analyzed, Table 1 and Fig. 3A-K). Double positive cells isolated from *mylpfa-myf5* expressing ERMS had a >6 fold increase in engraftment potential when compared with *kRAS*^{G12D} -alone expressing ERMS (p=0.0002, ELDA analysis). Importantly, engrafted tumors displayed similar histology following engraftment with sorted cells (Fig. 3B,E,H and Fig. S3). Quantitative real-time PCR of sorted cell fractions showed similar gene expression in either *kRAS*^{G12D}-expressing or *kRAS+myf5* expressing ERMS, with the exception of *myf5,* which was highly expressed in the G+R+ population (Fig. 3L,M). Taken together, these data show that re-expression of *myf5* can lead to acquisition of self-renewal potential in differentiated *mylpfa*-expressing ERMS cells.

MYF5 and MYOD expression define unique subsets of human RMS

To explore the role of *MRFs* in human RMS, we next assessed *MYF5* and *MYOD* transcript expression in human primary tumor samples. Analysis of microarray gene expression (n=133 samples; Davicioni et al. 2009) and RNA sequencing data sets (n=98 samples; Shern et al. 2014) uncovered that MYOD and MYF5 were co-expressed along with specific muscle genes and defined two distinct gene regulatory modules in human RMS. One gene module included the co-expression of *MYF5, MYF6* and *PAX7* while the other expressed *MYOD*, *CDH15*, and *MYOG* (Fig. 4A,B). This correlation in gene expression was seen in comparison of all human RMS or within tumors arising specifically in the ERMS subtype (Fig. S4), suggesting that MYF5 and MYOD likely sit atop a transcriptional hierarchy to regulate muscle-specific gene programs in RMS.

We next assessed a panel of human RMS cell lines for expression of MYF5 and MYOD following Western blot analysis. Remarkably, we found that the expression of these proteins was largely mutually exclusive in human RMS (Fig. 4C), suggesting that these proteins may act redundantly to regulate human RMS self-renewal. This analysis also uncovered that only the Rh18 cell line expressed MYF5 in our panel of commonly used human RMS cell lines. MYF5 and MYOD expression were also assessed at the single cell level through immunofluorescence and verified that MYF5 and MYOD were mutually exclusively expressed within single ERMS cells from in Rh18 and RD cells (Fig. S5). ChIP-seq was performed for MYF5 in Rh18 cells and compared with previously published ChIP-seq data for MYOD performed in RD cells (see Materials and Methods section). This analysis uncovered a common set of promoter and enhancer

regions bound by both MYOD and MYF5 (Fig. S6A). 86% of commonly bound genomic DNA regions were confined to enhancers as defined by H3K27 acetylation occupancy. Unbiased analysis of commonly bound target genes using GREAT revealed an enrichment of genes that regulate myogenic cell fate and cell cycle (Fig. S6). Enrichment of GO terms included "embryonic skeletal system development", "skeletal muscle tissue development" and "cyclin-dependent protein kinase holoenzyme complex" (binomial $p<1x10^{-9}$). Signal tracks of ChIP-seq and RNA-seq independently confirmed common binding of MYF5 and MYOD to genes that regulate myogenic cell fate and cell cycle (Fig. S6C). Collectively, our data show significant inter-tumoral heterogeneity in the expression of myogenic factors within both ERMS and ARMS and suggests convergence of these transcription factors on regulating a common set of genes that modulate myogenic cell fate and cell cycle.

MYF5 and MYOD are required for continued tumor growth in human ERMS

Human Rh18 ERMS cells express high levels of MYF5 and were utilized in loss-of-function studies to assess roles in regulating proliferation, growth, and apoptosis. MYF5 protein expression was effectively reduced following siRNA-MYF5 knockdown (Fig. 4D) and resulted in significant impairment of cell proliferation as assessed by EdU-incorporation and flow cytometry (Fig.4E, $p<0.001$, Student's t-test, N=3, triplicate). For example, si-MYF5 treated cells showed a remarkable 70% reduction in S-phase cycling cells following 48 hours of treatment ($p<0.001$, Student's t-test, Fig. 4D). siRNA-MYF5 treated cells also had impaired growth when assessed by manual nuclei counts following knockdown (Fig. 4F, $p <0.01$, Student's t-test, N=3, triplicate). Apoptosis was not

increased in siRNA-MYF5 treated cells (Fig. S7C). These results were independently confirmed using stable knock-down with three independent lentiviral shRNAs specific to MYF5 (Fig. 4G-I, protein knockdown ranged from 50%-95%). All shRNA-MYF5 knockdown cells showed a remarkable cell cycle arrest with a virtual abrogation of S-phase cycling cells (Fig. 4H and Fig. S7A,B; $p<0.001$, Student's t-test). This phenotype was accompanied by a significant 60% decrease in cell number as assessed by manual nuclei counts and compared with shRNA control treated cells (Fig. 4I, $N>3$, triplicate). As was seen in siRNA-treated cells, apoptosis was not elevated following shRNA-MYF5 knockdown (Fig. S7D), suggesting that the major mechanism regulated by MYF5 was regulation of cell cycle and proliferation.

Given the prominent role *MYF5* had in regulating cell growth in human ERMS and imparting self-renewal potential to zebrafish ERMS cells, we next wanted to assess if MYF5 was required for ERMS maintenance and growth *in vivo*. Rh18 cells were infected with shRNAs and harvested at 72 hours post-infection. *MYF*5 knock-down was confirmed by Western blot analysis (Fig. 5A). Luciferase-mKate expressing Rh18 cells were transplanted into the flanks of *NOD/SCID/IL2rg* null mice ($1x10^6$ viable cells in matrigel per site). Control shRNA cells were implanted subcutaneously into the left flank and *MYF5* knock-down cells into the right (n=6 animals, 2 independent shRNAs). 5 hours after injection, mice were injected with luciferin and bioluminescence was measured. This analysis confirmed that the same amount of control and knockdown cells had been injected into recipient mice (Fig. 5B, top panels). Serial bioluminescence imaging showed that as early as 7 days post-implantation, tumor volume was reduced in MYF5 knockdown cells while control cells continued to grow (Fig. S8). MYF5

knockdown cells continued to be further reduced at 14, 28, and 42 days post-transplantation, with *MYF5* knockdown cells being largely undetected at late time points ($p=0.01$, Student's t-Test; Fig. 5B,C and Fig. S8). Taken together, these data show that *MYF5* is required for continued tumor cell growth *in vivo* and confirm roles for MYF5 in tumor maintenance and cellular growth in human RMS.

To assess if other MRFs can drive continued tumor growth and proliferation, we next performed MYOD knockdown in human RD ERMS cells. siRNA or shRNA knock-down resulted in reduced proliferation and a striking reduction in S-phase cycling cells (Fig. 4J,K,M,N and Fig. S7E,F, $p<0.001$, Student's t-test). RD cell number was reduced >30% following stable shRNA-MYOD knockdown (Fig. 4O), yet cells did not exhibit increased apoptosis (Fig. S7G). These phenotypes were similar to those obtained following MYF5 knock-down in Rh18 cells, albeit with different kinetics and penetrance. Similar results were obtained following si-MYOD treatment of additional RMS cell lines including ERMS cell lines 381T and RMS559 and the ARMS cell line Rh3. These cells lines all had >30% reduction in S-phase cells following siRNA treatment. Along with our ChIP-seq analysis, our data suggest that both MYF5 and MYOD likely regulate common gene programs that control cell self-renewal, cell cycle and myogenic differentiation arrest in a wide range of human RMS.

Discussion

Rhabdomyosarcomas express bHLH myogenic regulatory transcription factors (MRFs), including MYF5 and MYOD (Clark et al. 1991; Kumar et al. 2000; Sebire and Malone 2003) but fail to activate terminal muscle differentiation programs. Several mechanisms have been shown to play a role in this differentiation arrest. These include disruption of the balance of MRF-E12 heterodimers and inhibitor complexes (Yang et al. 2009; MacQuarrie et al. 2013), presence of inhibitory miRNAs (MacQuarrie et al. 2012), and deregulation of cell cycle (Fiddler et al. 1996). These data have therefore led to the suggestion that MRFs do not have a role in RMS transformation or in sustained tumor growth, but are rather retained from the target cell of transformation (Keller and Guttridge 2013). Indeed, MYOD overexpression fails to differentiate ERMS cells (Yang et al. 2009), yet both MYF5 and MYOD potently reprogram fibroblasts into proliferating muscle cells (Tapscott et al. 1988; Braun et al. 1989). Our work using the zebrafish *kRASG12D* transgenic model has uncovered that endogenous *Myf5* expression marks tumor-propagating ERMS cells (Chen et al. 2013a, 2014; Ignatius et al. 2012), leading us to experimentally assess roles for MYF5 in regulating ERMS growth and self-renewal in the studies outlined here. Our experiments have shown that Myf5 can impart tumor-propagating potential to differentiated cells in the *kRAS*^{G12D}–induced zebrafish ERMS model, suggesting important roles for myogenic regulatory transcription factors in regulating self-renewal and growth. These data were confirmed by loss-of-function studies in human ERMS where MYF5 or MYOD loss suppressed RMS proliferation and reduced viability *in vitro*. Similar effects were also observed in xenograft studies, where MYF5-deficient ERMS cells failed to grow *in vivo*. Taken together, our results support

powerful and unappreciated roles of myogenic transcription factors in driving sustained ERMS growth, likely by deregulating both myogenic gene programs and cell cycle genes. These data strongly contrast with current thinking in the field that myogenic transcription factors are commonly expressed in tumors, indicative of cell-of-origin rather than having true functional effects on tumorigenesis.

It is becoming increasingly appreciated that developmental transcription factors and pathways are commonly co-opted by cancer to regulate growth and self-renewal. For example, the TAL1/SCL bHLH transcription factor is required for hematopoietic stem cell specification and self-renewal during development. TAL1/SCL is overexpressed in 60% of T-cell acute lymphoblastic leukemia (T-ALL) (Ferrando et al. 2002) and can reprogram thymocytes into self-renewing, pre-leukemic cells (Gerby et al. 2014). This same paradigm has also been seen in brain tumors. For example, the bHLH transcription factor OLIG2 is required for self-renewal of normal neural progenitor cells (Imayoshi and Kageyama 2014) and yet, is also a marker of glioblastoma TPCs and regulates self-renewal in both mouse and human disease (Ligon et al. 2007; Trépant et al. 2014; Suva et al. 2014; Beyeler et al. 2014). Our results in ERMS parallel those outlined for T-ALL and glioblastoma, showing that MYF5 is capable of reprogramming differentiated ERMS cells into self-renewing cells and is required for sustained proliferation, growth, viability, and self-renewal of human RMS. Our work has also uncovered redundancy in MRF function in RMS growth, with MYOD being expressed in a substantial fraction of human RMS and required for proliferation. Taken together, these results demonstrate that cancer pathways are likely shared with their non-malignant counterparts and suggest a dominant

way cancers drive elevated self-renewal is through aberrant activation of well-established developmental pathways that drive tissue specification, growth, and regeneration.

Our molecular analysis also uncovered that MYF5 and MYOD are largely mutually-exclusively expressed in human ERMS and each drives sustained growth in tumors that express these factors. For example, loss-of-function studies confirmed important roles for both MYF5 and MYOD in regulating proliferation both *in vitro* and *in vivo*. During skeletal muscle development, Myf5 and MyoD act redundantly to regulate muscle specification and differentiation (Buckingham and Rigby 2014). Myf5 and MyoD are also required for self-renewal of adult muscle satellite cells. For example, Haldar and colleagues have concluded that a subset of muscle progenitors are specified by MyoD without the contribution of Myf5 (Haldar et al. 2008, 2014). Tajbaksh and colleagues have shown that a subset of adult muscle progenitors express Myf5 and then MyoD sequentially during their specification with both being required for muscle regeneration following injury (Comai et al. 2014). This same redundancy of Myf5 and MyoD in development and muscle injury has been reported in zebrafish (Hinits et al. 2009; Siegel et al. 2013), *Drosophila* (Abmayr and Keller 1998) and *Xenopus* (Chanoine and Hardy 2003), showing a high conservation of these developmental pathways throughout evolution. Indeed, Myf5 and MyoD can act redundantly in reprogramming fibroblasts into muscle cell fates (Braun et al. 1989; Tapscott et al. 1988) and overlap in binding of common enhancer and promoter targets (Conerly et al. 2016). Our data in ERMS suggests a model where either MYF5 or MYOD are re-activated in RMS cells and act redundantly to sustain self-renewal and proliferation. We also posit that these factors regulate a common core self-renewal program in RMS downstream of either MYF5 or

MYOD, providing new and exciting avenues of study and potential new therapeutic strategies for the treatment of this disease.

Materials and Methods

Animals and protocol approvals

Studies were approved by the Massachusetts General Hospital Subcommittee on Research Animal Care under the protocol #2011N000127 (zebrafish) and #2013N000038 (mouse). Biosafety lentiviral work was approved by the Partners IBC under protocol #2013B000039. Zebrafish used in this work include: CG1 strain (Mizgirev and Revskoy 2006), *myf5*-GFP (Chen et al. 2007) and *mylpfa*-mCherry (previously *mylz2*-mCherry) (Xu et al. 1999) transgenic zebrafish lines and rag^{E450fs} homozygous fish (Tang et al. 2014; Tenente et al. 2014). *myf5-GFP/mylpfa-mCherry* double transgenic fish (AB strain) were outcrossed 10 times into CG1-strain zebrafish to generate compound syngeneic transgenic zebrafish (Ignatius et al. 2012). 6-week-old *NOD/SCID/Il2rg* null female mice were used in this work (N=12).

Micro-injection and ERMS generation in transgenic zebrafish

rag2-kRAS^{G12D} *and mylpfa-mCherry* constructs were described previously (Langenau et al. 2007; Smith et al. 2010). The *mylpfa-myf5* construct was obtained by gateway cloning using a zebrafish *myf5* ORF from 24hpf zebrafish embryo cDNA (http://tol2kit.genetics.utah.edu). *rag2-kRAS*^{G12D} *and mylpfa-myf5* constructs were linearized with XhoI, phenol:chloroform-extracted, ethanol-precipitated, resuspended in

0.5× Tris-EDTA + 0.1 M KCl, and injected into one-cell stage embryos of the respective backgrounds, as previously described (Tenente et al. 2014; Langenau et al. 2007).

Quantification of zebrafish RMS size, tumor onset, and penetrance.

Zebrafish were monitored every 3-4 days for time-to-tumor onset using an epi-fluorescent stereomicroscope. Animals were imaged at 10 days of life until 55 days of life. Primary tumor size was quantified from photomicrographs taken at 30 days of life and calculated by multiplying fluorescence intensity by D2 pixel area using the ImageJ software package as previously described (Chen et al. 2014). Kaplan-Meier tumor onset analysis was performed using Graphpad Prism® Software and statistically analyzed using the Log-rank statistic.

Zebrafish histology and immunohistochemistry

Paraffin embedding, sectioning and immunohistochemical analysis of zebrafish sections were performed as described (Chen et al. 2013a, 2014; Ignatius et al. 2012). Antibodies used for immunohistochemistry included: phospho-H3 (1:6000, Santa Cruz) and cleaved-caspase3 (1:250, Cell Signaling). All histopathology procedures were performed at the MGH and BWH DF/HCC Research Pathology Cores. Slides were imaged using a transmitted light Olympus BX41 microscope. Pathology review and staging were completed by G.P.N. Tumor histology classification was assigned as described in Supplemental Figure S1 with stage 1 being the least differentiated with tumors being comprised of only small round blue cells. Stage 2 and 3 ERMS were assigned based on the preponderance of rhabdomyoblast cells, fiberous and spindle cell

morphology, with a low proportion of interspersed smaller round blue cells. Staging was completed essentially as described (Storer et al., 2013).

Zebrafish ERMS cell transplantation

FACS analysis and RMS cell transplantation by intraperitoneal injection were completed essentially as described (Chen et al. 2014; Ignatius et al. 2012; Smith et al. 2010; Langenau et al. 2007). RMS tumor cells were stained with DAPI to exclude dead cells and sorted twice using a Laser BD FACSAria II Cell Sorter. Sort purity and viability were assessed after two rounds of sorting when possible, exceeding 85% and 95% respectively. Fish were monitored for tumor engraftment from 10 to 120 days post transplantation. Tumor-propagating cell frequency was quantified following transplantation into CG1 syngeneic recipient fish using the Extreme Limiting Dilution Analysis software (http://bioinf.wehi.edu.au/software/elda/). A subset of transplanted fish were fixed in 4% PFA, sectioned, stained with Hematoxylin and Eosin, and staged for differentiation score.

Gene expression analysis

Quantitative real-time PCR was completed using a Roche Lightcycler 480 machine. PCR primers and specific conditions are available in Supplemental Table 1. Relative quantification was performed using the -ΔΔCt method relative to 18S.

Human RMS cell lines

The human RD cell line was obtained from ATCC's cell biology collection (Manassas, Virginia). SMS-CTR, 381T, Rh3, Rh5 and Rh30 cell lines were kindly provided by Dr. Corrine Linardic (Duke University, North Carolina), the Rh18 cell line (fusion-negative) by Dr. Peter Houghton (Ohio State University, Ohio) and RMS559 by Dr. Jonathan Fletcher (Brigham and Women's Hospital, Massachusetts). The human MB1208-1 human skeletal muscle cell line was kindly provided by Dr. Louis Kunkel (Boston Children's Hospital, Massachusetts). Characteristics of these human RMS (Hinson et al. 2013; Sokolowski et al. 2014) and skeletal muscle (Alexander et al. 2011) cell lines have been reported previously.

Western blot analysis

Total cell lysates from human RMS cell lines were obtained following lysis in 2%SDS lysis buffer supplemented with protease inhibitors (Santa Cruz Biotechnology). Samples were boiled, vortexed and homogenized through a 28G syringe. 20-40 μg of protein was loaded in 4-20% Mini-Protean TGX gels (Biorad) and transferred onto PVDF membranes. Western blot analysis used primary antibodies: rabbit a-MYF5 (1:5000, Abcam ab125078), mouse a-MYOD1 (1:1000, Abcam ab16148), rabbit a-MYOD1 (1:1000, Abcam ab133627), rabbit a-GAPDH (1:2000, Cell Signaling 2118), mouse a-TUBULIN (1:2500, Abcam ab4074) and secondary antibodies: HRP anti-rabbit (1:2000, Cell Signaling 7074) or HRP anti-mouse (1:3000, GE Healthcare NA93IV). Blocking was completed using 5% skim milk/TBST. Membranes were developed using a ECL

reagent (Western Lightening Plus-ECL, Perkin Elmer or sensitive SuperSignal West femto Maximum Sensitivity Substrate, Thermo Scientific).

MYF5 and MYOD siRNA and immunofluorescence

Gene-specific smart-pool or control siRNAs (Dharmacon, GE Life Sciences) (0.01μM) were reverse-transfected into cells using RNAiMax lipofectamine transfection reagent (Life Technologies) in flat clear bottom 96 well plates. Cells were then fixed at 96 hours post transfection in 4% PFA/PBS, washed in x1 PBS and permeabilized in 0.5% TritonX-100/PBS. Antibodies used were rabbit a-Myf5 (1:400, Abcam ab125078) and mouse a-MyoD (1:200, Abcam ab16148) in 2% goat serum/PBS, Alexa 488 goat anti-mouse (1:1000, Invitrogen A11029) and Alexa 594 goat anti-rabbit (1:1000 Invitrogen A11037). Cells were incubated with DAPI (1 μg/ml), and imaged at 200x using a LSM710 Zeiss Laser scanning confocal microscope. Images were processed in ImageJ and Adobe Photoshop.

For EdU and AnnexinV assays, gene-specific smart-pool or control siRNAs (Dharmacon, GE Life Sciences) (5μM) were added to Rh18, RD, 381T, RMS559 and Rh3 cells in a 6-well plate and incubated for 24-72 hours prior to analysis.

MYF5 and MYOD lentiviral shRNA knock-down

Scrambled (SCR) control shRNA and hMYF5 or hMYOD1 specific shRNAs were delivered on the pLKO.1-background vector (from MGH Molecular Profiling Laboratory) and packaged using 293T cells (see Supplemental Material for sequences).

RMS cells were infected with viral particles for 24h at 37ºC with 8μg/ml of polybrene (EMD Millipore).

Cell viability, EdU proliferation analysis, and apoptosis assays

Nuclei counts were performed following incubation with NucBlue Live ReadyProbes® Reagent (Life Technologies). Cells were imaged at 100X and 400X magnification using an inverted fluorescent microscope. Manual cell counts were performed using the ImageJ® software. Three fields were counted per well and completed in triplicate. Cell cycle analysis was performed using the EdU Click-iT® plus EdU Flow Cytometry-AlexaFluor® 647 picol azide assay (Life Technologies) following 2h (RD, 381T, Rh3, RMS559) or 6h incubation (Rh18) with 10 μM EdU. Apoptosis was assessed using the AnnexinV-AlexaFluor® 647/PI assay (Life Technologies). Flow cytometric analysis was performed using the SORP4 Laser BD LSRII Flow Cytometer and processed with the FlowJo® Software.

Gene expression correlation analysis

Previously published microarray gene expression data were processed and normalized using Robust Multichip Average (RMA) normalization (Davicioni et al. 2006). Previously published RNAseq gene expression data from human RMS were processed and normalized using a standard Tuxedo pipeline (Shern et al. 2014, Trapnell et al. 2012). The resulting expression values from the microarray and RNAseq datasets were then log2 transformed. Pearson correlation was determined for the following genes: *CDH15, MYF5, MYF6, MYOD1, MYOG, PAX3,* and *PAX7*. The correlation heatmap was

plotted using the R package "fheatmap" (Fantastic Heatmap. R package version 1.0.1. http://CRAN.R-project.org/package=fheatmap) and processed using Adobe Photoshop®.

ChIP-seq of human RMS cell lines

Chromatin immunoprecipitations were performed on RH18 cells using the Chip-IT High sensitivity kit (Active Motif) and anti-H3K27ac (Active Motif) or anti-MYF5 (C-20, Santa Cruz) antibodies. Resultant purified immunoprecipitated DNA was used for library preparation using the TruSeq ChIP sample preparation kit (Illumina) without modifications. 11-18 library preps were mixed for multiplexed single read sequencing using the NextSeq500 (Illumina). Previously published MYOD ChIP-seq data from RD was downloaded and processed in parallel with the newly generated sequencing data (GSE50415). Reads were aligned to the hg19 reference using BWA. ChIP-seq peaks were identified using MACS 2.1 (Zhang et al. 2008). Gene ontology was performed using GREAT (McLean et al. 2010). Differential peak calling between RD and RH18 was performed using bedtools v2.25.0 and visualized using NGS plot (Shen et al. 2014). Genomic regions were visualized using IGV v2.3.40.

Mouse xenografts and luciferase imaging

Rh18 ERMS cells were co-infected with pLKO.1-shRNA lentivirus and pLKO.1-*luc-mKate* (gift from Drs. Matthijssens and Van Vlierberghe, Ghent University, Belgium). At 3 days post-infection, cells were collected and counted. An aliquot of cells was analyzed using the SORP4 Laser BD LSRII Flow Cytometer to determine viability following DAPI staining. A separated aliquot of cells were harvested and used for

Western blot analysis. Equal numbers of viable cells were then embedded into Matrigel (Corning) at a final concentration of $1x10^6$ of viable cells per 200 µl. Six-week-old *NOD/SCID/IL2rg* null female mice were anesthetized by isofluorane and transplanted with Rh18 scramble-shRNA/mKate-luc cells subcutaneously into the left flank whereas Rh18 sh-MYF5/mKate-luc cells injected on the right (200 µl/flank injection). Tumor growth was monitored by weekly bioluminescence imaging following subcutaneous injection into the loose tissue over the neck of 75mg/kg D-luciferin (Perkin Elmer) in 100 µl of PBS. Imaging was completed and analyzed using the IVIS Lumina II (Caliper Life Science). Comparison between groups was performed using a Student's t-test.

Acknowledgments

This work was supported by Alex's Lemonade Stand Foundation (D.M.L.), the Harvard Stem Cell Institute, and NIH grants R24OD016761 (D.M.L.), R01CA154923 (D.M.L.) and U54CA168512. I.M.T received funds from the Portuguese Foundation for Science and Technology (Fundação para a Ciência e Tecnologia – FCT). Q.T. is funded by the China Scholarship Council. We thank the Specialized Histopathology Services at Massachusetts General Hospital (MGH) and the Dana-Farber/Harvard Cancer Center (P30 CA06516), MGH Cancer Center/Molecular Pathology Confocal Core, the MGH Pathology Flow and Image Cytometry Research Core. The authors declare no competing financial interests. We thank Matthew Alexander for helpful suggestions and comments.

References

Abmayr SM, Keller CA. 1998. Drosophila myogenesis and insights into the role of nautilus. *Curr Top Dev Biol* **38**: 35–80.

Abraham J, Nuñez-Álvarez Y, Hettmer S, Carrió E, Chen HIH, Nishijo K, Huang ET, Prajapati SI, Walker RL, Davis S, et al. 2014. Lineage of origin in rhabdomyosarcoma informs pharmacological response. *Genes Dev* **28**: 1578–1591.

Alexander MS, Casar JC, Motohashi N, Myers J a, Eisenberg I, Gonzalez RT, Estrella E a, Kang PB, Kawahara G, Kunkel LM. 2011. Regulation of DMD pathology by an ankyrin-encoded miRNA. *Skelet Muscle* **1**: 27.

Beyeler S, Joly S, Fries M, Obermair F-J, Burn F, Mehmood R, Tabatabai G, Raineteau O. 2014. Targeting the bHLH transcriptional networks by mutated E proteins in experimental glioma. *Stem Cells* 1–16.

Blum JM, Añó L, Li Z, Van Mater D, Bennett BD, Sachdeva M, Lagutina I, Zhang M, Mito JK, Dodd LG, et al. 2013. Distinct and overlapping sarcoma subtypes initiated from muscle stem and progenitor cells. *Cell Rep* **5**: 933–40.

Braun T, Buschhausen-Denker G, Bober E, Tannich E, Arnold HH. 1989. A novel human muscle factor related to but distinct from MyoD1 induces myogenic conversion in 10T1/2 fibroblasts. *EMBO J* **8**: 701–9.

Buckingham ME, Rigby PWJ. 2014. Gene regulatory networks and transcriptional mechanisms that control myogenesis. *Dev Cell* **28**: 225–38.

Cavaco Rodrigues AM, Christen B, Marti M, Izpisua Belmonte JC. 2012. Skeletal muscle regeneration in Xenopus tadpoles and zebrafish larvae. *BMC Dev Biol* **12**: 9. http://www.biomedcentral.com/1471-213X/12/9.

Chanoine C, Hardy S. 2003. Xenopus muscle development: From primary to secondary myogenesis. *Dev Dyn* **226**: 12–23.

Chen EY, DeRan MT, Ignatius MS, Grandinetti KB, Clagg R, McCarthy KM, Lobbardi RM, Brockmann J, Keller C, Wu X, et al. 2014. Glycogen synthase kinase 3 inhibitors induce the canonical WNT/β-catenin pathway to suppress growth and self-renewal in embryonal rhabdomyosarcoma. *Proc Natl Acad Sci U S A* **111**: 5349–54.

Chen EY, Dobrinski KP, Brown KH, Clagg R, Edelman E, Ignatius MS, Chen JYH, Brockmann J, Nielsen GP, Ramaswamy S, et al. 2013a. Cross-species array comparative genomic hybridization identifies novel oncogenic events in zebrafish and human embryonal rhabdomyosarcoma. *PLoS Genet* **9**: e1003727.

Chen X, Stewart E, Shelat AA, Qu C, Bahrami A, Hatley ME, Wu G, Bradley C, McEvoy J, Pappo A, et al. 2013b. Targeting oxidative stress in embryonal rhabdomyosarcoma. *Cancer Cell* **24**: 710–24.

Chen Y-H, Wang Y-H, Chang M-Y, Lin C-Y, Weng C-W, Westerfield M, Tsai H-J. 2007. Multiple upstream modules regulate zebrafish myf5 expression. *BMC Dev Biol* **7**: 1.

Clark J, Rocques PJ, Braun T, Bober E, Arnold HH, Fisher C, Fletcher C, Brown K, Gusterson BA, Carter RL. 1991. Expression of members of the myf gene family in human rhabdomyosarcomas. *Br J Cancer* **64**: 1039–42.

Comai G, Sambasivan R, Gopalakrishnan S, Tajbakhsh S. 2014. Variations in the Efficiency of Lineage Marking and Ablation Confound Distinctions between Myogenic Cell Populations. *Dev Cell* **31**: 654–667.

Conerly ML, Yao Z, Zhong JW, Groudine M, Tapscott SJ. 2016. Distinct Activities of Myf5 and MyoD Indicate Separate Roles in Skeletal Muscle Lineage Specification and Differentiation Article Distinct Activities of Myf5 and MyoD Indicate Separate Roles in Skeletal Muscle Lineage Specification and Differentiation. *Dev Cell* **36**: 375–385.

Davicioni E, Anderson MJ, Finckenstein FG, Lynch JC, Qualman SJ, Shimada H, Schofield DE, Buckley JD, Meyer WH, Sorensen PHB, et al. 2009. Molecular classification of rhabdomyosarcoma-genotypic and phenotypic determinants of diagnosis: a report from the Children's Oncology Group. *Am J Pathol* **174**: 550–564.

Davicioni E, Finckenstein FG, Shahbazian V, Buckley JD, Triche TJ, Anderson MJ. 2006. Identification of a PAX-FKHR gene expression signature that defines molecular classes and determines the prognosis of alveolar rhabdomyosarcomas. *Cancer Res* **66**: 6936–46.

Ferrando AA, Neuberg DS, Staunton J, Loh ML, Huard C, Raimondi SC, Behm FG, Pui C-H, Downing JR, Gilliland DG, et al. 2002. Gene expression signatures define novel oncogenic pathways in T cell acute lymphoblastic leukemia. *Cancer Cell* **1**: 75–87.

Fiddler T, Smith L, Tapscott SJ, Thayer M. 1996. Amplification of MDM2 Inhibits MyoD-Mediated Myogenesis. *Mol Cell …* **16**: 5048–5057.

Gerby B, Tremblay CS, Tremblay M, Rojas-Sutterlin S, Herblot S, Hébert J, Sauvageau G, Lemieux S, Lécuyer E, Veiga DFT, et al. 2014. SCL, LMO1 and Notch1 reprogram thymocytes into self-renewing cells. *PLoS Genet* **10**: e1004768.

Haldar M, Karan G, Tvrdik P, Capecchi MR. 2008. Two cell lineages, myf5 and myf5-independent, participate in mouse skeletal myogenesis. *Dev Cell* **14**: 437–45.

Haldar M, Karan G, Watanabe S, Guenther S, Braun T, Capecchi MR. 2014. Response: Contributions of the Myf5-Independent Lineage to Myogenesis. *Dev Cell* **31**: 539–541.

Hatley ME, Tang W, Garcia MR, Finkelstein D, Millay DP, Liu N, Graff J, Galindo RL, Olson EN. 2012. A mouse model of rhabdomyosarcoma originating from the adipocyte lineage. *Cancer Cell* **22**: 536–46.

Hettmer S, Bronson RT, Wagers AJ. 2015. Distinct Malignant Behaviors of Mouse Myogenic Tumors Induced by Different Oncogenetic Lesions. *Front Oncol* **5**: 1–5.

Hettmer S, Li Z, Billin AN, Barr FG, Cornelison DDW, Ehrlich AR, Guttridge DC, Hayes-Jordan A, Helman LJ, Houghton PJ, et al. 2014. Rhabdomyosarcoma: Current Challenges and Their Implications for Developing Therapies. *Cold Spring Harb Perspect Med* **4**: a025650–a025650.

Hettmer S, Liu J, Miller CM, Lindsay MC, Sparks CA, Guertin DA, Bronson RT, Langenau DM, Wagers AJ. 2011. Sarcomas induced in discrete subsets of prospectively isolated skeletal muscle cells. *Proc Natl Acad Sci U S A* **108**: 20002–7.

Hinits Y, Osborn DPS, Hughes SM. 2009. Differential requirements for myogenic regulatory factors distinguish medial and lateral somitic, cranial and fin muscle fibre populations. *Development* **136**: 403–14.

Hinson ARP, Jones R, Crose LES, Belyea BC, Barr FG, Linardic CM. 2013. Human rhabdomyosarcoma cell lines for rhabdomyosarcoma research: utility and pitfalls. *Front Oncol* **3**: 183.

Ignatius MS, Chen EY, Elpek NM, Fuller AZ, Tenente IM, Clagg R, Liu S, Blackburn JS, Linardic CM, Rosenberg AE, et al. 2012. In vivo imaging of tumor-propagating cells, regional tumor heterogeneity, and dynamic cell movements in embryonal rhabdomyosarcoma. *Cancer Cell* **21**: 680–93.

Imayoshi I, Kageyama R. 2014. bHLH factors in self-renewal, multipotency, and fate choice of neural progenitor cells. *Neuron* **82**: 9–23.

Kashi VP, Hatley ME, Galindo RL. 2015. Probing for a deeper understanding of rhabdomyosarcoma: insights from complementary model systems. *Nat Rev Cancer* **15**: 426–439.

Keller C, Guttridge DC. 2013. Mechanisms of impaired differentiation in rhabdomyosarcoma. *FEBS J* **280**: 4323–4334.

Kikuchi K, Rubin BP, Keller C. 2011. Developmental origins of fusion-negative rhabdomyosarcomas. *Curr Top Dev Biol* **96**: 33–56.

Kumar S, Perlman E, Harris C a, Raffeld M, Tsokos M. 2000. Myogenin is a specific marker for rhabdomyosarcoma: an immunohistochemical study in paraffin-embedded tissues. *Mod Pathol* **13**: 988–93.

Langenau DM, Keefe MD, Storer NY, Guyon JR, Kutok JL, Le X, Goessling W, Neuberg DS, Kunkel LM, Zon LI. 2007. Effects of RAS on the genesis of embryonal rhabdomyosarcoma. *Genes Dev* **21**: 1382–95.

Le X, Langenau DM, Keefe MD, Kutok JL, Neuberg DS, Zon LI. 2007. Heat shock-inducible Cre/Lox approaches to induce diverse types of tumors and hyperplasia in transgenic zebrafish. *Proc Natl Acad Sci U S A* **104**: 9410–5.

Le X, Pugach EK, Hettmer S, Storer NY, Liu J, Wills A a, DiBiase A, Chen EY, Ignatius MS, Poss KD, et al. 2013. A novel chemical screening strategy in zebrafish identifies common pathways in embryogenesis and rhabdomyosarcoma development. *Development* **140**: 2354–64.

Ligon KL, Huillard E, Mehta S, Kesari S, Liu H, Alberta J a., Bachoo RM, Kane M, Louis DN, DePinho R a., et al. 2007. Olig2-Regulated Lineage-Restricted Pathway Controls Replication Competence in Neural Stem Cells and Malignant Glioma. *Neuron* **53**: 503–517.

Lisboa S, Cerveira N, Vieira J, Torres L, Ferreira AM, Afonso M, Norton L, Henrique R, Teixeira MR. 2008. Genetic diagnosis of alveolar rhabdomyosarcoma in the bone marrow of a patient without evidence of primary tumor. *Pediatr Blood Cancer* **51**: 554–7.

MacQuarrie KL, Yao Z, Fong AP, Tapscott SJ. 2013. Genome-wide binding of the basic helix-loop-helix myogenic inhibitor musculin has substantial overlap with MyoD: implications for buffering activity. *Skelet Muscle* **3**: 26. http://www.ncbi.nlm.nih.gov/pubmed/24175993.

MacQuarrie KL, Yao Z, Young JM, Cao Y, Tapscott SJ. 2012. miR-206 integrates multiple components of differentiation pathways to control the transition from growth to differentiation in rhabdomyosarcoma cells. *Skelet Muscle* **2**: 7.

McLean CY, Bristor D, Hiller M, Clarke SL, Schaar BT, Lowe CB, Wenger AM, Bejerano G. 2010. GREAT improves functional interpretation of cis-regulatory regions. *Nat Biotechnol* **28**: 495–501.

Mizgirev I V, Revskoy SY. 2006. Transplantable tumor lines generated in clonal zebrafish. *Cancer Res* **66**: 3120–5.

Parham DM. 2001. Pathologic Classification of Rhabdomyosarcomas and Correlations with Molecular Studies. *Mod Pathol* **14**: 506–514.

Reya T, Morrison SJ, Clarke MF, Weissman IL. 2001. Stem cells, cancer, and cancer stem cells. *Nature* **414**: 105–11.

Rubin BP, Nishijo K, Chen HIH, Yi X, Schuetze DP, Pal R, Prajapati SI, Abraham J, Arenkiel BR, Chen QR, et al. 2011. Evidence for an Unanticipated Relationship between Undifferentiated Pleomorphic Sarcoma and Embryonal Rhabdomyosarcoma. *Cancer Cell* **19**: 177–191.

Sebire NJ, Malone M. 2003. Myogenin and MyoD1 expression in paediatric rhabdomyosarcomas. *J Clin Pathol* **56**: 412–6.

Shen L, Shao N, Liu X, Nestler E. 2014. ngs.plot: Quick mining and visualization of next-generation sequencing data by integrating genomic databases. *BMC Genomics* **15**: 284.

Shern JF, Chen L, Chmielecki J, Wei JS, Patidar R, Rosenberg M, Ambrogio L, Auclair D, Wang J, Song YK, et al. 2014. Comprehensive genomic analysis of rhabdomyosarcoma reveals a landscape of alterations affecting a common genetic axis in fusion-positive and fusion-negative tumors. *Cancer Discov* **4**: 216–31.

Shinkoda Y, Nagatoshi Y, Fukano R, Nishiyama K, Okamura J. 2009. Rhabdomyosarcoma masquerading as acute leukemia. *Pediatr Blood Cancer* **52**: 286–7.

Siegel AL, Gurevich DB, Currie PD. 2013. A myogenic precursor cell that could contribute to regeneration in zebrafish and its similarity to the satellite cell. *FEBS J* **280**: 4074–88.

Smith ACH, Raimondi AR, Salthouse CD, Ignatius MS, Blackburn JS, Mizgirev I V, Storer NY, de Jong JLO, Chen AT, Zhou Y, et al. 2010. High-throughput cell transplantation establishes that tumor-initiating cells are abundant in zebrafish T-cell acute lymphoblastic leukemia. *Blood* **115**: 3296–303.

Sokolowski E, Turina CB, Kikuchi K, Langenau DM, Keller C. 2014. Proof-of-concept rare cancers in drug development: the case for rhabdomyosarcoma. *Oncogene* **33**: 1877–89.

Sorensen PHB, Lynch JC, Qualman SJ, Tirabosco R, Lim JF, Maurer HM, Bridge JA, Crist WM, Triche TJ, Barr FG. 2002. PAX3-FKHR and PAX7-FKHR Gene Fusions Are Prognostic Indicators in Alveolar Rhabdomyosarcoma: A Report From the Children's Oncology Group. *J Clin Oncol* **20**: 2672–2679.

Storer NY, White RM, Uong A, Price E, Nielsen GP, Langenau DM, Zon LI. 2013. Zebrafish rhabdomyosarcoma reflects the developmental stage of oncogene expression during myogenesis. *Development* **140**: 3040–50.

Suva ML, Rheinbay E, Gillespie SM, Patel AP, Wakimoto H, Rabkin SD, Riggi N, Chi AS, Cahill DP, Nahed B V, et al. 2014. Reconstructing and reprogramming the tumor-propagating potential of glioblastoma stem-like cells. *Cell* **157**: 580–94.

Tang Q, Abdelfattah NS, Blackburn JS, Moore JC, Martinez S a, Moore FE, Lobbardi R, Tenente IM, Ignatius MS, Berman JN, et al. 2014. Optimized cell transplantation using adult rag2 mutant zebrafish. *Nat Methods* **11**: 821–824.

Tapscott SJ, Davis RL, Thayer MJ, Cheng P, Lassar AB, Weintraub H. 1988. MyoD1 : a Myc Requiring Nuclear Phosphoprotein to Convert Region Homology Myoblasts Fibroblasts to Myoblasts. *Science* **242**: 405–411.

Tenente IM, Tang Q, Moore JC, Langenau DM. 2014. Normal and Malignant Muscle Cell Transplantation into Immune Compromised Adult Zebrafish. *J Vis Exp*.

Trapnell C, Roberts A, Goff L, Pertea G, Kim D, Kelley DR, Pimentel H, Salzberg SL, Rinn JL, Pachter L. 2012. Differential gene and transcript expression analysis of RNA-seq experiments with TopHat and Cufflinks. *Nat Protoc* **7**: 562–78.

Tremblay AM, Missiaglia E, Galli GG, Hettmer S, Urcia R, Carrara M, Judson RN, Thway K, Nadal G, Selfe JL, et al. 2014. The Hippo Transducer YAP1 Transforms Activated Satellite Cells and Is a Potent Effector of Embryonal Rhabdomyosarcoma Formation. *Cancer Cell* **26**: 273–287.

Trépant A-L, Bouchart C, Rorive S, Sauvage S, Decaestecker C, Demetter P, Salmon I. 2014. Identification of OLIG2 as the most specific glioblastoma stem cell marker starting from comparative analysis of data from similar DNA chip microarray platforms. *Tumor Biol* **36**: 1943–1953.

Walter D, Satheesha S, Albrecht P, Bornhauser BC, D'Alessandro V, Oesch SM, Rehrauer H, Leuschner I, Koscielniak E, Gengler C, et al. 2011. CD133 positive embryonal rhabdomyosarcoma stem-like cell population is enriched in rhabdospheres. *PLoS One* **6**: e19506.

Xu Y, He J, Tian HOL, Chan CHUA, Liao JI, Yan T, Lam TJ, Gong Z. 1999. Fast skeletal muscle-specific expression of a zebrafish myosin light chain 2 gene and characterization of its promoter by direct injection into skeletal muscle. *DNA Cell Biol* **18**: 85–95.

Yang Z, MacQuarrie KL, Analau E, Tyler AE, Dilworth FJ, Cao Y, Diede SJ, Tapscott SJ. 2009. MyoD and E-protein heterodimers switch rhabdomyosarcoma cells from an arrested myoblast phase to a differentiated state. *Genes Dev* **23**: 694–707.

Zhang Y, Liu T, Meyer CA, Eeckhoute J, Johnson DS, Bernstein BE, Nusbaum C, Myers RM, Brown M, Li W, et al. 2008. Model-based analysis of ChIP-Seq (MACS). *Genome Biol* **9**: R137.

kRAS^{G12D} Tumor #1					***kRAS^{G12D} + mylpfa:myf5 Tumor #1***				
Cell #	G^+	G^+R^+	R^+	*DN*	Cell #	G^+	G^+R^+	R^+	*DN*
1000	6 of 6	2 of 7	0 of 6	0 of 7	*1000*	2 of 3	4 of 5	0 of 6	0 of 6
100	5 of 9	0 of 9	0 of 8	0 of 10	*100*	6 of 10	2 of 10	0 of 8	0 of 7
10	0 of 8	0 of 8	0 of 9	0 of 7	*10*	3 of 10	1 of 10	0 of 10	0 of 8
TPC Freq.	1 in 140	1 in 3561	NA	NA	*TPC Freq.*	1 in 81	1 in 477	NA	NA
95% CI	59-329	872-13740	NA	NA	*95% CI*	40-165	201-1129	NA	NA
kRAS^{G12D} Tumor #2					***kRAS^{G12D} + mylpfa:myf5 Tumor #2***				
Cell #	G^+	G^+R^+	R^+	*DN*	Cell #	G^+	G^+R^+	R^+	*DN*
1000	6 of 6	0 of 6	0 of 6	0 of 6	*1000*	2 of 3	1 of 2	0 of 7	0 of 7
100	4 of 7	2 of 10	0 of 10	0 of 10	*100*	1 of 6	3 of 6	0 of 7	0 of 10
10	1 of 8	0 of 9	0 of 10	0 of 8	*10*	0 of 8	0 of 9	0 of 10	0 of 8
TPC Freq.	1 in 109	1 in 3495	NA	NA	*TPC Freq.*	1 in 809	1 in 467	NA	NA
95% CI	44-270	808-15120	NA	NA	*95% CI*	244-2685	137-1589	NA	NA
kRAS^{G12D} Tumor #3					***kRAS^{G12D} + mylpfa:myf5 Tumor #3***				
Cell #	G^+	G^+R^+	R^+	*DN*	Cell #	G^+	G^+R^+	R^+	*DN*
1000	2 of 3	0 of 2	0 of 3	0 of 4	*1000*	2 of 3	3 of 5	0 of 3	0 of 3
100	8 of 9	0 of 8	0 of 8	1 of 8	*100*	3 of 10	1 of 10	0 of 9	0 of 10
10	1 of 8	0 of 9	0 of 9	0 of 9	*10*	0 of 10	0 of 10	0 of 10	0 of 10
TPC Freq.	1 in 159	NA	NA	1 in 4840	*TPC Freq.*	1 in 530	1 in 1080	NA	NA
95% CI	63-401	NA	NA	632-37094	*95% CI*	194-1445	395-2957	NA	NA

Cumulative TPC frequency kRASG12D					***Cumulative TPC frequency kRAS^{G12D} + mylpfa:myf5***				
Cell #	G^+	G^+R^+	R^+	*DN*	Cell #	G^+	G^+R^+	R^+	*DN*
TPC Freq.	1 in 146	1 in 4206	NA	NA	*TPC Freq.*	1 in 377	1 in 639*	NA	NA
95% CI	87-245	1550-11409	NA	NA	*95% CI*	212-670	363-1125	NA	NA

Table 1. Limiting dilution cell transplantation shows that forced *myf5* expression confers tumor-propagating ability to *myf5-GFP+/mylpfa-mCherry+* cells. Engrafted animals per cell dose are noted. Experiments for three independent primary-derived tumors are shown. G+ (*myf5-GFP+/mylpfa-mCherry-)*, G+R+ (*myf5-GFP+/mylpfa-mCherry+)*, R+ (*myf5-GFP-/mylpfa-mCherry+)*, DN (*myf5-GFP-/mylpfa-mCherry-)*. Not applicable (NA); tumor-propagating cell frequency (TPC Freq.); 95% confidence interval (95% CI). Lower panel denotes cumulative TPC frequency for all three ERMS analyzed per genotype. Asterisk denotes p=0.0002 by ELDA analysis.

Figure Legends

Figure 1. Forced Myf5 expression in myosin-expressing ERMS cells elevates tumor cell differentiation, increases tumor size, and accelerates time to primary tumor-onset. (A-F) Histological analysis of primary ERMS developing in *myf5-GFP/mylpfa-mCherry* AB-strain zebrafish. Transgenic *kRASG12D*-expressing ERMS (A-C) compared with those that express both *kRASG12* and *mylpfa:myf5* (D-F). Animals imaged at 35 dpf (A,D). H&E-stained sections of representative tumors (B,E) and quantification of differentiation within individual tumors (C,F; 1-less differentiated and 3-most differentiated). Asterisk denotes p=0.015 by Chi square test. (G) Quantitative real-time PCR gene expression performed on bulk ERMS cells, confirming high *myf5* expression, increased differentiation, and high expression of self-renewal associated genes in ERMS that co-express *kRASG12D* and *mylpfa:myf5* (K+M). *kRASG12D* alone expressing ERMS (K). Average gene expression with 50% confidence intervals denoted by box, respectively (Mean, maximum, and minimum denoted). (H) Relative tumor size of primary ERMS at 30 dpf (Mean, maximum, and minimum denoted). Box shows 50% confidence interval. Asterisk denotes p=0.0108, Student's t-test. (I) Kaplan-Meijer analysis denoting time-to-tumor onset ($p<0.0001$, Log-rank Statistic, n=494 fish analyzed for K and n=470 for K+M). Scale bars: 2mm (A,D) and 50 μm (B,E). Asterisks in panels G-H denote *, $p<0.05$ and **, $p<0.01$ by Student's t-test.

Figure 2. Tumors with forced *Myf5* expression are fully transformed and retain a differentiated phenotype following engraftment into recipient animals. (A-F) Histological analysis of transplanted fish. *kRASG12D* expressing ERMS arising in *rag2*^{E450fs} transplant recipient fish (A-C) compared with those that express both *kRASG12* and *mylpfa-myf5* (D-F). Tumors were created in stable transgenic *myf5-GFP/mylpfa-mCherry* transgenic, AB-strain zebrafish and imaged following engraftment into recipient fish at 30 days post injection. H&E-stained sections of representative tumors (B,E) and quantification of differentiation within individual ERMS (C,F; 1-less differentiated and 3-most differentiated). Asterisk denotes $p<0.001$ by Chi square test. (G,H) Representative flow cytometric analysis of fluorescent-labeled ERMS cells isolated from transplanted *rag2*^{E450fs} zebrafish. (I) Graphical summary of ERMS cell subfractions that grow following engraftment into immune-deficient *rag2E450fs* mutant. Individual tumors are represented as separate bars with the proportion of G+ (green), G+R+ (yellow) and R+ (red) sub-populations denoted. (J) Kaplan-Meijer analysis showing time-to-tumor onset in transplanted ERMS arising in *rag2*^{E450fs} zebrafish ($p = 0.046$, Log-rank Statistic, $2x10^5$ cells/fish, $n>12$ animals per arm, representing ≥3 independently arising primary ERMS). (K) Relative tumor size at 30 days post engraftment (same animals analyzed as in J). (L) Similar results were obtained following engraftment of *myf5-GFP/mylpfa-mCherry* ERMS cells into syngeneic recipient fish (compare I to L, $p<0.0001$, Student's T-test, n> ≥3 independently arising primary ERMS and assessed in ≥2 animals per transplanted tumor). Scale bars equal 2mm (A,D) and 50 μm (B,E). *, $p<0.05$; **, $p<0.01$; ***, $p<0.001$ by Student's t-test.

Figure 3. Limiting dilution cell transplantation shows that forced *myf5* expression confers tumor-propagating ability to differentiated *myf5-GFP+/mylpfa-mCherry+* cells. Tumors were generated in *myf5/mylpfa-mCherry* CG1-stain syngeneic zebrafish. Representative tumors arising in primary transplanted fish (A-C) or following engraftment with highly purified *myf5*-GFP+, *mylpfa*-mCherry-negative (D-F) or *myf5*-GFP+, *mylpfa*-mCherry+ ERMS cells (G-I). Sort purity following FACS was >92% and is denoted in panels D and G. Cell viability was >95%. (J,K) Graphical summary of tumor engraftment following limiting dilution cell transplantation using highly purified sorted ERMS cells. Data is combined from all tumors shown in Table 1. ***, $p<0.0002$ by ELDA analysis. (L,M) Gene expression analysis of sorted G+ or G+R+ ERMS cells from representative $kRAS^{G12D}$ (L) or $kRAS^{G12D}$*; mylpfa-myf5* (M) expressing ERMS (SD, n=3 technical replicates per tumor). Asterisks denote **, $p<0.01$ and ***, $p<0.001$ by Student's t-test.

Figure 4. MYF5 and MYOD are required for human ERMS proliferation and growth. (A-B) Pearson correlation for gene co-expression in primary human RMS as assessed by microarray (A) or RNA-sequencing (B). (C) Western blot analysis for human RMS cell lines. (D-I) Rh18 ERMS cells following MYF5 knockdown with siRNA (D-F) or shRNA (G-I). (J-O) RD ERMS cells following MYOD knockdown with siRNA (J-L) or shRNA (M-O). Western blot analysis following knockdown at 72h (D,J) and 96h (G,M). EDU and Propidium Iodide (PI) cell cycle analysis assessed by flow cytometry at 48h (E,K) and 72h (H,N). Viability as assessed by manual nuclei counts of NucBlue+ cells at 72 hours (F,L) or 96 hours (I,O). Standard deviation denoted

in FACS plots and viability graphs. *, $p<0.05$; **, $p<0.01$; ***, $p<0.001$ by Student's t-test.

Figure 5. MYF5 is required for human ERMS growth and maintenance in xenograft transplants. (A) Western blot analysis following control and MYF5 shRNA knockdown in Rh18 cells. The percentage of MYF5 protein remaining following 48 hours of knockdown is noted. (B) Luciferase bioluminescent imaging of engrafted tumor cells following implantation into the flanks of *NOD/SCID/IL2g* null mice. Three representative animals are shown at each time point of analysis at day 0 (d0) and day 62 (d62). Control shRNA cells implanted into left flank and MYF5 knockdown into the right (N=6 mice per shRNA). Intensity represents total luminescence units measured per region of interest (L.U.) (C) Quantification of tumor volume from 0 and 62 days post implantation. Standard error of the mean. **, $p<0.01$ by Student's t-test.

Figure 1.

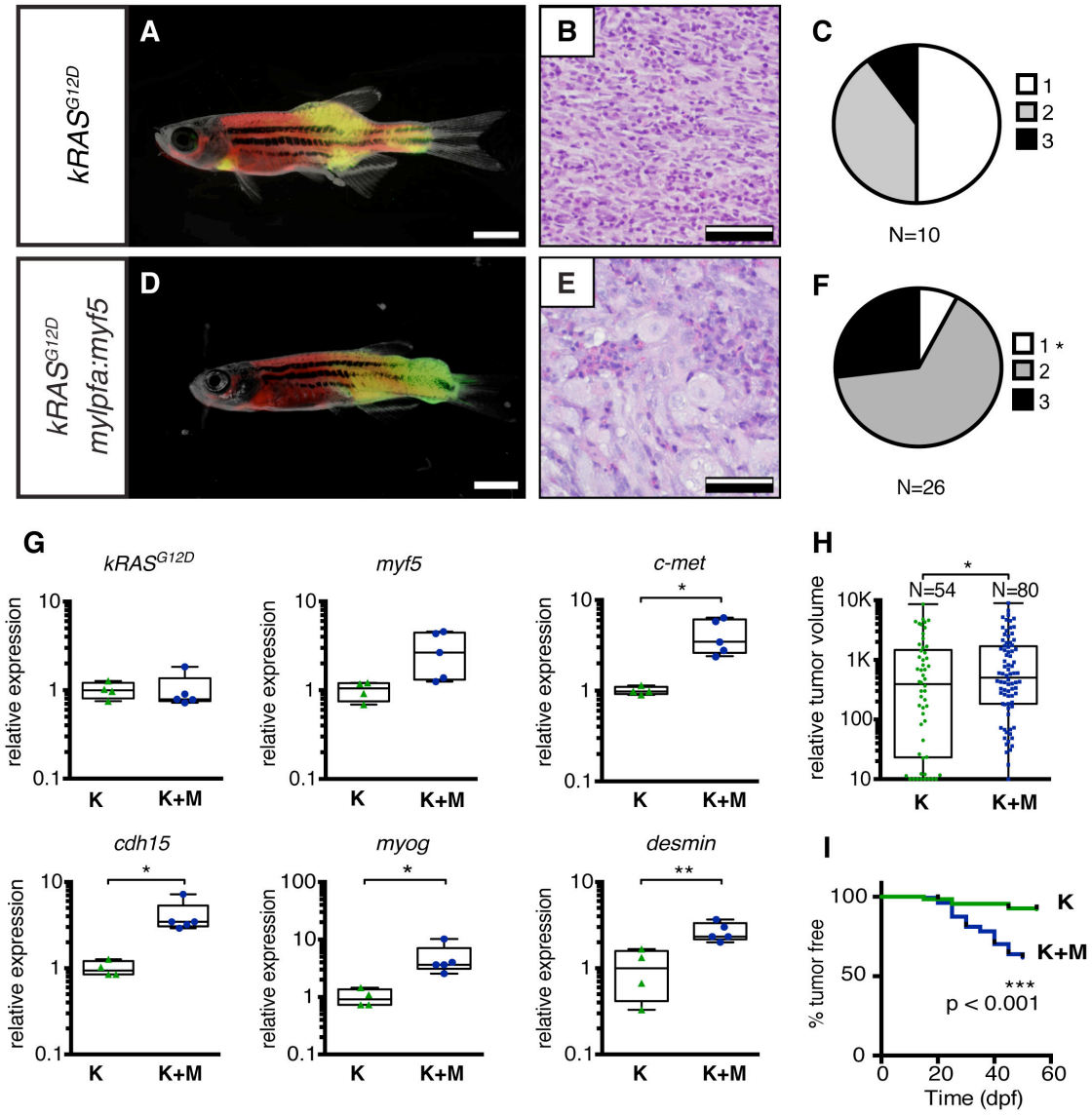
A
kRASG12D
B
C
1
2
3
N=10
D
kRASG12D
mylpfa:myf5
E
F
1 *
2
3
N=26
G
kRASG12D
myf5
c-met
cdh15
myog
desmin
relative expression
K
K+M
H
relative tumor volume
N=54
N=80
10K
1K
100
10
I
% tumor free
Time (dpf)
p < 0.001

Figure 2.

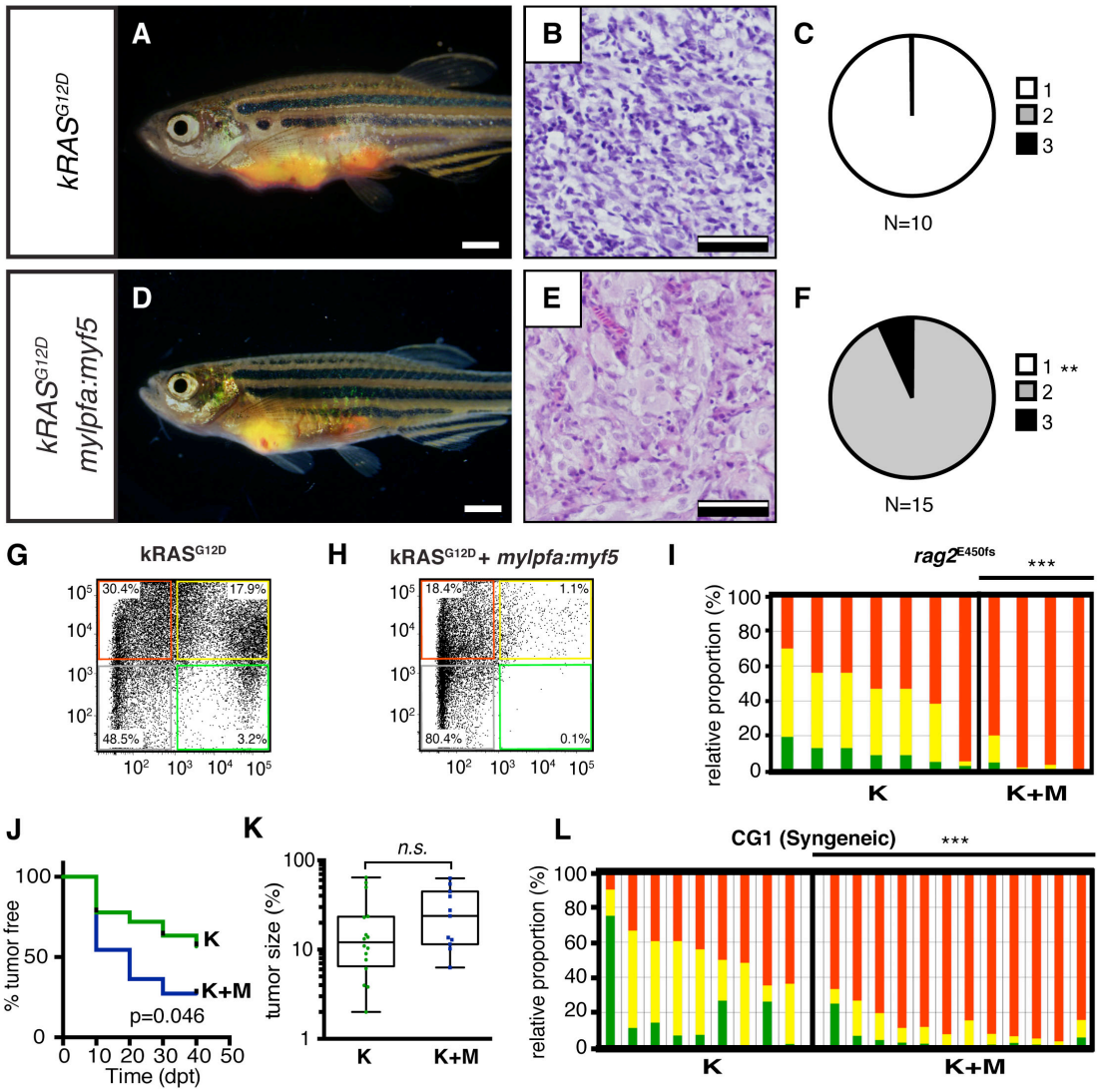
kRASG12D
A
B
C
1
2
3
N=10
kRASG12D mylpfa:myf5
D
E
F
1 **
2
3
N=15
G
kRASG12D
30.4%
17.9%
48.5%
3.2%
H
kRASG12D+ mylpfa:myf5
18.4%
1.1%
80.4%
0.1%
I
rag2E450fs
***
relative proportion (%)
K
K+M
J
% tumor free
K
K+M
p=0.046
Time (dpt)
K
n.s.
tumor size (%)
K
K+M
L
CG1 (Syngeneic)
***
relative proportion (%)
K
K+M

Figure 3.

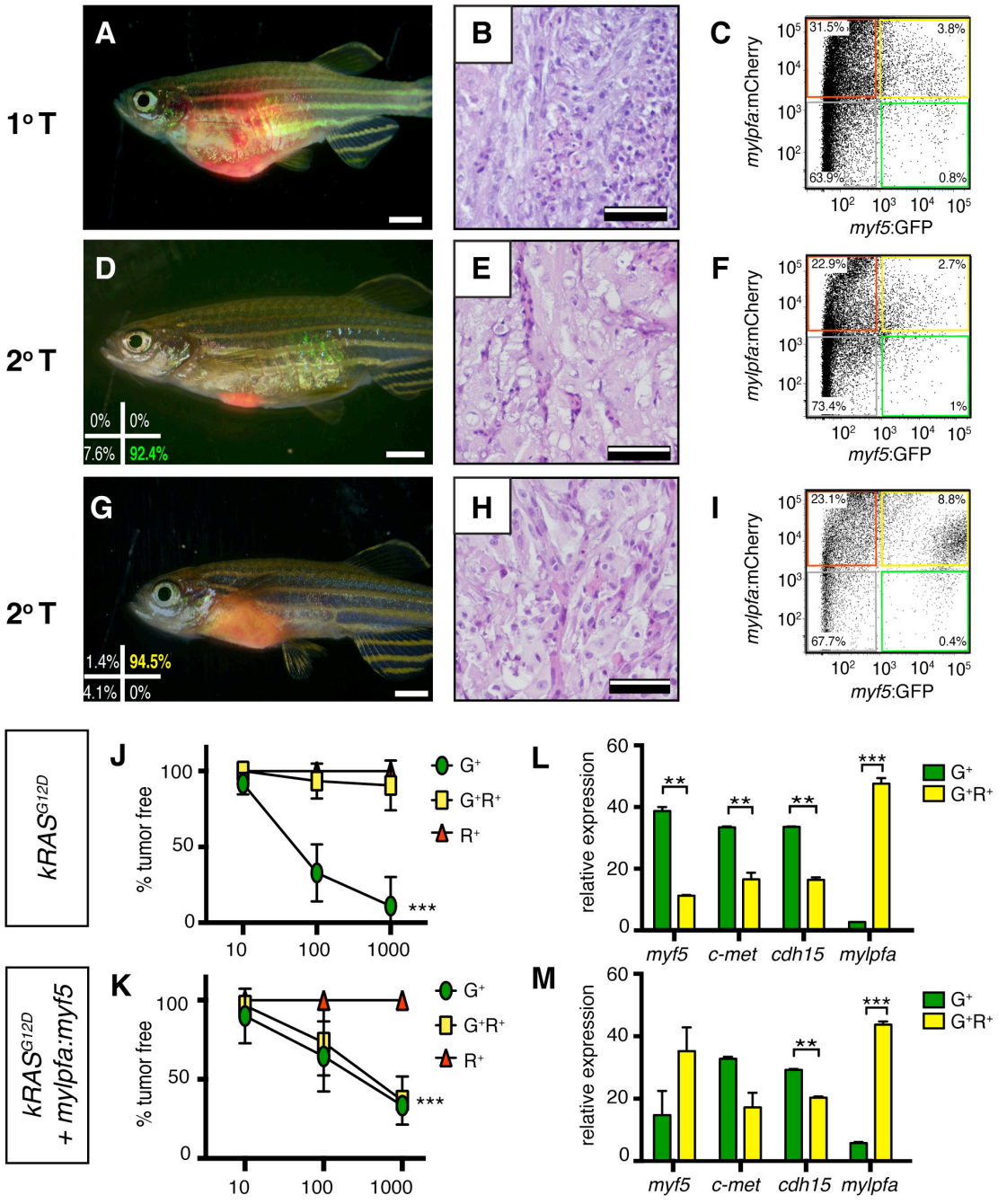
1° T
2° T
2° T
A
B
C
D
E
F
G
H
I
0%
0%
7.6%
92.4%
1.4%
94.5%
4.1%
0%
31.5%
3.8%
63.9%
0.8%
22.9%
2.7%
73.4%
1%
23.1%
8.8%
67.7%
0.4%
mylpfa:mCherry
myf5:GFP
kRASG12D
kRASG12D + mylpfa:myf5
J
K
% tumor free
G+
G+R+
R+
***
L
M
relative expression
myf5
c-met
cdh15
mylpfa
**
***

Figure 4.

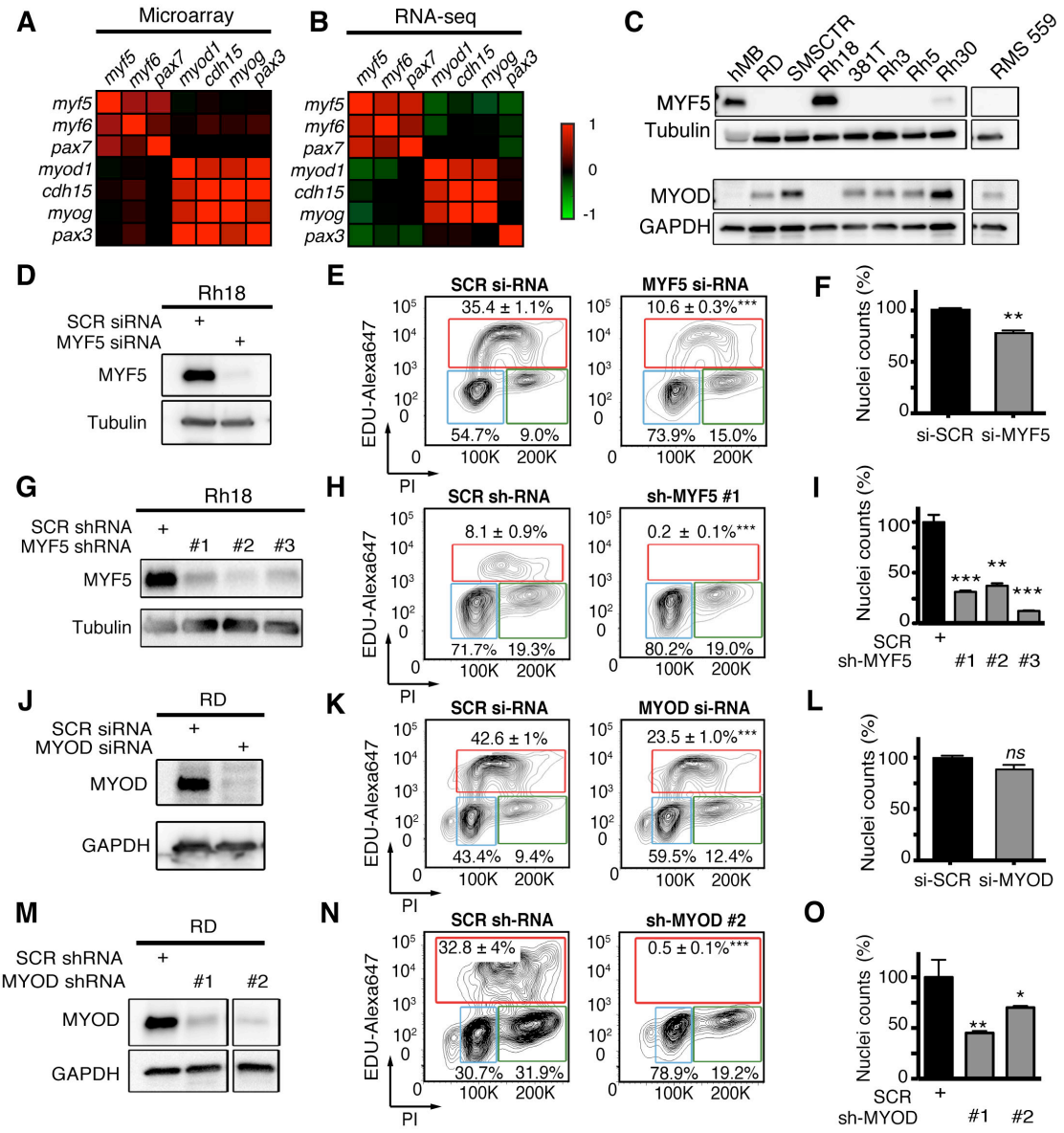
A
Microarray
myf5
myf6
pax7
myod1
cdh15
myog
pax3
B
RNA-seq
1
0
-1
C
hMB
RD
SMSCTR
Rh18
381T
Rh3
Rh5
Rh30
RMS 559
MYF5
Tubulin
MYOD
GAPDH
D
Rh18
SCR siRNA
MYF5 siRNA
E
SCR si-RNA
MYF5 si-RNA
35.4 ± 1.1%
10.6 ± 0.3%***
54.7%
9.0%
73.9%
15.0%
EDU-Alexa647
PI
F
Nuclei counts (%)
si-SCR
si-MYF5
G
Rh18
SCR shRNA
MYF5 shRNA
#1
#2
#3
H
SCR sh-RNA
sh-MYF5 #1
8.1 ± 0.9%
0.2 ± 0.1%***
71.7%
19.3%
80.2%
19.0%
I
sh-MYF5
J
RD
SCR siRNA
MYOD siRNA
K
SCR si-RNA
MYOD si-RNA
42.6 ± 1%
23.5 ± 1.0%***
43.4%
9.4%
59.5%
12.4%
L
si-MYOD
M
RD
SCR shRNA
MYOD shRNA
N
SCR sh-RNA
sh-MYOD #2
32.8 ± 4%
0.5 ± 0.1%***
30.7%
31.9%
78.9%
19.2%
O
sh-MYOD

Figure 5.

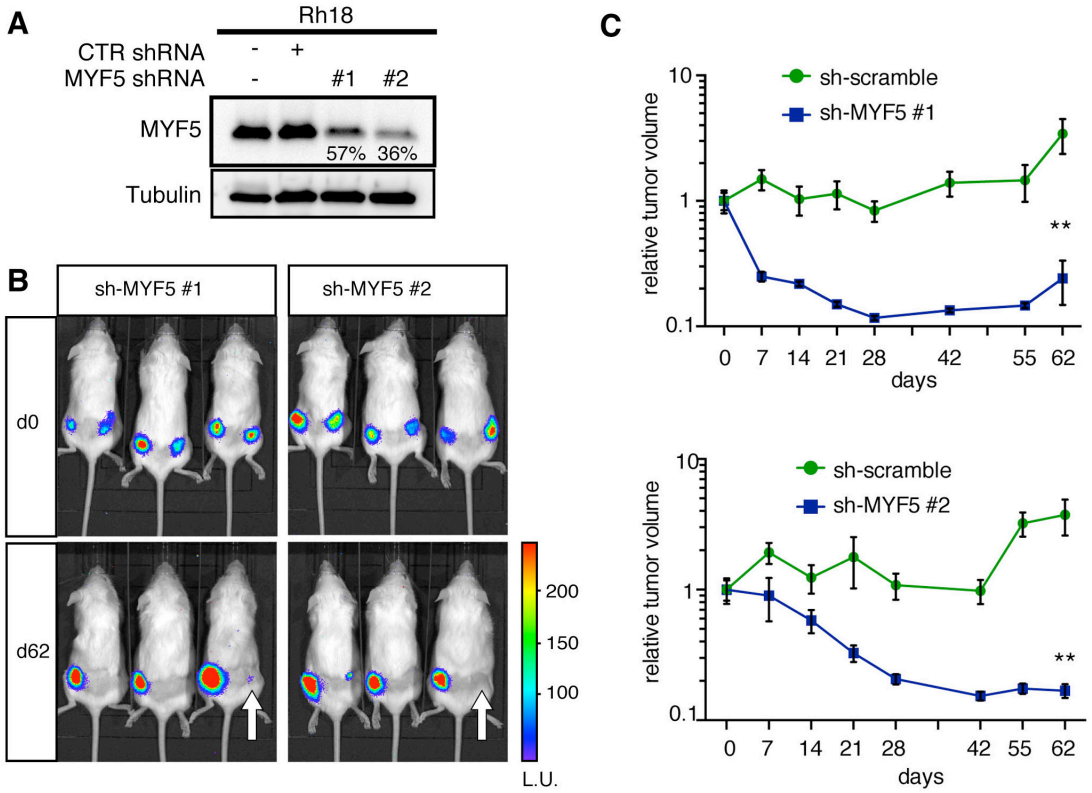
A
Rh18
CTR shRNA - +
MYF5 shRNA - #1 #2
MYF5
57% 36%
Tubulin
B
sh-MYF5 #1
sh-MYF5 #2
d0
d62
200
150
100
L.U.
C
sh-scramble
sh-MYF5 #1
relative tumor volume
10
1
0.1
**
0 7 14 21 28 42 55 62
days
sh-scramble
sh-MYF5 #2
relative tumor volume
10
1
0.1
**
0 7 14 21 28 42 55 62
days

Myogenic regulatory transcription factors regulate self-renewal and growth in embryonal rhabdomyosarcoma

Inês M. Tenente[1,2,3], Myron S. Ignatius[1,2], Karin McCarthy[1,2], Marielle Yohe[4], Sivasish Sindiri[4], Madeline Hayes[1,2], Berkley Gryder[4], Ashwin Ramakrishnan[1,2], Qin Tang[1,2], Eleanor Chen[5], G. Petur Nielsen[6], Javed Khan[4], David M. Langenau[1,2]

[1] Molecular Pathology, Cancer Center, and Regenerative Medicine, Massachusetts General Hospital, Boston, MA 02129, USA

[2] Harvard Stem Cell Institute, Cambridge, MA 02139, USA

[3] GABBA, Abel Salazar Biomedical Sciences Institute, University of Porto, Porto, 4099-003, Portugal

[4] Oncogenomics Section, Pediatric Oncology Branch, Advanced Technology Center, National Cancer Institute, Gaithersburg, MD 20877, USA

[5] Department of Pathology, University of Washington, Seattle, WA 98195, USA

[6] Department of Pathology, Massachusetts General Hospital, Boston, MA 02129, USA

*Corresponding Author: dlangenau@mgh.harvard.edu

INVENTORY OF SUPPLEMENTAL INFORMATION

Supplemental Figure and Table Legends

Supplemental Figure S1. Histological classification of zebrafish ERMS based on differentiation score. *This supplemental figure relates to Figures 1 and 2 and Supplemental Figure S3*. Representative H&E-stained sections of zebrafish ERMS assigned to each differentiation category. Primary RMS (A) and transplanted RMS (B). Scale bars, 100 μm.

Supplemental Figure S2. Immunohistochemistry analysis of proliferation and apoptosis in zebrafish primary ERMS. *This supplemental figure relates to Figure 1*. (A) Representative H&E-stained sections and immunohistochemistry for phospho-H3 (pH3) and cleaved caspase-3 (CC3). (B) Quantification of the total number of pH3-positive cells per 400x imaging field (n=average of 3 fields/tumor section). (C) Quantification of the total number of CC3-positive cells per 400x imaging field (n=average of 3 fields/tumor section). Boxes in B-C denote 50% confidence interval and mean, maximum, and minimum shown. *kRASG12D* [K] (N=5) and *kRAS^{G12D}; mylpfa:myf5* [K+M] (N=11). Scale bars, 100 μm (A). Not significant by Student's t-test (n.s.).

Supplemental Figure S3. Analysis of transplanted ERMS arising from *myf5-GFP/mylpfa-mCherry* transgenic, CG1-strain syngeneic zebrafish with forced *Myf5* expression. *This supplemental figure relates to Figures 2 and 3*. (A,D) Representative images of transplanted fish. ERMS were created in *myf5-GFP/mylpfa-mCherry*

transgenic, CG1-strain syngeneic zebrafish and imaged following 30 days of engraftment. (B,E) Representative histology of transplanted tumors. (C,F) Quantification of differentiation based on histological review (1-less differentiated and 3-most differentiated). **, $p<0.01$ by Chi-square test. (G-P) Representative examples of sort purity following FACS for cells used in limiting dilution cell transplantation experiments. (G-K) *kRASG12D*-alone expressing ERMS (data shown in main Figure 3J). (L-P) *kRASG12D* + *mylpfa:myf5* expressing ERMS (shown in Figure 3A-C). Sort purity following FACS shown in H-K and M-P. Scale bars equal 2mm (A,D) and 100μm (B,E).

Supplemental Figure S4. Pearson correlation of gene expression from RNA sequencing data of primary human RMS. *This supplemental figure relates to Figure 4.* (A) Analysis of RNA-sequencing data from primary ERMS (FN-RMS, N=70) and (B) fusion-positive ARMS (FP-RMS; N=33 samples).

Supplemental Figure S5. Immunofluorescence for MYF5 and MYOD in Rh18 and RD ERMS cell lines. *This supplemental figure relates to Figure 4.* (A) Confocal microscopy images of DAPI and antibody immunofluorescence-staining of Rh18 cells treated with control siRNA or si-MYF5 for 72 hours. (B) Confocal microscopy images of DAPI and antibody immunofluorescence-staining of RD cells treated with control siRNA or si-MYOD. Anti-MYOD (green) and anti-MYF5 (red) and counterstained with DAPI (blue). Merged image shown to right. Scale bar equals 100 μm. Arrows denote representative examples of MYF5+/MYOD-negative RH18 cells in A and MYF5-negative/MYOD+ RD cells in B.

Supplemental Figure S6. MYF5 and MYOD bind common promoter and enhancer regions and are predicted to regulate genes involved in muscle development and cell cycle. *This supplemental figure relates to text in Results*. (A) ChIP-seq identified genomic locations bound by MYOD in RD cells, MYF5 in RH18 cell, and H3K27 acetylation (H3K27ac). Common binding sites are denoted by boxed region at the top, with 86% of binding sites being found in enhancer regions (right panels). (B) GREAT gene ontology enrichment from regions bound by both MYOD in RD cells and MYF5 in RH18 cells. GO Biological Processes, GO Cellular Component predictions, and p-values denoted. (C) Signal tracks of ChIP-seq and RNA-seq surrounding MYOG (top) and CCND1 (bottom). Numbers to the right of each track indicate reads per million mapped reads.

Supplemental Figure S7. MYF5 and MYOD are required for human RMS proliferation and growth *in vitro*. *This supplemental figure relates to Figure 4 and text in Results*. (A-D) Rh18 ERMS cells following MYF5 knockdown with shRNA (A,B,D) or siRNA (C). (E-G) RD ERMS cells following MYOD knockdown with shRNA (E-F) or siRNA (G). (H-S) siRNA knockdown of MYOD completed in additional RMS cell lines. (H-K) 381T ERMS; (L-O) RMS559 ERMS; (P-S) Rh3 ARMS/FP-RMS cells. All analysis was completed at 72 hours after infection, with exception to I,J,M,N,Q, and R which were completed at 48 hours. Standard deviation is noted in bar graphs. *, $p<0.05$; **, $p<0.01$; ***, $p<0.001$, $p<0.0001$ by Student's t-test. Not significant (n.s.)

Supplemental Figure S8: MYF5 is required for human ERMS growth and maintenance following xenograft transplantation into *NOD/SCID/IL2g* null mice. *This supplemental figure relates to Figure 5*. (A) Luciferase bioluminescent imaging of representative animals shown at 0, 7, 14, 28, 55 and 62 days post-transplantation. Control shRNA cells were implanted into left flank and MYF5 knockdown into the right (white arrow). Intensity represents total luminescence units measured per region of interest (L.U.). (B,C) Quantification of tumor volume changes over time comparing sh-scramble vs. sh-MYF5 #1 (B) or sh-MYF5 #2 (C). N=6 animals per analysis. (D,E) Quantification of tumor volume at 0 and 62 days post implantation showing paired measurements of tumors arising in the same mouse over time. Standard error of the mean shown in B-C. **, $p<0.01$ by Student's t-test.

Supplemental Table 1. Primers and shRNA sequences.

Primer Name	Sequence (5'-3')
hKRAS-QRT-F	TTGATGGAGAAACCTGTCTCTTGG
hKRAS-QRT-R	CAAATACACAAAGAAAGCCCTCCC
zmyf5-QRT-F	CCAGACAGTCCAAACAACAGACC
zmyf5-QRT-R	TGAGCAAGCAGTGTGAGTAAGCG
zmyog-QRT-F	GTGGACAGCATAACGGGAACAG
zmyog-QRT-R	TCTGAAGGTAACGGTGAGTCGG
zcdh15-QRT-F	TGACATCCGAGACAACGTCTTTC
zcdh15-QRT-R	CACTGGGGCTCCTCAGAAAATC
zmylpfa-F	ACCGCAGAGGAGATGAAGAA
zmylpfa-R	TCCGTGTGTGATGACGTAGC
zdesmin-QRT-F	CGAGATTGACTCTCTCAAGGGCAC
zdesmin-QRT-R	GGGCGATAGTGTCCTGATAACCAC
zc-met-QRT-F	GTCATCCAGGTGGTGGTTTC
zc-met-QRT-R	CGTTGTGATGCTGTGGAGAC
z18s-QRT-1-F	TCGCTAGTTGGCATCGTTTATG
z18s-QRT-1-R	CGGAGGTTCGAAGACGATCA

sh-RNA	Target Sequence
pLKO.1-sh-hMYF5 #1	GCCACTTTATAAGAAAGTGTA
pLKO.1-sh-hMYF5 #2	GTCCTGATGTATCAAATGTAT
pLKO.1-sh-hMYF5 #3	CCCACCTCCAACTGCTCTGAT
pLKO.1-sh-hMYOD1 #1	CCTGTAAATAAGAGTTGCTTT
pLKO.1-sh-hMYOD1 #2	ACTTCTATGACGACCCGTGTT

Fig. S1

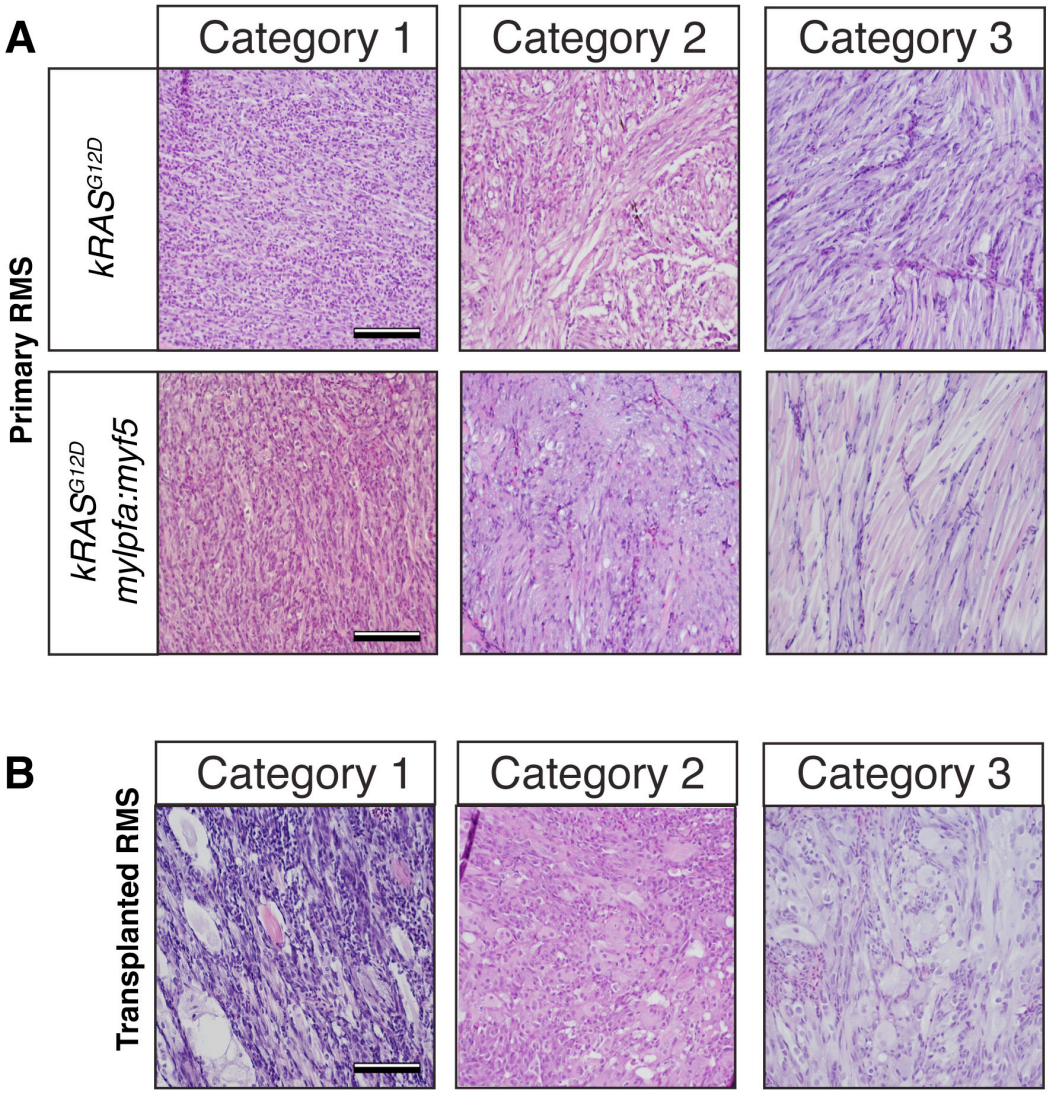
A
Category 1
Category 2
Category 3
Primary RMS
kRASG12D
kRASG12D
mylpfa:myf5
B
Category 1
Category 2
Category 3
Transplanted RMS

Fig. S2

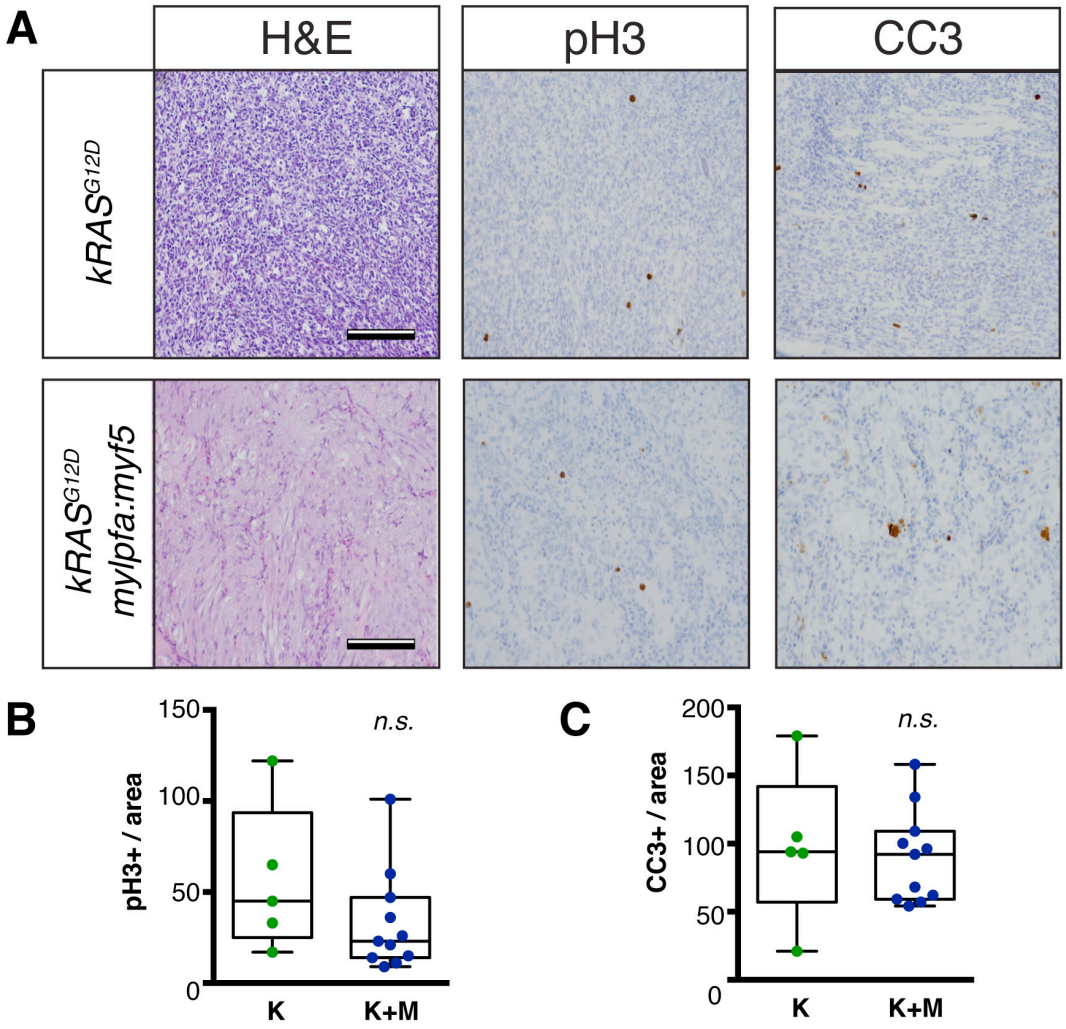
A
H&E
pH3
CC3
kRASG12D
kRASG12D mylpfa:myf5
B
pH3+ / area
150
100
50
0
n.s.
K
K+M
C
CC3+ / area
200
150
100
50
0
n.s.
K
K+M

Fig. S3

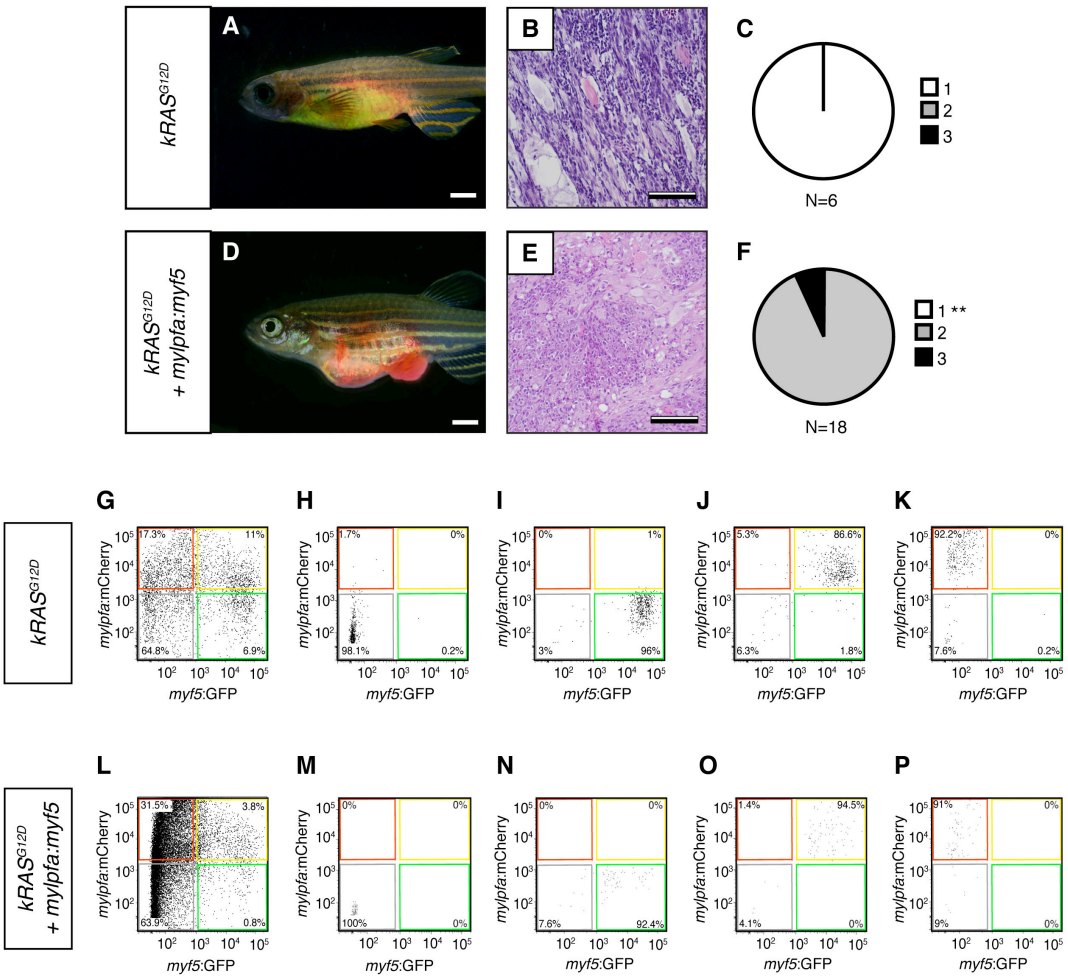
kRASG12D
A
B
C
1
2
3
N=6
kRASG12D + mylpfa:myf5
D
E
F
1 **
2
3
N=18
G
H
I
J
K
L
M
N
O
P
mylpfa:mCherry
myf5:GFP
17.3%
11%
64.8%
6.9%
1.7%
0%
98.1%
0.2%
0%
1%
3%
96%
5.3%
86.6%
6.3%
1.8%
92.2%
0%
17.6%
0.2%
31.5%
3.8%
63.9%
0.8%
0%
0%
100%
0%
0%
0%
7.6%
92.4%
1.4%
94.5%
4.1%
0%
91%
0%
9%
0%

Fig. S4

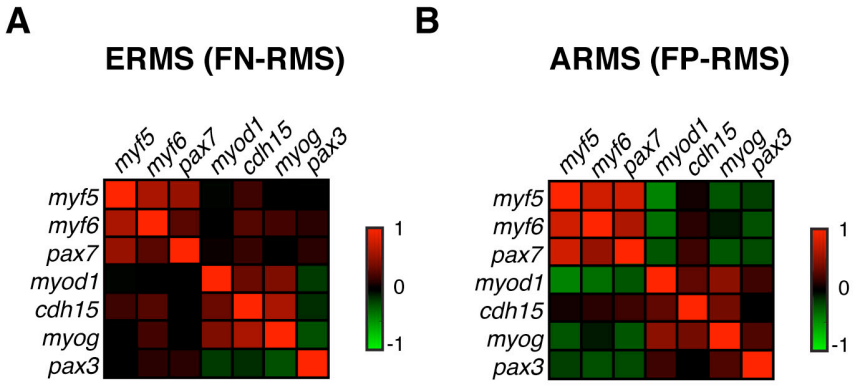
A
ERMS (FN-RMS)
B
ARMS (FP-RMS)
myf5
myf6
pax7
myod1
cdh15
myog
pax3
1
0
-1

Fig. S5

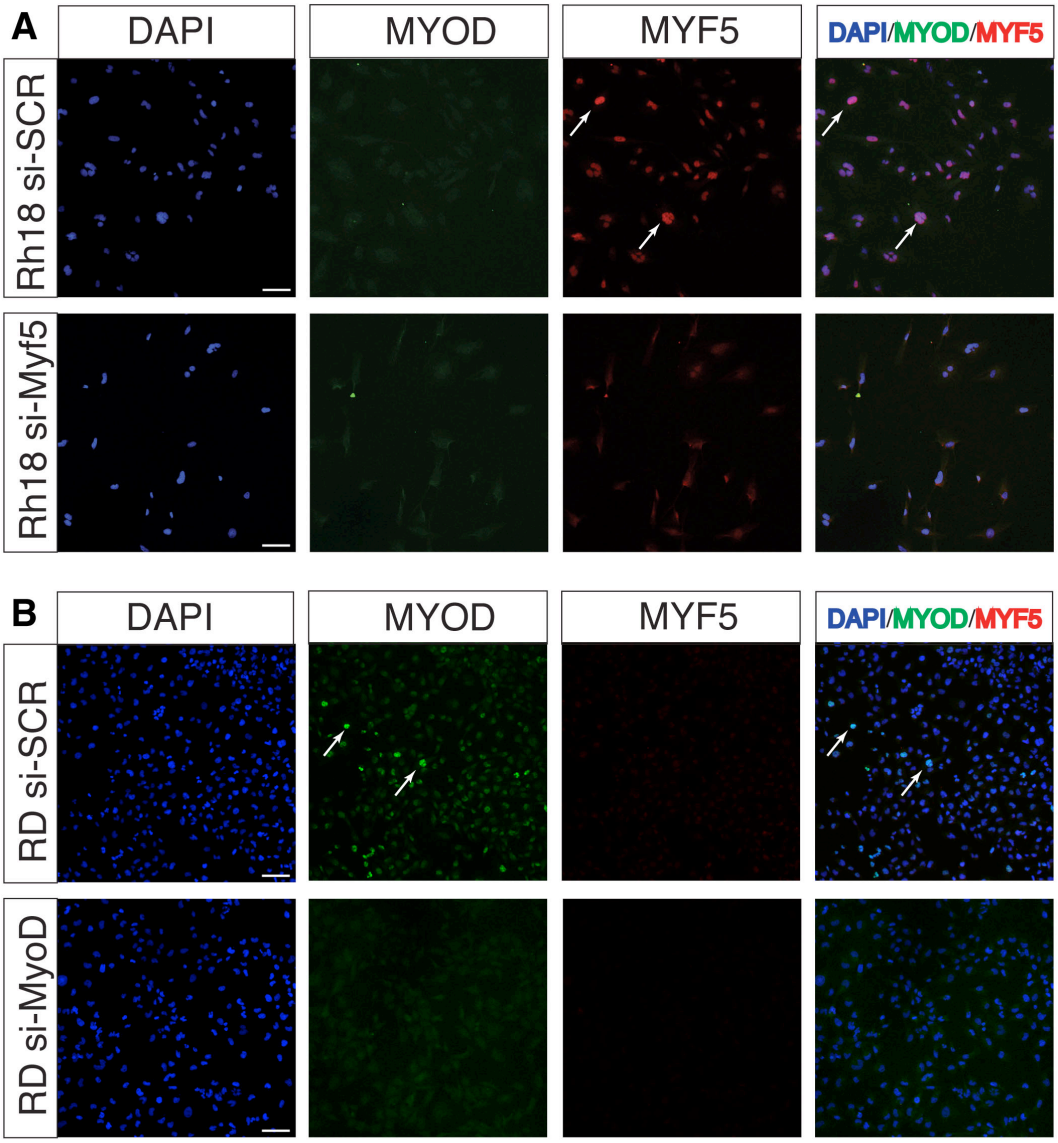
A
DAPI
MYOD
MYF5
DAPI/MYOD/MYF5
Rh18 si-SCR
Rh18 si-Myf5
B
DAPI
MYOD
MYF5
DAPI/MYOD/MYF5
RD si-SCR
RD si-MyoD

Fig. S6

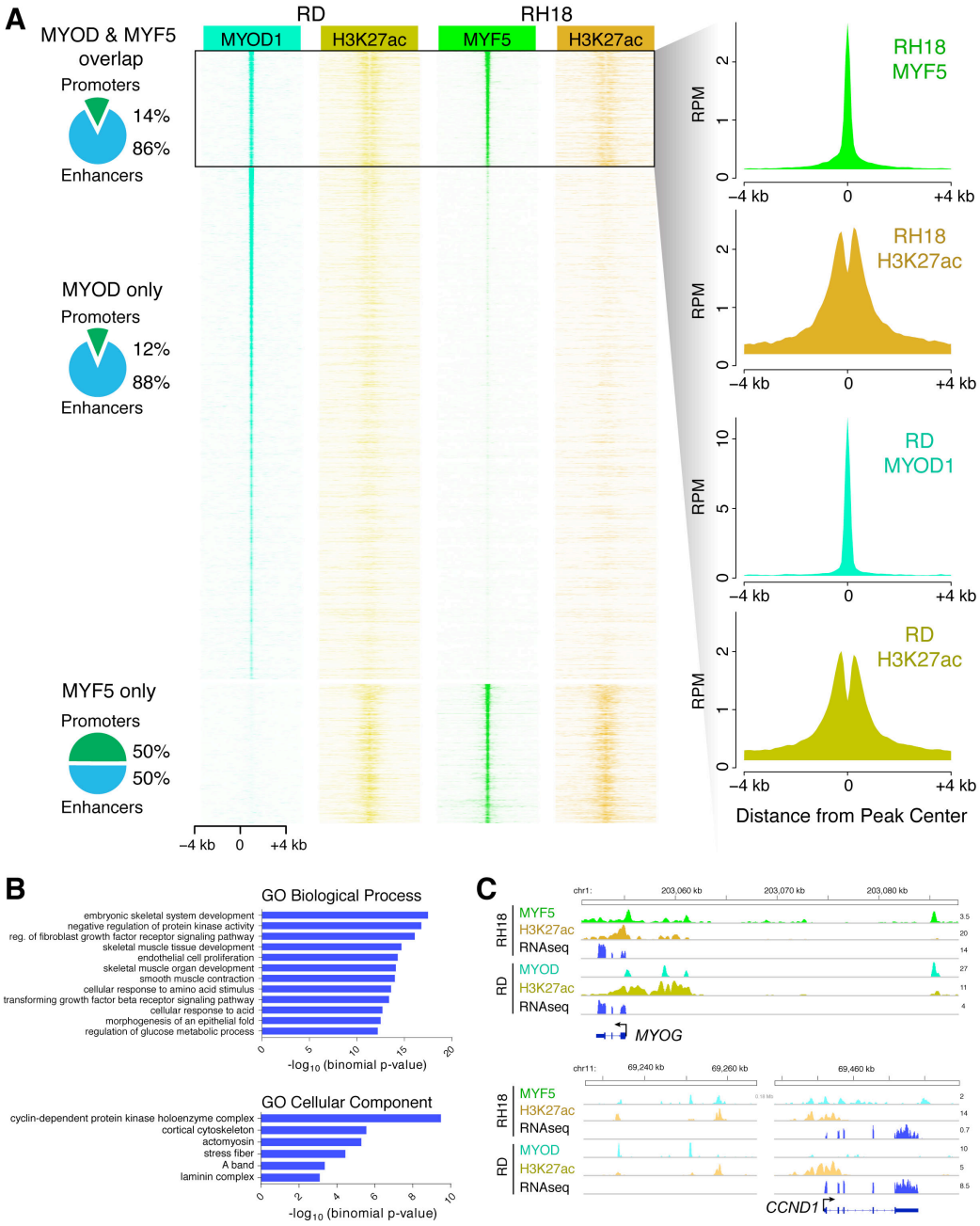
A
RD
RH18
MYOD1
H3K27ac
MYF5
H3K27ac
MYOD & MYF5 overlap
Promoters
14%
86%
Enhancers
MYOD only
Promoters
12%
88%
Enhancers
MYF5 only
Promoters
50%
50%
Enhancers
−4 kb
0
+4 kb
RPM
RH18 MYF5
RH18 H3K27ac
RD MYOD1
RD H3K27ac
Distance from Peak Center
B
GO Biological Process
embryonic skeletal system development
negative regulation of protein kinase activity
reg. of fibroblast growth factor receptor signaling pathway
skeletal muscle tissue development
endothelial cell proliferation
skeletal muscle organ development
smooth muscle contraction
cellular response to amino acid stimulus
transforming growth factor beta receptor signaling pathway
cellular response to acid
morphogenesis of an epithelial fold
regulation of glucose metabolic process
-log10 (binomial p-value)
GO Cellular Component
cyclin-dependent protein kinase holoenzyme complex
cortical cytoskeleton
actomyosin
stress fiber
A band
laminin complex
-log10 (binomial p-value)
C
chr1:
203,060 kb
203,070 kb
203,080 kb
RH18
MYF5
H3K27ac
RNAseq
RD
MYOD
H3K27ac
RNAseq
MYOG
chr11:
69,240 kb
69,260 kb
69,460 kb
CCND1

Fig. S7

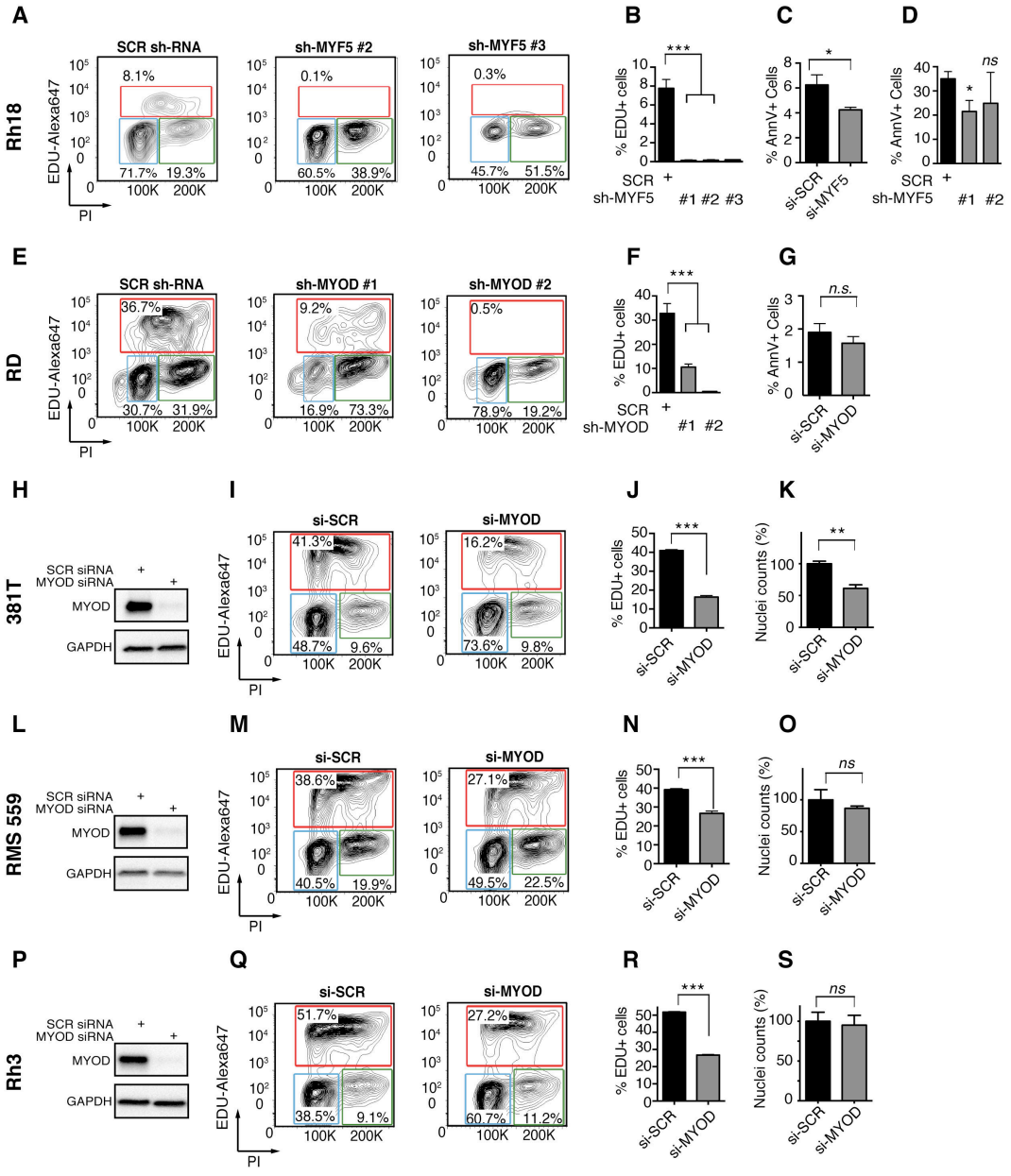
A
Rh18
SCR sh-RNA
sh-MYF5 #2
sh-MYF5 #3
EDU-Alexa647
PI
8.1%
71.7%
19.3%
0.1%
60.5%
38.9%
0.3%
45.7%
51.5%
100K
200K
B
% EDU+ cells
SCR +
sh-MYF5 #1 #2 #3
C
% AnnV+ Cells
si-SCR
si-MYF5
D
% AnnV+ Cells
SCR +
sh-MYF5 #1 #2
ns
E
RD
SCR sh-RNA
sh-MYOD #1
sh-MYOD #2
36.7%
30.7%
31.9%
9.2%
16.9%
73.3%
0.5%
78.9%
19.2%
F
% EDU+ cells
SCR +
sh-MYOD #1 #2
G
% AnnV+ Cells
n.s.
si-SCR
si-MYOD
H
381T
SCR siRNA
MYOD siRNA
MYOD
GAPDH
I
si-SCR
si-MYOD
41.3%
48.7%
9.6%
16.2%
73.6%
9.8%
J
% EDU+ cells
K
Nuclei counts (%)
L
RMS 559
M
38.6%
40.5%
19.9%
27.1%
49.5%
22.5%
N
O
P
Rh3
Q
51.7%
38.5%
9.1%
27.2%
60.7%
11.2%
R
S

Fig. S8

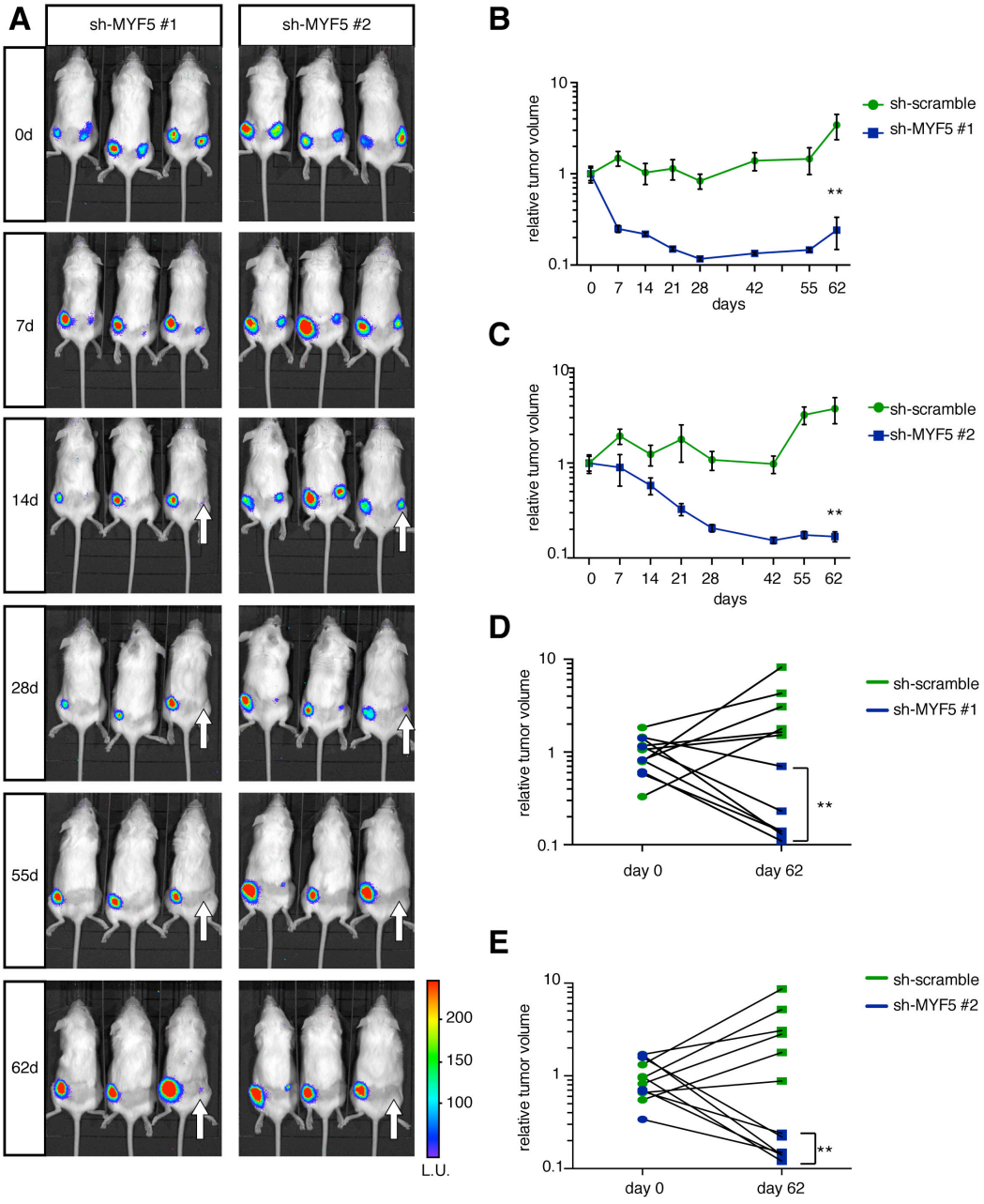
A
sh-MYF5 #1
sh-MYF5 #2
0d
7d
14d
28d
55d
62d
200
150
100
L.U.
B
relative tumor volume
10
1
0.1
0 7 14 21 28 42 55 62
days
sh-scramble
sh-MYF5 #1
**
C
relative tumor volume
10
1
0.1
0 7 14 21 28 42 55 62
days
sh-scramble
sh-MYF5 #2
**
D
relative tumor volume
10
1
0.1
day 0
day 62
sh-scramble
sh-MYF5 #1
**
E
relative tumor volume
10
1
0.1
day 0
day 62
sh-scramble
sh-MYF5 #2
**

5

Discussion, Conclusions and Future Directions

"Every discovery opens a new field for investigation of facts, shows us the imperfection of our theories. It has justly been said, that the greater the circle of light, the greater the boundary of darkness by which it is surrounded."

Sir Humphry Davy
The Collected Works of Sir Humphry Davy
(1840)

Rhabdomyosarcoma is a rare, predominantly pediatric cancer. The slow advancement in our understanding of this disease and in the development of innovative treatments thus comes from multiple branching factors: the lack of diverse and widely available *in vitro* and *in vivo* models and other specific research tools, the low number of patients that can be recruited into clinical trials, the scarcity of biopsied material for research and a generalized unawareness and lack of interest from the scientific, medical, pharmaceutical and general community and consequent lack of generalized expertise.

By the start of this study (2011-2012), the available mouse models of FN-RMS had several limitations that rendered its utilization for functionally studying the role of drivers and modifier genes difficult. These mouse models highlighted the role of the TP53 pathway in RMS initiation and suggested that RAS-pathway ac-

tivation could play a role. However, these required multiple genetic perturbations and complex genetic breeding and the tumors developed with long latency (Fleischmann et al., 2003; Nanni et al., 2003). Well established mouse models of FP-RMS were being employed (Keller and Capecchi, 2005; Keller et al., 2004a,b) , but the molecular basis of FN-RMS, being more complex than in FP-RMS PAX3- and PAX7-FOXO1, was still a matter of intense research and comprehensive whole-genome approaches had only recently been deployed in primary patient samples (Davicioni et al., 2006, 2009, 2010).

The prior report of a $KRAS^{G12D}$-driven zebrafish model by Langenau et al., 2007 undisputedly showed that RAS pathway activation is a potent oncogenic driver of tumors that morphologically and molecularly resemble ERMS. The emergence of the zebrafish ERMS model posited clear advantages. High penetrance (up to 40% of animals initiated tumors) and short latency (from 10d to 40d of age) allow for the study of hundreds of independently-generated and potentially genetically-diverse tumors, therefore providing a broad sample of heterogeneous tumor locations, aggressiveness or metastatic potential. Importantly, the zebrafish genome had a properly assembled version allowing for the employment of unbiased approaches (array or next-generation sequencing based). The facile mode of generation and the possibility to employ co-injection approaches to functionally assess oncogenic drivers of modifiers of disease, as well as labelling sub-populations with fluorescent protein transgenes (Langenau et al., 2008) further make it a powerful and attractive model to study the biological basis of this disease.

Since then, the field has benefited greatly from a concerted effort to further describe the molecular landscape of RMS (Chen et al., 2013; Shern et al., 2014), develop novel allograft or xenograft-based and genetic mouse models (reviewed in Kashi et al., 2015), critically assess and widely distribute cellular models (Hinson et al., 2013), and the utilization of these tools to address the main questions of the field:

- WHAT IS THE CELL OF ORIGIN OF RMS?
- ARE THERE COMMON MECHANISMS TO SARCOMAGENESIS?
- WHAT IS THE MOLECULAR BASIS OF FN-RMS TRANSFORMATION?
- CAN WE FURTHER DEFINE MOLECULAR SUBGROUPS WITHIN RMS WITH A DIFFERENTIAL BIOLOGICAL BASIS AND PROGNOSTIC VALUE?

- How can we devise a plethora of models in basic research and pre-clinical studies that accurately represents the intra- and inter-heterogeneity of RMS?
- Can we understand the mechanisms of RMS differentiation arrest so as to develop efficient Differentiation therapies?
- Can we understand and prevent relapsed disease in RMS?

The present study has implications in several of these unanswered questions, which are discussed in this Chapter.

5.1 Insights into intra-tumor heterogeneity, self-renewal and relapse

In order to assess self-renewal and differentiation potential of cancer cells, several functional assays can be deployed.

A combination of these methods has been used to assess RMS intra-tumor heterogeneity. These methods will be discussed below, in light of the observations here reported.

5.1.1 *In vitro* self-renewal assays

Self-renewing cells have been identified as CD133-expressing cells that are enriched in spheroid (rhabdosphere) cultures in serum-free media and sphere formation assays are now a standard assay to assess self-renewal effects *in vitro* (Walter et al., 2011). Despite being a valuable tool, it is an artificial and indirect assay and results should be interpreted with caution. In an ideal setting, cells would be isolated directly from patient material and cultured in serum-free media with defined growth factors such as the one used by Walter et al., 2011. This media is supposed to maintain cells in a self-renewing state. Sphere cells can then be analyzed by sequencing methodologies and its gene expression compared to both freshly-isolated cells and cells cultured as adherent cultures in regular serum-media to identify self-renewal signatures of those tumors (similar to what has been reported for RMS (Walter et al., 2011) and other tumors (Suva et al., 2009, 2014)).

Additionally, self-renewal capacity of cells can be indirectly assessed by performing sphere-forming assays. It is my view that the most accurate method is

to use previously-generated spheroid cultures or primary-derived material, dissociate these into single cells and re-plate these cells as single cells or 1-5 fluorescently-labelled cell mixes into multi-well plates. The number of wells with formed spheres over the total number of cells plated thus acts as a surrogate for the frequency of these self-renewing cells in the original tumor or culture (Suva et al., 2014). Another assay that is more routinely used in the field is the assessment of self-renewal of established RMS cell lines growing as adherent cultures upon genetic or chemical perturbation. Cells are plated at different doses in separate wells and the media is then switched to the serum-free sphere media. The number of detaching colonies is counted as a surrogate for TPC-frequency (Belyea et al., 2011; Chen et al., 2014). There are several limitations with this approach: some established cell lines seem to be able to undergo this transition more readily than others, limiting the assay to those cell lines; the assay is very sensitive to external conditions, passage and conditions in which cells are grown prior the essay; the essay is more effective in scoring all-or-none effects or other cancer properties, such as the capacity of these cells to grow attached to the plastic; most importantly, spheres can represent clusters of cells formed by aggregation of cells rather than representing cell clusters originating from one single self-renewing cell (my observations).

Due to these limitations, I was not able to deploy these assays in the experiments described in Chapter 4. The MYF5-positive Rh18 cell line (Hinson et al., 2013) utilized in this study does not promptly form spheres through this method. I am however currently exploring self-renewal effects *in vitro* upon *knock-down* of MYOD1 in MYOD1-positive RD cell cultures, since this is the cell line that more promptly forms rhabdospheres (data not shown and (Chen et al., 2014)). Unfortunately, due to the scarcity of RMS cases, it is not possible for us to obtain primary-derived xenograft or fresh primary cells of RMS at this time.

5.1.2 *In vivo* imaging and lineage-tracing

In any case, what better way to understand how cells organize within a tumor, interact and cooperate in tumor maintenance and growth than to look inside and observe what is going on?

In the experiments described in Chapter 3, we were able to visualize the process of tumor initiation and several cellular behaviors of developing zebrafish RMS tumors. Specifically, RMS mononuclear cells arise at the extreme outer borders of myotome segments and move toward the midline and remain initially incapable to bypass the horizontal myosepta, a single cell layer that separates

myotome segments, until a subset of cells is able to cross this first barrier. Then, more differentiated, tumor-derived cells are able to further cross a collagenous barrier analogous to tendons in mammals (see Chapter 3, Figure 1). Other processes, such as muscle fiber break-down, neovascularization and intravasation were also observed at single cell resolution in this study (Ignatius et al., 2012).

Moreover, due to the more recent generation of *rag2*^{E450fs} immune-compromized zebrafish in an optically clear *Casper* zebrafish line (Tang et al., 2014, 2016; Tenente et al., 2014; White et al., 2008), these processes can now also be followed by live-imaging in a transplant setting, without the confounding fluorescence coming from non-tumor derived tissue and allowing for the observation of these events in greater detail, in more advanced stages of tumor development and in interaction with fully-matured skeletal muscle tissue. Using this line, we were able to visualize *myf5-GFP*-labelled TPCs and *mylpfa-lyn-Cyan*-labelled differentiated cells, showing that consistent with what was reported in Ignatius et al., 2012 in primary tumors, these sub-populations remain in regionally defined niches and are not anatomically confined by proximity to the vasculature (Tang et al., 2016) (see Appendix A).

The fact that TPCs are relatively rare in tumors, despite being the main contributers to tumor growth, led to long-standing questions in the Cancer field: *How aren't TPCs more frequent in tumors? Wouldn't the process of cancer evolution and selection promote the expansion of these cell types? Is there a role for non-self-renewing cell types within tumors?*

The regional compartmentalization of MYOG seems to be conserved as seen in human RMS IHC sections (Ignatius et al., 2012) and MYOG is associated with increased aggression in RMS (Heerema-McKenney et al., 2008). Our description of a division of labour within RMS cell populations, with more differentiated, MYOG-positive cells playing a role in invasion and intravasation, provides a correlational explanation for these questions, suggesting that differentiated RMS populations play a role in tumor development that is independent of self-renewal capacity.

Overall, these reports show that Rhabdomyosarcoma recapitulate the hierarchical organization of the normal muscle tissue counterpart. However, other aspects of intra-tumor heterogeneity, such as the issue of clonality, are important to address. Blackburn et al., 2014 have utilized a MYC-induced zebrafish model of T-cell Acute Lymphoblastic Leukemia (T-ALL) (Langenau et al., 2003) to understand questions of T-ALL clonality and evolution. Taking advantage of the fact that T cells express unique somatically-rearranged T-cell Receptors (TCRs) and that

T-ALL recapitulate an arrested early thymocyte stage (Langenau et al., 2003), polyclonal leukemias could be identified. Monoclonal leukemias from primary polyclonal tumors were derived by single cell transplantation into syngeneic animals and self-renewal and aggression was assessed at each step. Furthermore, aggression/ growth and self-renewal were not necessarily linked. Cell competition of fluorescently-labelled clones determined that winning clones are generally the mostly aggressive. Thus, zebrafish have proven to be a useful tool in dissecting properties of intra-tumor clonality and tumor evolution.

Other more sophisticated multi-colour labelling approaches, through Cre recombinase/lox transgenes, have been useful as lineage-tracing tools to assess questions of intra-tumor heterogeneity, self-renewal and clonality in mouse models of cancer and stem cell biology (Blanpain and Simons, 2013). *Zebrabow* zebrafish have also been generated and utilized in lineage tracing experiments during embryonic development and regeneration (Blackburn and Langenau, 2014; Pan et al., 2011, 2013).

Besides genomic studies that reported clonal mutations (Chen et al., 2015), the clonality issue has not been directly assessed in an animal model to date in Rhabdomyosarcoma. Experiments combining the zebrafish RMS model, the novel transplantation tools here mentioned and the *Zebrabow* lines could provide useful in further exploring these questions.

5.1.3 FACS and Limiting Dilution Transplantation assays

To assess Tumor Propagating Cell potential, different populations of tumor cells can be isolated by FACS and transplanted into recipient animals (immunodeficient or syngeneic). Transplanting cells at limiting dilution allows for estimating the relative frequency of TPCs by scoring the fraction of tumors generated by the dose of transplanted cells (Beck and Blanpain, 2013).

Not all tumors were shown to date to contain bona-fide TPCs and this had not been demonstrated in RMS. Our report in Ignatius et al., 2012 (see Chapter 3) identifies for the first time a *MYF5-GFP*-expressing sub-population that enriches for 1:100 TPC frequency.

5.1.4 Plasticity of intra-tumor cell states and implications for differentiation therapies

A report by Chen et al., 2014 demonstrated that the proportions of *myf5-GFP*-positive (G+), *myf5-GFP*-positive;*mylpfa-mCherry*-positive (G+R+), and *mylpfa-*

mCherry-positive (R+) cells within zebrafish RMS tumors is regulated by beta-catenin-dependent WNT signaling and impacts self-renewal ability.

In Chapter 4, we also provide evidence that self-renewal ability and proportions of tumor sub-populations can be disrupted. Aberrant MYF5 expression in G+R+ RMS cells confers self-renewal to this population of cells. These cells re-express genes associated with classically-described G+ cells (Ignatius et al., 2012) such as MET and Cadherin 15 (CDH15), while retaining features of more differentiated RMS cells such as the expression of MYOG and Myosin (MYLPF). This incomplete reprogramming is however sufficient to confer TPC-ability to G+R+ cells and does not impact time to tumor onset, penetrance and tumor growth in primary or secondary tumors.

The idea of differentiation therapy assumes that pushing cells toward a more differentiated cell state will reduce tumor aggressiveness and eliminate TPCs completely. Our study shows that aggressive and differentiated tumors can concomitantly display comparable self-renewal ability to control tumors. The blurring of the previously compartmentalized lines and roles of these sub-populations raises several questions, that remain here unaswered:

- ARE THE CELLULAR BEHAVIORS OF THESE TUMORS DIFFERENT FROM THE ONES DESCRIBED PREVIOUSLY?

This is the obvious impending question from the observations reported in Chapter 4. Similar experiment to the ones reported in Ignatius et al., 2012, including EdU-incorporation in primary and transplanted *myf5-GFP; mylpfa-mCherry* RMS zebrafish, transplantation intramuscularly into optically clear *rag2*^{E450fs} zebrafish for live imaging and metastasis assays, should provide useful in the near future. Additional results here unreported suggest that these tumors may evolve an ever-increased differentiation concomitant with increased metastasis, without compromising transplantation-ability. We speculate that continuous aberrant MYF5 expression in these cells leads to tumors that mimic a different, more aggressive, morphologically and molecularly different ERMS subset.

- WHAT ARE THE DOWNSTREAM EFFECTORS OF MYOGENIC FACTOR 5 (MYF5) THAT ARE RESPONSIBLE FOR CONFERRING TUMOR-PROPAGATING ABILITY TO THE NEW POPULATION OF TPCS?

In order to address both of these questions, the performance of an unbiased transcriptomic analysis of these tumors would be very useful, for example,

through RNA-seq. By sequencing the transcripts of sorted populations in MYF5-aberrantly-expressing tumors as compared to control tumor subsets one could identify direct targets that elicit self-renewal. The potential of this approach is that by comparing the genetic signature of previously-defined control-tumor G+ and G+R+ cells (Ignatius et al., 2012) with G+ and G+R+ in these new tumors, one could arrive at a core small signature of genes that could be targetable and prioritize them for further research studies. Given the low numbers of G+ and G+R+ cells in transplanted MYF5-aberrantly expressing tumors, this option is technically very challenging. In alternative, primary and secondary unsorted tumors in control and experimental groups could already provide useful insights.

5.2 Insights into inter-tumor heterogeneity and the cell-of-origin in RMS

As discussed in Section 1.3 of the General Introduction, the questions of RMS heterogeneity and the cell-of-origin seem to be intrinsically linked.

In its original report, the cell-of-origin of the zebrafish RMS model was identified as a *DsRed*-expressing mononuclear cell located in between skeletal muscle fibers (Langenau et al., 2007). Subsequently, we showed by *in vivo* imaging that the first cells to over-proliferate and emerge are *myf5-GFP*-positive cells located in the outer borders of myotome segments (see Chapter 3 and Ignatius et al., 2012).

Our current understanding of late larval skeletal muscle development is still lagging behind that of mammals. Zebrafish display a mode of continued growth which, contrary to mammals, means that their size is subjected to a sense of external factors such as food availability, and that their body continues to grow throughout life. While in mammals a muscle resident stem cell, the satellite cell, has been long described, it seems that different populations of progenitor muscle cells may exist in late larval (>10 dpf) and in the adult stages, the period when zebrafish RMS tumors initiate (Siegel et al., 2013). Our initial observation that tumors arise from the outer borders of myotome segments and our observation of the location (juxtaposed to muscle fibers) and the behavior of normal, non-malignant muscle *myf5-GFP* cells (Ignatius et al., 2012 and my unpublished observations), suggests therefore that the cell-of-origin of zebrafish RMS is a cell similar to a satellite cell resident in zebrafish skeletal muscle and/or a cell of the External Cell Layer (ECL). ECL cells reside in the periphery of the myotome, are actively proliferating and contribute to muscle growth, equivalent to the amniote

dermomyotome (Siegel et al., 2013). Interestingly, ECL cells express PAX7, while zebrafish ERMS do not generally express PAX7 to detectable levels (Ignatius et al., 2012). A possible explanation is that tumors arise from resident PAX7-positive cells and later loose this expression. An alternative hypothesis is that the ECL cell pool is heterogeneous, as was described in mouse satellite cells (reviewed in Chang and Rudnicki, 2014).

Analogous to what was reported in mouse models of RMS by Rubin et al., 2011, the question of the cell-of-origin was tackled in zebrafish by targeting oncogenic human $KRAS^{G12D}$ to*rag2*- , *cdh15*- or *mylpfa*-expressing cell types (Storer et al., 2013). Tumors that were derived by targeting to satellite cell or early-myoblast specific promoters, *rag2* and *cdh15*, had a lower differentiation degree than that of tumors derived from oncogene induction under a late differentiating myoblast promoter, *mylpfa*. Importantly, both this and our work showed that tumor-propagating activity was enriched in the *myf5*-expressing cell populations.

Additional data that is not here reported supports the notion that different cells of origin elicit different morphological, histological and pathological features in RMS. We injected *rag2-*$KRAS^{G12D}$ into a loss-of-function MYF5 mutant zebrafish line (*myf5hu2022*) (Hinits et al., 2009; Hinits et al., 2011) that was crossed into the stable *myf5-GFP* transgenic line (Chen et al., 2007). This experiment aimed at assessing if MYF5 is required for RMS initiation, given its role in eliciting self-renewal when targeted to differentiated zebrafish RMS cells. Due to reduced viability of homozygous zebrafish, I developed a careful rearing and genotyping protocol that allowed for homozygous zebrafish to reach 10 to 30 dpf in order to observe tumor initiation. This was consistent with a recent report that loss of viability is due to aberrant esophageal muscle development (Minchin et al., 2013). To our initial surprise, homozygous mutant*myf5*-negative zebrafish initiated tumors, labelled with *myf5-GFP, mylpfa-mCherry or rag2-Dsred* to similar incidence that *wild-type* and heterozygous animals and with no difference in relative tumor size. Importantly, these tumors express similar levels of KRAS and other myogenic markers including *myoD*. Our initial hypothesis that this could reflect a mere hyperplastic overproliferation of muscle tissue rather than fully transformed cells was rejected after successful engraftment into optically clear immune-compromised zebrafish (Tang et al., 2016). However, these tumors display a much different morphology, histology and pathological characteristics. We are interested in further characterizing these tumors, but these preliminary results suggest that, similar to mammals, a *myf5*-independent (possibly *myod*-dependent) muscle progenitor population is the cell-of-origin of these tumors.

Overall, our studies support the view that the cell-of-origin influences the characteristics and histological presentation of RMS (my unpublished data). Importantly, genetic modifiers also influence tumor morphology and histology as in the reported tumors in Chapter 4. Moreover, our imaging studies reported in Chapter 3 and Ignatius et al., 2012 support a skeletal muscle origin for this RMS model.

5.3 Insights into MRF expression their role in human RMS

The Myogenic Regulatory Factors MYF5 and MYOD1 were here shown for the first time to be required for cell cycle progression and tumor growth *in vitro* and/or *in vivo* (Chapter 4). The dependence on lineage-determination bHLH transcription factors for cell cycle progression, self-renewal and growth has been reported in other cancers, such as OLIG1/2 in gliomas (Beyeler et al., 2014; Imayoshi and Kageyama, 2014; Ligon et al., 2007; Trépant et al., 2014) and TAL1 in T-ALL (Ferrando et al., 2002; Gerby et al., 2014). It is surprising to us that this requirement has not been shown or reported previously and that this has not been explored in our scientific community. In any case, several questions remain unsolved:

- WHAT ARE THE DIRECT MOLECULAR TARGETS OF MYF5 AND MYOD1 IN HUMAN RMS CELL LINES?

In Chapter 4, we report that MYF5 and MYOD1 bind promoter and enhancer sites in the respective ERMS cell lines analyzed. Importantly, transcribed sites that are common between these two ChIP-seq experiments enrich for GO terms *embryonic skeletal system development*, *skeletal muscle tissue development* and *cyclin-dependent protein kinase holoenzyme complex*, suggesting that these factors commonly regulate genes involved in skeletal muscle differentiation (as previously reported, Conerly et al., 2016) and cell cycle progression (consistent with our reported phenotypes) to lock acRMS cells in a self-renewing undifferentiated state.

However, in order to determine the direct target genes that these proteins are regulating, we ought to at least perform RNA-seq in control and the respective *knock-down* cells, experiments that we are actively performing at this time.

- IS MYOD1 SIMILARLY REQUIRED FOR RMS GROWTH IN VIVO?

In Chapter 4, we reported that Rh18 RMS cells expressing two independent sh-RNA hairpins against MYF5 have a dramatic reduction in tumor volume

(as assessed by bioluminescence) following orthotopic subcutaneous transplantation into immune-compromised mice. The question remains: *Does this dramatic reduction (<7 days) reflect an inability of MYF5-knocked-down cells to proliferate in vivo and/or their inability to engraft and self-renew in the transplantation setting?* In order to address this question, we aim to perform inducible *knock-down* experiments for both MYF5 and MYOD1 by transplanting stably-expressing Doxycycline-inducible sh-RNA cells, wait for tumors to engraft, and then *knock-down* cells. At the present time, the mouse experiment depicted in Chapter 4 is still ongoing. Rh18 cells are routinely used in xenograft-based research and pre-clinical trials by the NCI-supported Pediatric Preclinical Testing Consortium (PPTC) (Hinson et al., 2013). However, these cells are slowly-growing *in vitro* and *in vivo* (our data in Chapter 4). As soon as these tumors are palpable, we plan to perform traditional caliper measurements and at the final experiment end-point to perform a necropsy analysis of these tumors, followed by histology and IHC for relevant markers.

- WHAT ARE THE SPECIFIC DOWNSTREAM EFFECTS OF CELL CYCLE ARREST UPON MYF5 AND MYOD1 KNOCKDOWN, IN VIVO?

The cell cycle arrest phenotype here reported in Chapter 4 is very consistent between different *knock-down* methods (si- or sh-RNA) and is reproducible among different human cell lines. However, it is still unclear to us how this cell-cycle arrest phenotype relates to possible downstream cellular effects, namely apoptosis or senescence as well as the specific effectors of this arrest. We are seeking to resolve this question through a series of *in vitro* assays and IHC staining, upon MRF *knock-down*.

As is written in the epilogue above: *Every discovery opens a new field for investigation of facts, shows us the imperfection of our theories. It has justly been said, that the greater the circle of light, the greater the boundary of darkness by which it is surrounded.*

The work here presented is surely insufficient for a complete understanding of Rhabdomyosarcoma and general Cancer biology. It is certainly insufficient for a successful translation of the body of Knowledge toward the betterment of this underserved patient population. However, it is my hope that these contributions will be followed up by the field, validated (or not) and that they may inspire more and more questions to be pursued by others. On a personal note, this work certainly incited in me a passion for contributing to raising awareness, producing knowledge and/or contribute to the betterment of treatments in poorly understood pediatric cancers.

Bibliography

Abraham, J. et al. (2014). “Lineage of origin in rhabdomyosarcoma informs pharmacological response”. In: *Genes Dev.* 28.14, pp. 1578–1591.

Agaram, N. P., Chen, C.-L., Zhang, L., LaQuaglia, M. P., Wexler, L., and Antonescu, C. R. (2014). “Recurrent MYOD1 mutations in pediatric and adult sclerosing and spindle cell rhabdomyosarcomas: Evidence for a common pathogenesis”. In: *Genes, Chromosom. Cancer* 53.9, pp. 779–787.

Albacker, C. E., Storer, N. Y., Langdon, E. M., Dibiase, A., Zhou, Y., Langenau, D. M., and Zon, L. (2013). “The histone methyltransferase SUV39H1 suppresses embryonal rhabdomyosarcoma formation in zebrafish.” In: *PLoS One* 8.5, e64969.

Alix-Panabieres, C. and Pantel, K. (2016). “Clinical Applications of Circulating Tumor Cells and Circulating Tumor DNA as Liquid Biopsy”. In: *Cancer Discov.* 6.5, pp. 479–491.

Annavarapu, S. R., Cialfi, S., Dominici, C., Kokai, G. K., Uccini, S., Ceccarelli, S., McDowell, H. P., and Helliwell, T. R. (2013). “Characterization of Wnt/β-catenin signaling in rhabdomyosarcoma.” In: *Lab. Investig.* 93.10, pp. 1090–9.

Barr, F., Galili, N, Holick, J, Biegel, J., Rovera, G, and Emanuel, B. (1993). “Rearrangement of the pax3 paired box gene in the paediatric solid tumour alveolar rhabdomyosarcoma”. In: *Nat. Genet.* 3, pp. 113–117.

Barr, F. G. F. (2001). “Gene fusions involving PAX and FOX family members in alveolar rhabdomyosarcoma.” In: *Oncogene* 20.40, pp. 5736–46.

Beck, B. and Blanpain, C. (2013). “Unravelling cancer stem cell potential.” In: *Nat. Rev. Cancer* 13.10, pp. 727–38.

Bedard, P. L., Hansen, A. R., Ratain, M. J., and Siu, L. L. (2013). “Tumour heterogeneity in the clinic”. In: *Nature* 501.7467, pp. 355–364.

Belyea, B. C., Naini, S., Bentley, R. C., and Linardic, C. M. (2011). “Inhibition of the Notch-Hey1 axis blocks embryonal rhabdomyosarcoma tumorigenesis.” In: *Clin. Cancer Res.* 17.23, pp. 7324–36.

Beyeler, S., Joly, S., Fries, M., Obermair, F.-J., Burn, F., Mehmood, R., Tabatabai, G., and Raineteau, O. (2014). “Targeting the bHLH transcriptional networks by mutated E proteins in experimental glioma.” In: *Stem Cells*, pp. 1–16.

Blackburn, J. and Langenau, D. M. (2014). “Zebrafish as a model to assess cancer heterogeneity, progression and relapse.” In: *Dis. Model. Mech.* 7.7, pp. 755–762.

Blackburn, J., Liu, S., Raimondi, A. R., Ignatius, M. S., Salthouse, C. D., and Langenau, D. M. (2011). “High-throughput imaging of adult fluorescent zebrafish with an LED fluorescence macroscope.” In: *Nat. Protoc.* 6.2, pp. 229–41.

Blackburn, J., Liu, S., Wilder, J. L., Dobrinski, K. P., Lobbardi, R., Moore, F. E., Martinez, S. A., Chen, E. Y., Lee, C., and Langenau, D. M. (2014). “Clonal evolution enhances leukemia-propagating cell frequency in T cell acute lymphoblastic leukemia through Akt/mTORC1 pathway activation.” In: *Cancer Cell* 25.3, pp. 366–78.

Blanpain, C. and Simons, B. D. (2013). “Unravelling stem cell dynamics by lineage tracing.” In: *Nat. Rev. Mol. Cell Biol.* 14.8, pp. 489–502.

Blum, J. M. et al. (2013). “Distinct and overlapping sarcoma subtypes initiated from muscle stem and progenitor cells.” In: *Cell Rep.* 5.4, pp. 933–40.

Braun, T., Buschhausen-Denker, G, Bober, E, Tannich, E, and Arnold, H. H. (1989). “A novel human muscle factor related to but distinct from MyoD1 induces myogenic conversion in 10T1/2 fibroblasts.” In: *EMBO J.* 8.3, pp. 701–9.

Braun, T., Rudnicki, M., Arnold, H. H., and Jaenisch, R (1992). “Targeted inactivation of the muscle regulatory gene Myf-5 results in abnormal rib development and perinatal death.” In: *Cell* 71.3, pp. 369–382.

Braun, T., Bober, E, Rudnicki, M., Jaenisch, R, and Arnold, H. H. (1994). “MyoD expression marks the onset of skeletal myogenesis in Myf-5 mutant mice.” In: *Development* 120.11, pp. 3083–3092.

Breneman, J. C. et al. (2003). “Prognostic factors and clinical outcomes in children and adolescents with metastatic rhabdomyosarcoma–a report from the Intergroup Rhabdomyosarcoma Study IV.” In: *J. Clin. Oncol.* 21.1, pp. 78–84.

Buckingham, M. (1992). “Making muscle in mammals”. In: *Trends Genet.* 8.4, pp. 144–149.

Buckingham, M. E. and Montarras, D. (2008). “Skeletal muscle stem cells.” In: *Curr. Opin. Genet. Dev.* 18.4, pp. 330–6.

Buckingham, M. E. and Rigby, P. W. J. (2014). “Gene regulatory networks and transcriptional mechanisms that control myogenesis.” In: *Dev. Cell* 28.3, pp. 225–38.

Camboni, M., Hammond, S., Martin, L. T., and Martin, P. T. (2012). “Induction of a regenerative microenvironment in skeletal muscle is sufficient to induce embryonal rhabdomyosarcoma in p53-deficient mice.” In: *J. Pathol.* 226.1, pp. 40–9.

Cao, L., Yu, Y., Bilke, S., Walker, R. L., Mayeenuddin, L. H., Azorsa, D. O., Yang, F., Pineda, M., Helman, L. J., and Meltzer, P. S. (2010a). "Genome-wide identification of PAX3-FKHR binding sites in rhabdomyosarcoma reveals candidate target genes important for development and cancer." In: *Cancer Res.* 70.16, pp. 6497–508.

Cao, Y. et al. (2010b). "Genome-wide MyoD binding in skeletal muscle cells: a potential for broad cellular reprogramming." In: *Dev. Cell* 18.4, pp. 662–74.

Chamberlain, J. S., Metzger, J., Reyes, M., Townsend, D., and Faulkner, J. a. (2007). "Dystrophin-deficient mdx mice display a reduced life span and are susceptible to spontaneous rhabdomyosarcoma." In: *FASEB J.* 21.9, pp. 2195–2204.

Chang, N. C. and Rudnicki, M. (2014). *Satellite Cells: The Architects of Skeletal Muscle.* 1st ed. Vol. 107C. Elsevier Inc., pp. 161–181. ISBN: 9780124160224.

Charytonowicz, E., Cordon-Cardo, C., Matushansky, I., and Ziman, M. (2009). "Alveolar rhabdomyosarcoma: is the cell of origin a mesenchymal stem cell?" In: *Cancer Lett.* 279.2, pp. 126–36.

Chen, E. Y. et al. (2014). "Glycogen synthase kinase 3 inhibitors induce the canonical WNT/β-catenin pathway to suppress growth and self-renewal in embryonal rhabdomyosarcoma." In: *Proc. Natl. Acad. Sci. U. S. A.* 111.14, pp. 5349–54.

Chen, L. et al. (2015). "Clonality and Evolutionary History of Rhabdomyosarcoma". In: *PLOS Genet.* 11.3. Ed. by Grosveld, G. C., e1005075.

Chen, X. et al. (2013). "Targeting oxidative stress in embryonal rhabdomyosarcoma." In: *Cancer Cell* 24.6, pp. 710–24.

Chen, Y.-H., Wang, Y.-H., Chang, M.-Y., Lin, C.-Y., Weng, C.-W., Westerfield, M., and Tsai, H.-J. (2007). "Multiple upstream modules regulate zebrafish myf5 expression." In: *BMC Dev. Biol.* 7.5, p. 1.

Comai, G., Sambasivan, R., Gopalakrishnan, S., and Tajbakhsh, S. (2014). "Variations in the Efficiency of Lineage Marking and Ablation Confound Distinctions between Myogenic Cell Populations". In: *Dev. Cell* 31.5, pp. 654–667.

Conerly, M. L., Yao, Z., Zhong, J. W., Groudine, M., and Tapscott, S. J. (2016). "Distinct Activities of Myf5 and MyoD Indicate Separate Roles in Skeletal Muscle Lineage Specification and Differentiation Article Distinct Activities of Myf5 and MyoD Indicate Separate Roles in Skeletal Muscle Lineage Specification and Differentiation". In: *Dev. Cell* 36.4, pp. 375–385.

Cossu, G., Kelly, R, Tajbakhsh, S., Di Donna, S, Vivarelli, E, and Buckingham, M. E. (1996). "Activation of different myogenic pathways: myf-5 is induced by the neural tube and MyoD by the dorsal ectoderm in mouse paraxial mesoderm." In: *Development* 122.2, pp. 429–437.

Dalerba, P., Cho, R. W., and Clarke, M. F. (2007). “Cancer stem cells: models and concepts.” In: *Annu. Rev. Med.* 58.58, pp. 267–84.

Davicioni, E., Finckenstein, F. G., Shahbazian, V., Buckley, J. D., Triche, T. J., and Anderson, M. J. (2006). “Identification of a PAX-FKHR gene expression signature that defines molecular classes and determines the prognosis of alveolar rhabdomyosarcomas.” In: *Cancer Res.* 66.14, pp. 6936–46.

Davicioni, E. et al. (2009). “Molecular classification of rhabdomyosarcoma-genotypic and phenotypic determinants of diagnosis: a report from the Children’s Oncology Group.” In: *Am. J. Pathol.* 174.2, pp. 550–564.

Davicioni, E., Anderson, J. R., Buckley, J. D., Meyer, W. H., and Triche, T. J. (2010). “Gene expression profiling for survival prediction in pediatric rhabdomyosarcomas: a report from the children’s oncology group.” In: *J. Clin. Oncol.* 28.7, pp. 1240–6.

Demetri, G., Fletcher, C., Mueller, E, Sarraf, P, Naujoks, R, Campbell, N, Spiegelman, B., and Singer, S. (1999). “Induction of solid tumor differentiation by the peroxisome proliferator-activated receptor- gamma ligand troglitazone in patients with liposarcoma”. In: *Proc. Natl. Acad. Sci.* 96.March, pp. 3951–3956.

Demmerle, J., Koch, A. J., and Holaska, J. M. (2013). “Emerin and histone deacetylase 3 (HDAC3) cooperatively regulate expression and nuclear positions of MyoD, Myf5, and Pax7 genes during myogenesis.” In: *Chromosom. Res.* 3.21, pp. 765–779.

Dilworth, F. J. and Blais, A. (2011). “Epigenetic regulation of satellite cell activation during muscle regeneration.” In: *Stem Cell Res. Ther.* 2.2, p. 18.

Doucet, C., Gutierrez, G. J., Lindon, C., Lorca, T., Lledo, G., Pinset, C., and Coux, O. (2005). “Multiple phosphorylation events control mitotic degradation of the muscle transcription factor Myf5.” In: *BMC Biochem.* 6, p. 27.

Driessens, G., Beck, B., Caauwe, A., Simons, B. D., and Blanpain, C. (2012). “Defining the mode of tumour growth by clonal analysis.” In: *Nature* 488.7412, pp. 527–30.

Eyler, C. E. et al. (2011). “Glioma stem cell proliferation and tumor growth are promoted by nitric oxide synthase-2.” In: *Cell* 146.1, pp. 53–66.

Ferrando, A. A. et al. (2002). “Gene expression signatures define novel oncogenic pathways in T cell acute lymphoblastic leukemia”. In: *Cancer Cell* 1.1, pp. 75–87.

Fiddler, T., Smith, L, Tapscott, S. J., and Thayer, M. (1996). “Amplification of MDM2 Inhibits MyoD-Mediated Myogenesis”. In: *Mol. Cell. . . .* 16.9, pp. 5048–5057.

Fleischmann, A., Jochum, W., Eferl, R., Witowsky, J., and Wagner, E. F. (2003). “Rhabdomyosarcoma development in mice lacking Trp53 and Fos: tumor suppression by the Fos protooncogene.” In: *Cancer Cell* 4.6, pp. 477–82.

Fong, A., Yao, Z., Zhong, J., Johnson, N., Farr, G., Maves, L., and Tapscott, S. J. (2015). “Conversion of MyoD to a Neurogenic Factor: Binding Site Specificity Determines Lineage”. In: *Cell Rep.* 10.12, pp. 1937–1946.

Gayraud-Morel, B., Chrétien, F., Flamant, P., Gomès, D., Zammit, P. S., and Tajbakhsh, S. (2007). “A role for the myogenic determination gene Myf5 in adult regenerative myogenesis”. In: *Dev. Biol.* 312.1, pp. 13–28.

Gayraud-Morel, B. et al. (2012). “Myf5 haploinsufficiency reveals distinct cell fate potentials for adult skeletal muscle stem cells.” In: *J. Cell Sci.* 125.Pt 7, pp. 1738–49.

Gensch, N., Borchardt, T., Schneider, A., Riethmacher, D., and Braun, T. (2008). “Different autonomous myogenic cell populations revealed by ablation of Myf5-expressing cells during mouse embryogenesis.” In: *Development* 135, pp. 1597–1604.

Gerby, B. et al. (2014). “SCL, LMO1 and Notch1 reprogram thymocytes into self-renewing cells.” In: *PLoS Genet.* 10.12, e1004768.

Graveel, C. R., Tolbert, D., and Vande Woude, G. F. (2013). “MET: a critical player in tumorigenesis and therapeutic target.” In: *Cold Spring Harb. Perspect. Biol.* 5.7.

Haldar, M., Karan, G., Tvrdik, P., and Capecchi, M. R. (2008). “Two cell lineages, myf5 and myf5-independent, participate in mouse skeletal myogenesis.” In: *Dev. Cell* 14.3, pp. 437–45.

Haldar, M., Karan, G., Watanabe, S., Guenther, S., Braun, T., and Capecchi, M. R. (2014). “Response: Contributions of the Myf5-Independent Lineage to Myogenesis”. In: *Dev. Cell* 31.5, pp. 539–541.

Hatley, M. E., Tang, W., Garcia, M. R., Finkelstein, D., Millay, D. P., Liu, N., Graff, J., Galindo, R. L., and Olson, E. N. (2012). “A mouse model of rhabdomyosarcoma originating from the adipocyte lineage.” In: *Cancer Cell* 22.4, pp. 536–46.

Hawkins, D. S., Gupta, A. a., and Rudzinski, E. R. (2014). “What is new in the biology and treatment of pediatric rhabdomyosarcoma?” In: *Curr. Opin. Pediatr.* 26.1, pp. 50–6.

Heerema-McKenney, A. et al. (2008). “Diffuse myogenin expression by immunohistochemistry is an independent marker of poor survival in pediatric rhabdomyosarcoma: a tissue microarray study of 71 primary tumors including correlation with molecular phenotype.” In: *Am. J. Surg. Pathol.* 32.10, pp. 1513–1522.

Hettmer, S., Bronson, R. T., and Wagers, A. J. (2015). “Distinct Malignant Behaviors of Mouse Myogenic Tumors Induced by Different Oncogenetic Lesions”. In: *Front. Oncol.* 5.February, pp. 1–5.

Hettmer, S., Liu, J., Miller, C. M., Lindsay, M. C., Sparks, C. A., Guertin, D. A., Bronson, R. T., Langenau, D. M., and Wagers, A. J. (2011). “Sarcomas induced in discrete subsets of prospectively isolated skeletal muscle cells.” In: *Proc. Natl. Acad. Sci. U. S. A.* 108.50, pp. 20002–7.

Hettmer, S. et al. (2014). “Rhabdomyosarcoma: Current Challenges and Their Implications for Developing Therapies”. In: *Cold Spring Harb. Perspect. Med.* 4.11, a025650–a025650.

Hingorani, P., Missiaglia, E, Shipley, J., Anderson, J. R., Triche, T. J., Delorenzi, M., Gastier-Foster, J., Wing, M., Hawkins, D. S., and Skapek, S. X. (2015). “Clinical Application of Prognostic Gene Expression Signature in Fusion Gene-Negative Rhabdomyosarcoma: A Report from the Children’s Oncology Group”. In: *Clin. Cancer Res.* 21.20, pp. 4733–4739.

Hinits, Y., Osborn, D. P. S., and Hughes, S. M. (2009). “Differential requirements for myogenic regulatory factors distinguish medial and lateral somitic, cranial and fin muscle fibre populations.” In: *Development* 136.3, pp. 403–14.

Hinits, Y., Williams, V. C., Sweetman, D., Donn, T. M., Ma, T. P., Moens, C. B., and Hughes, S. M. (2011). “Defective cranial skeletal development, larval lethality and haploinsufficiency in Myod mutant zebrafish.” In: *Dev. Biol.* 358.1, pp. 102–12.

Hinson, A. R. P., Jones, R., Crose, L. E. S., Belyea, B. C., Barr, F. G., and Linardic, C. M. (2013). “Human rhabdomyosarcoma cell lines for rhabdomyosarcoma research: utility and pitfalls.” In: *Front. Oncol.* 3.July, p. 183.

Hosoyama, T. et al. (2011). “IL-4R drives dedifferentiation, mitogenesis, and metastasis in rhabdomyosarcoma.” In: *Clin. Cancer Res.* 17.9, pp. 2757–66.

Ignatius, M. S. et al. (2012). “In vivo imaging of tumor-propagating cells, regional tumor heterogeneity, and dynamic cell movements in embryonal rhabdomyosarcoma.” In: *Cancer Cell* 21.5, pp. 680–93.

Imayoshi, I. and Kageyama, R. (2014). “bHLH factors in self-renewal, multipotency, and fate choice of neural progenitor cells.” In: *Neuron* 82.1, pp. 9–23.

Ishibashi, J., Perry, R. L., Asakura, A., and Rudnicki, M. (2005). “MyoD induces myogenic differentiation through cooperation of its NH2- and COOH-terminal regions.” In: *J. Cell Biol.* 171.3, pp. 471–82.

Jothi, M., Nishijo, K., Keller, C., and Mal, A. K. (2012). “AKT and PAX3-FKHR cooperation enforces myogenic differentiation blockade in alveolar rhabdomyosarcoma cell”. In: *Cell Cycle* 11.5, pp. 895–908.

Kablar, B., Tajbakhsh, S., and Rudnicki, M. (2000). “Transdifferentiation of esophageal smooth to skeletal muscle is myogenic bHLH factor-dependent.” In: *Development* 127.8, pp. 1627–39.

Kablar, B., Krastel, K., Ying, C., Asakura, A., Tapscott, S. J., and Rudnicki, M. (1997). “MyoD and Myf-5 differentially regulate the development of limb versus trunk skeletal muscle.” In: *Development* 124.23, pp. 4729–38.

Kashi, V. P., Hatley, M. E., and Galindo, R. L. (2015). “Probing for a deeper understanding of rhabdomyosarcoma: insights from complementary model systems”. In: *Nat. Rev. Cancer* 15.7, pp. 426–439.

Keller, C. and Capecchi, M. R. (2005). “New genetic tactics to model alveolar rhabdomyosarcoma in the mouse.” In: *Cancer Res.* 65.17, pp. 7530–2.

Keller, C. and Guttridge, D. C. (2013). “Mechanisms of impaired differentiation in rhabdomyosarcoma”. In: *FEBS J.* 280.17, pp. 4323–4334.

Keller, C., Arenkiel, B. R., Coffin, C. M., El-Bardeesy, N., DePinho, R. A., and Capecchi, M. R. (2004a). “Alveolar rhabdomyosarcomas in conditional Pax3:Fkhr mice: cooperativity of Ink4a/ARF and Trp53 loss of function.” In: *Genes Dev.* 18.21, pp. 2614–26.

Keller, C., Hansen, M. S., Coffin, C. M., and Capecchi, M. R. (2004b). “Pax3:Fkhr interferes with embryonic Pax3 and Pax7 function: implications for alveolar rhabdomyosarcoma cell of origin.” In: *Genes Dev.* 18.21, pp. 2608–13.

Kikuchi, K., Rubin, B. P., and Keller, C. (2011). “Developmental origins of fusion-negative rhabdomyosarcomas.” In: *Curr. Top. Dev. Biol.* 96, pp. 33–56.

Kohsaka, S. et al. (2014). “A recurrent neomorphic mutation in MYOD1 defines a clinically aggressive subset of embryonal rhabdomyosarcoma associated with PI3K-AKT pathway mutations.” In: *Nat. Genet.* 46.6, pp. 595–600.

Komuro, H., Saihara, R., Shinya, M., Takita, J., Kaneko, S., Kaneko, M., and Hayashi, Y. (2007). “Identification of side population cells (stem-like cell population) in pediatric solid tumor cell lines.” In: *J. Pediatr. Surg.* 42.12, pp. 2040–5.

Langenau, D. M. et al. (2003). “Myc-induced T cell leukemia in transgenic zebrafish.” In: *Science* 299.5608, pp. 887–90.

Langenau, D. M., Keefe, M. D., Storer, N. Y., Guyon, J. R., Kutok, J. L., Le, X., Goessling, W., Neuberg, D. S., Kunkel, L. M., and Zon, L. (2007). “Effects of RAS on the genesis of embryonal rhabdomyosarcoma.” In: *Genes Dev.* 21.11, pp. 1382–95.

Langenau, D. M., Keefe, M. D. D., Storer, N. Y., Jette, C. a. a., Smith, A. C. H., Ceol, C. J., Bourque, C., Look, A. T., and Zon, L. (2008). “Co-injection strategies to modify radiation sensitivity and tumor initiation in transgenic Zebrafish.” In: *Oncogene* 27.30, pp. 4242–8.

Langenau, D. M., Sweet-Cordero, A., Wechsler-Reya, R. J., and Dyer, M. A. (2015). “Preclinical Models Provide Scientific Justification and Translational Relevance for Moving Novel Therapeutics into Clinical Trials for Pediatric Cancer”. In: *Cancer Res.* Pp. 1–12.

Le, X., Langenau, D. M., Keefe, M. D., Kutok, J. L., Neuberg, D. S., and Zon, L. (2007). “Heat shock-inducible Cre/Lox approaches to induce diverse types of tumors and hyperplasia in transgenic zebrafish.” In: *Proc. Natl. Acad. Sci. U. S. A.* 104.22, pp. 9410–5.

Ligon, K. L. et al. (2007). “Olig2-Regulated Lineage-Restricted Pathway Controls Replication Competence in Neural Stem Cells and Malignant Glioma”. In: *Neuron* 53.4, pp. 503–517.

Linardic, C. M., Naini, S., Herndon, J. E., Kesserwan, C., Qualman, S. J., and Counter, C. M. (2007). “The PAX3-FKHR fusion gene of rhabdomyosarcoma cooperates with loss of p16INK4A to promote bypass of cellular senescence”. In: *Cancer Res.* 67.14, pp. 6691–6699.

Lindon, C., Montarras, D., and Pinset, C. (1998). “Cell cycle-regulated expression of the muscle determination factor Myf5 in proliferating myoblasts.” In: *J. Cell Biol.* 140.1, pp. 111–8.

Lindon, C., Albagli, O., Domeyne, P., Montarras, D., and Pinset, C. (2000). “Constitutive instability of muscle regulatory factor Myf5 is distinct from its mitosis-specific disappearance, which requires a D-box-like motif overlapping the basic domain.” In: *Mol. Cell. Biol.* 20.23, pp. 8923–8932.

Lisboa, S., Cerveira, N., Vieira, J., Torres, L., Ferreira, A. M., Afonso, M., Norton, L., Henrique, R., and Teixeira, M. R. (2008). “Genetic diagnosis of alveolar rhabdomyosarcoma in the bone marrow of a patient without evidence of primary tumor.” In: *Pediatr. Blood Cancer* 51.4, pp. 554–7.

MacQuarrie, K. L., Yao, Z., Young, J. M., Cao, Y., and Tapscott, S. J. (2012). “miR-206 integrates multiple components of differentiation pathways to control the transition from growth to differentiation in rhabdomyosarcoma cells.” In: *Skelet. Muscle* 2.1, p. 7.

MacQuarrie, K. L., Yao, Z., Fong, A., Diede, S. J., Rudzinski, E. R., Hawkins, D. S., and Tapscott, S. J. (2013a). “Comparison of Genome-Wide Binding of MyoD in Normal Human Myogenic Cells and Rhabdomyosarcomas Identifies Regional and Local Suppression of Promyogenic Transcription Factors”. In: *Mol. Cell. Biol.* 33.4, pp. 773–784.

MacQuarrie, K. L., Yao, Z., Fong, A., and Tapscott, S. J. (2013b). “Genome-wide binding of the basic helix-loop-helix myogenic inhibitor musculin has substantial overlap with MyoD: implications for buffering activity.” In: *Skelet. Muscle* 3.1, p. 26.

Magee, J. A., Piskounova, E., and Morrison, S. J. (2012). “Cancer stem cells: impact, heterogeneity, and uncertainty.” In: *Cancer Cell* 21.3, pp. 283–96.

Mal, A. K. (2006). “Histone methyltransferase Suv39h1 represses MyoD-stimulated myogenic differentiation.” In: *EMBO J.* 25.14, pp. 3323–34.

Malempati, S. and Hawkins, D. S. (2012). “Rhabdomyosarcoma: Review of the Children’s Oncology Group (COG) soft-tissue Sarcoma committee experience and rationale for current COG studies”. In: *Pediatr. Blood Cancer* 59.1, pp. 5–10. arXiv:NIHMS150003.

Meacham, C. E. and Morrison, S. J. (2013). “Tumour heterogeneity and cancer cell plasticity.” In: *Nature* 501.7467, pp. 328–37.

Minchin, J. E. N., Williams, V. C., Hinits, Y., Low, S., Tandon, P., Fan, C.-M., Rawls, J. F., and Hughes, S. M. (2013). “Oesophageal and sternohyal muscle fibres are novel Pax3-dependent migratory somite derivatives essential for ingestion”. In: *Development* 140.20, pp. 4296–4296.

Missiaglia, E et al. (2010). “MicroRNA-206 expression levels correlate with clinical behaviour of rhabdomyosarcomas.” In: *Br. J. Cancer* 102.12, pp. 1769–77.

Mizgirev, I. V. and Revskoy, S. Y. (2006). “Transplantable tumor lines generated in clonal zebrafish.” In: *Cancer Res.* 66.6, pp. 3120–5.

Nanni, P., Nicoletti, G., De Giovanni, C., Croci, S., Astolfi, A., Landuzzi, L., Di Carlo, E., Iezzi, M., Musiani, P., and Lollini, P.-l. (2003). “Development of rhabdomyosarcoma in HER-2/neu transgenic p53 mutant mice.” In: *Cancer Res.* 63.11, pp. 2728–32.

Nitzki, F, Zibat, A, Frommhold, A, Schneider, A, Schulz-Schaeffer, W, Braun, T., and Hahn, H (2011). “Uncommitted precursor cells might contribute to increased incidence of embryonal rhabdomyosarcoma in heterozygous Patched1-mutant mice.” In: *Oncogene* 30.43, pp. 4428–36.

Nitzki, F, Cuvelier, N, Dräger, J, Schneider, a, Braun, T., and Hahn, H (2015). “Hedgehog/Patched-associated rhabdomyosarcoma formation from delta1-expressing mesodermal cells”. In: *Oncogene* August, pp. 1–9.

Nowell, P. (1976). “The Clonal Evolution of Tumor Cell Populations”. In: *Science (80-.).* 194.4260, pp. 23–28.

Ognjanovic, S., Linabery, A. M., Charbonneau, B., and Ross, J. A. (2009). “Trends in childhood rhabdomyosarcoma incidence and survival in the United States, 1975-2005”. In: *Cancer* 115.18, pp. 4218–4226.

Pan, Y. A., Livet, J., Sanes, J. R., Lichtman, J. W., and Schier, A. F. (2011). “Multicolor Brainbow Imaging in Zebrafish”. In: *Cold Spring Harb. Protoc.* 2011.1, pdb.prot5546–pdb.prot5546.

Pan, Y. A., Freundlich, T., Weissman, T. a., Schoppik, D., Wang, X. C., Zimmerman, S., Ciruna, B., Sanes, J. R., Lichtman, J. W., and Schier, A. F. (2013). “Zebrabow: multispectral cell labeling for cell tracing and lineage analysis in zebrafish.” In: *Development* 140.13, pp. 2835–46.

Park, S. W., Davison, J. M., Rhee, J., Hruban, R. H., Maitra, A., and Leach, S. D. (2008). “Oncogenic KRAS induces progenitor cell expansion and malignant

transformation in zebrafish exocrine pancreas." In: *Gastroenterology* 134.7, pp. 2080–90.

Patel, A. P. et al. (2014). "Single-cell RNA-seq highlights intratumoral heterogeneity in primary glioblastoma". In: *Science (80-.).* 344.6190, pp. 1396–1401.

Patton, E. et al. (2005). "BRAF mutations are sufficient to promote nevi formation and cooperate with p53 in the genesis of melanoma." In: *Curr. Biol.* 15.3, pp. 249–54.

Perez, E. a., Kassira, N., Cheung, M. C., Koniaris, L. G., Neville, H. L., and Sola, J. E. (2011). "Rhabdomyosarcoma in children: a SEER population based study." In: *J. Surg. Res.* 170.2, e243–51.

Raimondi, L et al. (2012). "Inhibition of Notch3 signalling induces rhabdomyosarcoma cell differentiation promoting p38 phosphorylation and p21(Cip1) expression and hampers tumour cell growth in vitro and in vivo." In: *Cell Death Differ.* 19.5, pp. 871–81.

Rheinbay, E. et al. (2013). "An aberrant transcription factor network essential for Wnt signaling and stem cell maintenance in glioblastoma." In: *Cell Rep.* 3.5, pp. 1567–79.

Riggi, N., Cironi, L., Provero, P., Suva, M. L., Kaloulis, K., Garcia-Echeverria, C., Hoffmann, F., Trumpp, A., and Stamenkovic, I. (2005). "Development of Ewing's sarcoma from primary bone marrow-derived mesenchymal progenitor cells." In: *Cancer Res.* 65.24, pp. 11459–11468.

Riggi, N., Suva, M. L., Cironi, L., Provero, P., Tercier, S., Joseph, J.-M., Stehle, J.-C., Baumer, K., Kindler, V., and Stamenkovic, I. (2008). "EWS-FLI-1 Expression Triggers a Ewing's Sarcoma Initiation Program in Primary Human Mesenchymal Stem Cells". In: *Cancer Res.* 68.7, pp. 2176–2185.

Roma, J., Masià, A., Reventós, J., Sánchez de Toledo, J., and Gallego, S. (2011). "Notch pathway inhibition significantly reduces rhabdomyosarcoma invasiveness and mobility in vitro." In: *Clin. Cancer Res.* 17.3, pp. 505–13.

Rossbach, H.-C., Lacson, A., Grana, N., and Barbosa, J. (1999). "Duchenne Muscular Dystrophy and Concomitant Metastatic Alveolar Rhabdomyosarcoma". In: *J. Pediatr. Hematol. Oncol.* 21.6, pp. 528–530.

Rota, R, Ciarapica, R., Giordano, A., Miele, L., and Locatelli, F. (2011). "MicroRNAs in rhabdomyosarcoma: pathogenetic implications and translational potentiality." In: *Mol. Cancer* 10.1, p. 120.

Roy, K., Serna, I. L. de la, and Imbalzano, A. N. (2002). "The myogenic basic helix-loop-helix family of transcription factors shows similar requirements for SWI/SNF chromatin remodeling enzymes during muscle differentiation in culture." In: *J. Biol. Chem.* 277.37, pp. 33818–24.

Rubin, B. P. et al. (2011). “Evidence for an Unanticipated Relationship between Undifferentiated Pleomorphic Sarcoma and Embryonal Rhabdomyosarcoma”. In: *Cancer Cell* 19.2, pp. 177–191.

Rudnicki, M., Braun, T., Hinuma, S, and Jaenisch, R (1992). “Inactivation of MyoD in mice leads to up-regulation of the myogenic HLH gene Myf-5 and results in apparently normal muscle development.” In: *Cell* 71.3, pp. 383–90.

Rudnicki, M., Schnegelsberg, P. N., Stead, R. H., Braun, T., Arnold, H. H., and Jaenisch, R (1993). “MyoD or Myf-5 is required for the formation of skeletal muscle.” In: *Cell* 75.7, pp. 1351–9.

Saab, R., Spunt, S. L., and Skapek, S. X. (2011). “Myogenesis and rhabdomyosarcoma the Jekyll and Hyde of skeletal muscle.” In: *Curr. Top. Dev. Biol.* 94, pp. 197–234.

Sabaawy, H. E., Azuma, M., Embree, L. J., Tsai, H.-J., Starost, M. F., and Hickstein, D. D. (2006). “TEL-AML1 transgenic zebrafish model of precursor B cell acute lymphoblastic leukemia.” In: *Proc. Natl. Acad. Sci. U. S. A.* 103.41, pp. 15166–71.

Sanchez-Gurmaches, J. and Guertin, D. A. (2014). “Adipocyte lineages: Tracing back the origins of fat”. In: *Biochim. Biophys. Acta - Mol. Basis Dis.* 1842.3, pp. 340–351.

Sanchez-Gurmaches, J., Hung, C.-M., Sparks, C. a., Tang, Y., Li, H., and Guertin, D. a. (2012). “PTEN loss in the Myf5 lineage redistributes body fat and reveals subsets of white adipocytes that arise from Myf5 precursors.” In: *Cell Metab.* 16.3, pp. 348–62.

Satheesha, S et al. (2015). “Targeting hedgehog signaling reduces self-renewal in embryonal rhabdomyosarcoma”. In: *Oncogene* April 2014, pp. 1–11.

Sebire, N. J. and Malone, M (2003). “Myogenin and MyoD1 expression in paediatric rhabdomyosarcomas.” In: *J. Clin. Pathol.* 56.6, pp. 412–6.

Shapiro, D., Sublett, J., Li, B., Downing, J., and Naeve, C. (1993). “Fusion of PAX3 to a Member of the Forkhead Family of Transcription Factors in Human Alveolar Rhabdomyosarcoma”. In: *Cancer Res.* 53, pp. 5108–5112.

Shern, J. F. et al. (2014). “Comprehensive genomic analysis of rhabdomyosarcoma reveals a landscape of alterations affecting a common genetic axis in fusion-positive and fusion-negative tumors.” In: *Cancer Discov.* 4.2, pp. 216–31.

Shinkoda, Y., Nagatoshi, Y., Fukano, R., Nishiyama, K., and Okamura, J. (2009). “Rhabdomyosarcoma masquerading as acute leukemia.” In: *Pediatr. Blood Cancer* 52.2, pp. 286–7.

Siegel, A. L., Gurevich, D. B., and Currie, P. D. (2013). “A myogenic precursor cell that could contribute to regeneration in zebrafish and its similarity to the satellite cell.” In: *FEBS J.* 280.17, pp. 4074–88.

Singh, K. and Dilworth, F. J. (2013). “Differential modulation of cell cycle progression distinguishes members of the myogenic regulatory factor family of transcription factors.” In: *FEBS J.* 280.17, pp. 3991–4003.

Smith, A. C. H. et al. (2010). “High-throughput cell transplantation establishes that tumor-initiating cells are abundant in zebrafish T-cell acute lymphoblastic leukemia.” In: *Blood* 115.16, pp. 3296–303.

Sokolowski, E, Turina, C. B., Kikuchi, K, Langenau, D. M., and Keller, C. (2014). “Proof-of-concept rare cancers in drug development: the case for rhabdomyosarcoma.” In: *Oncogene* 33.15, pp. 1877–89.

Stoletov, K. and Klemke, R. (2008). “Catch of the day: zebrafish as a human cancer model.” In: *Oncogene* 27.33, pp. 4509–20.

Stoletov, K., Montel, V., Lester, R. D., Gonias, S. L., and Klemke, R. (2007). “High-resolution imaging of the dynamic tumor cell vascular interface in transparent zebrafish”. In: *Proc. Natl. Acad. Sci.* 104.44, pp. 17406–17411.

Stone, R., Maguire, M., Goldberg, m. A., Antin, J. H., Rosenthal, D. S., and Mayer, R. J. (1988). “Complete remission in acute promyelocytic leukemia despite persistence of abnormal bone marrow promyelocytes during induction therapy: experience in 34 patients”. In: *Blood* 71.3, pp. 690–696.

Storer, N. Y., White, R. M., Uong, A., Price, E., Nielsen, G. P., Langenau, D. M., and Zon, L. (2013). “Zebrafish rhabdomyosarcoma reflects the developmental stage of oncogene expression during myogenesis.” In: *Development* 140.14, pp. 3040–50.

Suva, M. L. et al. (2009). “Identification of cancer stem cells in Ewing’s sarcoma.” In: *Cancer Res.* 69.5, pp. 1776–1781.

Suva, M. L. et al. (2014). “Reconstructing and reprogramming the tumor-propagating potential of glioblastoma stem-like cells.” In: *Cell* 157.3, pp. 580–94.

Svalina, M. and Keller, C. (2014). “YAPping About Differentiation Therapy in Muscle Cancer”. In: *Cancer Cell* 26.2, pp. 154–155.

Sweetman, D., Goljanek, K., Rathjen, T., Oustanina, S., Braun, T., Dalmay, T., and Münsterberg, A. (2008). “Specific requirements of MRFs for the expression of muscle specific microRNAs, miR-1, miR-206 and miR-133.” In: *Dev. Biol.* 321.2, pp. 491–9.

Szuhai, K., De Jong, D., Leung, W. Y., Fletcher, C. D. M., and Hogendoorn, P. C. W. (2014). “Transactivating mutation of the MYOD1 gene is a frequent event in adult spindle cell rhabdomyosarcoma”. In: *J. Pathol.* 232.3, pp. 300–307.

Tajbakhsh, S. (2009). “Skeletal muscle stem cells in developmental versus regenerative myogenesis.” In: *J. Intern. Med.* 266.4, pp. 372–389.

Tajbakhsh, S. and Buckingham, M. E. (1994). “Mouse limb muscle is determined in the absence of the earliest myogenic factor myf-5.” In: *Proc. Natl. Acad. Sci. U. S. A.* 91.2, pp. 747–751.

— (1995). “Lineage restriction of the myogenic conversion factor myf-5 in the brain.” In: *Development* 121.12, pp. 4077–4083.

Tajbakhsh, S., Rocancourt, D, and Buckingham, M. E. (1996). “Muscle progenitor cells failing to respond to positional cues adopt non-myogenic fates in myf-5 null mice.” In: *Nature* 384.6606, pp. 266–270.

Tajbakhsh, S., Vivarelli, E, Cusella-De-Angelis, G, Rocancourt, D, Buckingham, M. E., and Cossu, G. (1994). “A population of myogenic cells derived from the mouse neural tube”. In: *Neuron* 13.4, pp. 813–821.

Tajbakhsh, S., Borello, U, Vivarelli, E, Kelly, R, Papkoff, J, Duprez, D, Buckingham, M. E., and Cossu, G. (1998). “Differential activation of Myf5 and MyoD by different Wnts in explants of mouse paraxial mesoderm and the later activation of myogenesis in the absence of Myf5.” In: *Development* 125.21, pp. 4155–62.

Tang, Q. et al. (2014). “Optimized cell transplantation using adult rag2 mutant zebrafish.” In: *Nat. Methods* 11, pp. 821–824.

Tang, Q. et al. (2016). “Imaging tumour cell heterogeneity following cell transplantation into optically clear immune-deficient zebrafish”. In: *Nat. Commun.* 7, p. 10358.

Tapscott, S. J. (2005). *The circuitry of a master switch: Myod and the regulation of skeletal muscle gene transcription.* Tech. rep. 12, pp. 2685–95.

Tapscott, S. J., Davis, R. L., Thayer, M. J., Cheng, P.-f., Lassar, A. B., and Weintraub, H. (1988). “MyoD1 : a Myc Requiring Nuclear Phosphoprotein to Convert Region Homology Myoblasts Fibroblasts to Myoblasts”. In: *Science* 242.4877, pp. 405–411.

Tenente, I. M., Tang, Q., Moore, J. C., and Langenau, D. M. (2014). “Normal and Malignant Muscle Cell Transplantation into Immune Compromised Adult Zebrafish”. In: *J. Vis. Exp.* 94.

Tremblay, A. M. et al. (2014). “The Hippo Transducer YAP1 Transforms Activated Satellite Cells and Is a Potent Effector of Embryonal Rhabdomyosarcoma Formation”. In: *Cancer Cell* 26.2, pp. 273–287.

Trépant, A.-L., Bouchart, C., Rorive, S., Sauvage, S., Decaestecker, C., Demetter, P., and Salmon, I. (2014). “Identification of OLIG2 as the most specific glioblastoma stem cell marker starting from comparative analysis of data from similar DNA chip microarray platforms”. In: *Tumor Biol.* 36.3, pp. 1943–1953.

Wagers, A. and Conboy, I. M. (2005). “Cellular and molecular signatures of muscle regeneration: current concepts and controversies in adult myogenesis.” In: *Cell* 122.5, pp. 659–67.

Walter, D. et al. (2011). “CD133 positive embryonal rhabdomyosarcoma stem-like cell population is enriched in rhabdospheres.” In: *PLoS One* 6.5, e19506.

Weihkopf, T., Blettner, M., Dantonello, T., Jung, I., Klingebiel, T., Koscielniak, E., Lückel, M., Spix, C., and Kaatsch, P. (2008). “Incidence and time trends of soft tissue sarcomas in German children 1985-2004 - A report from the population-based German Childhood Cancer Registry”. In: *Eur. J. Cancer* 44.3, pp. 432–440.

White, R., Rose, K., and Zon, L. (2013). “Zebrafish cancer: the state of the art and the path forward.” In: *Nat. Rev. Cancer* 13.9, pp. 624–36.

White, R. M. et al. (2008). “Transparent Adult Zebrafish as a Tool for In Vivo Transplantation Analysis”. In: *Cell Stem Cell* 2.2, pp. 183–189.

Williamson, D. et al. (2010). “Fusion Gene-Negative Alveolar Rhabdomyosarcoma Is Clinically and Molecularly Indistinguishable From Embryonal Rhabdomyosarcoma”. In: *J. Clin. Oncol.* 28.13, pp. 2151–2158.

Yablonka-Reuveni, Z., Rudnicki, M., Rivera, A. J., Primig, M, Anderson, J. E., and Natanson, P (1999). “The transition from proliferation to differentiation is delayed in satellite cells from mice lacking MyoD.” In: *Dev. Biol.* 210, pp. 440–455.

Yan, D., Dong, X. D. E., Chen, X., Wang, L., Lu, C., Wang, J., Qu, J., and Tu, L. (2009). “MicroRNA-1/206 targets c-Met and inhibits rhabdomyosarcoma development.” In: *J. Biol. Chem.* 284.43, pp. 29596–604.

Yang, H. W., Kutok, J. L., Lee, N. H., Piao, H. Y., Fletcher, C. D. M., Kanki, J. P., and Look, A. T. (2004). “Targeted Expression of Human MYCN Selectively Causes Pancreatic Neuroendocrine Tumors in Transgenic Zebrafish”. In: *Cancer Res.* Pp. 7256–7262.

Yang, Z., MacQuarrie, K. L., Analau, E., Tyler, A. E., Dilworth, F. J., Cao, Y., Diede, S. J., and Tapscott, S. J. (2009). “MyoD and E-protein heterodimers switch rhabdomyosarcoma cells from an arrested myoblast phase to a differentiated state.” In: *Genes Dev.* 23.6, pp. 694–707.

Zhou, Q., Facciponte, J., Jin, M., Shen, Q., and Lin, Q. (2014). “Humanized NOD-SCID IL2rgâĂŞ/âĂŞ mice as a preclinical model for cancer research and its potential use for individualized cancer therapies.” In: *Cancer Lett.* 344.1, pp. 13–9.

Zhuravleva, J., Paggetti, J., Martin, L., Hammann, A., Solary, E., Bastie, J.-N., and Delva, L. (2008). “MOZ/TIF2-induced acute myeloid leukaemia in transgenic fish.” In: *Br. J. Haematol.* 143.3, pp. 378–82.

Zibat, a, Missiaglia, E, Rosenberger, A, Pritchard-Jones, K, Shipley, J., Hahn, H, and Fulda, S (2010). “Activation of the hedgehog pathway confers a poor prognosis in embryonal and fusion gene-negative alveolar rhabdomyosarcoma.” In: *Oncogene* 29.48, pp. 6323–30.

Appendix

Optimized cell transplantation using adult *rag2* mutant zebrafish

Qin Tang[1–4,8], Nouran S Abdelfattah[1–4,8], Jessica S Blackburn[1–4,8], John C Moore[1–4], Sarah A Martinez[1–4], Finola E Moore[1–4], Riadh Lobbardi[1–4], Inês M Tenente[1–4], Myron S Ignatius[1–4], Jason N Berman[5], Robert S Liwski[5], Yariv Houvras[6,7] & David M Langenau[1–4,8]

Cell transplantation into adult zebrafish has lagged behind mouse models owing to the lack of immunocompromised strains. Here we have created *rag2*^{E450fs} mutant zebrafish that have reduced numbers of functional T and B cells but are viable and fecund. Mutant fish engraft muscle, blood stem cells and various cancers. *rag2*^{E450fs} mutant zebrafish are the first immunocompromised zebrafish model that permits robust, long-term engraftment of multiple tissues and cancer.

© 2014 Nature America, Inc. All rights reserved.

Cell transplantations of human and mouse cells into immunocompromised mice have enhanced our understanding of stem cell function, regeneration and cancer. However, transplantation experiments in mice are expensive and routinely utilize small cohorts of animals, and engraftment is often difficult to visualize directly. By contrast, large-scale cell transplantation of fluorescent blood and cancer cells into syngeneic and irradiated zebrafish has now become routine[1–7]. However, these approaches require that donor cells are from the same strain of syngeneic zebrafish or that the recipient immune system is transiently ablated by whole-body γ-irradiation 2 d before transplantation. Irradiated recipients eventually recover their immune system by 20 d post irradiation and kill engrafted cells[1,2,6], making long-term engraftment studies difficult. To date, immunocompromised zebrafish have not been developed as a universal recipient for allograft cell transplantation.

To facilitate transplantation experiments in adult zebrafish, we capitalized on recently developed gene inactivation methods[8] and engineered zinc-finger nucleases to target the plant homeodomain (PHD) of the zebrafish recombination activating gene 2, *rag2* (refs. 9,10; **Fig. 1a**). Mutations in residues of the PHD disrupt the RAG2 protein interaction with trimethylated histone H3 to alter chromatin accessibility and to partially impair V(D)J recombination *in vivo*[11]. Similar residues are commonly mutated in Omenn syndrome, which is an autosomal recessive severe combined immunodeficiency. The impaired T- and B-cell receptor rearrangement in this disease leads to reduced numbers of functionally mature lymphocytes in human patients. We generated a mutant zebrafish line in the AB strain background that contained a frameshift at amino acid E450 resulting in premature termination (designated *rag2*^{E450fs}; **Fig. 1b**).

We incrossed heterozygous *rag2*^{E450fs} mutant fish and raised them to adulthood. Animals were genotyped at 3 months of age, revealing expected Mendelian ratios (146 wild type, 265 heterozygous and 129 *rag2*^{E450fs} mutant fish). *rag2*^{E450fs} mutants were similar in size to heterozygous and wild-type siblings (**Supplementary Fig. 1**), survived fin clip and remained healthy for >6 months when raised under standard laboratory conditions. Homozygous *rag2*^{E450fs} mutant zebrafish could reproduce, albeit at reduced fecundity when compared with heterozygous siblings (**Supplementary Table 1**). Histological analysis of 90-d-old *rag2*^{E450fs} mutant zebrafish revealed a notable reduction in thymic T cells and an altered thymic architecture including reduced numbers of epithelial cells with a preponderance of adipocytes ($n = 5$ of 6 mutant animals, **Fig. 1c**,**d**). This thymic involution is commonly observed in T cell–deficient lines of mice[12] and was not detected in wild-type siblings ($n = 6$, $P = 0.008$, Fisher's exact test). We also noted a similar reduction in thymocyte number in 5-d-old zebrafish (**Supplementary Fig. 2**). Analysis of whole kidney marrow revealed that adult homozygous *rag2*^{E450fs} zebrafish contained all blood cell lineages (**Fig. 1e**,**f**); however, quantification revealed a striking 75% reduction in lymphocytes of *rag2*^{E450fs} mutant zebrafish (**Fig. 1g** and **Supplementary Table 2**). Transcript expression for mature B- and T-cell markers was reduced in *rag2*^{E450fs} mutant marrow, including expression of immunoglobulin heavy constant mu (*ighm*, here referred to as *igm*), lymphocyte-specific protein-tyrosine kinase (*lck*), T-cell receptor alpha (*trac*, here referred to as *tcra*) and T-cell receptor beta (*trbc2*, here referred to as *tcrb*) (**Fig. 1h**). By contrast, *rag1* transcript levels were not reduced in marrow of mutant animals. This suggests that early B-cell precursors were not altered in *rag2*^{E450fs} mutant zebrafish (**Fig. 1h**). Homozygous *rag2*^{E450fs} mutants did not exhibit expression differences for myeloperoxidase (*mpx*) and l-plastin (*lcp1*), a result confirming that neutrophil, monocyte, macrophage and other cell lineages were not altered in *rag2*^{E450fs} mutant zebrafish (**Fig. 1h** and **Supplementary Table 2**).

To directly address the impact of the *rag2*^{E450fs} mutation on mature T and B cells, we assessed whole kidney marrow cells for

[1]Molecular Pathology Unit, Massachusetts General Hospital, Boston, Massachusetts, USA. [2]Cancer Center, Massachusetts General Hospital, Boston, Massachusetts, USA. [3]Center for Regenerative Medicine, Massachusetts General Hospital, Boston, Massachusetts, USA. [4]Harvard Stem Cell Institute, Cambridge, Massachusetts, USA. [5]Izaak Walton Killam Health Centre, Dalhousie University, Halifax, Nova Scotia, Canada. [6]Department of Surgery, Weill Cornell Medical College, New York, New York, USA. [7]Department of Medicine, Weill Cornell Medical College, New York, New York, USA. [8]These authors contributed equally to this work. Correspondence should be addressed to D.M.L. (dlangenau@mgh.harvard.edu).

RECEIVED 11 DECEMBER 2013; ACCEPTED 13 JUNE 2014; PUBLISHED ONLINE 20 JULY 2014; DOI:10.1038/NMETH.3031

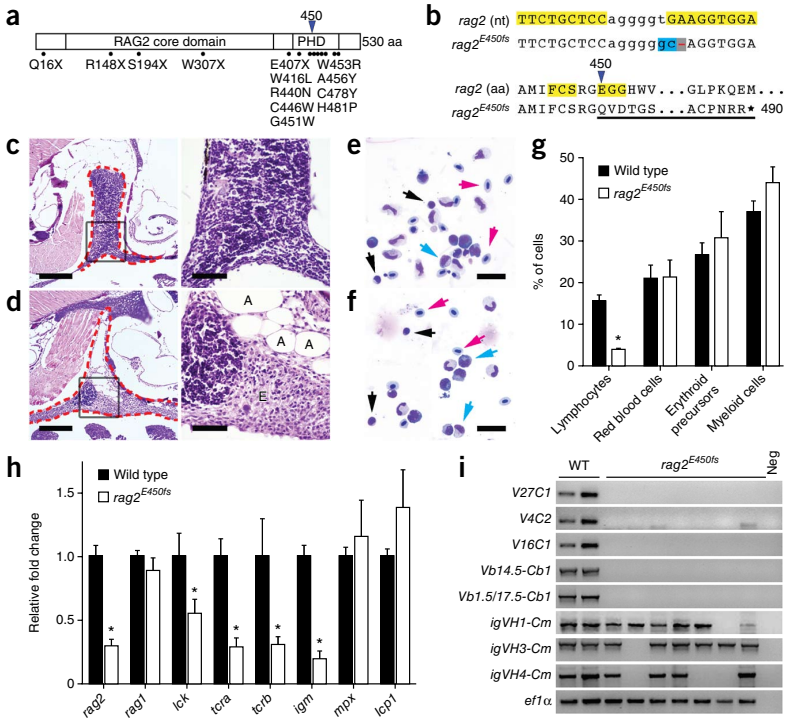

Figure 1 | *rag2*^{E450fs} mutant zebrafish lack mature T cells and have a reduced B-cell repertoire. (**a**) Human RAG2 protein with known severe combined immunodeficiency mutations denoted. Arrowhead, zinc-finger nuclease (ZFN) target region. aa, amino acids. (**b**) Nucleotide (nt) (top) and protein sequence (bottom) for the *rag2*^{E450fs} mutation. Yellow, ZFN target sites; blue, nucleotide additions; gray, nucleotide deletion; arrowhead, amino acid change at E450. Underlining shows the amino acid sequence following the frameshift, with the termination amino acid numbered. (**c**,**d**) Thymus sections of 90-d-old wild-type (**c**) and *rag2*^{E450fs} mutant zebrafish (**d**). Red dashed lines denote thymus (left). Right, amplified views of boxed regions with adipocytes (A) and vacant thymic epithelium (E) shown. (**e**,**f**) Whole kidney marrow cytospins of wild-type (**e**) and *rag2*^{E450fs} zebrafish (**f**) with lymphocytes (black arrows), erythrocytes (magenta arrows) and granulocytes (blue arrows) denoted. Scale bars: 200 µm (**c**,**d** left), 50 µm (**c**,**d** right) and 20 µm (**e**,**f**). (**g**) Cell counts from cytospins performed on whole kidney marrow. Error bars, ±1 s.d., $^*P < 0.05$ by Student's *t*-test. (**h**) Gene expression analysis of whole kidney marrow cells. Error bars, s.e.m.; $^*P < 0.05$ by Student's *t*-test. (**i**) PCR analysis for *tcrb* and *igm* rearrangement of whole kidney marrow cells from wild-type (WT) and *rag2*^{E450fs} zebrafish. Neg, negative control. Amplification of *tcrb* transcripts with primers specific to the variable (V) and constant (C) regions noted (top five rows) and *igm* transcripts spanning the variable H (VH) and constant mu (Cm) regions. *ef1α*, elongation factor 1 alpha.

tcrb and *igm* rearrangements[4,13]. Homozygous *rag2*^{E450fs} mutant fish lacked *tcrb* rearranged T cells ($n = 7$, **Fig. 1i**), whereas the B-cell immune repertoire was reduced in 3 of 7 animals tested. Thus, the *rag2*^{E450fs} mutation results in the production of a hypomorphic protein with reduced function in receptor recombination, leading to a lack of mature T cells and a variable reduction of functionally diverse B cells.

Immunocompromised mice, including those deficient in *Rag2*, have been successfully used for adoptive transfer of mouse and human cells. Yet, immunocompromised adult zebrafish have not been developed that permit stable engraftment of a range of cells and tissues. *rag1* mutant fish lack all mature T and B cells[13] but have not been widely used for cell transplantation approaches because of reduced viability of adult fish and failure to thrive following fin clip and genotyping. To assess whether hypomorphic, *rag2*-deficient zebrafish were amenable to cell transplantation, we first analyzed whether hematopoietic stem cell engraftment was enhanced in *rag2*^{E450fs} mutant lines. Specifically, we sublethally irradiated *rag2*^{E450fs} mutant and wild-type sibling adults with 10-Gy irradiation to clear the hematopoietic stem cell niche. Animals were transplanted 2 d after irradiation treatment by intraperitoneal injection with either 5×10^4 or 3×10^5 whole kidney marrow cells from unrelated ubiquitin-EGFP donor zebrafish[14] (ubi-EGFP, **Fig. 2a**). As expected, none of the wild-type

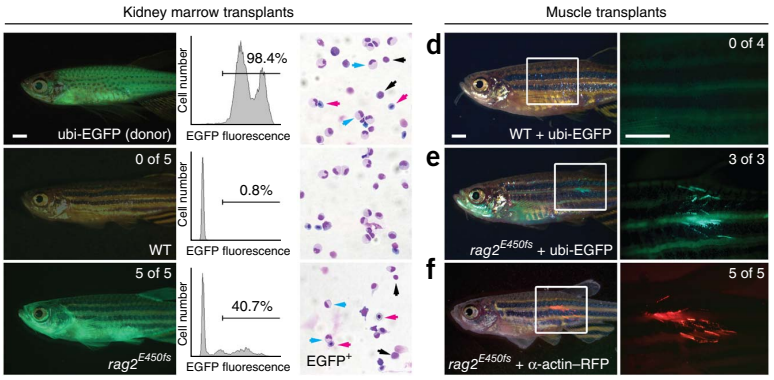

Figure 2 | *rag2*^{E450fs} mutant fish engraft hematopoietic and muscle stem cells. (**a**) ubi-EGFP transgenic donor fish. (**b**,**c**) Wild-type (WT; **b**) or homozygous *rag2*^{E450fs} recipient fish (**c**) transplanted with EGFP-labeled marrow and imaged at 45 d post transplantation (d.p.t.). Left, fluorescence images of whole fish with engraftment rates noted. Flow cytometry (center) and cytospin analysis (right) of whole kidney marrow from donor fish (**a**) and recipient fish (**b**,**c**). EGFP$^+$ cells sorted by flow cytometry are shown for cytospin analysis in c. Black arrows, lymphocytes; magenta arrows, red blood cells; blue arrows, granulocytes. (**d**,**e**) Fluorescence images of WT and *rag2*^{E450fs} mutant fish engrafted with muscle cells from ubi-EGFP transgenic fish imaged at 30 d.p.t. (**f**) *rag2*^{E450fs} fish engrafted with muscle cells from α-actin–RFP transgenic fish at 30 d.p.t. Engraftment rates for **d**–**f** are shown on magnified image panels to the right. Scale bars, 2 mm.

© 2014 Nature America, Inc. All rights reserved.

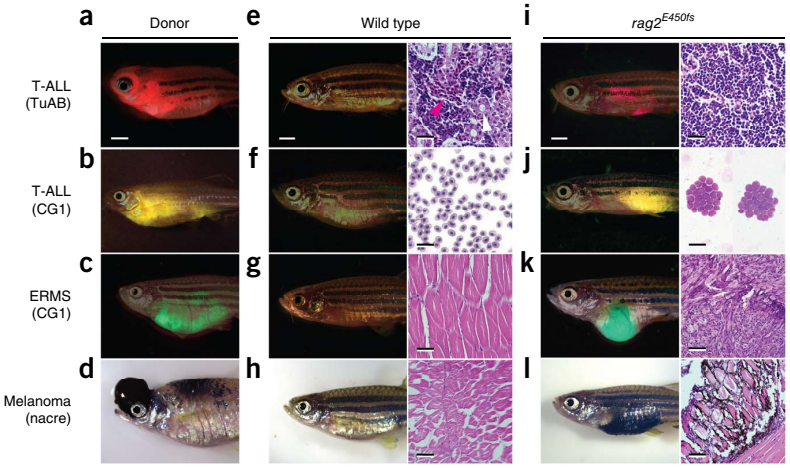

Figure 3 | Engraftment of zebrafish tumors into *rag2*^{E450fs} mutant fish. (**a**–**d**) Donor tumors used in cell transplantation studies. (**a**) dsRed-labeled *Myc*-induced T-cell acute lymphoblastic leukemia (T-ALL) arising in TuAB strain fish. (**b**) zsYellow-labeled T-ALL from CG1 strain fish. (**c**) EGFP-labeled embryonal rhabdomyosarcoma (ERMS) from CG1 strain fish. (**d**) *mitfa*- and *BRAF*^{V600E}-induced melanoma arising in *p53*-deficient nacre strain fish (**d**). (**e**–**l**) Left, merged bright-field and fluorescence images of wild-type (**e**–**h**) or *rag2*^{E450fs} mutant fish (**i**–**l**) at 30 d post transplantation. Right, images of whole kidney marrow sections (**e**,**i**), peripheral blood cytospins (**f**,**j**) and skeletal muscle (**g**,**k**,**h**,**l**). Magenta arrowhead, red blood cells; white arrowhead, renal tubules (**e**). Scale bars in fish images are 2 mm and in histopathology images are 25 μm (**e**,**i**), 20 μm (**f**,**j**) and 50 μm (**g**,**k**,**h**,**l**).

siblings engrafted blood cells (n = 10), whereas all *rag2*^{E450fs} mutant fish exhibited robust, multilineage blood cell engraftment that persisted past 45 days post transplantation (d.p.t., n = 6), a full 25 d after immune rejection is normally initiated in irradiated wild-type recipient fish[2,6] (**Fig. 2b**,**c**, P = 0.0002, Fisher's exact test; **Supplementary Fig. 3** and **Supplementary Table 3**). Engrafted *rag2*^{E450fs} homozygous mutant fish also commonly exhibited EGFP$^+$ circulating cells by 30 d.p.t. (**Supplementary Video 1**). These data show that hypomorphic *rag2*^{E450fs} can robustly engraft hematopoietic cells from unrelated donors.

To assess the broad utility of the *rag2*^{E450fs} model for engraftment of regenerative tissues, fluorescently labeled muscle cells from adult ubi-EGFP transgenic fish were transplanted by intramuscular injection into non-irradiated recipient animals (5×10^4 cells per fish, 2 μl per animal). Muscle cell viability was >85% following dissociation and single-cell preparation (**Supplementary Fig. 4**). Remarkably, EGFP$^+$ muscle fibers were readily detected in all *rag2*^{E450fs} mutant animals by 30 d.p.t. (n = 3 of 3) but not wild-type siblings (n = 4; P = 0.03, Fisher's exact test; **Fig. 2d**,**e** and **Supplementary Table 3**). Fluorescent fibers persisted in *rag2*^{E450fs} mutant fish for up to 60 d.p.t. Histological analysis revealed that EGFP$^+$ muscle fibers were viable, contained muscle striations and were indistinguishable from recipient muscle tissue (**Supplementary Fig. 5**). We next wanted to verify the specificity of our results using a muscle-specific, fluorescent transgenic line. Muscle cells were isolated from the dorsal musculature of α-actin–RFP transgenic fish[15] and injected into the dorsal musculature of recipient fish (2.5×10^5 cells per fish). Again, robust engraftment of fluorescent muscle was observed in only homozygous *rag2*^{E450fs} mutant fish by 30 d.p.t. (n = 5 of 5, **Fig. 2f** and **Supplementary Table 3**) and not heterozygous or wild-type siblings (n = 5 animals per genotype assessed, P = 0.008, Fisher's exact test). These data show that homozygous *rag2*^{E450fs} mutant fish can engraft cells even in the absence of preconditioning with low-dose irradiation.

We next wanted to assess the utility of our model to engraft a diversity of transgenic zebrafish cancers including T-cell acute lymphoblastic leukemia (T-ALL), embryonal rhabdomyosarcoma (ERMS) and melanoma. Specifically, primary *Myc*-induced T-ALL was generated in a mixed Tubingen/AB strain background[16,17] and transplanted into the peritoneal cavity of recipient animals (**Fig. 3a**,**e**,**i**). Homozygous *rag2*^{E450fs} mutant fish robustly engrafted T-ALL by 30 d.p.t. (n = 2 of 2, 1×10^5 cells per fish, **Fig. 3i**). By contrast, heterozygous and wild-type siblings failed to engraft T-ALL ($n \geq 7$ per genotype, $P < 0.03$, Fisher's exact test, **Fig. 3e**). Similar results were observed using three additional T-ALLs arising in syngeneic CG1 strain zebrafish (1×10^5 cells per fish). In total, 39 of 39 *rag2*^{E450fs} mutants engrafted T-ALL arising from CG1 strain fish, whereas 0 of 22 wild-type siblings engrafted leukemia ($P < 0.0001$, Fisher's exact test, **Fig. 3b**,**f**,**j** and **Supplementary Table 4**), suggesting that engraftment is not restricted to particular zebrafish strains or to fish with matched major histocompatibility complexes. Homozygous *rag2*^{E450fs} mutant zebrafish also successfully engrafted fluorescently labeled *KRAS*^{G12D}-induced ERMS generated in both the CG1 and AB strain background (n = 4 independent tumors analyzed, 1×10^4–1×10^6 cells per fish). In total, 24 of 27 homozygous *rag2*^{E450fs} mutant zebrafish engrafted ERMS, whereas 0 of 7 wild-type siblings engrafted disease[18] ($P < 0.0001$, Fisher's exact test, **Fig. 3c**,**g**,**k** and **Supplementary Table 4**). Finally, melanomas that harbor a *TP53* (*p53*) mutation and overexpress both *mitfa* and *BRAF*^{V600E} could successfully engraft into *rag2*^{E450fs} mutant zebrafish but not wild-type siblings[19,20] (n = 4 tumors analyzed, 5×10^5–1×10^6 cells per fish). In total, 25 of 25 homozygous *rag2*^{E450fs} mutant fish engrafted melanoma, whereas 0 of 16 wild-type siblings engrafted disease ($P < 0.0001$, Fisher's exact test, **Fig. 3d**,**h**,**l** and **Supplementary Table 4**). No instances of tissue rejection or tumor regression were observed in engrafted *rag2*^{E450fs} mutant fish (n = 104), showing that homozygous *rag2*^{E450fs} mutant zebrafish can robustly engraft cells from a diversity of genetic backgrounds and even in the absence of preconditioning of recipient animals with γ-irradiation.

Our experiments highlight the use of hypomorphic *rag2*^{E450fs} mutant fish as a universal recipient for allograft cell transplantation into adult fish, ushering in a new era of large-scale cell transplantation studies to directly visualize and assess stem cell self-renewal within normal tissues and clonal heterogeneity, therapeutic responses and growth in cancer.

METHODS

Methods and any associated references are available in the online version of the paper.

© 2014 Nature America, Inc. All rights reserved.

Accession codes. ZFIN: *rag2*^{E450fs} mutant information is available under construct number ZDB-GENO-140623-1 and is designated *rag2*^{fb101}.

Note: Any Supplementary Information and Source Data files are available in the online version of the paper.

ACKNOWLEDGMENTS

This work is supported by the Alex's Lemonade Stand Foundation (J.S.B., M.S.I., D.M.L.), the Leukemia & Lymphoma Society (J.S.B.), the American Cancer Society (D.M.L.), a Massachusetts General Hospital Howard Goodman Fellowship (D.M.L.) and US National Institutes of Health grants F32DK098875 (F.E.M.), R24OD016761 and 1R01CA154923 (D.M.L.). Q.T. is funded by the China Scholarship Council. J.N.B. is funded as the Cancer Care Nova Scotia Peggy Davison Clinician. We thank D. Traver, T. North and J. Rawls for their helpful comments and B. Li for advice.

AUTHOR CONTRIBUTIONS

Q.T., N.S.A., J.S.B., J.C.M., S.A.M., I.M.T. and D.M.L. designed and performed experiments. Q.T., J.C.M. and D.M.L. wrote the manuscript. F.E.M., R.L., I.M.T., M.S.I. and Y.H. contributed reagents and animals. Q.T., N.S.A., J.C.M., J.N.B., R.S.L. and D.M.L. performed data analysis and interpretation.

COMPETING FINANCIAL INTERESTS

The authors declare no competing financial interests.

Reprints and permissions information is available online at http://www.nature.com/reprints/index.html.

1. Traver, D. *et al. Nat. Immunol.* **4**, 1238–1246 (2003).
2. Traver, D. *et al. Blood* **104**, 1298–1305 (2004).
3. White, R.M. *et al. Cell Stem Cell* **2**, 183–189 (2008).
4. Blackburn, J.S. *et al. Leukemia* **26**, 2069–2078 (2012).
5. Ignatius, M.S. *et al. Cancer Cell* **21**, 680–693 (2012).
6. Smith, A.C. *et al. Blood* **115**, 3296–3303 (2010).
7. Moore, F.E. & Langenau, D.M. *Adv. Hematol.* **2012**, 478164 (2012).
8. Sander, J.D. *et al. Nat. Methods* **8**, 67–69 (2011).
9. Couëdel, C. *et al. J. Clin. Invest.* **120**, 1337–1344 (2010).
10. Villa, A. *et al. Blood* **97**, 81–88 (2001).
11. Ramón-Maiques, S. *et al. Proc. Natl. Acad. Sci. USA* **104**, 18993–18998 (2007).
12. Mombaerts, P. *et al. Cell* **68**, 869–877 (1992).
13. Wienholds, E., Schulte-Merker, S., Walderich, B. & Plasterk, R.H. *Science* **297**, 99–102 (2002).
14. Mosimann, C. *et al. Development* **138**, 169–177 (2011).
15. Higashijima, S., Okamoto, H., Ueno, N., Hotta, Y. & Eguchi, G. *Dev. Biol.* **192**, 289–299 (1997).
16. Langenau, D.M. *et al. Oncogene* **27**, 4242–4248 (2008).
17. Langenau, D.M. *et al. Science* **299**, 887–890 (2003).
18. Langenau, D.M. *et al. Genes Dev.* **21**, 1382–1395 (2007).
19. Patton, E.E. *et al. Curr. Biol.* **15**, 249–254 (2005).
20. Ceol, C.J. *et al. Nature* **471**, 513–517 (2011).

© 2014 Nature America, Inc. All rights reserved.

ONLINE METHODS

Animal use and creation of hypomorphic *rag2*^{E450fs} mutant zebrafish. Zebrafish studies were approved by the Massachusetts General Hospital Subcommittee on Research Animal Care, under protocol #2011N000127.

rag2^{E450fs} mutant zebrafish were created using the previously described zinc-finger nuclease (ZFN) pair that targeted the PHD of the zebrafish *rag2* gene[8]. Specifically, RNA was prepared for each ZFN arm and microinjected into AB strain zebrafish (500 ng/µl). F_0 injected animals were raised to adulthood, and single male-by-female matings performed. Resultant progeny were arrayed into 96-well plates and genomic DNA extracted (n = 12 individual embryos per cross). PCR was performed using forward primer (5′-ACTGCTCTAGTTGCAATTCCT) and reverse primer (5′-AGCTGGGGTCATCTTCAGT) to produce a 585-bp PCR amplicon. The PCR cycle parameters were (i) denaturation, 94 °C for 30 s; (ii) annealing, 54 °C for 30 s; and (iii) elongation, 68 °C for 45 s; repeated for 35 cycles. PCR samples were purified and sent for Sanger sequencing. From this analysis, one line was identified with a *rag2* frameshift mutation that starts at amino acid E450 and results in a premature stop codon mutation (designated *rag2*^{E450fs} in this manuscript with an official ZFIN.org allele designation of *rag2*^{fb101}). F_1 progeny were subsequently raised to adulthood, and heterozygous *rag2*^{E450fs} fish were identified by genotyping (see below).

Genotyping of *rag2*^{E450fs} mutant zebrafish. The *rag2*^{E450fs} mutant line is best maintained through heterozygous incrossing (**Supplementary Table 1**) and produces progeny at the expected Mendelian ratios. The *rag2*^{E450fs} allele introduces a *de novo* XcmI site, allowing for restriction enzyme–mediated identification of the mutant allele (diagrammed with representative results in **Supplementary Fig. 6**). Specifically, adult 2- to 4-month-old fish were fin clipped, and genomic DNA was prepared using the modified HotSHOT method[21]. Individual genomic DNA was diluted tenfold, and 2 µl were used in a standard 25-µl volume PCR using *Taq* DNA polymerase (New England BioLabs, Cat# M0273L) with forward primer (5′-ACTGCTCTAGTTGCAATTCCT) and reverse primer (5′- AGCTGGGGTCATCTTCAGT) to produce a 585-bp PCR amplicon. The PCR cycle parameters were (i) denaturation, 94 °C for 30 s; (ii) annealing, 54 °C for 30 s; and (iii) elongation, 68 °C for 45 s; repeated for 35 cycles. For enzymatic digestion, 15 µl of nonpurified PCR reaction were combined with 0.3 µl XcmI + 2 µl 10× NEB buffer 2.1 + 2.7 µl water. The 20-µl reaction was incubated at 37 °C for ≥4 h. Enzymatic digestion was visualized by electrophoresis on a 2% Tris-acetate-EDTA (TAE) agarose gel containing ethidium bromide. Wild-type fish produced a single band at 585 bp. Heterozygous *rag2*^{E450fs} fish produced three bands at 585, 372 and 212 bp due to digestion of the mutant allele, with the two higher molecular weight bands being most distinctive. Homozygous fish produced two bands at 372 and 212 bp. A representative image of genotyping analysis is shown in **Supplementary Figure 6.**

Characterization of the *rag2*^{E450fs} mutant line. RNA *in situ* hybridization of larval fish (**Supplementary Fig. 2**) and histological analysis of thymus of adult fish (**Fig. 1c**,**d**) were completed as previously described[22]. Two-tailed Student's *t*-test analysis was performed to assess larval thymus size differences (**Supplementary Fig. 2c**). For hematopoietic cell quantification (**Fig. 1g**), cytospins of whole kidney marrow from both *rag2*^{E450fs} mutant fish and wild-type siblings were reviewed by clinical hematopathologists (J.N.B. and R.S.L.). At least five 400× magnification fields were analyzed per slide and >200 cells counted per animal. Sample identification was blinded during counts and genotype revealed only after cell counting was completed. Two-tailed Student's *t*-test analysis was performed to assess changes in relative numbers of each blood cell lineage between wild-type and *rag2*^{E450fs} mutant fish. Quantitative real-time PCR (**Fig. 1h**) and nested PCR for *tcra* and *igm* rearrangements (**Fig. 1i**) were completed using the primers shown in **Supplementary Tables 5** and **6**, essentially as previously described[4,23]. Two-tailed Student's *t*-test analysis was performed to assess expression differences in hematopoietic marker genes using quantitative PCR (**Fig. 1h**). A threshold of $P \leq 0.05$ was considered significant for two-tailed Student's *t*-test.

Generation of transgenic zebrafish cancers. T-ALL and ERMS were created by co-injection of either *rag2-Myc* or *rag2-kRAS*^{G12D}, respectively, along with fluorescent reporters under the same promoter into one-cell-stage animals which have been previously described[16]. *Tg*(*mitfa*:*EGFP*);*mitfa*$^{-/-}$;*p53*$^{-/-}$;*Tg*(*mitfa*:*BRAF*(*V600E*)) melanoma-bearing fish were generated as previously described[19,20].

Whole kidney marrow transplantation. Donor ubi-EGFP fish were euthanized by tricaine overdose (Tricaine-S, Western Chemical). Kidney tissue was dissected, placed into a 1.5-ml Eppendorf tube containing 100 µl of suspension solution (0.9× PBS + 5% FBS) and manually pipetted ≥20 times using a 1-ml pipette tip. The kidney tissue suspension was filtered through a 40-µm strainer (Fisher Scientific, Cat# 352340). Total number of viable cells was calculated by Trypan blue (Life Technologies, Cat# 15250061) staining and hemocytometer counts. Cells were centrifuged at 1,000*g* for 10 min and then resuspended in desired volumes for cell transplantation (**Supplementary Table 3**). Recipient fish were preconditioned with 10-Gy γ-irradiation (Cs137 irradiation) 2 d before transplantation. Recipient fish were transplanted with the indicated number of viable kidney marrow cells (**Supplementary Table 3**) injected into the peritoneal cavity using a 26s-gauge Hamilton 80366 syringe (Sigma-Aldrich, 20779).

Whole kidney cell engraftment was assessed using whole-body epifluorescence imaging (Olympus stereomicroscope model MVX10, Olympus DP72 microscope digital camera, DP2-BSW software version 2.2), direct visualization of circulating cells within the tail vasculature beginning at 20 days post transplantation (d.p.t.) and/or flow cytometry. Flow cytometery of kidney marrow was completed in the presence of propidium iodide (PI) to exclude dead cells. The EGFP$^+$ cell fraction was isolated from the marrow of engrafted *rag2*^{E450fs} fish and analyzed following cytospin preparation.

Muscle cell transplantation. Dorsal musculature of donor ubi-EGFP or α-actin–RFP fish was excised from tricaine-overdosed animals. Specifically, the dorsal musculature of the tail posterior to the anus was harvested for muscle transplantation. The muscle tissue was combined from 10–12 animals and mechanically

© 2014 Nature America, Inc. All rights reserved.

disassociated by maceration by repeated dicing using a razor blade for 5 min on a 10-cm Petri dish containing 500 µl of suspension solution (0.9× PBS + 5% FBS). Samples were then supplemented with 5 ml of 0.9× PBS + 5% FBS, and a 5-ml serological pipette was used to suspend the homogenized tissue by repeated pipetting ≥30 times. Cells were then filtered through a 40-µm cell strainer and washed with 5 ml of 0.9× PBS + 5% FBS. Total number of viable cells was calculated by Trypan blue staining and hemocytometer counts. Cells were then centrifuged at 1,000*g* for 10 min and resuspended in desired volumes (**Supplementary Table 3**) before transplantations. No irradiation preconditioning was used before transplantation of muscle cells into *rag2*^{E450fs} mutant fish. Muscle cell transplantations were completed by injecting 2 µl of donor cell preparation into the dorsal musculature on the left side of the recipient fish, using a 26s-gauge Hamilton 80366 syringe.

Engraftment was assessed by visualization of fluorescently labeled muscle fibers using epifluorescence imaging at 10, 20, 30, 45 and 60 d.p.t. Engraftment of ubi-EGFP muscle fibers was confirmed by immunohistochemistry on section slides using an anti-EGFP antibody (JL-8, Living Colors, Cat# 632381). Viability of the muscle fibers was confirmed by the absence of cleaved caspase-3 expression (Cell Signaling, Cat# 9664) and TUNEL staining (customized Millipore S7100 kit, Specialized Histopathology & TMI Core at Dana-Farber Cancer Institute).

Cancer cell transplantation. Donor fish with T-ALL, ERMS and melanoma from different transgenic backgrounds were euthanized by tricaine overdose. Animals were imaged using epifluorescence microscopy and tumor cells isolated as previously described[24]. Specifically, tumors were excised from diseased animals and placed in 500 µl of 0.9× PBS + 5% FBS on a 10-cm Petri dish. Single-cell suspensions were obtained by maceration of tissue with a razor blade followed by manual pipetting to dissociate cell clumps. Cells were filtered through a 40-µm filter, centrifuged at 1,000*g* for 10 min and resuspended at the correct volume (**Supplementary Table 4**) in a total volume of 5 µl per recipient fish for cell transplantation. Cell viability ranged from 58% to 66% as assessed by PI staining and flow cytometry analysis of ERMS tumor cells. 5 µl of tumor cells were transplanted into the peritoneal cavity of each recipient fish using a 26s Hamilton 80366 syringe. No irradiation preconditioning was used for tumor cell transplantations outlined in this work.

Tumor engraftment was assessed at 10, 20, 30 and 45 d.p.t. by epifluorescence microscopy. Recipient fish were sacrificed when moribund or at 45 d.p.t. for animals that failed to engraft disease (wild type). A subset of transplanted animals was photographed, and either (i) these were fixed in 4% paraformaldehyde for sectioning or (ii) peripheral blood samples were collected for cytospins and histological examination.

Statistics. When possible, cell transplantation experiments were completed using ≥3 animals per arm to facilitate analysis using the Fisher's exact test. No animals were excluded from our analysis shown in **Supplementary Tables 3** and **4**, with the exception of *rag2*^{E450fs} mutant fish that engrafted ubi-EGFP^{+} marrow and were scored for circulating EGFP^{+} cells in the tail at ≥20 d.p.t. We did not include these animals in **Supplementary Table 3** because they were sectioned and marrow analysis by flow cytometry was not possible.

Cytospin analysis shown in **Figure 1e**–**g** and **Supplementary Table 2** was reviewed by clinical hematopathologists (J.N.B. and R.S.L.). Genotype was revealed only after cell counting was completed.

Two-tailed Student's *t*-test analysis was performed to assess (i) changes in relative numbers of each blood cell lineage between wild-type and *rag2*^{E450fs} mutant fish (**Fig. 1g**), (ii) expression differences in hematopoietic marker genes using quantitative PCR (**Fig. 1h**) and (iii) thymus size differences (**Supplementary Fig. 2c**). Fisher's exact tests were performed to assess (i) differences in adult thymus phenotypes between wild-type and *rag2*^{E450fs} mutant fish (**Fig. 1c**,**d**), (ii) engraftment rates of whole kidney marrow and muscle transplantations between genotypes (**Fig. 2** and **Supplementary Table 3**) and (iii) tumor cell transplantations (**Fig. 3** and **Supplementary Table 4**). $P \leq 0.05$ was considered significant for all statistical methods.

21. Meeker, N.D., Hutchinson, S.A., Ho, L. & Trede, N.S. *Biotechniques* **43**, 610–614 (2007).
22. Langenau, D.M. *et al. Proc. Natl. Acad. Sci. USA* **102**, 6068–6073 (2005).
23. Blackburn, J.S. *et al. Cancer Cell* **25**, 366–378 (2014).
24. Le, X. *et al. Proc. Natl. Acad. Sci. USA* **104**, 9410–9415 (2007).

© 2014 Nature America, Inc. All rights reserved.

doi:10.1038/nmeth.3031

nature COMMUNICATIONS

ARTICLE

Received 20 Apr 2015 | Accepted 2 Dec 2015 | Published 21 Jan 2016

DOI: 10.1038/ncomms10358 OPEN

Imaging tumour cell heterogeneity following cell transplantation into optically clear immune-deficient zebrafish

Qin Tang[1,2], John C. Moore[1,2], Myron S. Ignatius[1,2], Inês M. Tenente[1,2,3], Madeline N. Hayes[1,2], Elaine G. Garcia[1,2], Nora Torres Yordán[1,2], Caitlin Bourque[4,5], Shuning He[2,6], Jessica S. Blackburn[1,2,7], A. Thomas Look[2,6], Yariv Houvras[4,5] & David M. Langenau[1,2]

Cancers contain a wide diversity of cell types that are defined by differentiation states, genetic mutations and altered epigenetic programmes that impart functional diversity to individual cells. Elevated tumour cell heterogeneity is linked with progression, therapy resistance and relapse. Yet, imaging of tumour cell heterogeneity and the hallmarks of cancer has been a technical and biological challenge. Here we develop optically clear immune-compromised *rag2*^{E450fs} *(casper)* zebrafish for optimized cell transplantation and direct visualization of fluorescently labelled cancer cells at single-cell resolution. Tumour engraftment permits dynamic imaging of neovascularization, niche partitioning of tumour-propagating cells in embryonal rhabdomyosarcoma, emergence of clonal dominance in T-cell acute lymphoblastic leukaemia and tumour evolution resulting in elevated growth and metastasis in *BRAF*^{V600E}-driven melanoma. Cell transplantation approaches using optically clear immune-compromised zebrafish provide unique opportunities to uncover biology underlying cancer and to dynamically visualize cancer processes at single-cell resolution *in vivo*.

[1] Molecular Pathology, Cancer Center, and Regenerative Medicine, Massachusetts General Hospital, Boston, Massachusetts 02129, USA. [2] Harvard Stem Cell Institute, Harvard University, Cambridge, Massachusetts 02139, USA. [3] Abel Salazar Biomedical Sciences Institute, University of Porto, Porto 4099-003, Portugal. [4] Department of Surgery, Weill Cornell Medical College, New York, New York 10065, USA. [5] Department of Medicine, Weill Cornell Medical College, New York, New York 10065, USA. [6] Pediatric Oncology, Dana-Farber Cancer Institute, Boston, Massachusetts 02115, USA. [7] Department of Molecular and Cellular Biochemistry, University of Kentucky, Lexington, Kentucky 40506, USA. Correspondence and requests for materials should be addressed to D.L. (email: dlangenau@mgh.harvard.edu).

The conversion of phenotypically normal cells into malignant cells is often associated with acquired 'hallmarks of cancer' including elevated growth potential, suppression of cell death pathways, development of new vascular networks to feed the growing tumour and acquired cell motility that lead to invasion and metastasis[1,2]. Despite our increased understanding that cancer is driven by molecular changes that convert normal cells into malignant cells, it has become well recognized that not all cancer cells are created equal. For example, the process of clonal evolution that is responsible for initiating cancer is also a critical driver of intra-tumoral heterogeneity that is constantly arising throughout the lifespan of a cancer cell[3]. This heterogeneity provides a rich diversity of cell types and mutations on which natural selection can act, ultimately leading to a subset of cancers that elevate metastatic potential and therapy resistance[4–6]. Despite our new found ability to genetically map individual mutations that are acquired during tumour cell evolution and progression[7–9], it is been difficult to directly visualize how these mutations affect tumour growth in live animals. Access to optically clear animal models would permit the dynamic visualization of the cancer hallmarks and provide unprecedented access to dissect the molecular underpinnings of cancer progression at single-cell resolution.

Over the past two decades, the field of cancer research has been empowered by intra-vital imaging (IVM) in mouse models[10,11]. Refined imaging tools, including confocal, multi-photon and light sheet microscopy, have now been applied to a wide range of cancers to facilitate the discovery of underlying mechanisms that drive cancer growth *in vivo*. For example, Kedrin *et al.* have utilized photoactivatable fluorescent proteins and cell lineage tracing to visualize the tumour cell niche in mammary carcinoma. These studies uncovered that cells adjacent to the vasculature drive invasion and metastasis[12]. Using similar approaches, Calabrese *et al.* discovered that Nestin+ brain tumour stem cells reside in a perivascular niche[13]. Metastasis has also been observed using IVM. For example, a single extravasated C26 colorectal cancer cell has been shown to proliferate and to produce highly mobile pre-metastatic lesions in the liver[14]. Sophisticated fluorescent labelling techniques, including cell lineage tracing using Confetti and brainbow constructs[15,16], have now been successfully integrated with high-resolution microscopy to visually dissect intra-tumoral heterogeneity. For example, Zomer *et al.* utilized the Confetti strategy to label individual mammary tumour cells, and performed proof-of-concept experiments to show that tumour stem cells can become alternatively active or quiescent during tumour development[17]. Despite these successes, challenges presented by the opacity of furred rodents, and the requirement for invasive surgical implantation of imaging windows have limited the application of IVM. Furthermore, requirements of imaging through pre-defined windows often prohibit simultaneous observation of tumour cells from the primary and metastatic sites within the same animal.

Zebrafish have been developed as a robust model of human cancer and have now been widely used for visualizing cancer processes in live animals. For example, our group has used fluorescent transgenic approaches to label embryonal rhabdomyosarcoma (ERMS) cells based on differentiation status. Using these approaches, we have been able to dynamically visualize tumour cell heterogeneity *in vivo*, identifying the existence of a molecularly defined tumour-propagating cell (TPC) that expresses myf5-GFP and other differentiated cell types that express myogenin and drive invasion[18]. Others have utilized cell transplantation into irradiated, optically clear *casper* strain adult zebrafish to visualize melanoma invasion[19], and conversion of T-lymphoblastic lymphoma into leukaemia[20]. Importantly, these initial successes utilized cell transplantation into either syngeneic strains of zebrafish or irradiated recipient animals that only transiently dampen immune responses. Using genome-editing approaches[21], our group has recently developed homozygous $rag2^{E450fs}$ zebrafish. These fish are viable as adults, have deficiencies in T and B cells, and enable robust engraftment of fluorescently labelled zebrafish tumour cells from a wide range of cancers and strains of zebrafish[22]. Despite the utility of the $rag2^{E450fs}$ model for cell engraftment studies, the $rag2^{E450fs}$ mutation was created on the pigmented AB-strain and thus it has been difficult to image tumour cells at single-cell resolution in engrafted animals.

Here we create transparent *casper* strain, $rag2^{E450fs}$ mutant zebrafish and utilize these animals for transplantation studies to image heterogeneity and various 'hallmarks of cancer'. For example, confocal imaging permits the dynamic visualization of TPCs in ERMS and the emergence of clonal dominance in T-cell acute lymphoblastic leukaemia (T-ALL). Serial imaging studies also detail the evolution of metastasis in a subset of $BRAF^{V600E}$-driven melanomas and facilitate the direct visualization of micro-metastatic disease. Our work provides a universal transplantation model for imaging cancer cell processes, opening new avenues for visualizing the functional consequences of cancer cell heterogeneity and clonal evolution at single-cell resolution in the zebrafish.

Results

Engraftment of allogeneic tumours. We have previously reported the production of lymphocyte-deficient $rag2^{E450fs}$ mutant zebrafish that engraft a wide variety of normal and malignant zebrafish cells[22] (ZFIN allele $rag2^{fb101}$). However, these initial studies utilized pigmented, AB-strain zebrafish, making it difficult to directly visualize tumour cells at high resolution *in vivo*. To facilitate imaging of cancer in live zebrafish, the $rag2^{E450fs}$ mutation was bred into the *casper* background—a transparent zebrafish that lacks melanocytes and iridophores[19]. As expected, $rag2^{E450fs}$ (*casper*) zebrafish efficiently engrafted fluorescently labelled T-ALL[23], neuroblastoma[24], ERMS[18,25] and melanoma[26,27] (Fig. 1, Supplementary Fig. 1 and Supplementary Table 1). Tumours derived from *CG1*, AB and *nacre* strain zebrafish engrafted efficiently into $rag2^{E450fs}$ *(casper)* zebrafish and did not require matching at the major histocompatibility complex or pre-conditioning with γ-irradiation. Importantly, engrafted tumours exhibited similar histology as donor tumours (Fig. 1). As has been reported previously for AB-strain wild-type transplant recipients[22], tumours failed to engraft into unconditioned *casper*-strain animals that have an intact rag2 locus (Supplementary Table 1 and Supplementary Fig. 1).

Visualizing the dynamics of tumour neovascularization. Neovascularization is an important hallmark of cancer and has been imaged in a variety of cancers[18,28,29]. To assess the utility of adult $rag2^{E450fs}$ *(casper)* fish for imaging neovascularization in the transplantation setting, green fluorescent protein (GFP)-labelled $BRAF^{V600E}$, $tp53^{-/-}$ amelanotic melanoma[27] cells were implanted into the dorsal musculature of 3-month-old $rag2^{E450fs}$ *(casper)* fish (5×10^5 cells in 2 μl per animal). Because engraftment was initially limited to the dorsal musculature, melanomas developed adjacent to the skin epidermis. Neovascularization could be directly visualized by confocal microscopy following injection of crimson quantum dots[30] into the blood stream at 25 days post transplantation (d.p.t.; Fig. 2a, $n = 8$ animals). Crimson quantum dots were chosen because they excite in far-red wavelengths and can be easily differentiated from

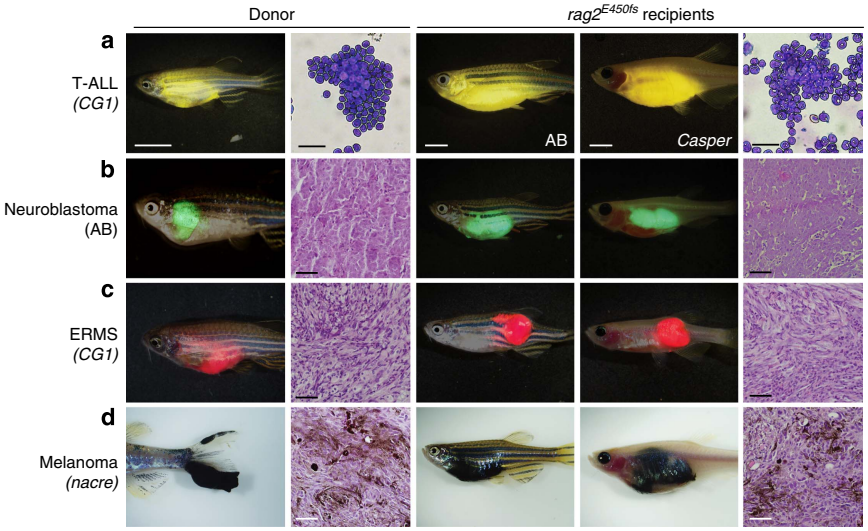

Figure 1 | Zebrafish cancers engraft into homozygous *rag2*^{E450fs} *(casper)* animals. Donor animals shown in the left two panels while transplant recipients are to the right. (**a**) ZsYellow-labelled *Myc*-driven T-ALL from the syngeneic *CG1* background, (**b**) EGFP-labelled neuroblastoma from AB background, (**c**) mCherry-labelled *kRAS*^{G12D}-driven ERMS from *CG1* background, and (**d**) *BRAF*^{V600E}-induced melanoma arising in *tp53*$^{-/-}$ *nacre* background. Tumour cells were transplanted intra-peritoneally (**a**,**b**,**d**) or intra-muscularly (**c**) into both *rag2*^{E450fs} (AB) and *rag2*^{E450fs} *(casper)*-recipient fish. Merged brightfield and fluorescent images are shown at 30 d.p.t. Cytospins of leukaemia cells are shown in **a**, whereas haematoxylin and eosin (H&E)-stained sections are shown in **b**–**d**. Scale bars equal 5 mm in whole animals images, 20 μm for cytospins shown in **a**, and 50 μm for histology sections shown in **b**–**d**.

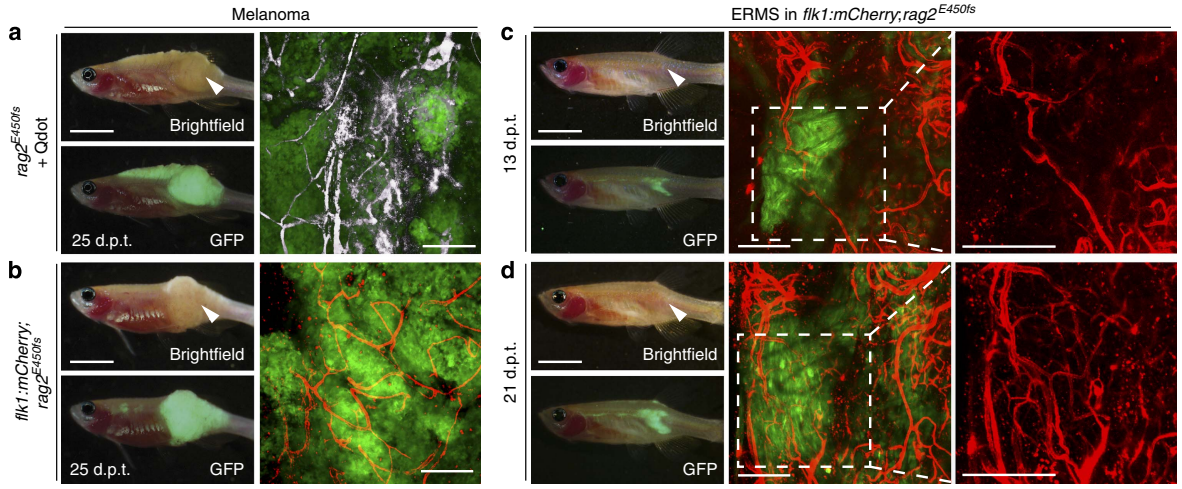

Figure 2 | Imaging neovascularization in *rag2*^{E450fs} *(casper)* zebrafish engrafted with fluorescently labelled melanoma and ERMS. (**a**) GFP-labelled, amelanotic melanoma implanted into *rag2*^{E450fs} *(casper)* fish ($n=8$ animals) and imaged following intravascular injection of crimson quantum dots (Qtracker 655). Whole animal images to the left and confocal images to the right ($\times 100$ magnification, 100–200 μm z-stack). Quantum dot fluorescence has been pseudo-coloured white. (**b**) GFP-labelled, amelanotic melanoma implanted into *flk1:mCherry; rag2*^{E450fs} *(casper)* transgenic zebrafish ($n=4$ animals). (**c**–**d**) GFP-labelled ERMS engrafted into *flk1:mCherry; rag2*^{E450fs} *(casper)* transgenic zebrafish ($n=5$ animals) and serially imaged over time (**c**, 13 d.p.t. and **d**, 21 d.p.t.). White arrowheads denote the site of intra-muscular injection of tumour cells. Scale bars equal 5 mm in whole animal images and 200 μm in confocal images.

other fluorescent proteins used to label tumour cells in this study, including AmCyan, GFP, ZsYellow, DsRED and mCherry. To further refine imaging of neovascularization within solid tumours, we next created *flk1:mCherry*; *rag2*^{E450fs} *(casper)* fish with fluorescently labelled vasculature. Animals were injected intra-muscularly with GFP-labelled melanoma (5×10^5 cells in 2 μl per animal). Following successful engraftment at the site of injection, vessels were readily visualized by confocal microscopy ($\times 100$ magnification, 105.71 μm = 10 z-stacks, $n=4$ animals, Fig. 2b). Finally, we have been able to visualize how neovascularization changes over time within the same animal, which results in the creation of dense vascular networks associated with ERMS growth ($\times 100$ magnification, 223.64 μm = 10 z-stacks, Fig. 2c,d). Together, these experiments demonstrate the ease and utility of

imaging neovascularization in solid tumours using the *rag2*^{E450fs} (*casper*) fish.

Imaging ERMS heterogeneity at single-cell resolution. We next wanted to dynamically visualize tumour cell heterogeneity at single-cell resolution using a transgenic model of *kRAS*^{G12D}-driven ERMS[25]. We have previously created primary ERMS in triple transgenic *myf5:GFP; myogenin-H2b:mRFP; mylpfa:lyn-cyan* zebrafish, which enables the labelling of tumour cells based on differentiation status[18]. To achieve direct imaging of heterogeneous tumour cell populations in adult zebrafish, we engrafted these fluorescent transgenic ERMS by intra-muscular injection into 3-month-old adult *flk1:mCherry*; *rag2*^{E450fs} (*casper*) strain zebrafish (4×10^5 cells in 2 µl per animal, Fig. 3a,b). Confocal microscopic imaging revealed that GFP-labelled TPCs and AmCyan-labelled differentiated cells were largely confined to distinct regions of the tumour (× 100 magnification, Fig. 3c, left panel), consistent with previous reports[18]. Remarkably, the vasculature transects areas of regional tumour cell heterogeneity. We have also noted that in this particular case, juxtaposition of specific ERMS cell subtypes near vascular beds was not observed. Higher magnification imaging of areas enriched with differentiated ERMS cells revealed the presence of *myf5-GFP*+ TPCs, albeit at reduced numbers when compared with other regions of the tumour (× 400 magnification, Fig. 3c, right panel). Our data suggest that ERMS cells largely reside in regionally defined niches based on differentiation status and are not anatomically confined by proximity to vessels. The combination of fluorescent transgenic labelling of tumour cell subpopulations and subsequent cell transplantation will be important for defining how niche topology is established and ultimately influences continued tumour growth in ERMS and a wide range of cancers.

Detailing emergence of clonal dominance in T-ALL. We next wanted to use our model to dynamically visualize the functional consequences of tumour cell heterogeneity and emergence of clonal dominance in T-ALL. It is well known that human leukaemias and myelomas are oligoclonal at diagnosis; however, relapse is often driven by emergence of an underrepresented clone contained within the primary malignancy[31–35]. We have previously created Myc-induced T-ALLs that express a variety of fluorescent proteins and then used cell transplantation to create T-ALLs derived from single leukaemia cells[36]. Using these monoclonal T-ALLs, our experiments sought to dynamically visualize how individual T-ALL clones grow when combined together, testing the hypothesis that inherent functional differences between cells drive the emergence of clonal dominance.

First, we assessed the kinetics of leukaemia regrowth in clones that exhibited wide differences in leukaemia-propagating cell (LPC) frequency and latency. Specifically, we mixed equal numbers of AmCyan, ZsYellow and DsRED-labelled cells isolated from three independent T-ALLs (Supplementary Fig. 2a–c). Following transplantation into the dorsal musculature (3.3×10^4 of each clone, 1.0×10^5 total cells per recipient animal), engrafted fish were imaged by confocal microscopy at 14 and 25 d.p.t. Consistent with our expectations, ZsYellow-labelled T-ALL cells with the highest LPC frequency and fastest growth outcompeted the other clones at each of the time points analysed, making up 48.7% of the leukaemia by 14 d.p.t. and 72.3% by 25 d.p.t. (Supplementary Fig. 2d,e). These data suggest that clonal dominance can result from inherent functional differences between clones.

We next wanted to examine emergence of clonal dominance in T-ALL that had similar LPC frequency and growth kinetics, exploring the notion that clonal dominance may also emerge stochastically *in vivo*. For example, Lgr5+ intestinal crypt stem cells exhibit a pattern of neutral drift, ultimately resulting in

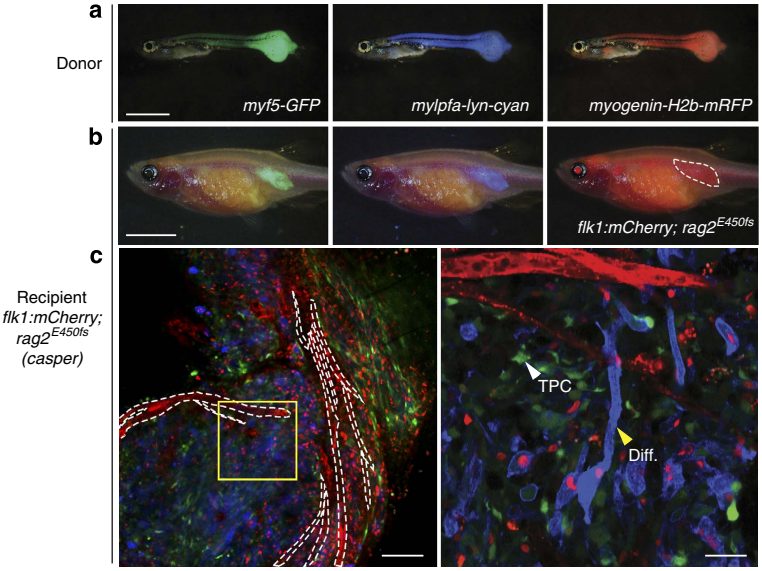

Figure 3 | Resolving tumour cell heterogeneity in ERMS at single-cell resolution following engraftment into *flk1:mCherry; rag2*^{E450fs} *(casper)* zebrafish. (**a**) Epi-fluorescent images of primary ERMS in a 32-day-old *myf5:GFP; myogenin-H2b:mRFP; mylpfa:lyn-cyan* triple transgenic zebrafish. (**b**) Epi-fluorescent images of *flk1:mCherry; rag2*^{E450fs} *(casper)*-recipient fish engrafted intra-muscularly with fluorescently labelled ERMS at 28 d.p.t. ($n = 4$ animals). (**c**) Confocal image with mCherry-labelled vasculature outlined by white dashed lines (left, × 100 magnification). Higher magnification of boxed region (right, × 400 magnification). Myosin-expressing, differentiated cells (Diff.) and less frequent *myf5-GFP*+ tumour-propagating cell (TPC) denoted by arrowheads. Scale bar equals 2 mm in **a**, 5 mm in **b**, 100 µm (**c**, left panel) and 25 µm (**c**, right panel).

regional dominance of a single clone within each villus[37]. In the cancer setting, elegant cell lineage tracing experiments have confirmed that clonal drift can impart regional dominance of Lgr5+ intestinal crypt stem cells in mouse intestinal adenomas[38]. To assess if clonal drift may also account for dominance of T-ALL clones over time, T-ALL clones that had similar growth rates and LPC frequencies were transplanted into recipient *rag2*^{E450fs} *(casper)* fish (3.3×10^4 of each clone, 1.0×10^5 total cells per recipient animal). Despite these leukaemias having similar growth rates, latency and LPC frequencies (Fig. 4a–c), the AmCyan+ clone was consistently outcompeted over time, comprising only $9.8 \pm 6.4\%$ of the leukaemia by 22–24 d.p.t. (Fig. 4d,e). By contrast, the remaining leukemias contained both mCherry+ and ZsYellow+ cells and in some instances dominance of one clone prevailed (Fig. 4f, $n = 16$ animals). To rule out the potential effects of fluorescent labelling may have on the proliferation of leukaemia cells, we repeated the same experiment with another combination of AmCyan, ZsYellow and mCherry T-ALL clones that also shared similar LPC frequency and latency. Interestingly, with this combination, the ZsYellow-labelled cells was reproducibly outcompeted by the AmCyan- or mCherry-labelled cells, with dominance of these latter clones being observed in animals over time ($n = 13$ animals total, 2 independent experiments, Supplementary Fig. 3). We conclude that clonal dominance can result from inherent genetic and epigenetic differences between different tumour clones, which was not revealed using traditional limiting dilution cell transplantation approaches that only analyse the growth of individual clonal populations of cells. Moreover, our experiments provided additional evidence that neutral stochastic drift can account for emergence of clonal dominance over time.

Tumour evolution and metastasis in melanoma. Metastasis is a major clinical challenge for those diagnosed with melanoma and is associated with poor prognosis[39,40]. Not all cancer cells can enter the circulation and seed new areas of tumour growth, suggesting that heterogeneity and continued clonal evolution

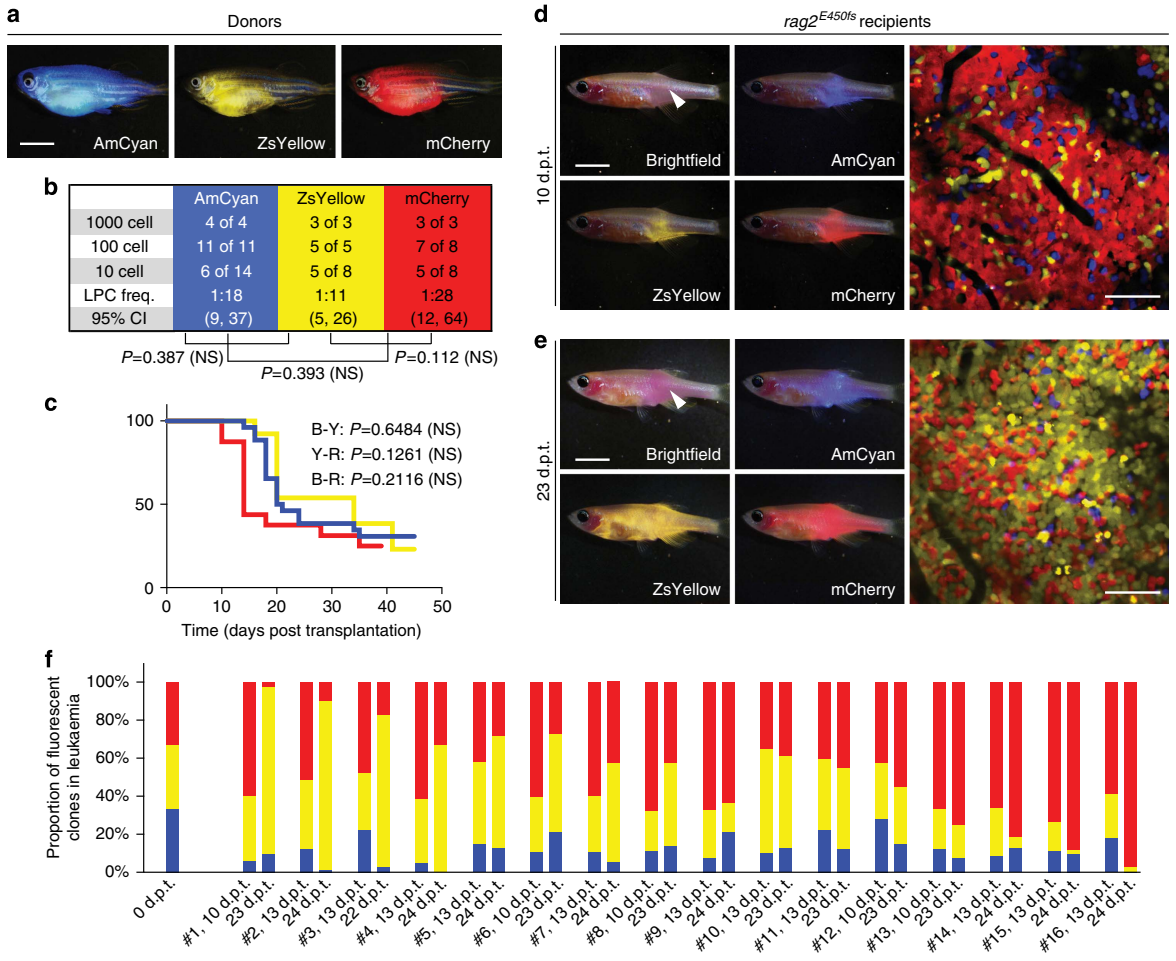

Figure 4 | Visualizing the emergence of clonal dominance in Myc-induced T-ALL. (**a**) Donor animals engrafted with monoclonal T-ALL arising in the *CG1* background. (**b**,**c**) Monoclonal T-ALLs were implanted into the syngeneic *CG1* strain fish and assessed for LPC frequency by limiting dilution cell transplantation (**b**) or latency of regrowth (**c**). *P*-values are noted within each panel. Not significant (NS). (**d**,**e**) Confocal imaging of engrafted *rag2*^{E450fs} *(casper)* fish at 10 d.p.t. (**d**) and 23 d.p.t. (**e**). White arrow denotes site of injection, and the location for confocal imaging. (**f**) Relative proportions of each fluorescent clone contained within leukaemias from individual engrafted animals ($n = 16$ animals). Imaging was completed on the same animals at 10–13 d.p.t. and 22–24 d.p.t. The ZsYellow+ clone dominates leukaemia regrowth in animals #1–3, whereas mCherry+ dominates in animals #13–16. Scale bars equal 5 mm in whole animal images and 50 μm in confocal images.

likely drive metastasis in a large subset of cancers[41]. Yet, to date, zebrafish models of *bona fide* metastatic progression have not been fully described. To recapitulate metastasis in adult zebrafish, we first transplanted melanoma cells retro-orbitally into the recipient *rag2*^{E450fs} *(casper)* fish. Robust engraftment was observed at the site of injection, followed by local infiltration into structures adjacent the gill, head kidney and kidney marrow (Fig. 5a,b). Yet, with a stringent definition of metastasis, we could not document a single case where metastasis originated from haematogenous spread or was delineated by growth clearly separated from the primary site.

To further refine methods to assess metastatic spread, we next injected GFP-labelled, *BRAF*^{V600E}, *tp53*$^{-/-}$ melanoma cells into the dorsal musculature of *rag2*^{E450fs} *(casper)* zebrafish, reasoning that infiltration into muscle would be clearly distinguished from seeding of distant sites within the visceral organs. Using this approach, three out of six primary melanomas metastasized to structures near the thymus and head musculature that were clearly distinct from the primary lesion (Fig. 5c and Supplementary Table 2). In total, 8 of 58 engrafted animals harboured distant metastasis by 30 d.p.t. (Supplementary Table 2). Metastatic growth was easily quantified over time following serial imaging of the same animal (Fig. 5d). GFP+ metastatic lesions were independently confirmed by histo-pathological analysis for morphology, pigmentation and anti-GFP immunostaining on section (Fig. 5e). Using similar approaches, we have also dynamically visualized metastatic tumour growth in neuroblastoma and ERMS (Supplementary Fig. 4), suggesting this approach will likely be broadly useful for assessing the kinetics of metastatic colonization and growth in a wide range of solid tumours.

We next wanted to assess how metastatic potential may change in the same tumour over time and whether serial passaging of individual melanomas could result in phenotypic changes, including increased aggression, invasion and acquisition of metastatic characteristics. Specifically, two non-metastatic *BRAF*^{V600E}, *p53*$^{-/-}$ melanomas at the 1° passage were implanted into the dorsal musculature of *rag2*^{E450fs} *(casper)* zebrafish and animals assessed for local engraftment, invasion and metastatic growth following serial passaging. Sectioning and microscopic analysis confirmed that early passaged melanomas were not metastatic and tumours were confined to the site of injection (Fig. 6a and Supplementary Fig. 5a). Following serial passaging, one melanoma continued to resemble the parental tumour and did not change its growth rate or metastatic potential (8 passages, total 191 days *in vivo*, Supplementary Fig. 5b,c). By contrast, the second melanoma lost pigmentation, had significantly accelerated growth and harboured metastatic lesions (7 passages, total 134 days *in vivo*, Fig. 6b,c). With this particular tumour, GFP+ lesions were found to have metastasized to the mesonephric trunk kidney by 6 d.p.t., which eventually spread to the regions adjacent to the thymus and head kidney by 12 d.p.t.

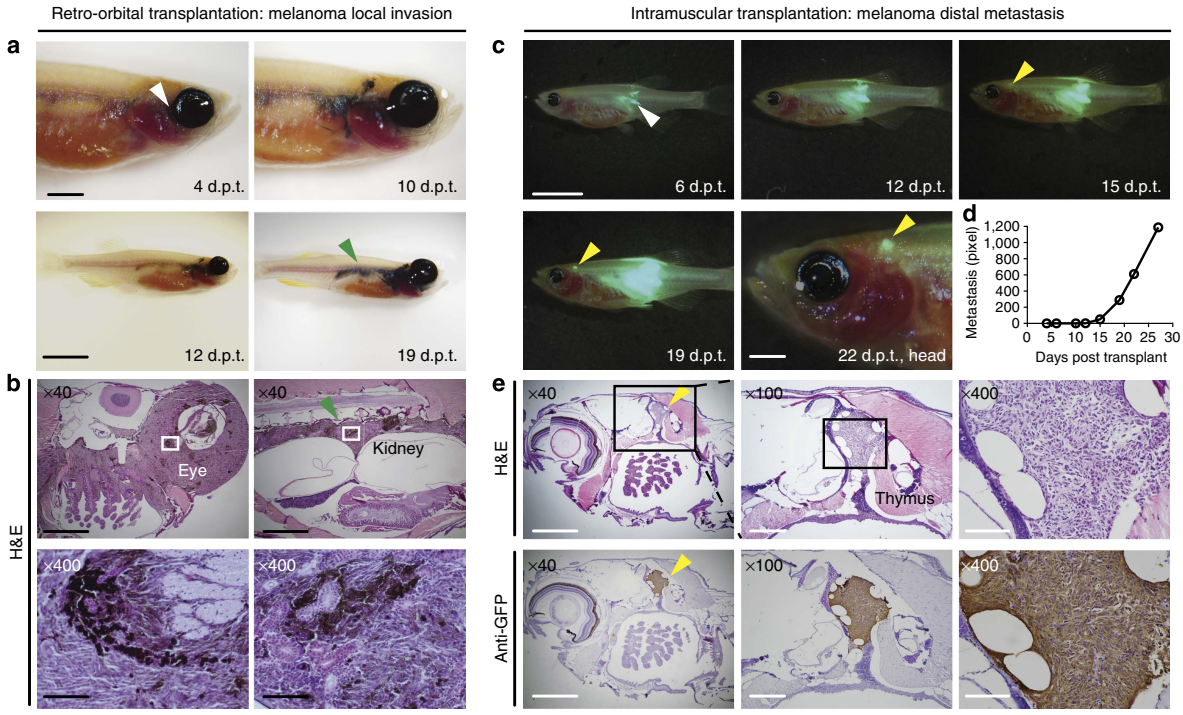

Figure 5 | Visualizing melanoma invasion and metastasis following engraftment into *rag2*^{E450fs} *(casper)* mutant fish. (**a**) Invasion assays using retro-orbital transplantation of a *BRAF*^{V600E}, *tp53*$^{-/-}$ pigmented melanoma. White arrow denotes the site of injection. Green arrow denotes spread to the kidney marrow that is contiguous with primary tumour growth that has arisen adjacent to the eye. Histological examination confirmed the presence of pigmented melanoma cells at the site of injection (**b**, left panels) and contiguous with the trunk kidney (**b**, right panels). (**c**) Metastasis assays using implantation of non-pigmented, GFP-labelled melanoma cells into the dorsal musculature of *rag2*^{E450fs} *(casper)*-recipient fish. White arrow denotes the site of injection. Yellow arrow denotes site of distal metastasis. (**d**) Quantification of metastatic growth as assessed by epi-fluorescence microscopy over time. (**e**) Haematoxylin and eosin-stained sections of the same animal imaged in **c**, confirming metastatic growth of melanoma adjacent to the thymus (top panels) and confirmed by anti-GFP immunostaining on section (bottom panels). Scale bars equal 5 mm for whole animal images, 2 mm in images of heads, 1 mm in ×40 histological images; 300 μm in ×100 histological images and 100 μm in ×400 histological images.

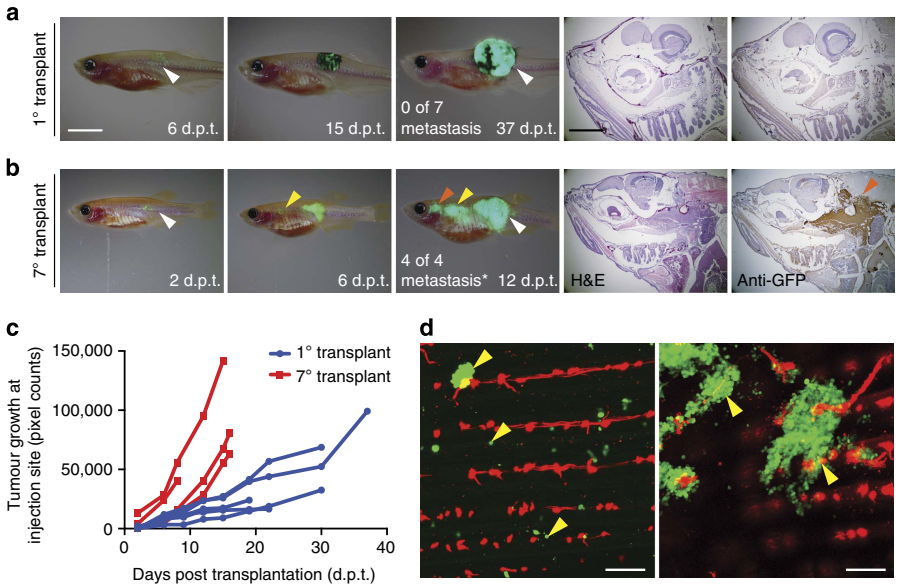

Figure 6 | Assessing metastatic potential and the functional consequences of tumour evolution in melanoma. (**a**,**b**) Serial imaging of engrafted GFP-labelled melanoma implanted into adult *rag2*^{E450fs} *(capser)* mutant fish. The 1° transplant was pigmented (**a**), whereas the 7° transplanted melanoma had lost pigmentation (**b**). Number of animals with metastatic growth is noted (*$P = 0.003$, Fisher's exact test comparing 1° and 7° transplant). White arrow indicates the site of injection. Yellow and red arrows denote sites of distal metastases. Histological staining (H&E and anti-GFP) of distal metastasis is shown in the right panels. (**c**) Quantification of tumour growth at the site of initial engraftment over time. (**d**) Confocal imaging of micro-metastatic lesions found adjacent to the tail vasculature of *flk1:mCherry; rag2*^{E450fs} *(casper)*-recipient fish engrafted with 7° transplant melanoma. Yellow arrows denote micro-metastatic lesions. Scale bars equal 5 mm for whole animal images in **a**,**b**, 2 mm for histology shown in **a**,**b** and 200 μm in **d**.

($n = 4$ of 4, $P = 0.003$, two-tailed Fisher's exact test). Confocal imaging revealed seeding of GFP-labelled cells to distal sites within the tail of the recipient fish, suggesting the formation of micro-metastatic lesions adjacent to *flk1:mCherry*-labelled vasculature ($n = 2$, Fig. 6d). Our experiments confirm that not all melanoma cells have metastatic capacity and that evolution of metastatic potential occurs in melanoma, consistent with that have been reported for human melanoma[42,43]. In total, our model provides a dynamic imaging platform to visualize the tropism of metastasis.

Discussion

Imaging cancer cell heterogeneity and the hallmarks of cancer in live animals has been a challenge. Many investigators have developed imaging modalities and complex surgical approaches in rodent models to gain optical access to developing tumours. These approaches often require implantation of imaging windows for repeated high-resolution IVM[10,11]. Using these experimental platforms, investigators have successfully imaged several hallmarks of cancer, including migration[44], intravasation[45], extravasation[46], invasion[47] and metastasis[12,14], as well as responses to chemotherapies *in vivo*[48]. In hope of bypassing the need for surgical intervention and overcoming the limitation of visualizing cancer cells only within predetermined imaging windows, we engrafted fluorescently labelled cancers into optically clear immune-compromised zebrafish and directly imaged tumours using confocal microscopy. Engraftment of fluorescent cancers into the *rag2*^{E450fs} *(casper)* zebrafish has facilitated the direct visualization of single cancer cells, functional differences between tumour cell clones and several hallmarks of cancer including acquisition of elevated growth potential, development of new vascular networks and acquired cell motility leading to invasion and metastasis.

The functional consequences of tumour cell heterogeneity have only recently begun to be explored using IVM, and a number of interesting and unexpected tumour cell behaviours have been revealed. For example, our group has utilized fluorescent transgenic approaches to label ERMS cells based on muscle differentiation status[18]. Our experiments uncovered that differentiated ERMS cells seed new areas of growth, followed later by slow-moving, less-differentiated myf5+ TPCs, challenging the notion that cancer stem cells drive invasion and metastasis. Imaging approaches have not been limited to analysis of primary tumours. Rather, Chapman *et al.* have used xenograft cell transplantation of human melanoma cells into larval zebrafish to assess the effects of intra-tumoral heterogeneity on growth[49]. They found that tumours with high invasive capacity could impart migratory potential to poorly invasive cell types. Moreover, the poorly invasive cells could also enhance colonization by aggressive melanomas when co-implanted into larval fish, suggesting cell–cell cross-talk and collaborative signalling networks can enhance migratory and invasive behaviour between melanoma subclones. Using differential labelling of human melanoma cells with GFP and mCherry, these authors were able to dynamically image these processes in live engrafted fish. Here, we performed proof-of-concept experiments to assess the utility of *rag2*^{E450fs} *(casper)* zebrafish for visualizing engraftment of heterogeneous ERMS cells in live animals. For example, we directly visualized niche partitioning based on differentiation status using fluorescently labelled ERMS cells. These niches are not anatomically confined by proximity to vessels, in contrast to what has been observed in osteosarcoma[50] and brain tumours[13,51] where cancer stem cells lie in unique niches adjacent vessels. Furthermore, cell transplantation into orthotopic sites in the *rag2*^{E450fs} *(casper)* zebrafish permitted imaging of cells at single-cell resolution in live animals. We envision that similar strategies will likely aid in assessing stromal

cell contributions to tumour growth. In total, our cell transplantation and imaging approaches will likely facilitate efforts in defining how niche topology is established and ultimately influences continued tumour growth.

Evidence for continued clonal evolution and selection following treatment has now been seen in a wide range of human cancers. For example, human leukaemias and myelomas are oligoclonal at diagnosis; however, relapse is commonly driven by an underrepresented clone contained within the primary malignancy[31–35]. Similar dynamics of heterogeneity has also been observed in solid tumours. For example, triple-negative breast cancers are comprised of heterogeneous clones that harbour a wide spectrum of mutations that can change from the time of diagnosis to relapse[52,53]. Altering frequencies of specific clones have also been observed during tumour progression in pancreatic cancer[54,55] and brain tumours[56]. Elegant cell lineage tracing experiments in mice have shown experimentally that stochastic clonal drift can contribute to regional dominance of Lgr5+ intestinal crypt stem cells in mouse intestinal adenomas[38]; yet it is unclear if this pattern applies to a wider array of cancer subtypes. Here, we have experimentally recreated tumour cell heterogeneity by implanting equal numbers of fluorescently labelled T-ALL clones into the *rag2*^{E450fs} *(casper)* zebrafish. By competing these T-ALL clones together, we find that one clone was consistently outcompeted over time despite having equal self-renewal potential and overall growth kinetics. Our data suggest that subtle functional variations can exist within clones that may not be uncovered using traditional cell transplantation assays that assess tumour regrowth of only single clones, likely underestimating differences in latency and LPC frequency. Alternatively, these data may suggest that clones actively suppress the growth of other clones and/or secrete factors to enhance growth of only related cells. This interpretation is consistent with recent findings in breast cancer where paracrine factor signalling from one clone can alter growth of unrelated clones within the tumour[57]. Taken together, these *in vivo* competition experiments have uncovered interesting and potentially new biology that could not have been discovered using traditional limiting dilution cell transplantation approaches, facilitating the dynamic emergence of clonal dominance within the same animal overtime.

Metastasis can be experimentally assessed in mouse models by engrafting tumour cells into the vasculature and then identifying metastatic lesions at necropsy. Alternatively, luciferase bioluminescent imaging and non-invasive, whole-body imaging methods have also been developed, including computed X-Ray tomography, positron emission tomography and magnetic resonance imaging. These imaging modalities are limited to detection of tumours that are 200 μm in diameter, expensive and largely inaccessible to many laboratories[58–60]. Here, we have optimized cell transplantation into adult, immune-deficient *rag2*^{E450fs} *(casper)* zebrafish in order to dynamically visualize tumour cell migration, invasion and metastasis at high resolution. We performed cell transplantation of fluorescently labelled zebrafish tumour into the optic vessels and dorsal musculature, establishing that metastatic progression is best assessed following injection into the dorsal musculature. Furthermore, we have been able to visualize the dissemination of micro-metastatic lesions to sites adjacent to the tail vasculature in *flk1:mCherry; rag2*^{E450fs} *(casper)* zebrafish using simple confocal imaging. Finally, using serial transplantation, we were able to evolve melanomas with high metastatic potential, providing a novel platform for identifying driver mutations that are specifically correlated with progression. We envision that facile genetic approaches including transgenesis and genetic knock-out using CRISPR/Cas9 will quickly make zebrafish the choice experimental model for assessing gene pathways that modulate tumour progression and metastasis, especially in the transplantation setting.

Methods

Creation of *rag2*^{E450fs} *(casper)* homozygous mutant zebrafish. Zebrafish studies were approved by the Massachusetts General Hospital Subcommittee on Research Animal Care (protocol #2011N000127).

rag2^{E450fs} *(casper)* homozygous mutant zebrafish were created by crossing *rag2*^{E450fs} (*rag2*^{fb101}) mutant fish into the *casper* background[19]. Animals were maintained as *rag2*$^{E450fs/+}$; *roy*$^{-/-}$; *mitfa*$^{-/-}$ lines and in-crossed to generate triple mutant animals. Resulting progeny were fin clipped and genotyped using the same method as we previously published[22]. Specifically, genomic DNA was extracted using the Hotshot method described by Meeker *et al.*[61], and subjected to PCR using forward primer 5′-ACTGCTCTAGTTGCAATTCCT-3′ and reverse primer 5′-AGCTGGGGTCATCTTCAGT-3′. PCR was completed using 94 °C denaturation for 30 s, 54 °C annealing for 30 s and 68 °C elongation for 45 s (35 cycles). PCR-amplified products were then incubated at 37 °C overnight with XcmI, which created a single cut in the mutant allele. Finally, DNA products were resolved either on a 2% agarose gel or using the Qiaxcel genotyping system. For neovascularization studies, *flk1:mCherry* transgenic fish[62] were crossed with *rag2*^{E450fs} *(casper)* fish and in-crossed to create compound mutant animals.

Tumour creation and cell transplantation into zebrafish. Primary and serially passaged tumours were derived from established transgenic zebrafish models. For example, T-ALLs were created by co-microinjection of linearized *rag2:cMyc* and fluorescent transgenic reporters into one-cell stage *CG1* fish[36,63] (Figs 1 and 4 and Supplementary Figs 1–3). GFP-labelled ERMS were created by co-microinjection of linearized *rag2:kRAS*^{G12D} and *rag2:GFP* transgenes into one-cell stage *CG1* fish[64] (Fig. 2); double-fluorescent ERMS were created by microinjection of linearized *rag2:kRAS*^{G12D} into one-cell-stage stable transgenic *myf5:GFP; mylpfa:mCherry CG1* fish[18] (Fig. 1 and Supplementary Fig. 4). Triple-fluorescent transgenic ERMSs were created by microinjecting the linearized *rag2:kRAS*^{G12D} transgene into one-cell stage stable transgenic *myf5:GFP; myogenin-H2b:mRFP; mylpfa:lyn-cyan* zebrafish in the AB background (Fig. 3). Melanomas were created by overexpression of MiniCoopR-EGFP in the embryos of *Tg (mitfa:BRAF*^{V600E}*); mitfa*$^{-/-}$; *tp53*$^{-/-}$ or *Tg (mitfa:BRAF*^{V600E}*); mitfa*$^{-/-}$; *tp53*$^{-/-}$; *alb*$^{-/-}$ zebrafish[27] (Figs 1,2,5 and 6 and Supplementary Fig. 5), and were a kind gift from the Houvras laboratory. The official ZFIN designation for the *tp53*$^{-/-}$ zebrafish line is *zdf1*^{M214K}, originally reported by Berghmans *et al.*[65]. Neuroblastomas were a kind gift from the Look laboratory[24].

Cell transplantation experiments utilized both male and female *rag2*^{E450fs} *(casper)* homozygous mutant zebrafish. Recipient animals were transplanted at 2–4 months of age. Tumour cell transplantations were completed by intra-peritoneal, intra-muscular and retro-orbital injections[66–68]. Intra-muscular and retro-orbital injections were completed using microinjection of 2–3 μl of cell suspension. Recipient fish were scored for tumour engraftment, growth, invasion or metastasis by epi-fluorescent microscopy every 3–4 days until 30 d.p.t. or when animals were moribund.

Confocal imaging of neovascularization and micro-metastasis. *rag2*^{E450fs} *(casper)* animals were engrafted with GFP-labelled ERMS or melanoma. To visualize tumour vasculature, animals were injected with Quantum dot 655 reagent (Qtracker 655, 405–615 nm excitation, 655 nm emission, 2.0 μM, Life Technologies Cat# Q21021MP). Specifically, animals were injected with freshly prepared 1:3 diluted reagent (1 volume Qtracker 655 solution diluted in 2 volumes of 0.9x PBS, yielding a final concentration of 0.66 μM) using a 26s gauge Hamilton syringe (4 μl injected intra-peritoneally, and 2 μl directly into the dorsal aorta). After 30 min, animals were anaesthetized using 168 mg l^{-1} Tricaine (MS-222, pH = 7.5) and placed onto a 12.0-mm glass bottom imaging plate (Thermo Scientific, Cat# 150680). Under anaesthesia, motor functions of the animal were greatly reduced and operculum movements were significantly slowed. Each animal was imaged under anaesthesia for 1–2 min, allowing enough time for z-stack imaging or multi-position single plane imaging using confocal microscopy. To ensure optimal survival of the adult zebrafish being imaged, anaesthetized animals were simply laid down on the side in the imaging dish, with the tumour facing towards the lens. No agarose embedding of the sample was used. Imaging was completed using an inverted Zeiss LSM 710 confocal microscope. For neovascularization (Fig. 2) and micro-metastasis imaging (Fig. 6d), z-stack imaging at ×100 magnification was achieved with a ×10 objective (numerical aperture = 0.45, coverglass thickness = 0.17 mm, working distance = 2.0 mm). Image series were acquired in the ZEN software (single pass point scanning at ~10 μm per step over 100–200 μm distances). Fluorescent imaging was completed using the following settings: GFP: excitation = 488 nm, emission = 503–528 nm; mCherry/mRFP: excitation = 561 nm, emission = 602–624 nm; Qtracker 655: use AlexaFlour647 setting, excitation = 633 nm, emission = 638–755 nm. Laser intensity percentages were set to be between 10 and 20% depending on the brightness of the fluorescent labels used. The 'Best Signal' option in the 'Smart Setup' was used for easy modulation of the gating of each colour. For imaging fluorescent combinations, gate settings were manually adjusted to avoid overlap of fluorescent signals. For z-stack images,

planes were merged based on maximum intensity in Fiji (ImageJ). After imaging, fish were immediately transferred into recovery tanks that contained fresh system water, and later returned to the facility.

Confocal imaging of heterogeneity in ERMS and T-ALL. Multi-colour confocal fluorescence imaging was completed in both ERMS and T-ALL. Specifically, in ERMS (Fig. 3) and T-ALL (Fig. 4 and Supplementary Figs 2,3), we simultaneously imaged using three-colour combinations including AmCyan (excitation = 458 nm, emission = 472–508 nm), GFP (excitation = 488 nm, emission = 493–586 nm), ZsYellow (excitation = 514 nm, emission = 521–547 nm), DsRED (excitation = 561 nm, emission = 575–703 nm) and mCherry/mRFP (excitation = 561 nm, emission = 602–623 nm). Laser intensity percentages were set to be 18%. For imaging at single-cell resolution, × 400 magnification was achieved with a × 40 water emersion objective (NA = 1.3, coverglass thickness = 0.14–0.19 mm, working distance = 0.62 mm for 0.17 mm coverglass). The 'Best Signal' option in the 'Smart Setup' was used for easy modulation of the gating of each colour. For T-ALL, proportions of each clone were quantified in the Fiji (ImageJ) software by measure of area covered by each fluorescent colour (Fig. 4 and Supplementary Fig. 2,3f), or manual cell counts (Supplementary Fig. 3g). Both quantification methods produce consistently similar results.

Histological examination. Tumour histology was performed on animals as previously described[22]. Briefly, animals were fixed in 4% paraformaldehyde, embedded in paraffin and step sectioned. Adjacent slides were stained with haematoxylin and eosin or anti-GFP (Living Colors Monoclonal Antibody JL-8, Clontech, 1:1,000 dilution).

Statistical methods. Leukaemia propagating cell frequencies were calculated using the extreme limiting dilution analysis software (http://bioinf.wehi.edu.au/software/elda/). Differences in the LPC frequency were reported with a 95% confidence interval. Differences of latency were assessed by log-rank (Mantel-Cox) tests (Fig. 4 and Supplementary Figs 2,3). In the melanoma evolution experiments (Fig. 6), increased metastatic potential was assessed by Fisher's exact test, comparing the number of animals with metastatic disease at 1° transplant with those found after 7° transplant.

References

1. Hanahan, D. & Weinberg, R. A. Hallmarks of cancer: the next generation. *Cell* **144,** 646–674 (2011).
2. Hanahan, D. & Weinberg, R. A. The hallmarks of cancer. *Cell* **100,** 57–70 (2000).
3. Janiszewska, M. & Polyak, K. Clonal evolution in cancer: a tale of twisted twines. *Cell Stem Cell* **16,** 11–12 (2015).
4. Burrell, R. A. & Swanton, C. Tumour heterogeneity and the evolution of polyclonal drug resistance. *Mol. Oncol.* **8,** 1095–1111 (2014).
5. Easwaran, H., Tsai, H. C. & Baylin, S. B. Cancer epigenetics: tumor heterogeneity, plasticity of stem-like states, and drug resistance. *Mol. Cell* **54,** 716–727 (2014).
6. Polyak, K. Tumor heterogeneity confounds and illuminates: a case for Darwinian tumor evolution. *Nat. Med.* **20,** 344–346 (2014).
7. Almendro, V. *et al.* Inference of tumor evolution during chemotherapy by computational modeling and in situ analysis of genetic and phenotypic cellular diversity. *Cell Rep.* **6,** 514–527 (2014).
8. Gerlinger, M. *et al.* Genomic architecture and evolution of clear cell renal cell carcinomas defined by multiregion sequencing. *Nat. Genet.* **46,** 225–233 (2014).
9. McFadden, D. G. *et al.* Genetic and clonal dissection of murine small cell lung carcinoma progression by genome sequencing. *Cell* **156,** 1298–1311 (2014).
10. Pittet, M. J. & Weissleder, R. Intravital imaging. *Cell* **147,** 983–991 (2011).
11. Ellenbroek, S. I. & van Rheenen, J. Imaging hallmarks of cancer in living mice. *Nat. Rev. Cancer* **14,** 406–418 (2014).
12. Kedrin, D. *et al.* Intravital imaging of metastatic behavior through a mammary imaging window. *Nat. Methods* **5,** 1019–1021 (2008).
13. Calabrese, C. *et al.* A perivascular niche for brain tumor stem cells. *Cancer Cell* **11,** 69–82 (2007).
14. Ritsma, L. *et al.* Intravital microscopy through an abdominal imaging window reveals a pre-micrometastasis stage during liver metastasis. *Sci. Transl. Med.* **4,** 158ra145 (2012).
15. Livet, J. *et al.* Transgenic strategies for combinatorial expression of fluorescent proteins in the nervous system. *Nature* **450,** 56–62 (2007).
16. Snippert, H. J. *et al.* Intestinal crypt homeostasis results from neutral competition between symmetrically dividing Lgr5 stem cells. *Cell* **143,** 134–144 (2010).
17. Zomer, A. *et al.* Intravital imaging of cancer stem cell plasticity in mammary tumors. *Stem Cells* **31,** 602–606 (2013).
18. Ignatius, M. S. *et al.* In vivo imaging of tumor-propagating cells, regional tumor heterogeneity, and dynamic cell movements in embryonal rhabdomyosarcoma. *Cancer Cell* **21,** 680–693 (2012).
19. White, R. M. *et al.* Transparent adult zebrafish as a tool for in vivo transplantation analysis. *Cell Stem Cell* **2,** 183–189 (2008).
20. Feng, H. *et al.* T-lymphoblastic lymphoma cells express high levels of BCL2, S1P1, and ICAM1, leading to a blockade of tumor cell intravasation. *Cancer Cell* **18,** 353–366 (2010).
21. Sander, J. D. *et al.* Selection-free zinc-finger-nuclease engineering by context-dependent assembly (CoDA). *Nat. Methods* **8,** 67–69 (2011).
22. Tang, Q. *et al.* Optimized cell transplantation using adult rag2 mutant zebrafish. *Nat. Methods* **11,** 821–824 (2014).
23. Langenau, D. M. *et al.* Myc-induced T cell leukemia in transgenic zebrafish. *Science* **299,** 887–890 (2003).
24. Zhu, S. *et al.* Activated ALK collaborates with MYCN in neuroblastoma pathogenesis. *Cancer Cell* **21,** 362–373 (2012).
25. Langenau, D. M. *et al.* Effects of RAS on the genesis of embryonal rhabdomyosarcoma. *Genes Dev.* **21,** 1382–1395 (2007).
26. Patton, E. E. *et al.* BRAF mutations are sufficient to promote nevi formation and cooperate with p53 in the genesis of melanoma. *Curr. Biol.* **15,** 249–254 (2005).
27. Ceol, C. J. *et al.* The histone methyltransferase SETDB1 is recurrently amplified in melanoma and accelerates its onset. *Nature* **471,** 513–517 (2011).
28. Tobia, C., Gariano, G., De Sena, G. & Presta, M. Zebrafish embryo as a tool to study tumor/endothelial cell cross-talk. *Biochim. Biophys. Acta* **1832,** 1371–1377 (2013).
29. Zhao, C. *et al.* A novel xenograft model in zebrafish for high-resolution investigating dynamics of neovascularization in tumors. *PLoS ONE* **6,** e21768 (2011).
30. Michalet, X. *et al.* Quantum dots for live cells, in vivo imaging, and diagnostics. *Science* **307,** 538–544 (2005).
31. Mullighan, C. G. *et al.* Genomic analysis of the clonal origins of relapsed acute lymphoblastic leukemia. *Science* **322,** 1377–1380 (2008).
32. Clemente, M. J. *et al.* Clonal drift demonstrates unexpected dynamics of the T-cell repertoire in T-large granular lymphocyte leukemia. *Blood* **118,** 4384–4393 (2011).
33. Bahlis, N. J. Darwinian evolution and tiding clones in multiple myeloma. *Blood* **120,** 927–928 (2012).
34. Ding, L. *et al.* Clonal evolution in relapsed acute myeloid leukaemia revealed by whole-genome sequencing. *Nature* **481,** 506–510 (2012).
35. Landau, D. A. *et al.* Evolution and impact of subclonal mutations in chronic lymphocytic leukemia. *Cell* **152,** 714–726 (2013).
36. Blackburn, J. S. *et al.* Clonal evolution enhances leukemia-propagating cell frequency in T cell acute lymphoblastic leukemia through Akt/mTORC1 pathway activation. *Cancer Cell* **25,** 366–378 (2014).
37. Lopez-Garcia, C., Klein, A. M., Simons, B. D. & Winton, D. J. Intestinal stem cell replacement follows a pattern of neutral drift. *Science* **330,** 822–825 (2010).
38. Schepers, A. G. *et al.* Lineage tracing reveals Lgr5+ stem cell activity in mouse intestinal adenomas. *Science* **337,** 730–735 (2012).
39. Barth, A., Wanek, L. A. & Morton, D. L. Prognostic factors in 1,521 melanoma patients with distant metastases. *J. Am. Coll. Surg.* **181,** 193–201 (1995).
40. Dadras, S. S. *et al.* Tumor lymphangiogenesis: a novel prognostic indicator for cutaneous melanoma metastasis and survival. *Am. J. Pathol.* **162,** 1951–1960 (2003).
41. Goswami, R. S. *et al.* Hotspot mutation panel testing reveals clonal evolution in a study of 265 paired primary and metastatic tumors. *Clin. Cancer Res.* **21,** 2644–2651 (2015).
42. Herlyn, M. Human melanoma: development and progression. *Cancer Metastasis Rev.* **9,** 101–112 (1990).
43. Shi, H. *et al.* Acquired resistance and clonal evolution in melanoma during BRAF inhibitor therapy. *Cancer Discov.* **4,** 80–93 (2014).
44. Patsialou, A. *et al.* Intravital multiphoton imaging reveals multicellular streaming as a crucial component of *in vivo* cell migration in human breast tumors. *Intravital* **2,** e25294 (2013).
45. Dovas, A., Patsialou, A., Harney, A. S., Condeelis, J. & Cox, D. Imaging interactions between macrophages and tumour cells that are involved in metastasis in vivo and in vitro. *J. Microsc.* **251,** 261–269 (2013).
46. Stoletov, K. *et al.* Visualizing extravasation dynamics of metastatic tumor cells. *J. Cell Sci.* **123,** 2332–2341 (2010).
47. Hulit, J. *et al.* The use of fluorescent proteins for intravital imaging of cancer cell invasion. *Methods Mol. Biol.* **872,** 15–30 (2012).
48. Burrell, K. *et al.* A novel high-resolution in vivo imaging technique to study the dynamic response of intracranial structures to tumor growth and therapeutics. *J. Vis. Exp.* e50363 (2013).
49. Chapman, A. *et al.* Heterogeneous tumor subpopulations cooperate to drive invasion. *Cell Rep.* **8,** 688–695 (2014).
50. Siclari, V. A. & Qin, L. Targeting the osteosarcoma cancer stem cell. *J. Orthop. Surg. Res.* **5,** 78 (2010).
51. Gilbertson, R. J. & Rich, J. N. Making a tumour's bed: glioblastoma stem cells and the vascular niche. *Nat. Rev. Cancer* **7,** 733–736 (2007).

52. Shah, S. P. *et al.* The clonal and mutational evolution spectrum of primary triple-negative breast cancers. *Nature* **486,** 395–399 (2012).
53. Curtis, C. *et al.* The genomic and transcriptomic architecture of 2,000 breast tumours reveals novel subgroups. *Nature* **486,** 346–352 (2012).
54. Yachida, S. *et al.* Distant metastasis occurs late during the genetic evolution of pancreatic cancer. *Nature* **467,** 1114–1117 (2010).
55. Campbell, P. J. *et al.* The patterns and dynamics of genomic instability in metastatic pancreatic cancer. *Nature* **467,** 1109–1113 (2010).
56. Sottoriva, A. *et al.* Intratumor heterogeneity in human glioblastoma reflects cancer evolutionary dynamics. *Proc. Natl Acad. Sci. USA* **110,** 4009–4014 (2013).
57. Marusyk, A. *et al.* Non-cell-autonomous driving of tumour growth supports sub-clonal heterogeneity. *Nature* **514,** 54–58 (2014).
58. Rehemtulla, A. *et al.* Rapid and quantitative assessment of cancer treatment response using in vivo bioluminescence imaging. *Neoplasia* **2,** 491–495 (2000).
59. Edinger, M. *et al.* Advancing animal models of neoplasia through *in vivo* bioluminescence imaging. *Eur. J. Cancer* **38,** 2128–2136 (2002).
60. Sato, A., Klaunberg, B. & Tolwani, R. *In vivo* bioluminescence imaging. *Comp. Med.* **54,** 631–634 (2004).
61. Meeker, N. D., Hutchinson, S. A., Ho, L. & Trede, N. S. Method for isolation of PCR-ready genomic DNA from zebrafish tissues. *Biotechniques* **43,** 610, 612, 614 (2007).
62. Wang, Y. *et al.* Moesin1 and Ve-cadherin are required in endothelial cells during in vivo tubulogenesis. *Development* **137,** 3119–3128 (2010).
63. Smith, A. C. *et al.* High-throughput cell transplantation establishes that tumor-initiating cells are abundant in zebrafish T-cell acute lymphoblastic leukemia. *Blood* **115,** 3296–3303 (2010).
64. Langenau, D. M. *et al.* Co-injection strategies to modify radiation sensitivity and tumor initiation in transgenic Zebrafish. *Oncogene* **27,** 4242–4248 (2008).
65. Berghmans, S. *et al.* tp53 mutant zebrafish develop malignant peripheral nerve sheath tumors. *Proc. Natl Acad. Sci. USA* **102,** 407–412 (2005).
66. Blackburn, J. S., Liu, S. & Langenau, D. M. Quantifying the frequency of tumor-propagating cells using limiting dilution cell transplantation in syngeneic zebrafish. *J. Vis. Exp.* e2790 (2011).
67. Tenente, I. M., Tang, Q., Moore, J. C. & Langenau, D. M. Normal and malignant muscle cell transplantation into immune compromised adult zebrafish. *J. Vis. Exp.* e52597 (2014).
68. Pugach, E. K., Li, P., White, R. & Zon, L. Retro-orbital injection in adult zebrafish. *J. Vis. Exp.* e1645 (2009).

Acknowledgements

This work was supported by Alex's Lemonade Stand Foundation (J.S.B., M.S.I., D.M.L.), the Live Like Bella Foundation for Childhood Cancer (D.M.L.), American Cancer Society (D.M.L.), the MGH Howard Goodman Fellowship (D.M.L.) and NIH grants R24OD016761, R01CA154923 and U54CA168512. Q.T. is funded by the China Scholarship Council. I.M.T. is funded by Fundação para a Ciênca e Tecnologia, Portugal (SFRH/BD/51288/2010). We thank the Specialized Histopathology Services at Massachusetts General Hospital and the Dana-Farber/Harvard Cancer Center (P30 CA06516), Massachusetts General Hospital Cancer Center/Molecular Pathology Confocal Core and the Harvard Center for Biological Imaging for technical support; Drs Fabrice Laroche and Hui Feng for helpful suggestions; Brian Millet and Anthony Sinagra for helpful statistical advice.

Author contributions

Q.T. and D.M.L. designed the study. Q.T., J.C.M., M.S.I. and J.S.B. performed the experiments. M.S.I., J.S.B., I.M.T., M.N.H., E.G.G., N.T.Y., C.B., S.H., A.T.L. and Y.H. provided reagents and animals. Q.T. and D.M.L. analysed the data and wrote the manuscript with input from all authors.

Additional information

Supplementary Information accompanies this paper at http://www.nature.com/naturecommunications

Competing financial interests: The authors declare no competing financial interests.

Reprints and permission information is available online at http://npg.nature.com/reprintsandpermissions/

How to cite this article: Tang, Q. *et al.* Imaging tumour cell heterogeneity following cell transplantation into optically clear immune-deficient zebrafish. *Nat. Commun.* 7:10358 doi: 10.1038/ncomms10358 (2016).

This work is licensed under a Creative Commons Attribution 4.0 International License. The images or other third party material in this article are included in the article's Creative Commons license, unless indicated otherwise in the credit line; if the material is not included under the Creative Commons license, users will need to obtain permission from the license holder to reproduce the material. To view a copy of this license, visit http://creativecommons.org/licenses/by/4.0/